Antenna Systems for Vehicle-to-Everything (V2X) Communication at 5.9 GHz Considering the Vehicle Body

M. Sc. Miguel Angel Bueno Diez
geboren in Barcelona, Katalonien

Vollständiger Abdruck der von der Fakultät für Elektrotechnik und Informationstechnik der Universität der Bundeswehr München zur Erlangung des akademischen Grades eines

Doktor-Ingenieurs
(Dr.-Ing.)

genehmigten Dissertation.

Vorsitzender des Promotionsausschusses:	Prof. Dr.-Ing. Wilfrid Pascher
1. Berichterstatter:	Prof. Dr.-Ing. Stefan Lindenmeier
2. Berichterstatter:	Prof. Dr.-Ing. Jan Hesselbarth

Die Dissertation wurde am 12.03.2020 bei der Universität der Bundeswehr München eingereicht und durch die Fakultät für Elektrotechnik und Informationstechnik am 22.10.2020 angenommen.
Die mündliche Prüfung fand am 20.11.2020 statt.

Neubiberg, den 01. Dezember 2020

Abstract

Vehicle-to-Everything (V2X) communication was born as a worldwide service, within the framework of Intelligent Transportation Systems (ITS) in the 5.9 GHz spectrum, to reduce fatal accidents and keep the traffic flowing in time-varying environments. The reasonably high frequency of operation with regard to most other automotive applications offers short range communications (up to 1 km) with a high data rate, low weather-dependence, and global compatibility and interoperability. However, the increasing trend to miniaturize and hide the antennas to preserve the aesthetics of the automobile has a negative impact on the antenna performance. This framework represents a great challenge from the antenna engineering perspective, and it opens the door to numerous investigations on new antenna concepts and placements to cope with the demanding requirements inherent in a safety system. Omnidirectional radiation patterns are required to be able to receive and send any kind of alert in any direction of space in the horizontal plane in which car traffic runs. The circularity of the far-field patterns in the horizontal plane is notably affected by the proximity of the V2X antenna to other neighboring antennas and by the actual location of the antenna in the automobile. This dissertation investigates the several electromagnetic propagation effects in the 5.9 GHz ITS spectrum affecting the performance of the antennas when considering the vehicle body and the different materials of the car in close proximity to the antennas. The dissertation also investigates different solutions for various antenna placements. From shark-fin antennas on the roof of the car through various mounting positions to implement decentralized macro-diversity antenna systems, to completely hidden micro-diversity antenna systems underneath the roof of the car. The performance of the different antenna solutions is analyzed by means of statistics and exploratory data analysis (EDA) to characterize the stochastic behavior of the radiation patterns at 5.9 GHz under the influence of the vehicle. Full-wave, asymptotic and hybrid simulation techniques are performed depending on the nature of the electromagnetic issue and the results are corroborated by measurements done in an anechoic chamber when dealing with stand-alone antennas or in an Open Area Test Site (OATS) when measuring with the vehicle. Statistical tests are computed to analyze the agreement between measurements and simulations.

KURZFASSUNG

Vehicle-to-Everything (V2X) Kommunikation wurde als weltweiter Dienst im Rahmen für intelligente Verkehrssysteme (ITS) im 5,9-GHz-Spektrum etabliert, um tödliche Unfälle zu reduzieren und den Straßenverkehr in zeitvariablen Umgebungen aufrechtzuerhalten. Die relativ hohe Frequenz im Vergleich zu den meisten anderen Automobilanwendungen bietet eine Kurzstreckenkommunikation (bis zu 1 km) mit hoher Datenrate, geringer Wetterabhängigkeit und globaler Kompatibilität und Interoperabilität. Der zunehmende Trend zur Miniaturisierung und Verdeckung der Antennen zur Erhaltung der Ästhetik des Automobils wirkt sich jedoch negativ auf die Antennenleistung aus. Dieser stellt aus Sicht der Antennentechnik eine große Herausforderung dar und öffnet die Tür zu zahlreichen Untersuchungen von neuen Antennenkonzepten und Platzierungen, um den hohen Anforderungen an ein Sicherheitssystem gerecht zu werden. Omnidirektionale Strahlungsdiagramme sind erforderlich, um jede Art von Alarm in jeder Raumrichtung in der horizontalen Ebene, in der der Autoverkehr läuft, empfangen und senden zu können. Die Rundheit der Antennen-Fernfelddiagramme in der horizontalen Ebene wird insbesondere durch die Nähe der V2X-Antenne zu anderen benachbarten Antennen und durch die tatsächliche Position der Antenne im Automobil beeinflusst. Diese Dissertation untersucht die verschiedenen elektromagnetischen Ausbreitungseffekte im 5,9 GHz ITS-Spektrum, die sich auf die Leistung der Antennen auswirken, wenn man die Fahrzeugkarosserie und die verschiedenen Materialien des Autos in der Nähe der Antenne mitbetrachtet. Die Dissertation untersucht auch verschiedene Lösungen für diverse Antennenplatzierungen. Von Haifischflossenantennen auf dem Autodach über unterschiedliche Einbaulagen zur Realisierung dezentraler Makro-Diversity-Antennensysteme bis hin zu komplett versteckten Mikro-Diversity-Antennensystemen unter dem Autodach. Die Leistungsfähigkeit der verschiedenen Antennenlösungen wird mittels Statistik und explorativer Datenanalyse (EDA) analysiert, um das stochastische Verhalten der Strahlungsdiagramme bei 5,9 GHz unter dem Einfluss des Fahrzeugs zu charakterisieren. Vollwellen-, asymptotische und hybride Simulationstechniken werden je nach Art des elektromagnetischen Problems durchgeführt und die Ergebnisse werden bei Einzelantennen durch Messungen im Absorberraum oder bei Messungen mit dem Fahrzeug in einem Freifeld-Testgelände (Open Area Test Site, OATS auf Englisch) verifiziert. Statistische Tests werden durchgeführt, um die Übereinstimmung zwischen Messung und Simulation zu analysieren.

Dedication and acknowledgements

Firstly, I would like to express my sincere gratitude to my Ph.D. advisor Prof. Dr.-Ing. habil. Stefan Lindenmeier for the continuous support of my Ph.D. study and related research. For his patience, immense motivation, and his countless excellent explanations on antenna theory, design and related antenna diversity techniques. For his excellent mathematical proofs based on S-parameter theory and statistical derivations. His guidance helped me in all the time of research and his oratory and conviction skills taught me to know how to highlight the advantages and unique points of each of the concepts researched.

A special thanks to Prof. Dr.-Ing. Jan Hesselbarth for being part of the dissertation chair and for his valuable corrections of the thesis. For his confidence in me from the beginning of my career and for introducing me to the fascinating world of antenna engineering.

My warmest thanks to Prof. Dr.-Ing. habil. Wilfrid Pascher for the long and interesting theoretical discussions on electromagnetic propagation and his reviews of the conference papers. Thanks to him I can say that I have been able to develop a certain ability to see and almost feel the behaviour of electromagnetic waves. Thank you also for giving me the opportunity to participate in the teaching activities, which gave me a lot of fun and expertise.

My sincere thanks also goes to Apl. Prof. Dr.-Ing. Leopold Reiter for the technical discussions and the immense experimental guidance, for his patience and for the countless references to excellent books, scientific journals and articles. With him I have really learned the concept of learning by doing, and I still dream of him publishing a book with all that practical experience that no other book has taught me.

Equally, I would like to thank Apl. Prof. Dr.-Ing. habil. Jochen Hopf, that together with Apl. Prof. Dr.-Ing. Leopold Reiter, not only did we spent an excellent time playing music, but I am also deeply indebted to them for the amount of hours I have stolen from their time on the open area test site and the radome. I think over time I have learned to love the smell of scorched electronics.

I also sincerely thank Dr.-Ing. Simon Senega for the interesting and fruitful technical discussions with him with regard to antenna diversity and in general on radio frequency topics.

Special thanks to Oliver Kindt and Markus Mittermeier for their great professionalism and precision in the construction of antenna prototypes and PCB's. Some of their prototypes could even be exhibited in art galleries.

My most sincere thanks to all my wonderful colleagues for the friendly and inspiring working atmosphere and for providing a helping hand whenever it was needed. A special mention to Dr.-Ing. Alexander Böge, Dipl. Ing. Ali Nassar, and Dipl. Ing. Sertan Hastürkoğlu for some important reasons. To Dr.-Ing. Alexander Böge for welcoming me as an office-mate during the dissertation and for the countless experiences lived with him that have made him a friend and part of my life. Thanks to him, I feel a little more Bavarian. To Dipl. Ing. Ali Nassar for all during this years, for being a friend and an example to follow, for the long hours and days spent at the university, no one knows what I mean better than you, and for the discipline in the gym routine.

To Dipl. Ing. Sertan Hastürkoğlu for his extensive RF knowledge, for the interesting technical discussions and exchange of books, for the good times spent laughing, and for his generous help. To all of you, one way or another, I will always be indebted to you.

I also want to thank all my colleagues at the Institut für Hochfrequenztechnik (IHF) at the Universität Stuttgart, especially to Dipl. Ing. Tobias Blersch for being my first personal CST trainer and office-mate during my master's thesis, and to Dipl. Ing. Robert Vilaltella for being like a brother during the Erasmus Programme.

And last but not least, my most loving thanks to all my friends in Munich and Barcelona and to my lovely family. To my parents for teaching me to discern between good and bad and for their continuous encouragement in all aspects of life. To my sister for teaching me the ability to reason and for being an example of success to follow. And to Cristina, for her warmth, patience and enormous support.

To all of them, my sincerest thanks.

TABLE OF CONTENTS

List of Abbreviations

3GPP	3rd Generation Partnership Project
5GAA	5th Generation Automotive Association
ACK	Acknowledgement
AI	Artificial Intelligence
AM	Amplitude Modulation
AP	Access Point
ARIB	Association Of Radio Industries And Businesses
AUT	Antenna Under Test
AWGN	Additive White And Gaussian Noise
CAD	Computer Aided Design
CDF	Cumulative Distribution Function
CEN	European Committee For Standardization (Comité Européen De Normalisation)
CPW	Co-Planar Waveguide
C-V2X	Cellular-Vehicle-to-Everything
C-ITS	Cooperative-Intelligent Transportation System
C2C	Car-to-Car
C2X	Car-to-Everything
DC	Direct Current
DCS	Digital Cellular System
DG	Diversity Gain
DOA	Direction Of Arrival
DSRC	Dedicated Short Range Communication
ECC	Envelope Correlation Coefficient
ECU	Electronic Control Unit
EDA	Exploratory Data Analysis
EGC	Equal Gain Combining
EIRP	Effective Isotropic Radiated Power
ESD	Electrostatic Discharge
ETSI	European Telecommunications Standards Institute
FAKRA	Automobile Expert Group (Fachkreis Automobil)
FCC	U.S. Federal Communications Commission
FDM	Frequency-Division Multiplexing
FEM	Finite Element Method
FIT	Finite Integration Technique
FM	Frequency Modulation
FSS	Frequency Selective Surface
GLONASS	Global Navigation Satellite System (Global'naya Navigatsionnaya Sputnikovaya Sistema)
GNSS	Global Navigation Satellite System
GO	Geometrical Optics
GPS	Global Positioning System
GPU	Graphic Processing Unit
GSM	Global System For Mobile Communications
GTD	Geometrical Theory Of Diffraction
ICNIRP	International Commission On Non-Ionizing Radiation Protection
IEEE	Institute Of Electrical And Electronics Engineers
IP	Internet Protocol
IR	Infrared
ISM	Industrial, Scientific, And Medical
ITS	Intelligent Transportation System

ITU-R	International Telecommunication Union Radiocommunication Sector
LOS	Line-Of-Sight
LTE	Long Term Evolution
MIMO	Multiple Input Multiple Output
MOM	Method Of Moments
MPI	Message Passing Interface
MRC	Maximum-Ratio Combining
NASTRAN	Nasa Structural Analysis System
NLOS	Non-Line-Of-Sight
OATS	Open Area Test Site
OFDM	Orthogonal Frequency-Division Multiplexing
OFDMA	Orthogonal Frequency-Division Multiple Access
OSI	Open System Interconnection
PBA	Perfect Boundary Approximation
PCB	Printed Circuit Board
PDF	Probability Density Function
PEC	Perfect Electric Conductor
PVB	Polyvinyl Butyryl
Q-FACTOR	Quality Factor
Q-Q	Quantile-Quantile
QAM	Quadrature Amplitude Modulation
RAM	Random Access Memory
RCS	Radar Cross-Section
RF	Radio Frequency
RKE	Remote Keyless Entry
RMS	Root Mean Square
RSU	Road Side Unit
SAE	Society Of Automotive Engineers
SB	Shadow Boundary
SBR	Shooting And Bouncing Rays
SC	Switch Or Selection Combining
SC-FDM	Single Carrier Frequency Division Multiplex
SDARS	Digital Audio Radio Service
SIM	Subscriber Identity Module
SMA	SubMiniature Version A
SMB	SubMiniature Version B
SNR	Signal-to-Noise Ratio
SUV	Sport Utility Vehicle
TCP	Transmission Control Protocol
TDM	Time-Division Multiplexing
TE	Transverse Electric
TEM	Transverse Electromagnetic
TM	Transverse Magnetic
TST	Thin Sheet Technique
UDP	User Datagram Protocol
UHF	Ultra High Frequency
UMTS	Universal Mobile Telecommunications System
UTD	Uniform Geometrical Theory Of Diffraction
UV	Ultraviolet
UWB	Ultra-Wideband
V2I	Vehicle-to-Infrastructure
V2N	Vehicle-to-Network
V2V	Vehicle-to-Vehicle
V2X	Vehicle-to-Everything
VSWR	Voltage Standing Wave Ratio
WAVE	Wireless Access In Vehicular Environments
WCDMA	Wideband Code Division Multiple Access
WIMAX	Worldwide Interoperability For Microwave Access
WLAN	Wireless Local Area Network
XPR	Cross-Polarization Ratio

CHAPTER 1

INTRODUCTION AND THESIS OVERVIEW

Nowadays, and with the development of radio communication technology for Intelligent Transportation Systems (ITS) during the past decade, the car has become intelligent. By means of different technologies surrounding the vehicles based on artificial intelligence (AI), image recognition, and multiple and sophisticated sensors, cars become increasingly autonomous. A new critical technology in making autonomous vehicles a reality is known by many different acronyms or initials (e.g., V2X, V2V, V2I, C2X, C2C, DSRC, ITS, C-ITS, C-V2X; where for the first five initials V means vehicle, C means car, X means everything, and I means infrastructure. DSRC means Dedicated Short Range Communications. ITS, Intelligent Transportation System. In C-ITS, C means cooperative, and in the last one, C means cellular). For brevity and consistency, the generic term V2X (Vehicle-to-Everything) will be used throughout this thesis, and covers both Vehicle-to-Vehicle (V2V) and Vehicle-to-Infrastructure (V2I) communications. The existing sensors are a complementary technology to V2X and add redundancy to improve the robustness of such safety-related systems.

V2X encompasses a broad set of standards and technologies in the 5.9 GHz ITS spectrum (C-band) that allow vehicles to communicate with each other and with other road infrastructures to aid the driver and enhance the driving experience, as depicted in Fig. 1.1. Born as a worldwide initiative to reduce fatal accidents in the ever increasing road traffic, V2X is gaining momentum and broad ecosystem support from automotive and telecom industries. V2X also allows greener and more efficient transportation, managing to keep the traffic flowing in time-varying environments like urban scenarios, and bringing fuel savings and thereby a reduction of emissions. Non-safety application are also transforming the in-vehicle experience, bringing commercial wireless applications into the car. The technical justification for the 5 GHz spectrum lies on the fact that it can offer communications with a high data rate, ranges up to 1 km, low weather-

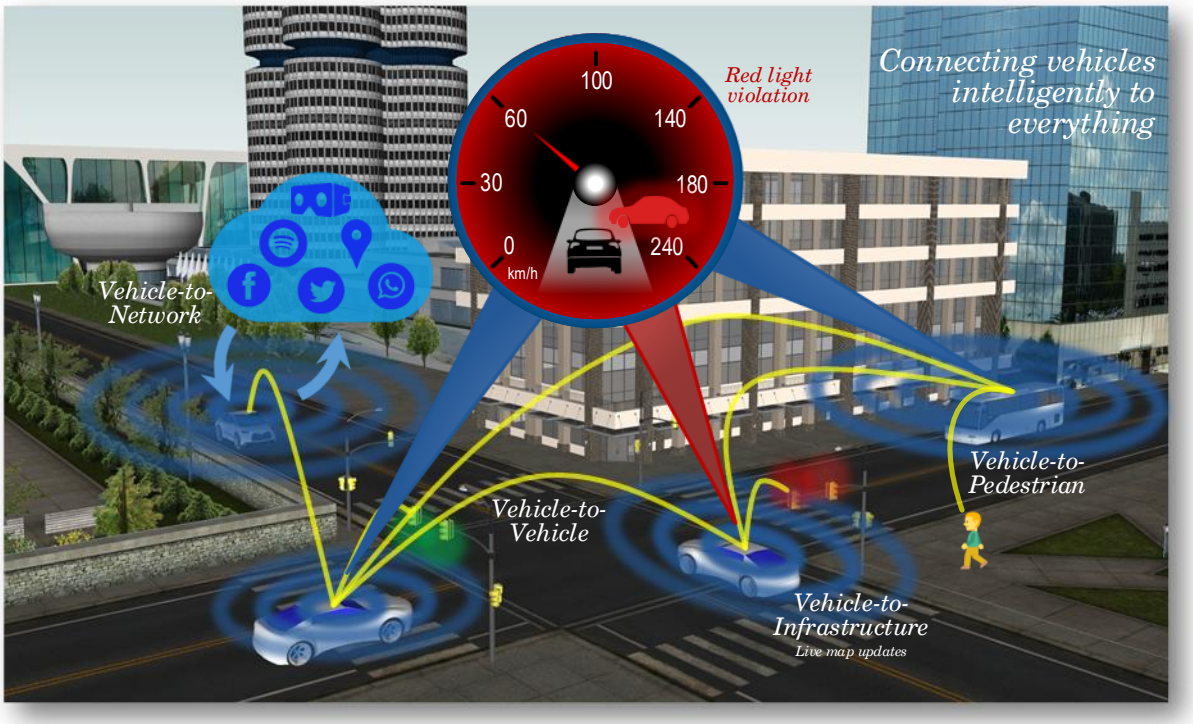

Figure 1.1: V2X overview: Connecting vehicles intelligently to everything (other vehicles, cloud, and surroundings), transforming the in-vehicle experience, and paving the road to autonomous driving.

dependence, and global compatibility and interoperability. A dedicated spectrum must be used for safety critical ITS applications. Therefore, an amendment to the WLAN IEEE 802.11a, the IEEE 802.11p, is created for such purposes. The reason lies on the fact that sharing the spectrum with users of public WLAN channels causes unacceptable levels of interference to safety critical applications.

With the increasingly accuracy improvement of position and speed data given by Global Positioning Systems (GPS) combined with high-resolution maps, dynamic data of the surroundings of the car can be produced with constantly updates, enabling situational awareness and the capability to identify potential hazards.

A comparison between the different levels of driving automation according to the Society of Automotive Engineers (SAE) showing the evolution of V2X towards autonomous driving is shown in Fig. 1.2 [100]. In September 2016, a group of leading companies from the automotive and telecommunication industries formed the 5th Generation Automotive Association (5GAA) [11] in order to accelerate the development and deployment of C-V2X technology around the world, and to contribute to pave the road to autonomous driving.

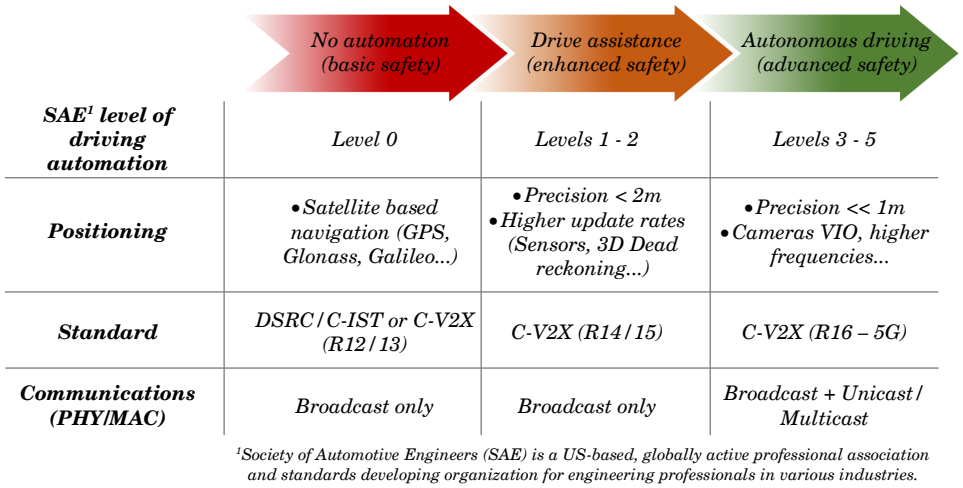

Figure 1.2: V2X evolution towards autonomous driving (5G) [100].

1.1 Motivation. Vehicle-to-Everything (V2X) Communication: Shaping the Future of Automotive

Since more than a decade, the V2X established technologies have been the US-developed Dedicated Short-Range Communications (DSRC) and the European Cooperative Intelligent Transport Systems (C-ITS). The development of the V2X standards has taken so long that the mobile communications industry has seized the opportunity to break into the market with its own standard, the Cellular-V2X (C-V2X). The C-V2X standard published as Release 14 (september 2016), was developed by the 3rd Generation Partnership Project (3GPP), which was created in 1998 with its first development being 3G (2000) and followed by several evolutions up to the next expected 5G mobile standard [59].

In 1999, the US Federal Communications Commission (FCC) allocated 75 MHz in the 5.850 GHz to 5.925 GHz band for high-priority road safety and traffic management purposes [35], and latter the European Telecommunications Standards Institute (ETSI) allocated 70 MHz in the 5.855 GHz to 5.925 GHz band for similar safety purposes and non-safety applications [2]. In Japan, the 5.8 GHz band is in use for toll collection applications, and the 700 MHz band is being investigated as a potential candidate [10]. A summary of the spectrum allocation in various regions around the world can be seen in Fig. 1.3. The industrial, scientific, and medical radio band (ISM band) is also shown in the figure, which corresponds to the frequency band not intended for communication closest to the V2X bands around the world.

Table 1.1 compares different aspects of V2X communications in Japan, USA, and Europe, emphasizing the main RF characteristics in terms of frequency range, number of channels, waveform, data rate per channel, output power, type of communication, and upper protocol in the stack, according to the standards that apply in each region of the world.

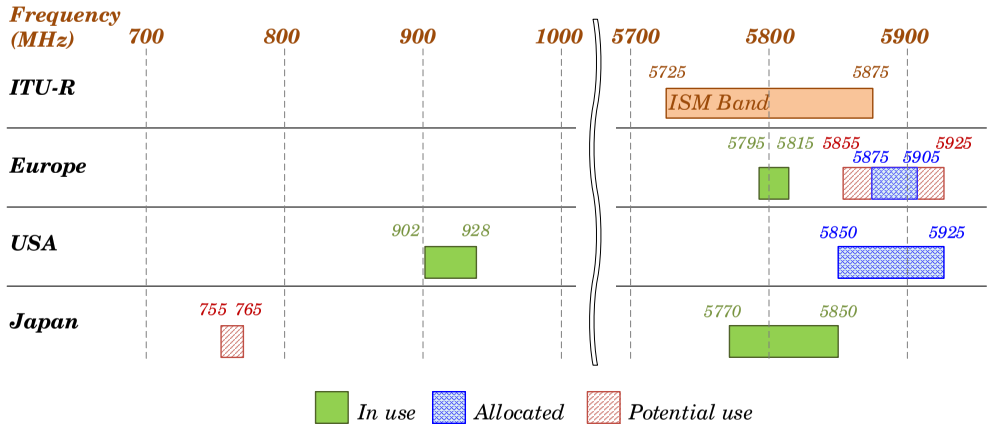

Figure 1.3: V2X frequency spectrum allocation in various regions worldwide [2, 35].

	Japan	USA	Europe
Standard (committee)	ITS-Forum	IEEE 802.11p/1609.x	CEN/ETSI EN 302 663
Frequency range	755 - 765 MHz	5850 - 5925 MHz	5855 - 5925 MHz
Number of channels	One 10 MHz channel	Seven 10 MHz channels (Two 20 MHz channels formed by combining 10 MHz channels)	Seven 10 MHz channels
Waveform	OFDM (For C-V2X R14/15, SC-FDM; For R16, likely OFDMA but many options available)		
Data rate per channel	3 - 18 Mbit/s	3 - 27 Mbit/s	3 - 27 Mbit/s
Output power	20 dBm (Antenna input)	23 - 33 dBm (EIRP)[1]	23 - 33 dBm (EIRP)
Communication	One direction multicasting service (broadcast without ACK)	One direction multicasting service, One to Multicommunication, Simplex communication (broadcast without ACK, multicast, unicast with ACK)	
Upper protocol	ARIB STD-T109	WAVE (IEEE 1609)/TCP/IP)	ETSI EN 302 665 (incl. e.g. GeoNetworking) TCP/UDP/IP

Table 1.1: Global overview of V2X communication comparing different aspects in Japan, USA, and Europe [136].

[1]Equivalent Isotropically Radiated Power (EIRP) is the product of transmitter power and the antenna gain in a given direction relative to an isotropic antenna of a radio transmitter.

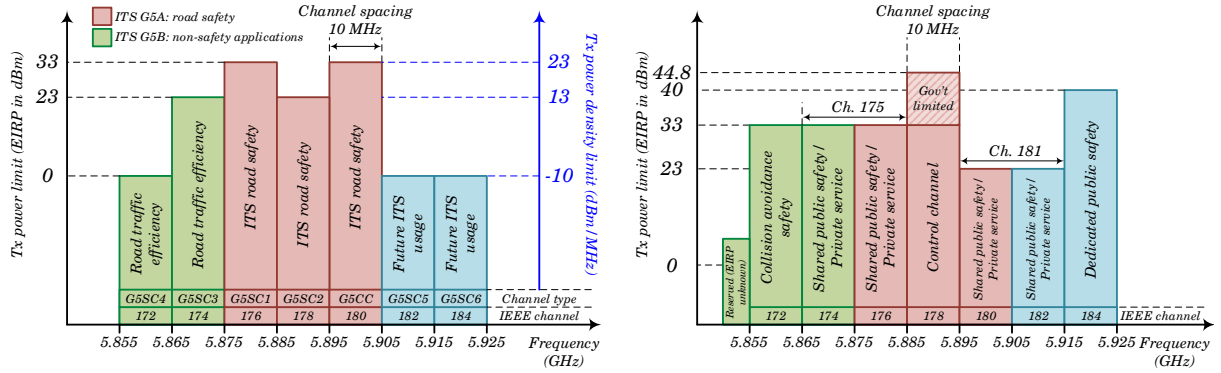

(a) Europe V2X channel allocation [2].

(b) USA V2X/DSRC channel allocation [35].

Figure 1.4: V2X channel plans in Europe and USA (not to scale).

Fig. 1.4 illustrates the V2X channel plans in Europe and USA and the requirements for maximum limit of mean spectral power density (in dBm/MHz) in Europe and the transmitted power limit in dB m considering a channel spacing of 10 MHz for the plans of Europe and USA. The channel allocation in Japan for V2X safety applications is not graphically shown due to its simplicity, since it is composed of only one 10 MHz channel in the 700 MHz band centered at 760 MHz. The requirement for maximum limit of mean spectral power density (in mW/MHz) for the transmitter antenna is specified to be ≤10 mW per 1 MHz bandwidth. The purpose of using channels with a bandwidth of 10 MHz (instead of 20 MHz as in IEEE 802.11a) is to obtain larger communication ranges and to reduce the symbol interference. Separating the 20 MHz channel bandwidth into two 10 MHz channels increases the Guard Interval (GI), which is necessary to cope with the severe multipath in vehicular environments.

The IEEE 802.11p amendment to the IEEE standard 802.11 for WiFi communication developed during the years 2005 to 2012 [2], on which the physical layer (PHY layer in terms of the Open Systems Interconnection (OSI) model) of all standards are based, reduces the impact of Doppler shifts and multipath fading in the outdoor, cluttered, and high-speed automotive environment. It defines the physical layer in the frequency band around 5.9 GHz. For the higher layers, the Wireless Access in Vehicular Environments (WAVE) and ETSI ITS-G5 standards have been developed in the US and Europe, respectively. Although DSRC and C-ITS are very similar at the physical and data link layers, they diverge significantly at the network and transport level (layers 3 and 4, respectively) depending on regional and/or regulatory issues. C-V2X uses the same 5.9 GHz spectrum as DSRC and C-ITS for device-to-device mode direct communications. However, C-V2X can also operate in the so-called Vehicle-to-Network (V2N) mode, where it uses traditional mobile bands to communicate with the mobile network.

The requirements for V2X communication have been drafted according to an extensive set of ITS-related use cases classified in safety and non-safety applications. Safety applications set the

critical requirements in terms of reliability, maximum latency, and message frequency.

A summary of the different technologies up to date, namely IEEE 802.11p/DSRC and C-V2X in its different releases, with a comparison of their RF characteristics, is given in table 1.2. C-V2X offers enhanced functionality relative to IEEE 802.11p/DSRC adding "in-coverage" technology (device-to-network mode) through the existing cellular network infrastructure along roadways. This new capability over IEEE 802.11p/DSRC (based only on "out-of-coverage" functionality, i.e. direct communications or device-to-device) offers a robust platform to provide the vehicles with enhanced situation awareness through V2I and V2N communications without the need to rely on deployment of new, DSRC-capable infrastructure, and therefore, reducing the overall deployment costs.

When it comes to safety applications, it is very important to ensure enough alert time, transmission range, and reliability to be able to react in time in case of a hazardous situation. C-V2X offers up to a few additional seconds of alert time and more than twice the range of IEEE 802.11p/DSRC, as shown in table 1.2.

Finally, an important distinction between both V2X technologies is the evolution roadmap that exists for C-V2X communications, which will benefit greatly from the advantages of millimeter wave bands used for low-latency high-volume data transfer in 5G technologies (due to the higher spectrum size than that below 6 GHz) that will come over the next few years.

	802.11p	*C-V2X R14/15*	*C-V2X R16 (expected design)*
Specification completed	*Completed*	*R14 completed in 2016. R15 to be completed in 2018*	*Expected for 2019*
Synchronization	*Asynchronous*	*Synchronous*	*Synchronous*
Channel size	*10/20 MHz*	*R14 - 10/20 MHz. R15 - 10/20/Nx20 MHz*	*10/20 MHz and wideband (e.g. 40/60/80/100/... MHz)*
Multiplexing	*TDM only*	*TDM and FDM*	*TDM and FDM possible*
MIMO support	*No support standardized*	*Rx diversity for 2 antennas mandatory. Tx diversity for 2 antennas supported*	*Support up to 8 Tx/Rx antennas. Mandatory support for 2 Tx/Rx antennas. Both diversity and spatial multiplexing supported*
Modulation support	*Up to 64 QAM*	*Up to 64 QAM*	*Up to 256 QAM*
Support for low latency direct communications	✓	✓ *(R14 - 4ms)*	✓ *(≤ 1ms)*
Support for network communications	*Limited (via APs only)*	✓	✓
Can operate without network assistance	✓	✓	✓
SIM-less operation	✓	✓	✓
Coexistence in 5.9 GHz	✓ *(Adjacent channel with 3GPP technology)*	✓ *(Adjacent channel with 802.11p; co-channel coexistence from R14 onwards)*	✓ *(Adjacent channel with 802.11p; co-channel coexistence from R14 onwards and WiFi)*
High mobility support	✓ *Up to relative speeds of 500 km/h with advanced receiver implementation*	✓ *Up to relative speeds of 500 km/h as a minimum requirement*	✓ *Up to relative speeds of 500 km/h as a minimum requirement*
Transmission range 90% error, 280 km/h relative speed	*Up to ≈ 225m*	*Over 450m using direct mode. Very large via cellular infrastructure*	*Over 450m using direct mode. Very large via cellular infrastructure*
Typical transmission frequency for periodic traffic	*Once every 100ms (50ms is also possible)*	*Once every 100ms (20ms is also possible)*	*Supports packet periodicities of a few ms.*
Evolution path	✗	✓	✓ *Compatible with R14/15*

Table 1.2: V2X technologies: Comparison between IEEE 802.11p and C-V2X technologies [100].

1.2 Problem Statement and Challenges of Automotive V2X Antenna Integration

As stated in the previous section, the potential of V2X communication systems to reduce the number of traffic accident rates and to enhance traffic efficiency on the way to the autonomous car is currently promoting research both in the automotive industry and in the academic sector, accelerating its commercialization for the coming years. Active safety-related communication applications in the context of cooperative ITS require robust and reliable vehicular communication systems in the 5.9 GHz range, whose quality depends on the communication link in terms of antenna frontend performance, vehicle dynamics and channel propagation conditions. The presence of multiple vehicles and scattering objects in the horizontal plane where communication takes place, and the relative high-dynamic channel characteristics with rapidly varying conditions and time-frequency selective fading behavior is affecting the performance of V2X systems.

A crucial aspect to which attention should be paid to ensure reliable safety-related communications is the behavior of the antenna frontend considering its vehicular mounting conditions. Although theory and design of stand-alone antennas are already well characterized, little knowledge has been gained about the performance of such antennas in the 5.9 GHz band when they are placed in conventional automotive mounting positions, as those depicted in Fig. 1.5. This thesis is aimed to cover this gap by reviewing the principal causes of antenna degradation and investigating new cost-effective concepts to overcome the system impairments caused by vehicular antenna integration for V2X communication.

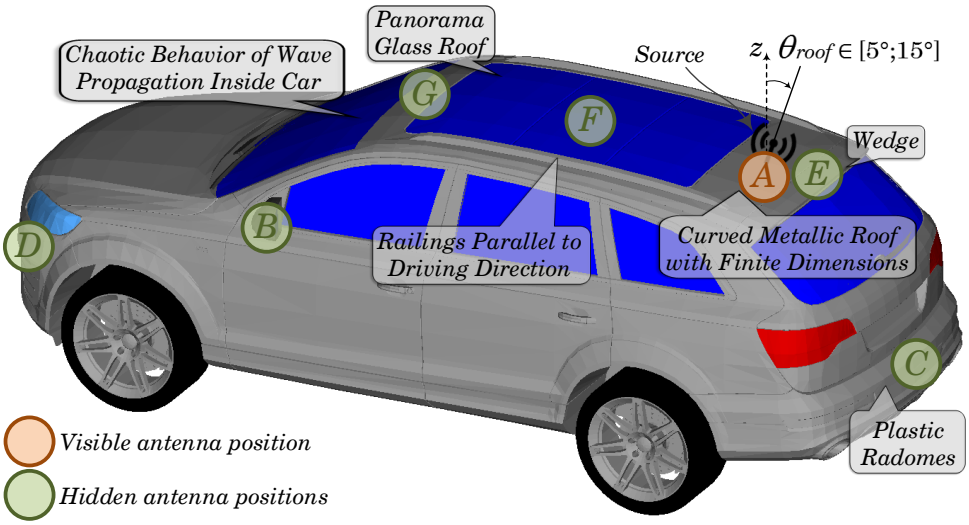

Figure 1.5: V2X antenna mounting positions and relevant vehicle features challenging the antenna integration.

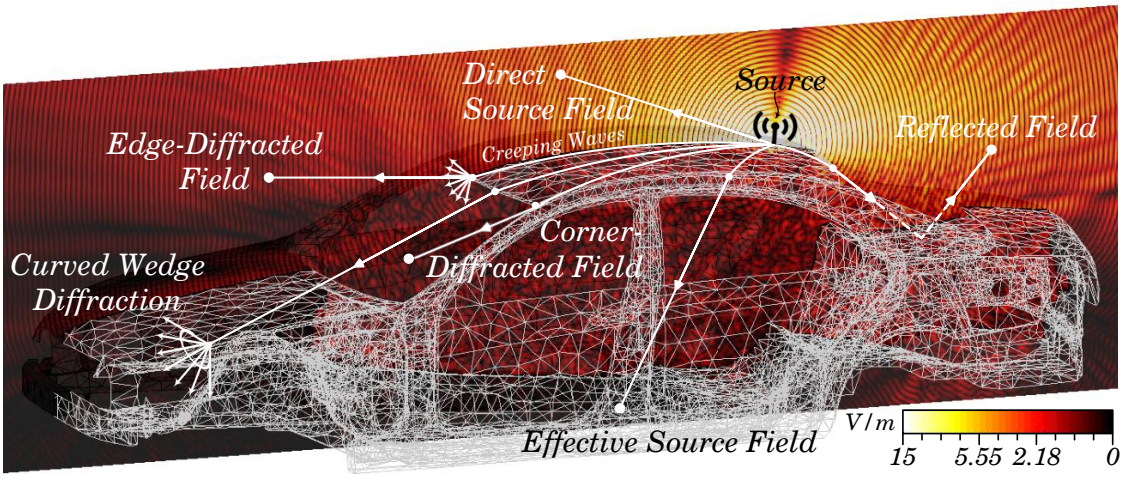

Figure 1.6: V2X wave propagation phenomena for a monopole-like antenna placed on the typical roof-top mounting position in a sedan-type car.

The great amount of different ITS use cases to be covered (e.g. urban scenarios with intersections, rural areas, highways...), and the relative movement and direction of vehicles restricted to the horizontal plane, are requiring terrestrial coverage of the V2X antennas. An omnidirectional coverage for all azimuth angles φ or at least elliptical antenna patterns in azimuth with the semi-major axis oriented in driving direction, both with maximum gain at elevation angles close to θ =90° are highly desired.

The conventional mounting positions for communication antennas defined by the automotive industry degrade the desired radiation patterns required for safety-related applications. A commonly used antenna location due to the reasonably Line-of-Sight (LOS) properties throughout the 360° azimuth angles and its elevation with respect to the ground, is the roof-top position. For aesthetic reasons, the roof-top antenna module is located centered at the back of the vehicle roof near the rear rim, as shown in Fig. 1.6. The roof of the car itself negatively affects the radiation properties of the antenna, even if the antenna had to be placed centered exactly in the middle of the roof. Discontinuities along the roof and deviations from an infinite ground plane, such as the curved designs of modern cars or the edges of the finite roof, distort the required omnidirectional characteristic in the horizontal plane, as illustrated in Fig. 1.6 through a snapshot in time of the electric field distribution of a quarter-wave monopole on the rear roof-top position.

As illustrated in Fig. 1.7, the various types of vehicle bodys (e.g. hatchback, sedan, convertible, SUV, sports car, etc.) and extra equipment (e.g. railings, sunroofs, etc.) is affecting the performance of the antennas in a different way.

With regard to ideal conditions of a flat metallic infinite ground plane and according to Fig. 1.8 A, the vehicle's roof represents a curved finite metallic surface sometimes equipped with non-metallized sunroofs and/or railings oriented in parallel to the driving direction as indicated

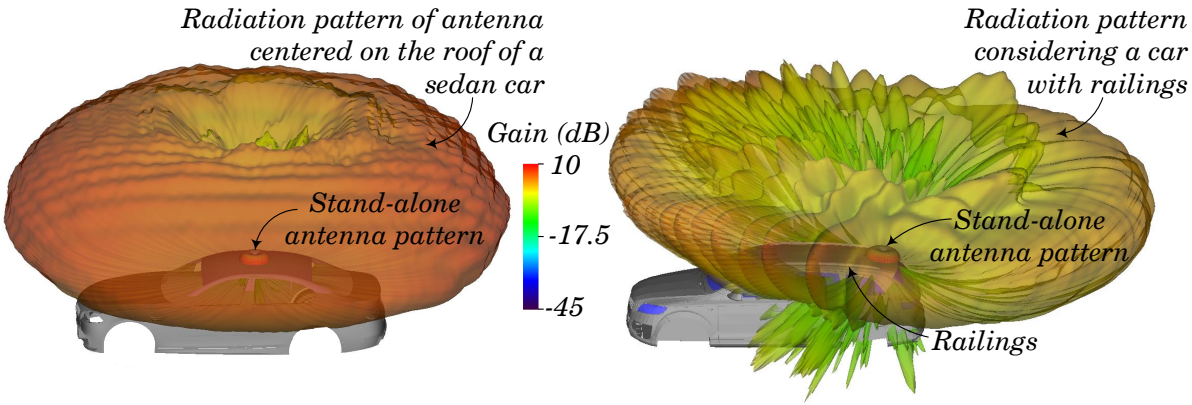

Figure 1.7: 3D radiation patterns of a monopole-like antenna placed centered on the middle of the roof of a sedan-type car (left) and on the commonly used roof-top position of a SUV-type vehicle with railings oriented in parallel to the driving direction (right).

in Fig. 1.5, causing an uplift of the main beam direction of the pattern in elevation to an angular range $\Delta\theta$ between 70° to 80° and an added ripple in the azimuth pattern of about ±1.5 dB if equipped with railings (Fig. 1.8 D). The convex curved roof and the finite bent angle θ_{roof} at the mounting position (typically in the range about 5° to 15° for a common sedan car), reduces the gain progressively in an angular sector of about 180° in driving direction due to shadowing effects up to roughly 5 dB in ±30° around $\varphi = 0°$ (Fig. 1.8 C). Thus, it yields an SNR reduction at the transceiver, worsening the performance of the overall system. This gain is further reduced if the roof is equipped with a glazed roof. Depending on the relative position of the antenna with respect to the sunroof window and its dimensions, up to 15 dB to 25 dB less gain than the case where the antenna is placed in the middle of the roof is observed (Fig. 1.8 E to be compared with Fig. 1.8 B). This phenomenon is due to the destructive interference pattern of the surface wave along the roof and the coupled and guided wave inside the sunroof window.

For cases where the roof-top position is no longer available, as occurs in convertibles, other antenna placements should be investigated. Antennas hidden behind the front and rear bumpers or inside the side mirrors are the mounting positions that offer the best performance if the roof-top position is no longer available, but they suffer from huge shadowing effects from the whole vehicle structure behind them and reflections from the road are more severe. According to Fig. 1.8 (cases F and G), antennas in such positions only offer 180° angle of view, so that combinations of at least two antennas in form of macro-diversity are mandatory if an omnidirectional coverage is demanded.

Looking back at the evolution of automotive antennas, there was always the need to design them as small as possible or embedded in some parts of the vehicle body in order not to disturb so much the aesthetics of the car. Nowadays, and with the increasing number of wireless services in modern automobiles, completely hidden mounting positions are required, while the antenna

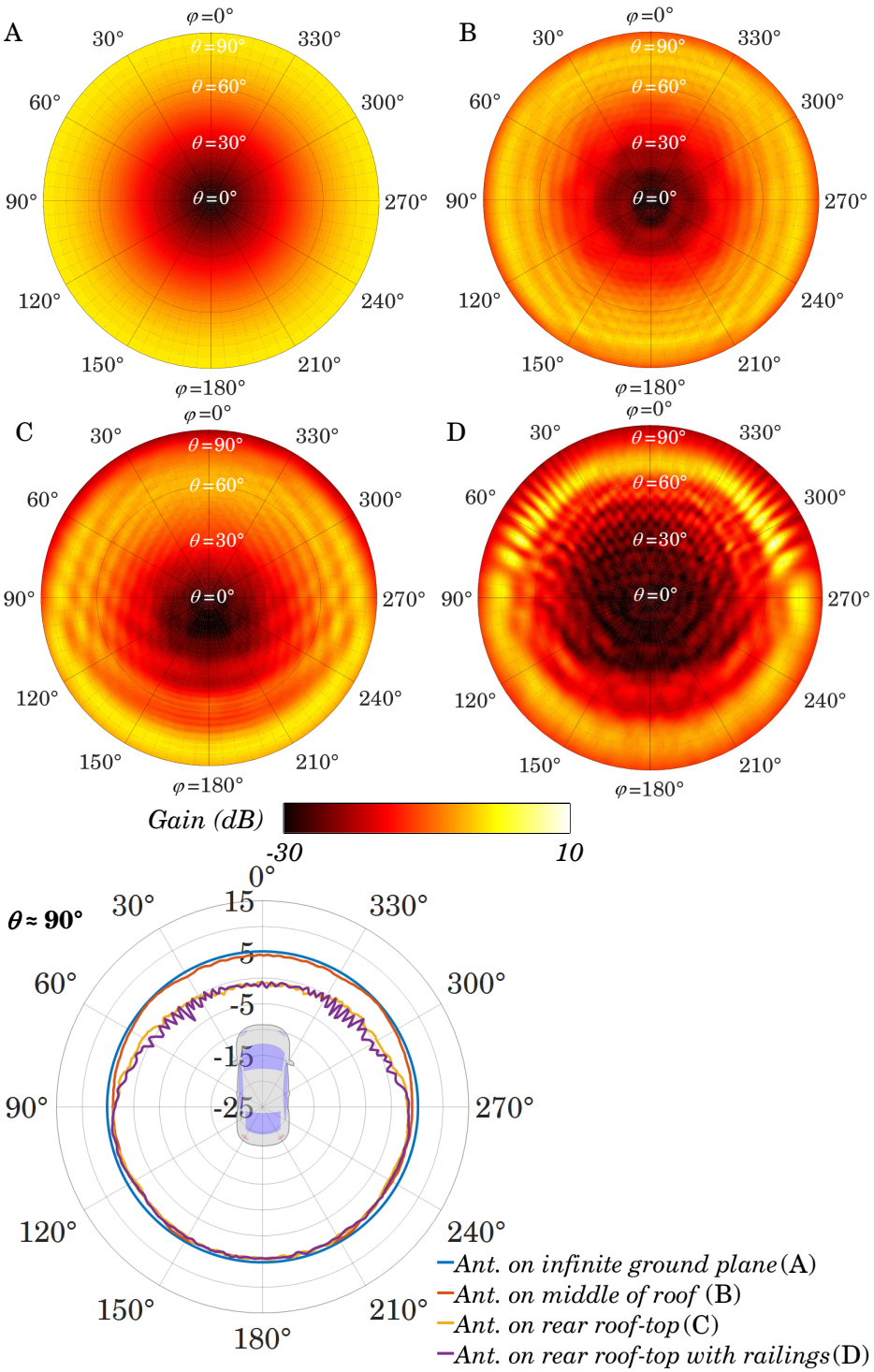

Figure 1.8: Antenna radiation patterns considering different vehicle types and features and various antenna mounting positions. The 3D radiation patterns (upper hemisphere, ($\theta \in [0°;90°], \varphi$)) are illustrated in polar contour form (top). A) $\lambda/4$-monopole on infinite ground plane (reference). B) Monopole-like antenna centered on the middle of the roof of a sedan-type car. C) Monopole-like antenna centered on the back of the roof (near the rear rim) of a sedan-type car. D) Monopole-like antenna centered on the back of the roof of a SUV-type car equipped with railings. 1° resolution.

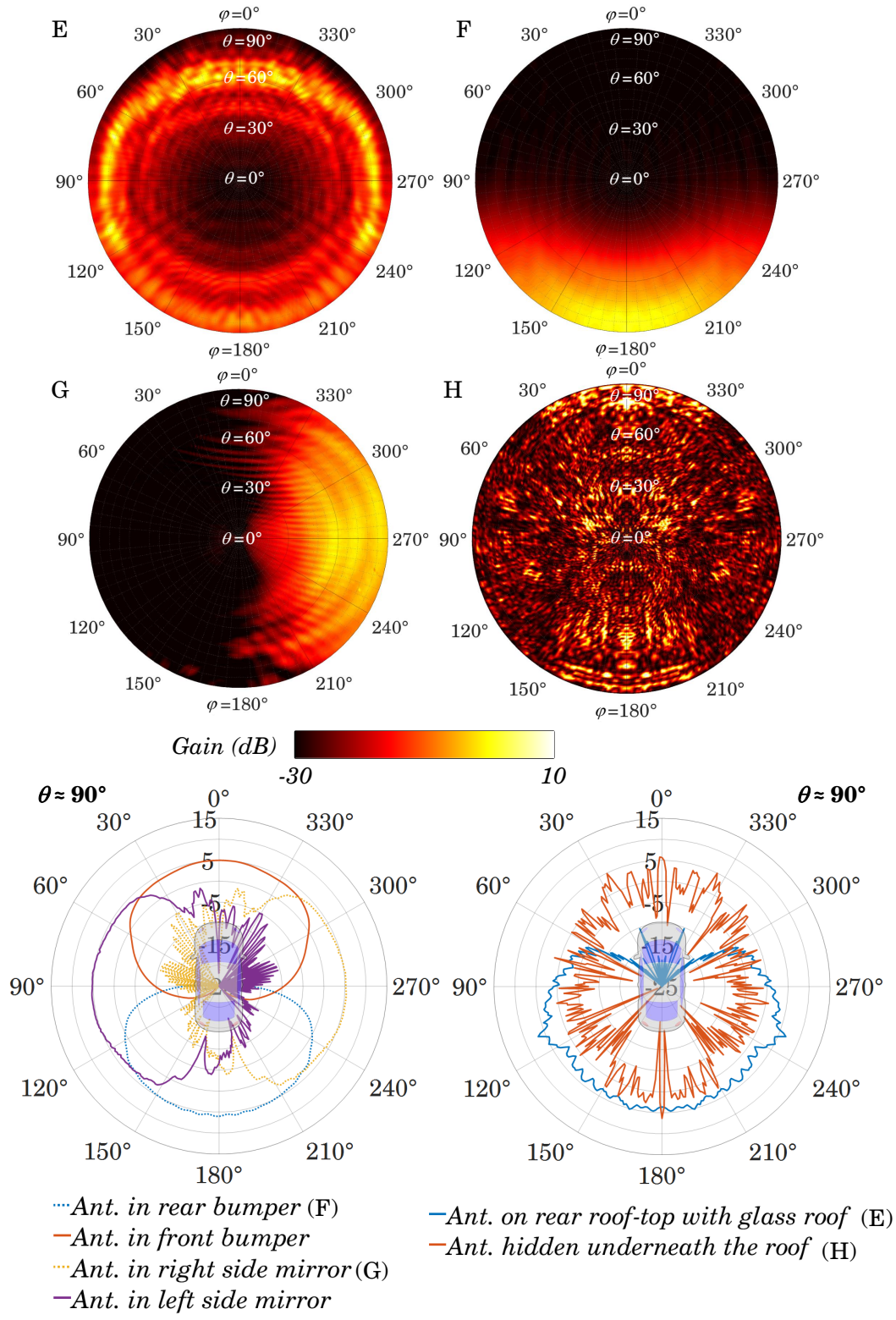

Figure 1.8 (cont.): E) Monopole-like antenna centered on the back of the roof of a SUV-type car equipped with panorama glass roof. F) Monopole-like antenna centered in the rear bumper of a sedan-type car. G) Monopole-like antenna in the right-side mirror of a sedan-type car. H) Monopole-like antenna centered underneath the roof of a sedan-type car. 1° resolution.

specifications to be fulfilled remain high in order to offer the best possible performance and to ensure the reliability of the active safety-related communication applications like V2X.

Hidden antenna placements in cavities in the roof or in the spoiler, like those described in [9, 47], are commonly used for Long-Term Evolution (LTE) and satellite services. Their far-field patterns suffer from large fadings and ripples, due to the enclosed and reduced metal volume and other dielectric parts of the vehicle body in close proximity to the near-field of the antenna. Detuning of the resonance frequency and changes on the input impedance behavior are also expected due to the metal walls and dielectric covers in the reactive and radiated near-field region of the antennas, especially at the low LTE frequencies.

As an example of a new candidate for hidden mounting position, the radiation pattern of a monopole-like antenna placed centered underneath the roof is shown in Fig. 1.8 H. As inferred from Fig. 1.8 H, the pillars and the cabin of the car distort the antenna pattern due to shadowing effects and multiple reflections and diffractions, spreading out the radiated fields in elevation to a great extent, even at low elevation angles where the amplitude of radiation pattern is no longer negligible. Such antenna patterns are unacceptable for safety-related communications and diversity approaches are mandatory to improve the radiation characteristics. This thesis is aimed to investigate the feasibility of hidden antenna systems underneath the car roof for V2X applications at 5.9 GHz by means of linear micro-diversity combinations.

The strong ripple induced in the far-field pattern of some antenna mounting positions and the randomness of the problem make it suitable to be treated with a statistical approach, where the radiation pattern at a given time t is a stochastic process as a function of θ and φ. From a practical point of view, the goal is to quantify the probability that the performance of an antenna system at a given position is being degraded and to what extent is the radiation pattern degraded. Statistical approaches will be used throughout this thesis to evaluate the performance of new antenna concepts considering their mounting positions.

1.3 State of the Art

The first published articles concerning DSRC antennas date back to the early 1990s. But it was not until the beginning of the second decade of the 21st century that the number of publications and patents under the acronym V2V increased considerably, reflecting the growing interest of the automotive industry in such technology.

The main themes of the different publications can be classified following the same scheme used to develop this thesis. In this way, and citing only some of the most significant articles, the publications can be classified as follows.

Articles [5, 27, 33, 39, 40, 42, 83, 101, 124, 128, 135, 137] investigate multi-band antennas for V2V, LTE, GPS, and/or cellular, or rooftop modules that house in a single shark-fin module different antennas for the services mentioned above. The articles [4, 34, 37, 38, 46, 53, 58, 70,

97, 103, 115] address the degradation of the performance of V2V antennas in the presence of the body of the car or the surrounding environment. The publications [3, 36, 61, 64, 68, 110, 129, 130] deal with the performance improvement of V2V antennas when using MIMO and diversity configurations. Only a few articles around 2012 like [73, 131, 138] investigate the performance of circularly polarized V2V antennas.

In [137], a low-profile, low-cost antenna system with improved gain based on a quarter-wave monopole surrounded by a circular arrangement of eight parasitic elements is analyzed. In [135], a concept for a multi-band rooftop antenna with a bandwidth from 780 MHz to 5.9 GHz and a near circular radiation pattern on the horizontal plane with an average gain of 3 dB (at 5.9 GHz) is proposed. In [27], a compact and wideband modified squared monopole with a shark-fin form factor operating at DCS1800, WCDMA2100, LTE2800, WiMAX, WLAN, and C2C bands with omnidirectional radiation patterns in the azimuth plane is investigated. In [5], a multiservice PCB antenna deploying a modified planar inverted-F antenna (PIFA) and a Y-shaped monopole sharing a common aperture for DCS1800, IEEE 802.11b/g/n, WiMAX, LTE and V2V/V2I operation is presented. In [40], a low-profile, multi-band PCB antenna fed from a co-planar waveguide (CPW) is investigated and optimized to cover the bands 2.4 GHz and 5.4 to 6 GHz. The improvement of antenna performance by means of diversity is also outlined. In [101], the concept, design, and measurements of a low-profile integrated microstrip antenna for dual-band applications are presented. The antenna operates at both the GPS L1 band around 1.575 GHz with right-handed circular polarization and the DSRC band with vertical polarization. In [83], the same authors as the previous publication compare the free-space performance of the antenna with the results above a large rolled-edge ground plane representing the metallic roof of a vehicle.

In [42], a study of four potential DSRC antenna elements to determine the appropriate location within a shark-fin rooftop multiband antenna module capable of receiving GPS L1 band, LTE, UMTS, and DSRC is discussed and measured on a vehicle roof model. In [124], a new generation of intelligent multiband antenna systems designed with a shark-fin form factor and based on active modules which contain the passive antenna radiators and active transceivers and software defined radio platforms are presented together with measurement results in dynamic outdoor scenarios. In [39], the performance of a shark-fin rooftop antenna equipped with LTE, GSM, UMTS, GPS, C2C and RKE antennas is presented. In [33], V2V functionality at 5.9 GHz is integrated into an existing rooftop quad-band antenna (north american cell phone bands, GPS and XM satellite radio). In [128], the application of the finite volume time domain method for evaluation and development of rooftop wideband automotive antennas operating at GSM, UMTS, GPS, SDARS, LTE, WiMAX, and V2V frequencies is discussed.

Concerning the performance of antennas in the presence of the car or the surrounding materials and environment, in [38], a design and experimental validation of a linearly polarized windscreen patch array for V2V communication is presented. Due to the presence of the glass

superstrate, a valuable miniaturization effect is obtained. Article [97] shows the results of on-glass patch and slot antennas in the 5.8 GHz band. In [34], the effects of the shark-fin shaped antenna radome on the radiation pattern of antennas at 5.9 GHz are presented and techniques to compensate for such unwanted dielectric lens effects are discussed. In [4], the radiation pattern at the horizon of a raised monopole DSRC antenna printed on a PCB with one, two and three directors for enhanced gain coverage towards front and rear of the vehicle is investigated. In [70], the influence of car panorama glass roofs on the radiation pattern of V2V antennas is presented by means of measurements. In [46], the impact of vehicular integration effects on the performance of DSRC communications in field experimental tests is investigated. In [37], the performance of V2V antennas integrated within a rooftop module and placed on a real car roof is evaluated by means of measurements. In [53], the effect of the car antenna position on the radio propagation characteristics at intersections for 760 MHz is analyzed. In [58], an analysis of the reliability of V2V communications with reconfigurable V2V antennas is discussed. In [115], an investigation of the feasibility to substitute complex V2V measurements with numerical simulations based on RCS to account for reflecting objects in the communication path is presented. In [103], the influence of antenna placement on the V2V communication channel is characterized by means of a three-dimensional ray tracing simulation tool.

Concerning MIMO and diversity configurations to improve the performance of the antennas in real scenarios, in [36], a vehicular rooftop multiband MIMO antenna configuration for terrestrial communications covering the V2V band is presented. In [64, 129, 130], results of multielement antenna performance in 5.85 GHz V2V scenarios using diversity combining or spatial multiplexing to enhance the link quality or increase the channel capacity are evaluated. In [3, 68, 110], measurement-based analysis are performed to quantify the effect of different antenna configurations and complementary antennas based on diversity combinations. In [61], empirical results from a study examining the effects of antenna diversity and placement on the V2V link performance are discussed.

In the field of antenna diversity for automobiles, it is also worth noting the excellent and exhaustive research carried out at the Institute of High Frequency Technology and Mobile Communication of the Universität der Bundeswehr in Munich since the early 1980s. Much of the research conducted for this thesis is based on concepts previously developed at the institute. Among the vast number of publications, it is worth highlighting the articles [14, 75, 77, 78, 90, 117, 118, 120–122] as they are considered relevant for the development of the content of this dissertation. In each of them, different aspects of the fast *scan-phase* antenna diversity system conceived at the institute and applied to different automotive services such as FM, SDARS or GPS are extensively researched.

1.4 Organization of the Thesis, Definition of Targets and Summary of Achievements

This thesis is aimed to investigate new antenna concepts as integrated systems in their mounting position considering the electromagnetic effects of the vehicle body. The goal is to counteract the performance degradation of state-of-the-art antennas in common and new hidden antenna placements for the upcoming active safety-related V2X communications around 5.9 GHz.

The general structure of the thesis is organized as follows:

- *Chapter 1* provides the introduction and overview of the thesis. With Vehicle-to-Everything (V2X) communication as a motivation background, the problem statement and challenges of automotive V2X antenna integration are briefly presented. The definition of targets, organization of the thesis, and summary of achievements are shortly discussed to conclude the chapter.

- *Chapter 2* introduces the electromagnetic radiation characteristics and wave propagation effects of automotive V2X antennas under the influence of the vehicle body and the ground. First, the required omnidirectional radiation patterns for V2X-communication are presented. Second, the distortions of the patterns caused by the interaction of the antenna with the various mounting positions in the vehicle are analyzed. The electromagnetic effects of finite curved roofs, railings, panorama glass roofs, decentralized positions behind bumpers or side mirrors and hidden positions underneath the roof are discussed in detail. Third, the mounting position effects on the input impedance of V2X antennas installed in the vehicle have been determined. And finally, the electromagnetic effects of the ground on the radiation pattern of V2X antennas have been explained and examples have been shown in order to be able to interpret the measurements in open area test sites or radomes. The content of this chapter is based on publications [23–25, 79].

- *Chapter 3* investigates V2X shark-fin antennas capable of counteracting the effects that degrade the omnidirectional radiation pattern due to the mounting position on the vehicle's roof. Multi-band LTE-V2X antennas that fit inside commercially available shark-fin covers are investigated. The aim of the multi-band antenna research is to reduce the space occupied by the antennas and the electromagnetic coupling between them, resulting in a single structure with a single feeding point. The part of the antenna covering the V2X frequencies has been designed in such a way that it radiates with a directive nature on an infinite and flat ground plane. When the antenna is installed on a finite, curved roof typical of a sedan-type car, the antenna radiates omnidirectionally. The content of this chapter is based on publications [20, 23, 79, 80].

- *Chapter 4* moves the discussion towards decentralized macro-diversity antenna systems. First, the radiation characteristics of decentralized positions behind the bumpers and inside

the side mirrors are explored, comparing with the almost omnidirectional behaviour of antennas placed above the roof near the rear edge and the almost perfect pattern of antennas on the middle of the roof. Second, possibilities for optimizing the radiation characteristics of such positions are discussed. And finally, the system's reliability improvement through macro-diversity antenna sets with linear combining techniques such as selection/switch combining (SC), equal gain combining (EGC), and maximum-ratio combining (MRC) is investigated. The content of this chapter is based on publication [25].

- *Chapter 5* investigates micro-diversity antenna systems hidden underneath the roof of the car. First, the electromagnetic performance of single antennas underneath the roof is characterized and statistical tools are used to describe their behaviour. Second, the improvement of the radiation pattern through antenna diversity and linear combining techniques is investigated. Different benchmark scenarios like downed side windows or the presence of the driver on the radiation patterns have been considered. Third, frequency selective surface (FSS) structures in the metal layer of the front and rear windows fitted with the so-called energy saving glass are investigated to let the wave scape from the interior of the car without modifying the thermal properties of such glass windows. Four, the electromagnetic effects of defogger grids in the rear screen on the radiation pattern of the antenna are explored by means of simulations. And finally, the compliance with the electromagnetic exposure guidelines of antennas hidden underneath the roof of the car in the presence of human beings is discussed. The content of this chapter is based on publications [21, 22].

- *Chapter 6* gives a final overview of the achieved results and concludes the dissertation.

To show the impact of the vehicle body on the reliability of the antenna system, Fig. 1.9 shows a statistical performance evaluation of various antenna mounting positions and vehicle equipment by means of the Cumulative Distribution Function (CDF) in a logarithmic scale. It shows the gain levels over azimuth at 5.9 GHz. The wave propagation effects and other related electromagnetic effects have been presented in the previous section and will be discussed in detail in Chapter 2. All curves that depart from that of the antenna on the middle of the roof show some degree of degradation of the required omnidirectional coverage of the antenna. The curves of Fig. 1.9 that are not solid lines, can no longer be considered omnidirectional, and some kind of improvement is needed. By means of linear diversity combination techniques or beamforming, the gain values over azimuth at low cumulative probability levels can be improved towards more omnidirectional diagrams, thus, increasing the slope of the CDF curve. Adding more antenna elements, not only it is possible to achieve diversity gain, but also array gain, shifting the CDF curves in the same way to the right towards higher gain values but keeping the same slope.

For antennas placed on the rear roof-top position in the form of a shark-fin cover, modifications of the structure to give the antenna a directive behavior in an infinite ground plane can improve

the roundness of the radiation pattern considering the vehicle without the need to add more antenna elements enlarging the volume needed and disturbing the aesthetics of the car. This will be discussed in Chapter 3.

When antennas can no longer be positioned on the roof, as the case of convertibles, linear macro-diversity approaches can be used to enlarge the coverage to 360° in azimuth. Such decentralized systems will be investigated in Chapter 4.

The feasibility of new completely hidden positions will be investigated in Chapter 5. By means of linear micro-diversity and a compact antenna set of a size smaller than $10 \times 48 \times 48$ mm^3 placed hidden underneath the roof of the car, not only it is possible to counteract the worsening effects on radiation pattern for antennas hidden underneath the roof, but also serves for improving the Signal-to-Noise Ratio (SNR) in real V2X fading scenarios.

Chapter 6 will give a final conclusion highlighting the most important achieved results throughout this thesis.

Starting with the roof-top mounting position near the rear rim, compact antennas with heights lower than 55 mm able to achieve an omnidirectional radiation pattern in the horizontal plane are investigated. The beamforming with directive behavior in driving direction over an infinite ground plane (to mitigate the gain reduction through shadowing and curvature of the roof) is accomplished by means of mutual coupling between the strips of different lengths and spacings that form the structure. Such antennas are designed to have only one feeding point and to work without the need of an external matching network.

Multiband vertically-polarized antenna structures, as the ones shown in Fig. 1.10, have been investigated to cover the whole V2X, WLAN, and LTE frequency bands with only one compact and robust radiator made of metal, ensuring low losses and providing high efficiency [20]. They are based on broadband conical antennas in the form of a cage, with capacitive loading to reduce the overall height of the radiator. Adjusting the lengths and spacing of the strips conforming the conical cage structure, directional patterns over infinite ground planes can be formed, which become omnidirectional under the presence of the vehicle. Due to their compact form factor, they are suitable to be installed under state-of-the-art shark-fin covers of various shapes. The easy fabrication technique from a single metal plate based on a milling process to give the proper form to the antenna and providing the volume through a punch and bent technique (see Fig. 1.10), offers a low-cost antenna suitable for the mass production in automotive applications.

Wideband impedance matching to a $50\,\Omega$ impedance system, as illustrated in Fig. 1.11, without further matching networks is achieved over the whole frequency range of interest. A Voltage Standing Wave Ratio (VSWR) lower than 3 over the whole bands is obtained, in accordance with the minimum requirements for proper operation of automotive LTE receivers. It is worth noting that the physical height of the antenna lower than 55 mm corresponds to about $\lambda/8$ at the lowest LTE frequency. Together with the fact that the low LTE band covers roughly 260 MHz bandwidth, the strength requirements to be fulfilled in terms of impedance matching

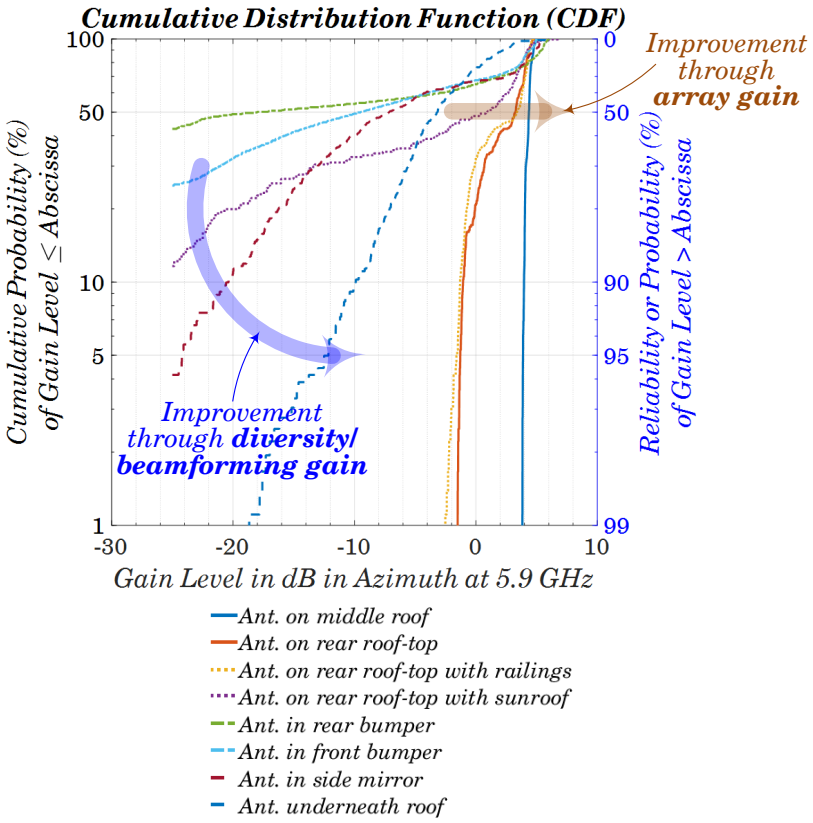

Figure 1.9: Statistical performance evaluation of various antenna mounting positions: Cumulative Distribution Function (CDF) (left axis) and reliability (right axis), both in a logarithmic scale, of the gain levels over azimuth for various mounting positions and vehicle equipment. The antenna on the middle of the roof (blue solid line) serves as a reference. Gain values over azimuth at low cumulative probability levels can be improved by means of diversity or beamforming. The whole curves are shifted to the right if the antenna gain is increased the same way in all azimuthal directions.

become challenging.

Figure 1.11 compares also the impedance matching performance of the stand-alone antenna with the antenna under the ESD and design covers to evaluate the effects of dielectric losses. Very good agreement between simulation and measurements is obtained. On the right side of Fig. 1.11, the input impedance behavior as a function of frequency of such wideband antennas is depicted in form of Smith chart, highlighting the various frequency bands with different colors [20].

Before performing the simulations with the whole car, antennas are simulated alone in free space over an infinite ground plane by means of full-wave techniques in a commercial software based on the Finite Integration Technique (FIT) or Finite Element Method (FEM), volume discretization methods based on hexahedral and tetrahedral mesh cells, respectively [79]. An example for the V2X-LTE multiband antenna is shown in Fig. 1.13, where the complete workflow

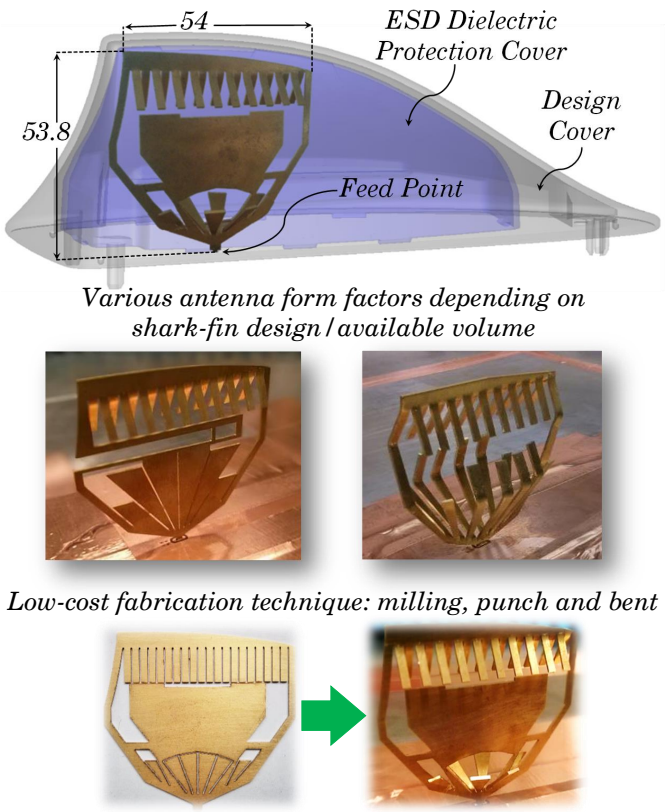

Figure 1.10: V2X/WLAN/LTE multiband shark-fin antennas to mitigate the shadowing effects for antennas placed on the rear roof-top position. Prototype inside a shark-fin cover (top) with overall height and length dimensions in millimeters. Antenna prototypes with various form factors (middle). Low-cost fabrication technique from a single metal panel (bottom).

for the simulation of antennas considering the vehicle body is illustrated schematically. Electric and magnetic fields at the operating frequencies are sampled on a tight box (Huygens surface) enclosing the antenna and lying inside the reactive near-field region at about $\lambda/10$ from a surface touching the antenna structure. The Huygens surface is placed in the mounting position of the vehicle after converting it into equivalent electric and magnetic current sources, as shown in Fig. 1.13. This is more accurate for antennas, whose ground plane is a part of the chassis of the car, than using the far-field representation of them. The reason is that the equivalent current sources can interact with the platform in the near-field region where antennas are placed, leading to more accurate results. Once the antenna is fully characterized by means of full-wave techniques, the radiation pattern considering the whole vehicle is computed by means of asymptotic or full-wave simulation approaches based on the high-frequency Shooting and Bouncing Rays (SBR) technique or by means of the Method of Moments (MoM) or FIT/FEM. Although for asymptotic techniques is not so important to have a robust and topologically closed meshed Computer Aided Design (CAD) model of the car as for full-wave techniques, there are some important aspects that

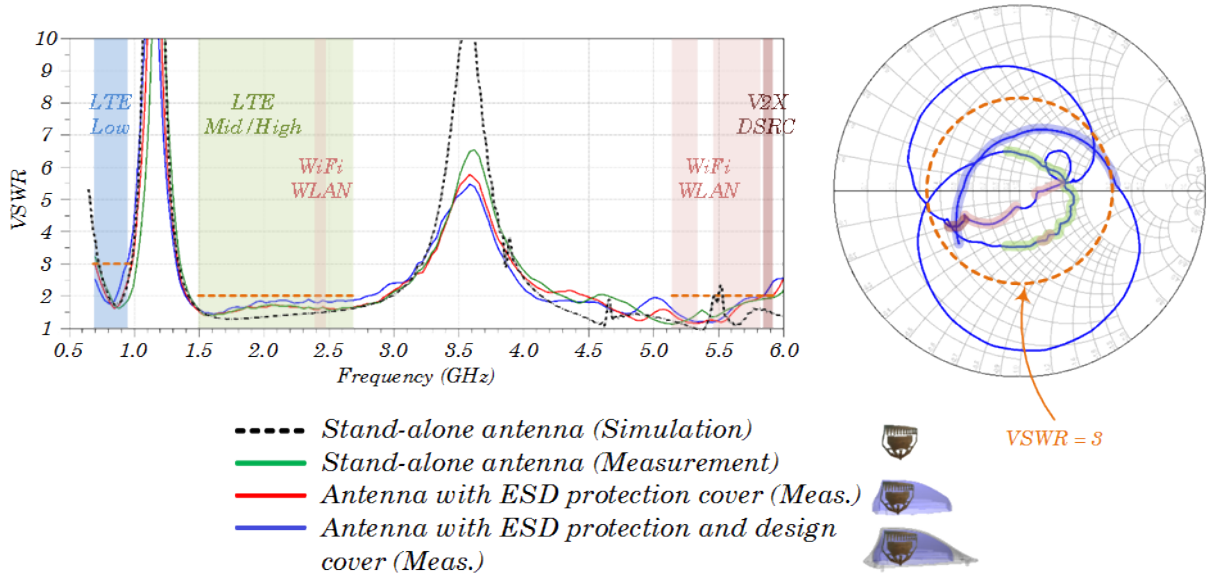

Figure 1.11: Broadband impedance matching (referred to 50 Ω) of V2X/WLAN/LTE multiband shark-fin antennas without the need of external matching networks. Comparison of Voltage Standing Wave Ratio (VSWR) between simulation and measurement results of the stand-alone antenna, and the measured lossy effects of the shark-fin covers (left). Input impedance behavior in the Smith chart for the stand-alone antenna (right). The limit of $VSWR = 3$ has been drawn as a reference in form of an orange dashed line and circle.

must be taken into account. A model meshed finely enough is desired to prevent scintillations (sharp peaks) in the resulting radiation pattern. Surface curvature information of the facet model is needed to prevent from divergence errors on the volumetric ray tubes (representing a spherical wavefront) at convex and concave surfaces and to increase the accuracy of the results. Asymptotic techniques or methods based on surface discretization of the model are not suitable for simulations considering a sunroof or panorama glass roof, since the guided wave effects are not taken into account. Full-wave volume discretization methods should be avoided, since they require a great amount of computational resources. If they have to be used, subgridding techniques are highly recommended to reduce the number of mesh cells in electromagnetically irrelevant locations [22, 23, 79].

A new approach, which consists of finding the electromagnetically relevant parts and neglecting the rest, has been investigated as shown in Fig. 1.13, leading to a significant reduction of the computational effort in memory and processor resources up to a factor of 166.6 without compromising the accuracy of the results. This technique allows the use of full-wave methods with high degree of accuracy [25].

Radiation pattern measurements of the Antennas Under Test (AUTs) as receiving antennas are performed using the comparison method with a reference antenna in the outdoor far-field test range shown in Fig. 1.12. It is equipped with a broadband log-periodic transmitting antenna

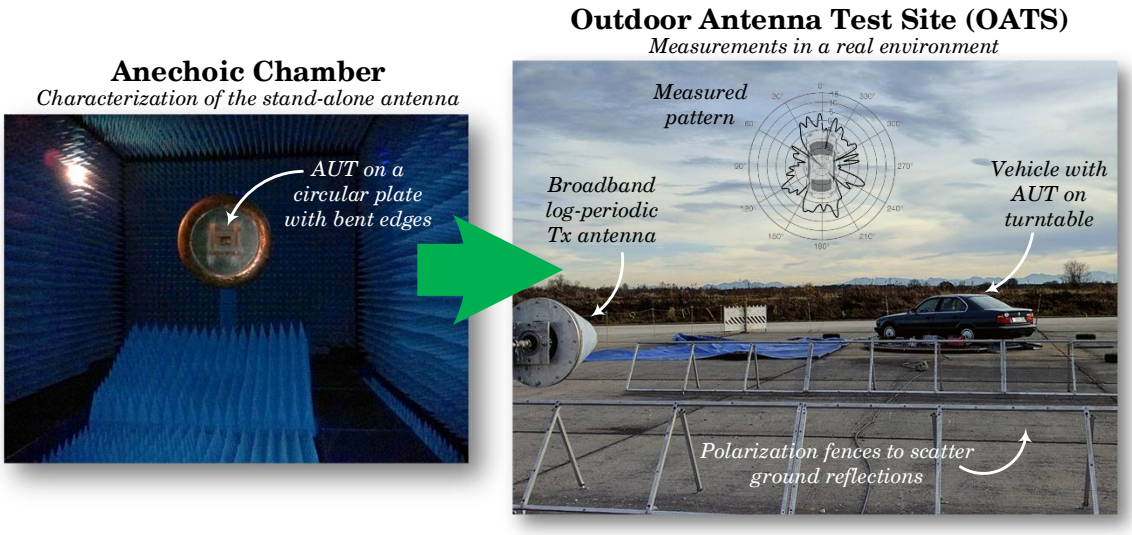

Figure 1.12: Measurement workflow: Characterization of the stand-alone antenna in a controlled scenario (anechoic chamber) (left), and outdoor far-field test range (right) for measuring the horizontal plane of radiation patterns of antennas considering the vehicle.

placed 20 m away from the turntable where the vehicle rotates in azimuth to record the horizontal cut of the antenna pattern with a resolution of 5° in azimuth. More than 40 dB of dynamic range is ensured with a previously amplified transmitting antenna, to allow the measurement of the deep nulls common in various mounting positions without distorting the pattern [20, 21].

Direct comparison of the great horizontal cut of the measured radiation patterns with the ones obtained in simulations considering the vehicle without ground can be done, because the open area test site (OATS) is equipped with polarization fences to scatter the ground reflections, so that only the direct wave is considered. Very good agreement between measurements and simulations is obtained. As a matter of proof, confidence bands derived from the two-sample Kolmogorov-Smirnov test (two-sided) have been applied to the results in form of CDF to validate the agreement. Other statistical ways used throughout this thesis to illustrate the good agreement is the use of Quantile-Quantile plots (Q-Q plots), where a high correlation degree between the values obtained by measurements and simulations is given by a straight line with an inclination of 45°.

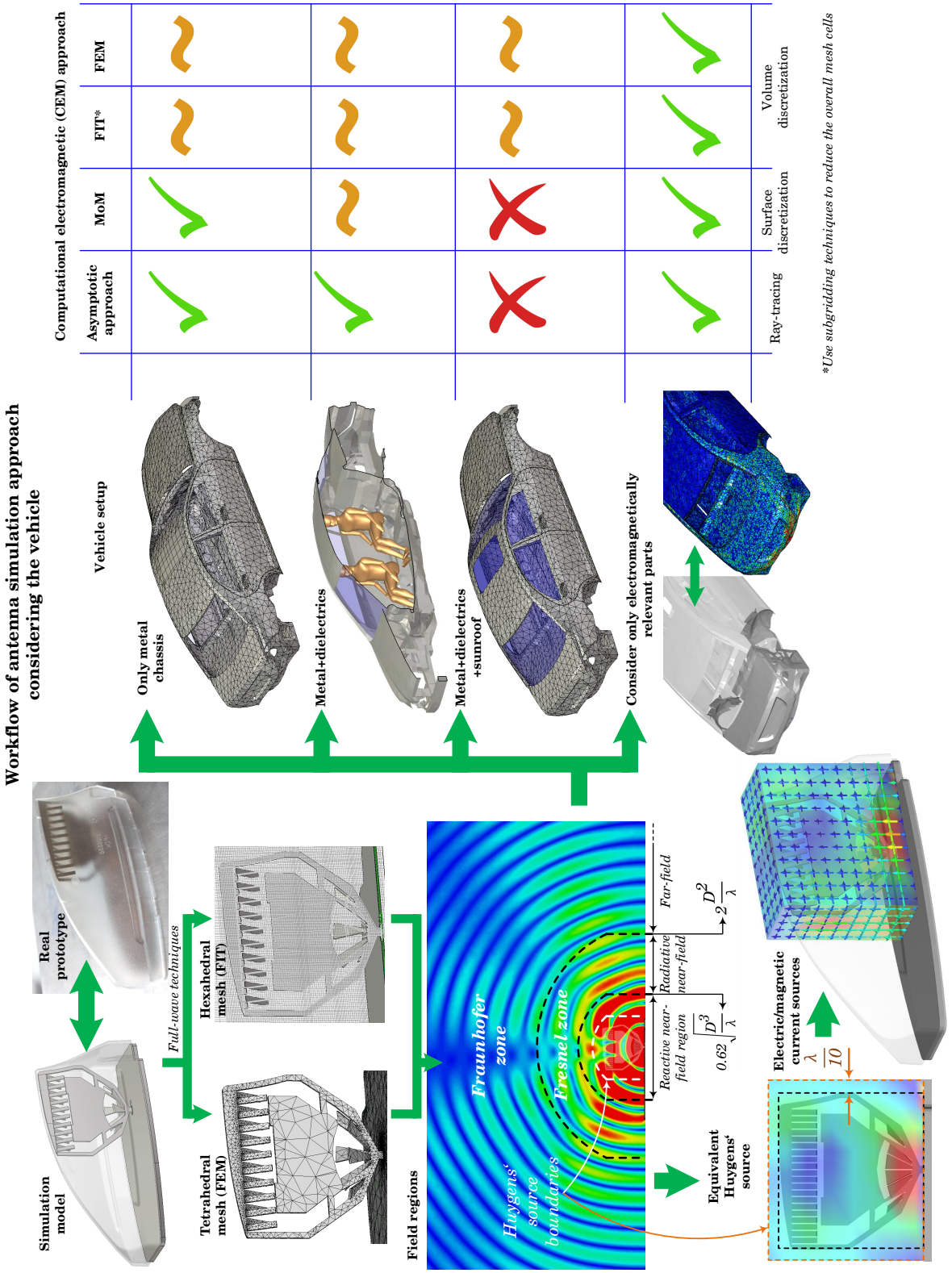

Figure 1.13: Workflow of antenna simulation approach considering the electromagnetic effects of the vehicle.

The improvement on radiation pattern under the influence of the vehicle for antennas on the back of the roof is illustrated in Fig. 1.14. Omnidirectional behavior is obtained overcoming the shadowing effects of the curved roof in driving direction and achieving results comparable to the patterns when the antennas are placed on the middle of the roof. Looking closer at the CDF (Fig. 1.14, bottom), for cumulative probability values greater than 1 % or with a reliability of 99 %, the gain levels over azimuth of the V2X-LTE multiband antenna are greater than 0.8 dB, approaching the values obtained with a monopole-like antenna in the best mounting position on the middle of the roof with differences smaller than ≈1 dB for cumulative probability levels greater than 50 %. In 10 % of cases, the V2X-LTE multiband antenna gain is higher than that of the reference antenna on the middle of the roof.

In case of convertibles or when the roof-top mounting position is no longer available, one single radiator in front/rear bumpers or in left/right side mirrors is not enough to ensure omnidirectional coverage in the horizontal plane [25], due to the chassis blockage effects seen in Fig. 1.8. In these cases, even a directive beamforming of the radiation pattern, as the concept discussed before, would not cover the whole azimuthal plane. Chapter 4 investigates the antenna pattern improvement by means of decentralized macro-diversity systems formed by two and four antennas. Fig. 1.15 summarizes the resultant radiation patterns considering the vehicle in form of polar plots and CDF. Combinations of two antennas still show deep fadings up to −10 dB.

For such decentralized cases, selection/switch combining show better results than equal gain combining in the vast majority of azimuthal angles. This is due to the fact that, when the radiation pattern of one of the antennas for a particular angle φ is in the visibility zone, the others show a gain difference (power imbalance) greater than ≈7.65 dB, so that the equal gain combination is worse than choosing the single antenna with higher gain (switch/selection combining). Combinations of two antennas placed in the front/rear bumpers show some advantage over the antennas placed inside the side mirrors, since an elliptical radiation pattern is obtained, favorable to cover the azimuthal directions in which communication occurs with a higher probability due to the so-called *canyon effect*.

Macro-diversity systems with four antennas match the performance of the reference antenna on the middle of the roof by means of switch/selection combining and even outperform it in the case of maximum-ratio combining by roughly 1 dB, as shown in Fig. 1.15. The CDF plot shows how by means of diversity, the slope is much steeper than in the case of single antennas. This leads to much rounder radiation patterns.

To mitigate the worsening effects on radiation pattern of antennas placed hidden underneath the roof, linear micro-diversity combining techniques have been applied by means of a compact circular array of four antennas of a size smaller than $10 \times 48 \times 48$ mm^3. The feasibility of such hidden positions has been investigated, showing tremendous advantages for V2X services comparing with other common hidden sites when using diversity techniques [21]. The electromagnetic waves leave the inside of the car through the windows, ensuring more effective area to let microwaves

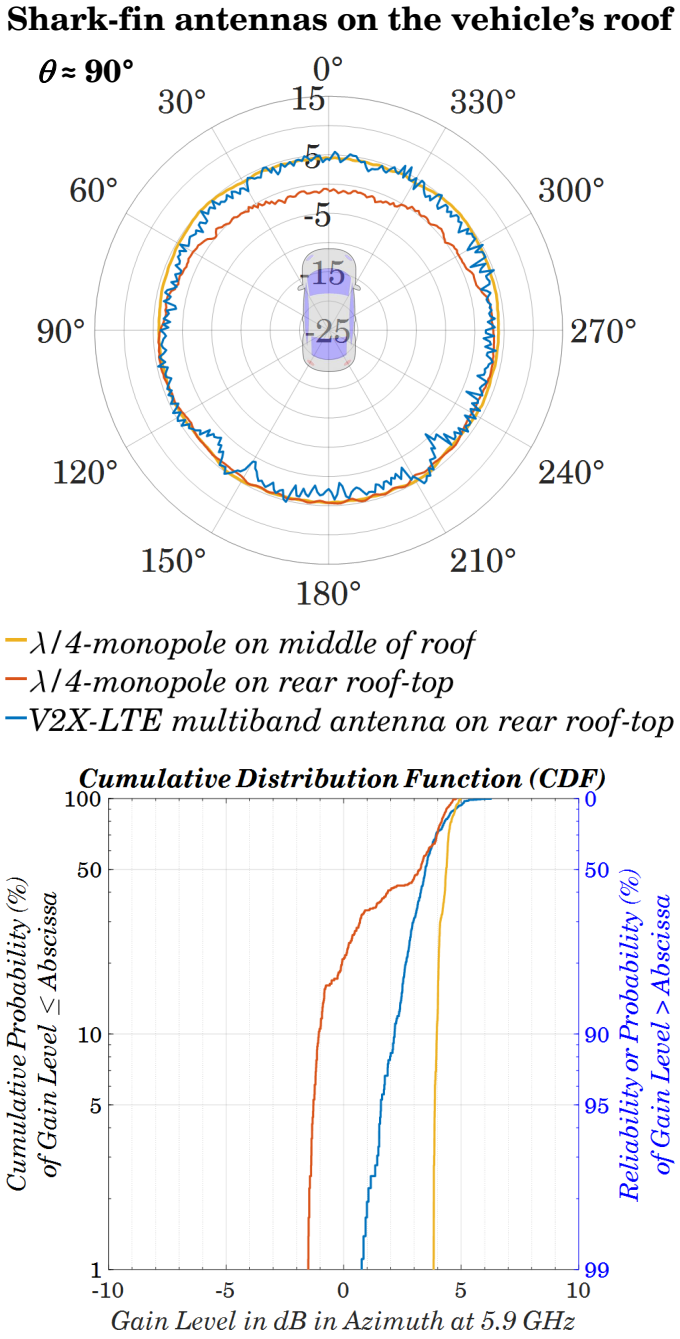

Figure 1.14: Radiation pattern improvement of antennas on rear roof-top position through directive pattern behavior over infinite ground plane: Conical or great circle horizontal cut of radiation pattern (top) comparing the V2X-LTE multiband shark-fin antenna on the rear roof-top position with a quarter-wave monopole in the same position and on the middle of the roof. CDF of the gain levels over azimuth for the three cases to statistically evaluate their performance.

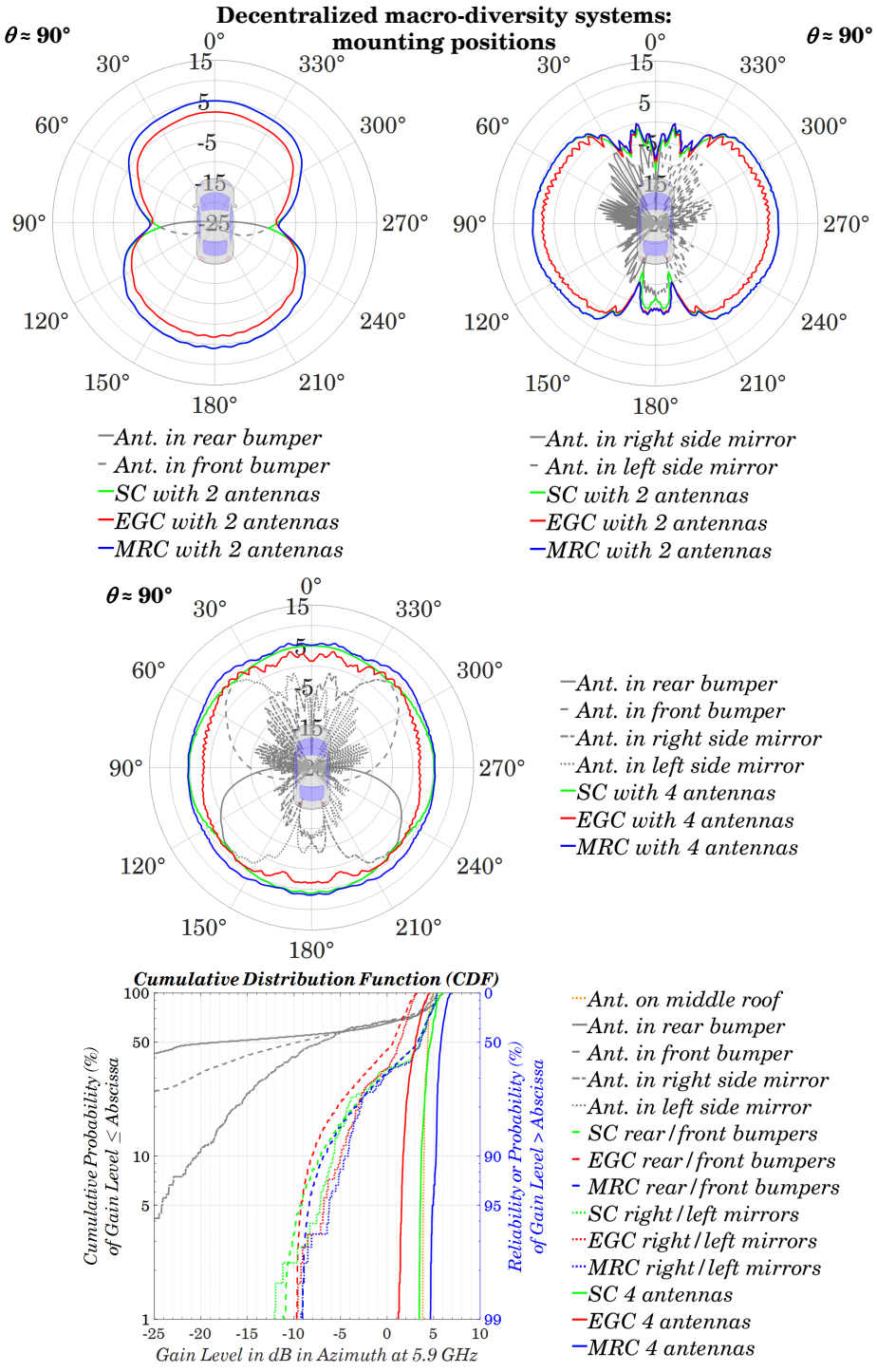

Figure 1.15: Radiation pattern improvement of antennas in rear/front bumpers and right/left side mirrors through linear macro-diversity combining techniques: Conical or great circle horizontal cut of radiation pattern for diversity combinations of 2 antennas (top) and 4 antennas (middle). CDF of the gain levels over azimuth for single antennas and diversity combinations of 2 and 4 antennas to statistically evaluate their performance (bottom). SC means selection/switch combining, EGC equal gain combining, and MRC maximum ratio combining. A quarter-wave monopole on the middle of the roof (orange dotted line) is added as a reference.

pass through than in common concealed metal chassis cavities. Moreover, since no metallic walls are in close proximity to the antenna, no input impedance changes are expected regarding the impedance of the antenna over an infinitely large ground plane.

Various positions centered underneath the middle of the roof and underneath the back roof have been investigated, showing the latter an elliptical diagram in the horizontal plane, and better coverage and more reliability in the back half, as shown in Fig. 1.16 [21, 22]. Envelope correlation coefficients from far-field and S-parameters have been computed, leading the former to values lower than 0.5, even for arrays whose antenna spacing is of the order of 0.3λ. Laminated glass windows and windscreens with energy-saving glass with a transparent electrically conducting layer blocking all microwave radiation have also been taken into account. Frequency Selective Surface (FSS) structures laser-drilled or etched in the metal coating have been investigated to assess the extent to which they can be considered as electromagnetically transparent at the frequency of interest of 5.9 GHz, improving the radiation characteristics comparing with completely metal-coated windows. The performance of antennas in the presence of rear windows with defogger grids have been investigated considering the defogger grid a kind of FSS structure of the complementary type with regard to teh slotted case. Due to the Babinet's principle, some effects are expected for the vertical heater grid orientation. The horizontal defogger grid should be electrically transparent for the impinging wave coming from a vertically polarized antenna placed underneath the roof. The electromagnetic effect of human bodies inside the car has been investigated in terms of the degree of worsening of the radiation pattern and in terms of compliance with electromagnetic exposure.

Neither the laminated window glass nor the rear window defogger grid or the human bodies indicate a representative change in the horizontal cut of the radiation pattern of antennas placed hidden underneath the roof. Only small differences can be seen for vertical heater grid orientations, however, the statistical distribution of the gain values over azimuth lies almost entirely between the upper and the lower 99 % confidence bands derived from Kolmogorov-Smirnov test statistics, showing that the radiation pattern remains almost unchanged with regard to a rear window without defroster grid. FSS structures in the form of horizontal slots or slotted squares, as shown in Fig. 1.16, in the windscreen or rear screen of the vehicle, have shown to be electromagnetically transparent at 5.9 GHz, and show a very low visual impact.

The CDF of Fig. 1.16, shows that not only it is possible to achieve diversity gains of up to 12.6 dB at 10 % probability level (DG 90 %) with such a compact antenna set, but also the array gain is improved. This leads to radiation patterns, considering maximum-ratio combining with four antennas underneath the rear roof of the car, better than reference antennas above the roof with a probability or reliability greater than 70 %. Side windows open means about 1 dB more gain in median comparing with closed windows. Thus, the use of spatial micro-diversity systems can overcome the fast-fading effects from randomly distributed stuff inside the car, enabling new hidden antenna mounting positions for active safety-related V2X communications.

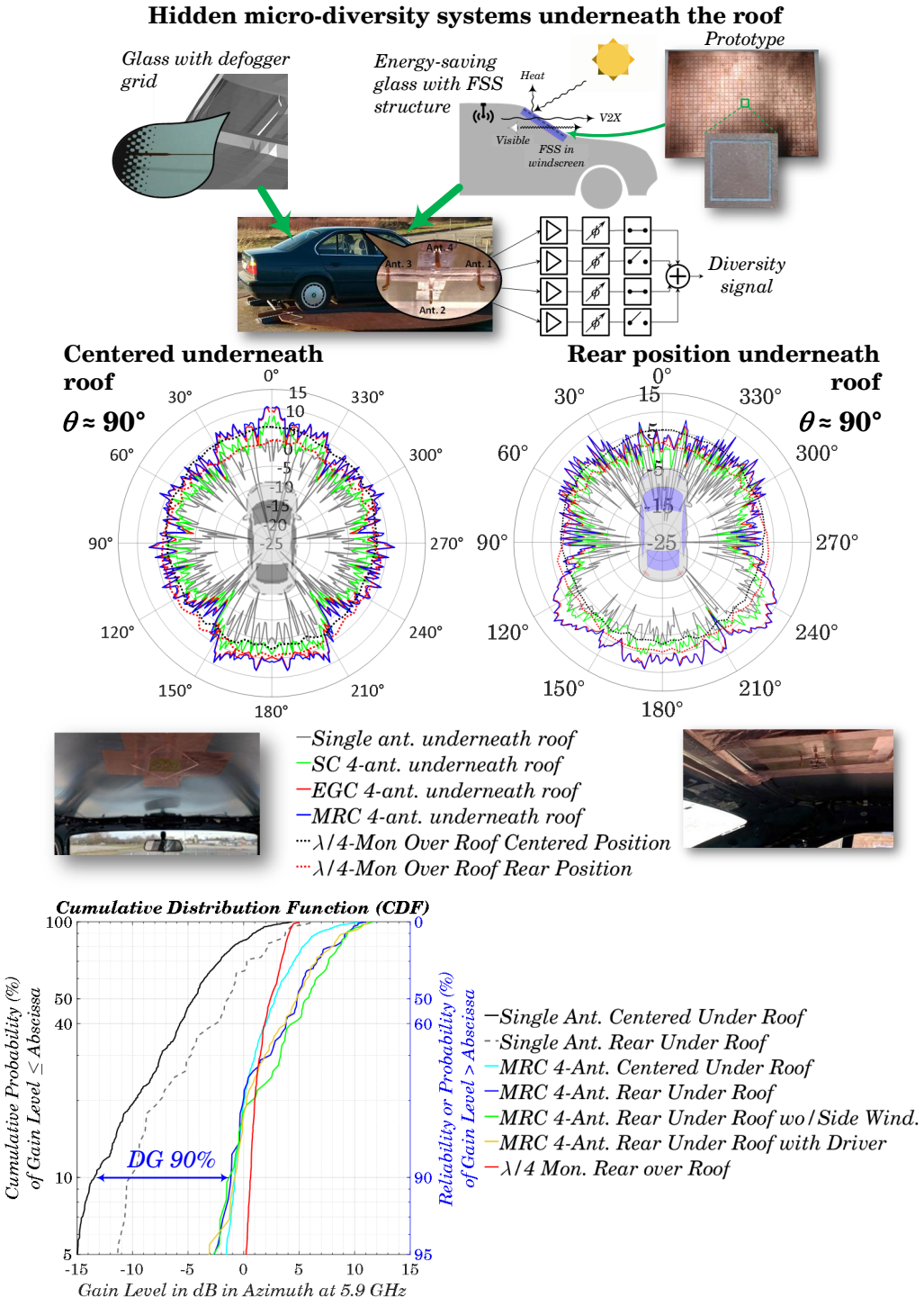

Figure 1.16: Radiation pattern improvement of antennas hidden underneath the roof through linear micro-diversity combining techniques: Antenna array prototype in measurement setup (top), conical or great circle horizontal cut of radiation pattern for diversity combinations of 4 antennas (middle). CDF of the gain levels over azimuth for single antennas and diversity combinations of 4 antennas at various positions underneath the roof to statistically evaluate their performance (bottom). SC means selection/switch combining, EGC equal gain combining, and MRC maximum ratio combining. Quarter-wave monopoles above the roof are added as reference.

CHAPTER 2

Radiation Characteristics and Wave Propagation of Automotive Antennas Under the Influence of the Vehicle and the Ground

Radiation characteristics of automotive antennas are significantly affected by the vehicle body and the real ground below them. Induced currents on nearby surfaces modify the radiation pattern and the input impedance accordingly. Although the antennas are first designed in free-space conditions to effectively analyze their radiation characteristics, their actual performance installed in the car and in real propagation conditions should be evaluated.

When the space radiation launched from an antenna installed in a car hits some parts of the vehicle, it may partially or completely change the direction of propagation by means of reflection or diffraction, the speed at which the wave travels, as occurs when the wave propagates through dielectric parts like the glass windows, or it may even change its polarization. The relative effect on wave propagation depends on the largest cross dimension of the obstacle in terms of the electrical length $\beta = 2\pi/\lambda$ per unit distance. If the electrical dimensions of the obstacle become much larger than $1/\beta$, as occurs with the car at V2X frequencies, the optical ray theory becomes the best way to explain the radiation mechanisms taking place at 5.9 GHz under consideration of the vehicle body and real ground conditions.

For terrestrial communication, the energy radiated from a transmitting V2X-antenna may reach the receiving antennas of vehicles in the nearby through the so-called ground-wave propagation. The ground-wave signal is divided into the space wave and the surface wave. The space wave contains the direct wave, which is defined as the signal that travels the direct path between transmitter and receiver, and the ground-reflected wave, which is the signal arriving at the receiving antenna after being reflected from the surface of the ground. On the other side, the surface wave is the wave guided along the surface of the ground, whose attenuation is directly

affected by the distance to the source, the frequency, and the dielectric constants of the ground along where it propagates.

If the antennas are placed directly over the surface of the ground, the direct and ground-reflected wave in the space wave cancel each other, and propagation takes place entirely by means of the surface wave. At frequencies in the decimeter and centimeter band (reasonably high), as the ones where V2X and LTE are defined, the attenuation of the surface wave is extremely large, so that propagation would be limited to very short distances, much more than the distances to be covered defined in the standards. Fortunately, automotive antennas are installed on the roof of the car or embedded at some parts of the vehicle, e.g. bumpers, so that they are raised several wavelengths above the ground at the lowest frequency.

Hence, the case of interest in practice is the one where transmitting and receiving antennas are elevated above the ground, about 0.3 to 1.6 m in a sedan-type car. In this case, the space wave is no longer zero, and the signal at the receiving antennas is approximately the vector sum of the direct and the ground-reflected wave. Due to the electrical properties of the ground, a worsening of the far-field characteristic to lower levels than the ones obtained with perfectly conducting ground is expected. At some elevation angles above the horizon the direct and ground-reflected waves add exactly in phase, leading to a theoretical increase in field strength of 6 dB with regard to the free-space pattern. At other elevation angles, the two waves are completely out of phase and the resultant field shows a null. The elevation pattern will be formed by multiple lobes and nulls depending on the electrical height h/λ (in terms of the wavelength) of the antenna above ground [13].

Approximate expressions for the radiated fields can be obtained if the source of radiation is placed high enough above a plane ground, so that the waves hitting the surface can be assumed to be plane over a local area. Under such assumptions, the reflected wave is computed so as it comes from an image source by means of the image theory of reflection, and the reflection coefficients obtained for uniform plane waves can be used. Since V2X-communication is a short-range communication system (up to 1000 m), the assumption of a plane earth is accurate enough.

2.1 Effects of the Vehicle Body on Radiation Characteristics

Automotive antennas are placed somewhere in the car in close proximity to the metal chassis or in the nearby of composite and dielectric materials. The vehicle body, which corresponds to the scattering geometry in radio-frequency terms, also acts as a finite ground plane for the antennas considered in this thesis. The radiation characteristics of the antennas installed in the car are profoundly affected by the scattering objects found in the near-field of them, since induced currents in the metal parts modify the current distribution in the antenna itself and therefore, the radiation pattern and input impedance of them[1]. The vehicle parts which mainly contribute

[1]Recall that the radiation pattern is a three-dimensional Fourier transform of the current distribution in the antenna.

to distortions from the free-space pattern of a $\lambda/4$-monopole antenna on the roof top of the car near the rear rim are summarized in Fig. 2.1.

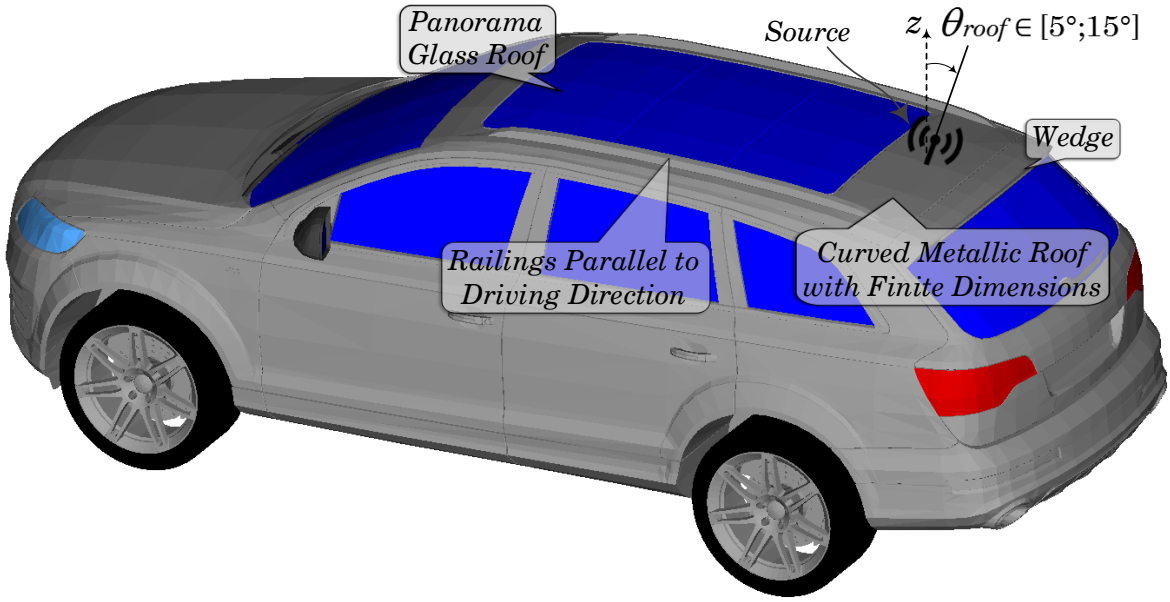

Figure 2.1: Parts of the vehicle close to the antenna which distort its corresponding free-space radiation pattern.

Due to the reasonably high frequency at which LTE and V2X-communication work and the growing trend of hiding antennas to preserve the aesthetics and design of the car, more random behavior is obtained in the shape of the radiation patterns. The random behavior is the result of summing all wave propagation effects (e.g., specular, coherent and incoherent (diffuse) reflections, diffractions, shadowing effects) taking place in such scenarios. The strong ripple induced in the far-field diagrams and the randomness of the problem when considering even different vehicle types, introduce so many variables that a mathematical solution would be very complex for practical applications. It is thus appropriate to treat the analysis of the results with a statistical approach, where the radiation pattern at a given time t_i or position r_i is a stochastic process as a function of the elevation angle θ and the azimuth angle φ. Unlike a laborious mathematical approach for a complicated particular problem, the statistical analysis holds for a variety of situations, and conclusions based on electromagnetic theory and wave propagation can be derived.

From a practical point of view, the goal of the analysis is to quantify the probability that the performance of an antenna system at a given location in the car is being degraded. In other words, and in order to achieve a reliable antenna system, the envelope of the radiation pattern should not be less than a threshold value at a given probability. This section is intended to analyze the

main effects at 5.9 GHz to quantify the deviation from the ideal radiation characteristics in free space of the investigated antennas in this thesis by means of statistics and Exploratory Data Analysis (EDA).

2.1.1 Required Radiation Patterns for V2X-Communication

Communication between vehicles or vehicles and pedestrians or other road side units (RSU) in a V2X scenario takes place mainly in the horizontal plane where the vehicles move. The same occurs for other automotive terrestrial services like LTE or audio broadcast, where communication with cell-phone towers or radio broadcasting antennas is confined at low elevation angles counting from horizon.

According to [102], a study of the angular power spectrum for V2X-communication in an urban road intersection scenario (t-junction), has shown that the angle of arrival in elevation for rooftop mounted antennas is confined at $\theta \in [80°, 90°]$ for vehicles far away from each other in NLOS conditions, and as long as the vehicles approach each other, the angle of arrival in elevation spreads to $\theta \in [40°, 90°]$. This means that the most relevant elevation angles are those comprised near horizon. Thus, the horizontal great circle of the radiation pattern of V2X antennas $\underline{\boldsymbol{C}}(\theta = 90°, \varphi)$, where $\underline{\boldsymbol{C}}(\bullet)$ denotes the normalized complex radiation pattern in spherical coordinates; as well as horizontal conical cuts near grazing angles ($\theta \approx 90°$) $\underline{\boldsymbol{C}}(\theta \in [70°; 90°], \varphi)$, are of the utmost importance.

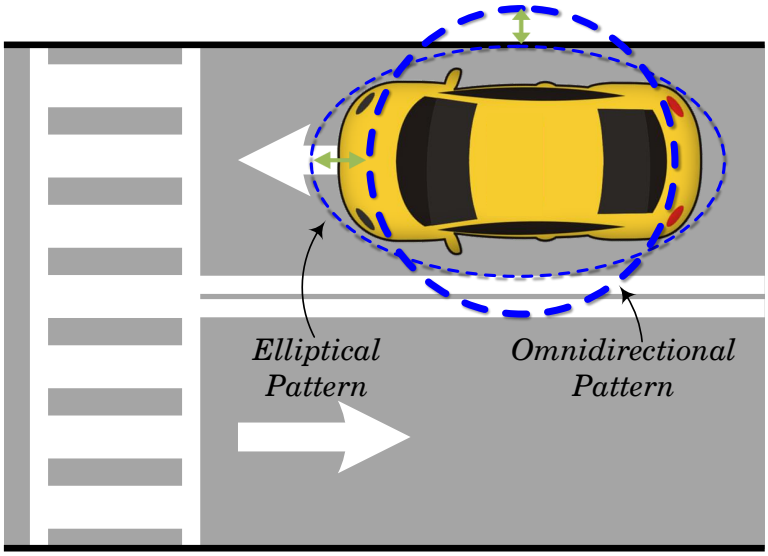

Figure 2.2: Overview of the required patterns for V2X-Communication at 5.9 GHz.

As depicted in Fig. 2.2, omnidirectional radiation patterns or elliptical ones in the horizontal plane are highly desired. While the former may also be advantageous for covering intersections or curved roads in rural scenarios at V2X frequencies, the latter has shown to provide better

down-range coverage with an adequate cross-road coverage, as required in highways, urban intersections or in crowded urban scenarios where the so-called *canyon effect* occurs. The investigation done in [102] shows that even at urban intersections, azimuth angles around driving direction are the most important ones in horizontal patterns. There, such elliptical patterns can be advantageous.

In the following chapters, emphasis will be placed on radiation patterns in the horizontal plane because of their importance for V2X and LTE. Nevertheless, some mentions will be made for radiation patterns in elevation, in the sense that disturbances in the shape of the elevation patterns cause changes of the absolute gain in the azimuth patterns.

2.1.2 Wave Propagation Considering the Vehicle and Its Effect on Radiation Pattern

To identify the deviations on the radiation pattern of antennas installed in an automobile with regard to the patterns of the antennas in free space, the field distribution is computed on and around the vehicle structure. Due to the relatively high frequency employed by V2X-communication, around 5.9 GHz, the Uniform geometrical Theory of Diffraction (UTD) is used in its graphical form to obtain a physical picture for the mechanisms of wave radiation and scattering in terms of rays. Introduced by Keller in the 1950's [62], the Geometrical Theory of Diffraction (GTD) overcomes the failure of Geometrical Optics (GO) in shadow regions of impenetrable objects, where GO based on incident, reflected and refracted rays following the *generalized Fermat's principle* predicts a zero in the electromagnetic field. The UTD [96], by means of the so-called *UTD transition functions* provides a solution to keep the fields bounded and continuous at and near ray-shadow boundaries and caustics where the GTD fields exhibit a singularity, and thus infinite electromagnetic fields.

2.1.2.1 Antennas Placed on the Roof of the Car

Electrically large complex antenna and scattering problems, like the antenna placement ones discussed in this thesis, can be decomposed into a few dominant reflected and diffracted rays, as shown in Fig. 2.3 associated to well-known canonical structures (e.g., curved wedges, discontinuities in surface impedances and curvatures, convex surfaces or vertices) found in typical scattering geometries of automotive applications and summarized in Figures 2.3, 2.6, 2.10, and 2.34. The diffracted rays, which are typically generated at geometrical or electrical discontinuities, propagate like GO-rays away from the diffraction point. The total field is thus the sum of incident (or direct field, if observation point and source lie under LOS conditions) and scattered field, where the scattered field is the superposition of all such dominant ray field contributions.

The rays traced on the CAD models of Figures 2.3, 2.6, 2.10, and 2.34 are one-dimensional representations of volumetric ray tubes (astigmatic ray tubes, ray pencils or flux tubes) of the spherical wave fronts generated at the source antenna, which at large distances from the source

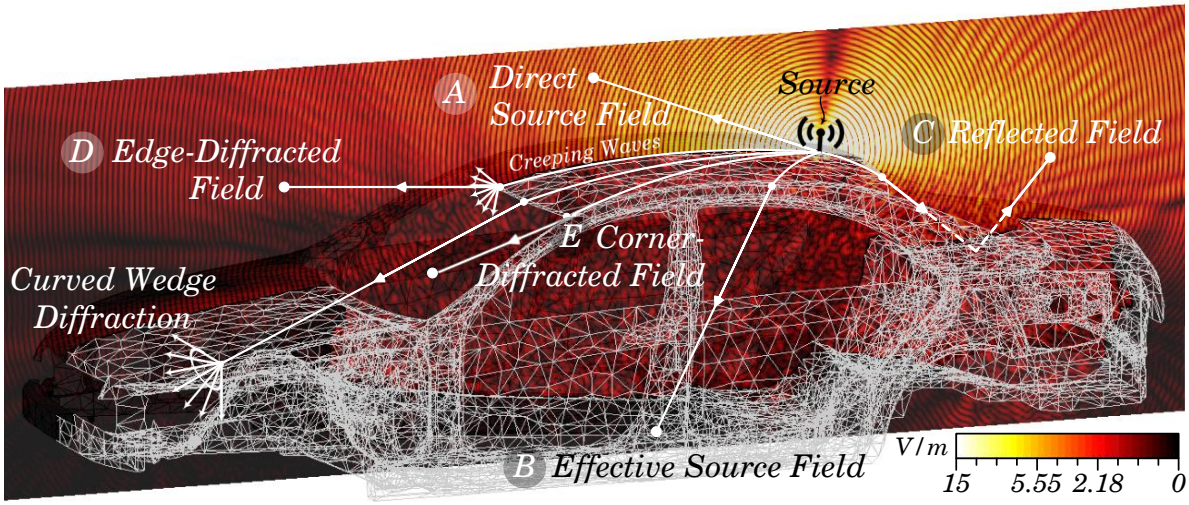

Figure 2.3: Physical picture in terms of rays based on UTD for explaining the mechanisms of wave radiation and scattering of antennas installed on the roof of a car. Rays are shown in their order of importance from A to E. A snapshot in time of the electric field distribution in a logarithmic scale of V/m (perspective cross-section view of a wireframe CAD model of a car) of a $\lambda/4$-monopole antenna on the roof of a car near the rear rim has been overlaid for completeness.

can be considered to be locally plane. A sketch of a general astigmatic ray tube can be seen in Fig. 2.4, as well as a spherical and plane wave ray tube in Fig. 2.5.

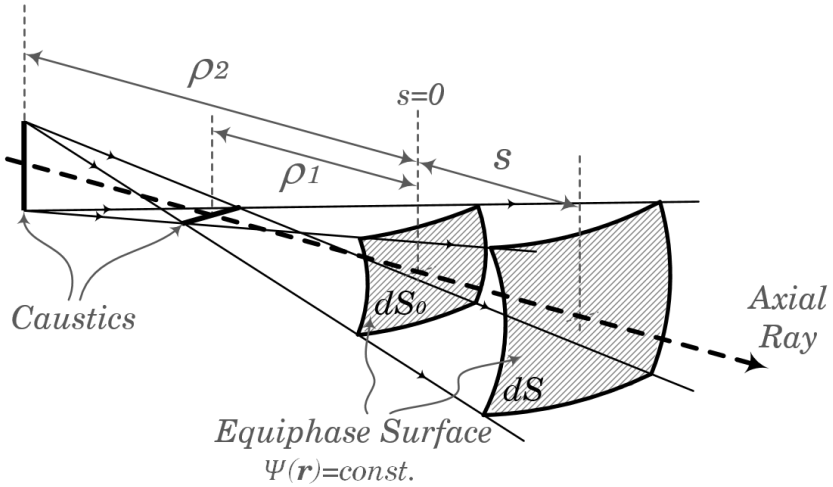

Figure 2.4: Infinitesimally narrow general diverging astigmatic ray tube. ρ_1 and ρ_2 are the principal radius of curvature of the wavefront dS_0 (striped surface) at the reference point $s = 0$. A positive (negative) radius of curvature represents diverging (converging) rays. The reception point is at a distance s from the reference point $s = 0$.

Each ray represents the high-frequency electromagnetic field or ray-optic field, which can

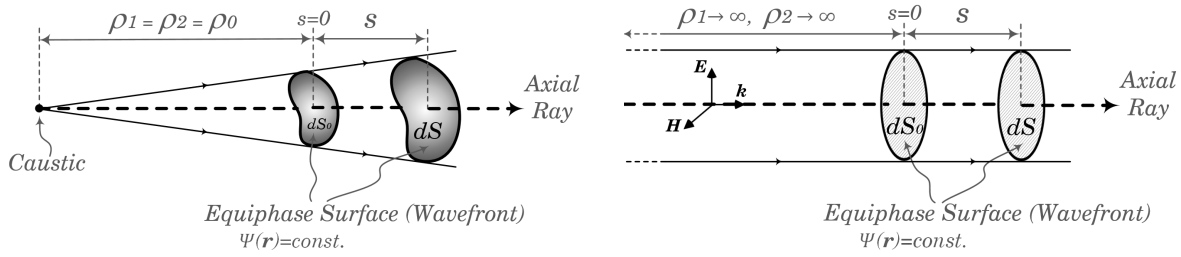

(a) Spherical wave ray tube.

(b) Plane wave ray tube.

Figure 2.5: Infinitesimally narrow astigmatic ray tubes for spherical and plane waves. The wave fronts (dS_0, dS) represent surfaces of equal phase.

be written as a Luneberg-Kline expansion for a source-free region ($\underline{\boldsymbol{J}} = \underline{\rho} = 0$) surrounded by an isotropic and homogeneous material with constitutive parameters ϵ and $\mu = \mu_0$ in the form of [87]

$$\underline{\boldsymbol{E}}(\boldsymbol{r},\omega) \sim e^{-jk\Psi(\boldsymbol{r})} \sum_{n=0}^{\infty} \frac{\underline{\boldsymbol{E}}_n(\boldsymbol{r})}{(j\omega)^n} \tag{2.1}$$

for the electric field (the magnetic counterpart is similar), where an $e^{j\omega t}$ time dependence is assumed, $\sim$ means "equal to" in the asymptotic sense, $k = \omega\sqrt{\mu_0\varepsilon}$ is the wave number of the medium and $\Psi(\boldsymbol{r})$ is the phase function. As ω increases, equation (2.1) becomes an increasingly accurate representation of the electromagnetic field [87].

After substituting equation (2.1) into the vector wave equation (Helmholtz equation) for the electric field, namely $\left(\Delta + k^2\right)\underline{\boldsymbol{E}}(\boldsymbol{r}) = 0$,[2] and integrating the resulting transport equation for the lowest order term ($n = 0$), the wave propagation in free space of the GO field for the general astigmatic ray is obtained, whose mathematical expression at the reception point s is given by

$$\underline{\boldsymbol{E}}(\boldsymbol{r}) \sim \underline{\boldsymbol{E}}_0(\boldsymbol{r}) e^{-jk\Psi(\boldsymbol{r})} \Rightarrow \underline{\boldsymbol{E}}(s) \sim \underline{\boldsymbol{E}}_0(s) e^{-jk\Psi(s)} = \underline{\boldsymbol{E}}(s=0) \sqrt{\frac{\rho_1\rho_2}{\left(\rho_1+s\right)\left(\rho_2+s\right)}}\, e^{-jks}, \tag{2.2}$$

where $\underline{\boldsymbol{E}}(s=0)$ contains the electric field amplitude, phase ($e^{-jk\Psi(s=0)}$), and polarization of the wave at the reference point $s = 0$, s is the distance traveled by the ray from the reference point $s = 0$ to the reception point $s = s$, e^{-jks} represents the phase shift along the ray path from the reference point $s = 0$, the term $S(s) = \sqrt{\rho_1\rho_2/\left(\rho_1+s\right)\left(\rho_2+s\right)}$ is the divergence factor (or spreading factor), which gives the amplitude variation of the GO field along the ray path, and ρ_1 and ρ_2 are the principal radius of curvature of the wavefront dS_0 at the reference point $s = 0$. The positive branch of the square root defined in $S(s)$ is chosen with $s > 0$ in the direction of wave propagation. A positive (negative) radius of curvature represents diverging (converging) rays. The GO rays

[2]Recall that the Laplace operator Δ is a second order differential operator given by the divergence ($\nabla\cdot$) of the gradient (∇f) of a function f, so that $\Delta f = \nabla^2 f = \nabla\cdot\nabla f$, where $\nabla = \left(\frac{\partial}{\partial x_1},\ldots,\frac{\partial}{\partial x_n}\right)$ is the vector differential operator Nabla, which may denote the *gradient* (locally steepest slope) of a scalar field f (grad $f \equiv \nabla f$), the *divergence* of a vector field $\boldsymbol{v}$ (div $\boldsymbol{v} \equiv \nabla\cdot\boldsymbol{v}$), or the *curl* (rotation) of a vector field $\boldsymbol{v}$ (curl $\boldsymbol{v} \equiv \nabla\times\boldsymbol{v}$).

are thus straight lines in a homogeneous medium[3], and they are everywhere orthogonal to the wavefronts or surfaces of constant phase in an isotropic medium[4].

The divergence factor $S(s)$ depends on the type of wave and takes the form of

$$S(s) = \begin{cases} \rho_0/(\rho_0+s) & \text{, for spherical wave } (\rho_1 = \rho_2 = \rho_0) \\ \sqrt{\rho_0/(\rho_0+s)} & \text{, for cylindrical wave } (\rho_{1,2} = \rho_0 \text{ and } \rho_{2,1} \to \infty) \\ 1 & \text{, for plane wave } (\rho_1 \to \infty \text{ and } \rho_2 \to \infty). \end{cases} \tag{2.3}$$

Although planes waves do not exist in reality, for reception points far away from the source and in a small solid angle sector, the waves can be treated as locally plane.

The one-dimensional rays shown in the physical pictures of radiation considering the vehicle correspond to the axial rays of Fig. 2.5 and lie in the center of the volumetric ray tubes, whose cross sections correspond to equiphase planes ($\Psi(\boldsymbol{r})$ =const.) called wavefronts, as depicted in Fig. 2.5. Due to the spherical nature of the wavefronts launched from the source antenna, the increase in cross-sectional area of the ray tubes is directly proportional to r^2, where r is the propagation distance. This means that the fields of the ray tubes decrease as $1/r$ with a phase term e^{-jkr}, phenomenon which is known as *ray-tube divergence*.

Although the UTD approach is used here to provide a physical picture for the computed electromagnetic radiation of antennas installed in an automobile, it is out of the scope of this thesis to treat the analysis mathematically. Exact solutions based on electromagnetic field theory of complex geometries by rigorously solving Maxwell's equations are only possible with numerical methods. Approximated analytic expressions based on asymptotic solutions of Maxwell's equations, as the case of UTD, make sense for simple canonical forms at high frequencies, where the asymptotic solution converges to the exact solution as $\lambda \to 0$. Only the general form of the fields will be given here and the mathematical expressions for diffraction coefficients of canonical forms can be found in [87, 95]. Due to the complexity, variety of car types, and constantly change and evolution of automotive wireless services, fast and efficient statistical analysis to quantify the reliability of an antenna system in a given location are much more demanded than theoretical analysis of a particular scattering geometry. Statistical approaches offer great advantages for making general conclusions of antennas intended to work in a multitude of different platforms and scenarios, as will be discussed later.

As shown in Fig. 2.3 for rooftop antennas and due to the almost optimum position of the antenna with direct LOS in almost 50% of angular directions (see Fig. 3.2 in the next chapter), the main contribution to the radiated fields is that from the source radiating spherical waves. Due to the smoothly convex surface of the roof where the antenna sits, creeping waves propagate along

[3]This property does not hold for inhomogeneous media, where the ray paths are usually curved due to the change in the constitutive parameters of the material.

[4]An isotropic medium is one whose constitutive parameters of permittivity ϵ, and permeability μ are uniform in all directions. Unlike homogeneity, which does not depend on the direction, isotropy is based on the direction of the properties of the medium.

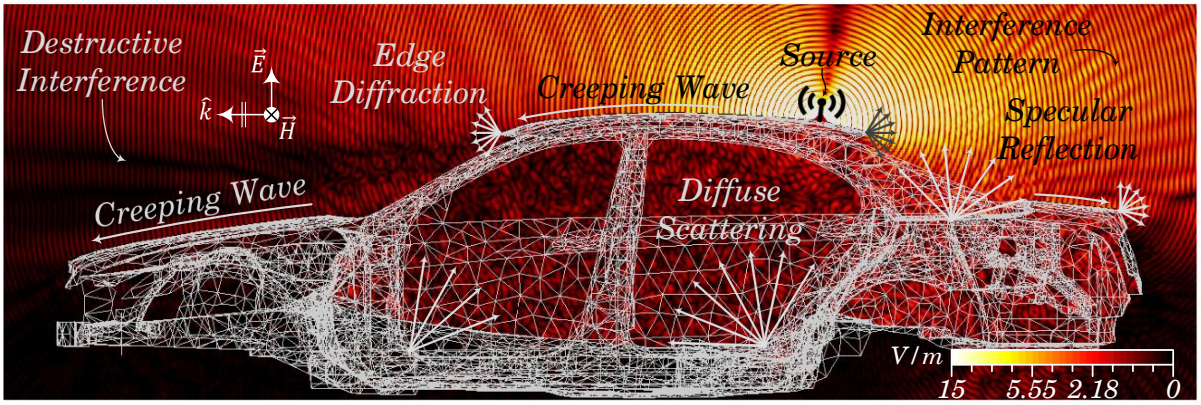

Figure 2.6: Wave propagation effects describing the electromagnetic radiation of antennas installed on the roof of a car. Snapshot in time of the electric field distribution in a logarithmic scale of V/m (longitudinal cross-section view of a wireframe CAD model of a car) of a $\lambda/4$-monopole antenna on the roof of a car near the rear rim.

it up to the end of the roof where the field reaches the observation point after being diffracted or refleted somehow as illustrated in Fig. 2.3 with letters B to E.

Creeping waves represent the electromagnetic fields that propagate along geodesic paths[5] tangentially shedding straight rays to the space along their direction of travel. Fig. 2.6 describes the electromagnetic phenomena seen in terms of rays by means of a snapshot in time of the electric field distribution created by an antenna placed on the roof near the rear rim [21]. As seen in Fig. 2.6, when the spherical wave of the source antenna reaches the boundaries of the roof, it propagates onwards after being diffracted at the roof's edges. Thus, the main electromagnetic effects for antennas on the roof are the creeping wave and the edge diffractions at the boundaries of the roof.

The general form of the UTD diffracted fields is given by

$$\underline{\boldsymbol{E}}_d(s) = \underline{\boldsymbol{E}}_i(s=0)\left[\underline{\boldsymbol{D}}\right] S(s) e^{-jks} \tag{2.4}$$

where the spreading factor $S(s)$ and the diffraction coefficients of the diffraction matrix $\left[\underline{\boldsymbol{D}}\right]$ depend on the incoming wavefront, and the geometrical form of the obstacle related to well-known canonical forms, whose asymptotic high-frequency approximation of the exact solution based on field theory can be found in [87, 95]. $\underline{\boldsymbol{E}}_i(s=0)$ is the incident electric field at the reference wavefront, the point where the wave is diffracted.

To get a better graphical insight on the diffraction phenomena than the analytical expressions derived from the UTD do, the effect has been graphically illustrated in Fig. 2.7 for the edge

[5]Minimum path distance that electromagnetic waves follow. The geodesic path resides on the surface along where the wave travels. On a sphere, the geodesic path is always the arc of a great circle.

diffraction at the rear rim of the car's roof. The Huygen's principle[6] is used together with the well-known results of a knife-edge (sharp edge) diffraction. The graphical explanation of the resultant field can be seen in Fig. 2.8.

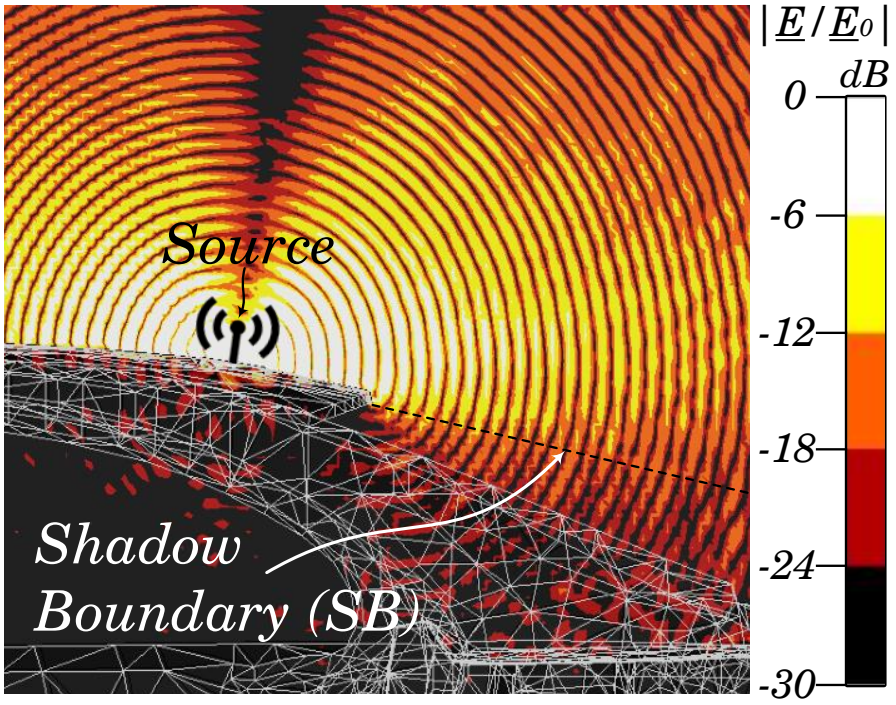

Figure 2.7: Rear roof's edge diffraction phenomena for antennas on the top roof: Snapshot in time of the normalized electric field distribution in dB of a $\lambda/4$-monopole antenna near the rear rim of the roof of a CAD model of a car (longitudinal cross-section view around the C-pillar). At the shadow boundary, the relative field is 6 dB less than that without the obstacle.

An easy model to compute analytically the normalized electric field strength in the presence of edge diffractions is given by the knife-edge or sharp-edge diffraction model. The results obtained by means of UTD or with the knife-edge diffraction are very similar [41]. The derivation of the analytical expression for the knife-edge diffraction can be found in [41], and for sources of spherical waves the final result is given by the equation

$$\left|\frac{\underline{E}(\boldsymbol{r})}{\underline{E}_0(\boldsymbol{r})}\right| = \frac{1}{\sqrt{2}}\sqrt{\left[\frac{1}{2}-C(v)\right]^2+\left[\frac{1}{2}-S(v)\right]^2} \tag{2.5}$$

[6]The Huygen's principle states that each point of a primary wave front can be regarded as the source of a secondary spherical wave called wavelet. The tangent curve along the multiple wavelet fronts (elementary spherical waves) builds the primary wave front, so that the total field results.

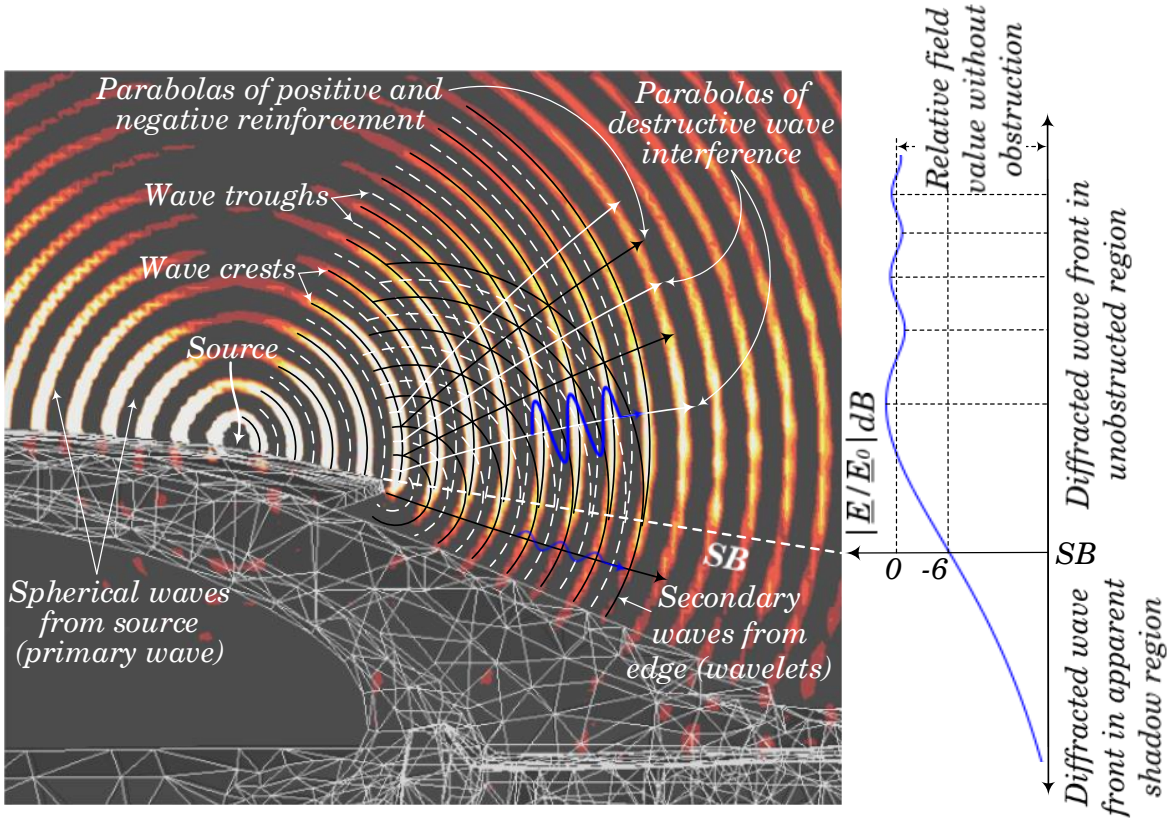

Figure 2.8: Physical picture of the rear roof's edge diffraction phenomena in terms of the Huygen's principle. The spherical waves from the antenna (primary wave front) interfere with the waves originated at the rear edge, which can be regarded as a source of secondary waves. Destructive and constructive interferences lead to a ripple in the radiated field (as seen in the curve of relative field strength) and the parabola of maximum positive and negative reinforcement lifts up the main beam in elevation. The effects deteriorate the radiation pattern in the far-field. The normalized field strength curve is computed according to equation (2.5).

where $C(v)$ and $S(v)$ are the real Fresnel integrals[7] defined as

$$C(v) = \int_0^v \cos\left(\frac{\pi t^2}{2}\right) dt \tag{2.6}$$

and

$$S(v) = \int_0^v \sin\left(\frac{\pi t^2}{2}\right) dt \tag{2.7}$$

where v is a normalized factor directly proportional to the height at which the field is evaluated and which depends on the wavelength, and the distance from source to the reception point with respect to the edge.

[7] Some important properties of the real Fresnel integrals are that $C(v=0) = S(v=0) = 0$, $C(v\to\infty) = S(v\to\infty) \to 1/2$, and they are odd functions, so that $C(-v) = -C(v)$.

The field distributions of Figures 2.7 and 2.8 are computed by means of numerical full wave methods because in the near field of the edge, equation (2.5) is no longer valid. However, the computation of equation (2.5) yields almost identical results and can be regarded as a good approximation to the diffraction phenomena at the boundaries of the roof. The axes of Fig. 2.7 have been scaled so that there is a 6 dB difference between the consecutive colour grades. This makes it easier to perceive that at the shadow boundary ($\upsilon = 0$), the field decays 6 dB in relation to the field that would exist without the obstacle ($\left|\underline{E}/\underline{E}_0\right| = 1/2$ in a linear scale). This property is independent of the frequency of operation as inferred from equation (2.5), since $C(\upsilon = 0) = S(\upsilon = 0) = 0$, and thus $\left|\underline{E}/\underline{E}_0\right| = 1/2$, $\forall\lambda$. As the frequency increases, the transition between the diffracted fields in the unobstructed region and the ones in the apparent shadow region of Fig. 2.8 becomes more abrupt. In the limit for $\lambda \to 0$, only the GO field would exist [41].

The next electromagnetic effect in order of importance for antennas placed on the top of the roof is the specular reflection on the trunk lid and the coherent and diffuse scattering around the trunk region and in the tray between the back seats and the trunk, as depicted in Figures 2.3 and 2.6.

For reflection on flat surfaces, the ratio of ray divergence remains the same after reflection, but it changes for curved surfaces depending on the curvature type. For convex curved surfaces the ratio of ray-tube divergence increases, and for concave surfaces decreases up to converging into a focus point (caustic), before diverging again.

Other electromagnetic effects like specular reflections, curved wedge diffractions on the edges of the motor hood and trunk and diffuse scattering in rough surfaces in the inside of the car, create interference pattern musters in the radiated field which lead to ripples in the far-field pattern. In order to emphasize the weak scattering effects in the shadow region of the antenna, a logarithmic scale is used in Figures 2.3 and 2.6. The radiation patterns in the upper hemisphere for different antenna placements on the roof of an automobile are displayed as a contour plot in Fig. 2.9. Contour plots, unlike great circle or conical cuts, are a useful tool to capture in two dimensions the behavior of the antenna throughout the whole upper hemisphere without having to superimpose many curves on a single diagram as in the case of the great circle or conical cuts in polar form. Case A, which shows the ideal quarter-wave monopole antenna on an infinite ground plane, is included as a reference. Case B illustrates the distortions caused by the roof of a car when the antenna is placed on the middle of the roof. Case C shows the radiation pattern of a monopole-like antenna on the rear roof-top mounting position. And case D adds railings oriented in parallel to the driving direction to a rear roof-top mounted antenna. The omnidirectionality is lost when the antenna is placed on the back of the roof of the car. And a ripple is observed when metal rails are added as a consequence of the multiple reflections in them. At the bottom of Fig. 2.9, the great circle cuts ($\theta = 90°, \varphi$) in polar form for all four cases are included for completeness.

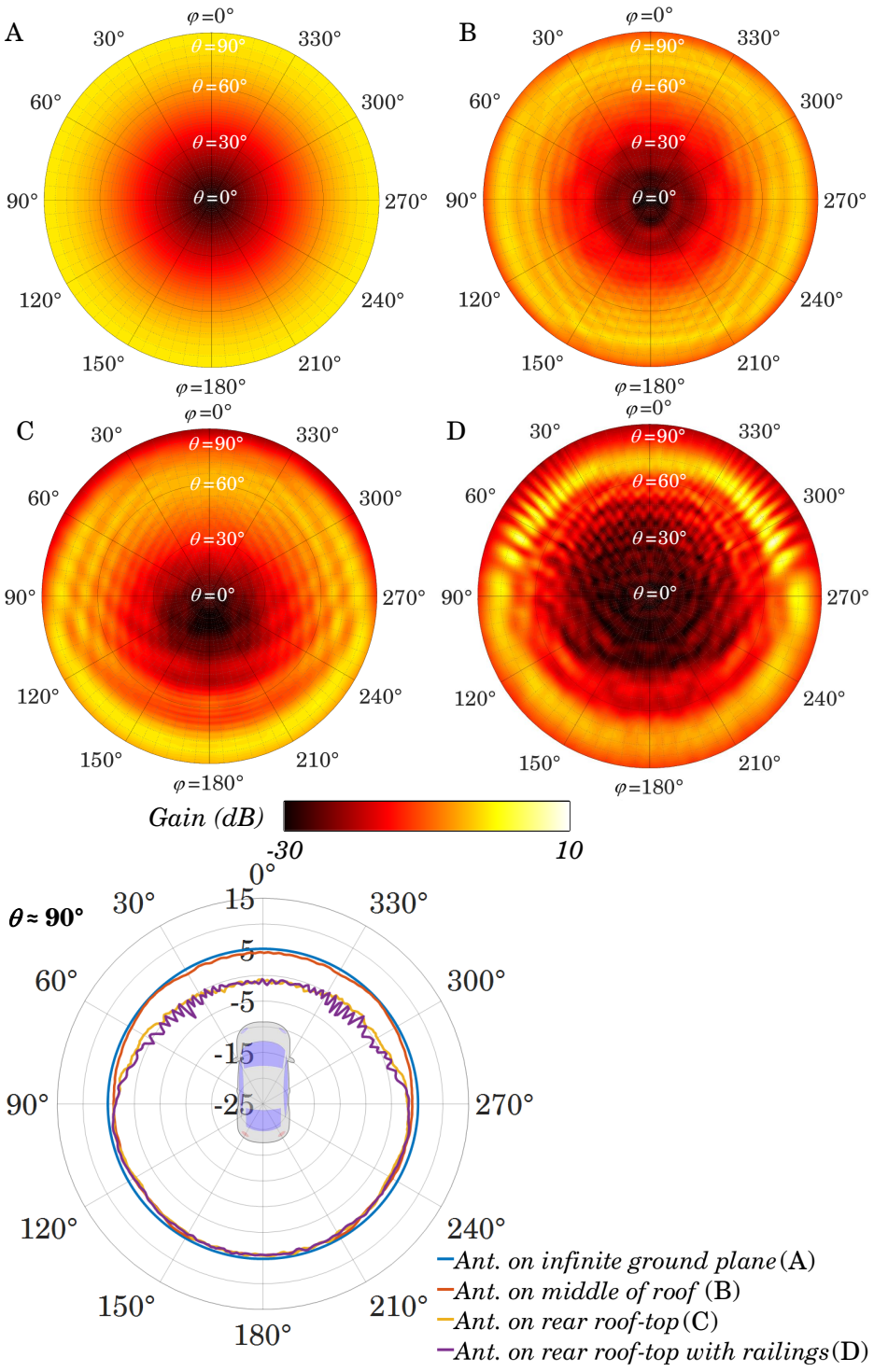

Figure 2.9: Distorting effects on radiation pattern of antennas in typical roof-top mounting positions: Antenna radiation patterns (realized gain) of antennas placed in typical roof-top mounting positions illustrated in contour polar form (top) and polar horizontal great circle cuts ($\theta = 90°, \varphi$) (bottom). Case A: Ideal $\lambda/4$-monopole antenna on infinite ground plane. Case B: Monopole-like antenna on the middle of the roof. Case C: Monopole-like antenna on the rear roof-top mounting position. Case D: Same case as C but with railings oriented in parallel to driving direction. 1° resolution.

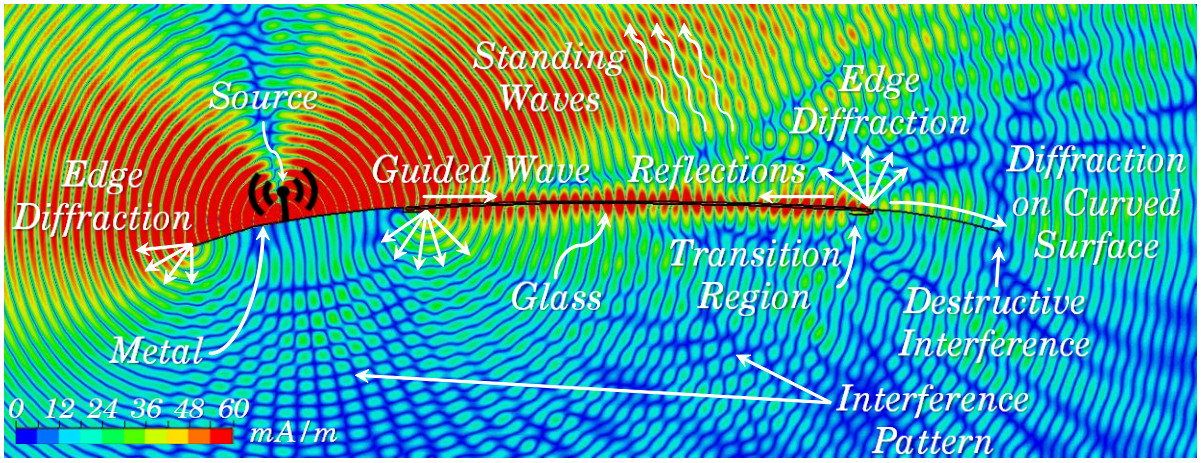

Figure 2.10: Wave propagation effects describing the electromagnetic radiation of antennas on panorama glass roofs. Snapshot in time of the magnetic field distribution in mA/m (longitudinal cross-section view) of a $\lambda/4$-monopole antenna in close proximity to a panorama glass window.

2.1.2.2 Antennas Placed on Sunroofs or Panorama Glass Roofs

New automotive design trends have increased the overall glazed area in modern vehicles, incorporating the glass as a structural component and reducing the use of heavy materials to guarantee the structural integrity of vehicles. Modern cars use around 20% more glass than they did 20 years ago [98]. However, the average glass content in a modern vehicle represents only 3% of the vehicle weight [60], due to the development of the glass industry and the efforts to reduce weight while increasing safety and security for the passengers.

In a modern automobile equipped with a panorama glass roof, the glazed area can represent around 50% of the total roof area, considering a roof with dimensions $\approx 1.6 \times 1.2\text{m}^2$, and a panorama glass window with dimensions $\approx 1.0 \times 0.9\text{m}^2$. Therefore, the electromagnetic effect of the growing use of dielectrics like glass and plastics in up-to-date car's chassis should be investigated to predict the behavior of a source of radiation when placed in the vicinity of such materials. In this section, the radiation characteristics of antennas place in close proximity to glazing areas has been investigated.

In Fig. 2.10, the wave propagation effects that describe the electromagnetic radiation of antennas placed on sunroofs or panorama glass roofs in close proximity of glass windows are highlighted [25]. Comparing with Figures 2.3 and 2.6, the main difference lies on the electromagnetic phenomena in and around the glass. The destructive interference caused by the superposition of the travelling wave from the source antenna, propagating as a surface wave above the glass, with the different mode waves entering and scaping the glass film due to various propagation phenomena, yields to an attenuation and ripple of the azimuth radiation pattern at $\theta \approx 90°$ in an azimuth sector of about 120° in driving direction, as shown in Fig. 2.32.

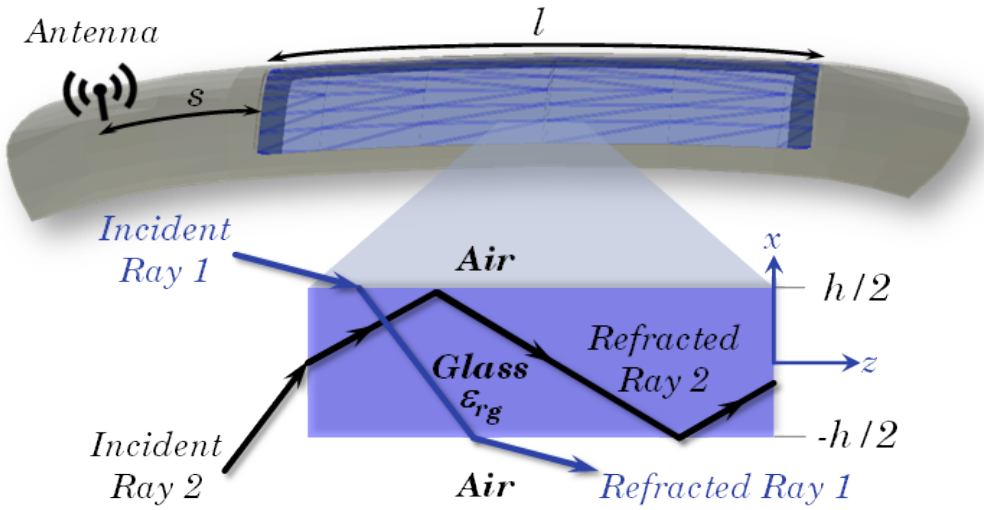

Figure 2.11: Electromagnetic phenomena in and around glass windows on the roof: CAD model of a panorama sunroof (top), and path of rays in and around the glass (bottom). The antenna is placed near the rear rim, at a distance s from the rear edge of the panorama glass. Driving direction corresponds to the longitudinal $\hat{z}$-direction, according to waveguide's nomenclature for wave propagation direction.

From a microwave point of view, the sunroof of a car essentially behaves as a planar, symmetrical, dielectric slab waveguide consisting of a film (glass), with a height h =6.76 mm and dielectric permittivity $\varepsilon_{r_g} = 6.9$, sandwiched between air, as shown in Fig. 2.11 [24]. The smooth curvature of the roof (with radii of curvature of about 90λ at 5.9 GHz in a common sedan-type car) does not play the main role regarding the electromagnetic effects of the sunroof, as it will be shown, so that a flat roof can be considered to reduce the complexity of the analysis and the computational effort in simulations.

The electromagnetic phenomena occuring in and around the glass window can be explained by means of the different modes present in dielectric waveguides and excited in the region of the glass film. They can be first divided according to their polarization, namely in transverse electric (TE) modes with zero longitudinal electric field ($E_z = 0$), and transverse magnetic (TM) modes with zero longitudinal magnetic field ($H_z = 0$). Each of both polarizations can support guided and radiation modes. A mode of the dielectric waveguide is defined as an electric or magnetic field solution of Maxwell's equations that satisfy the boundary conditions at the interfaces of the waveguide and which has the general form of a harmonic, periodic time-dependence field

$$\begin{aligned} \underline{\boldsymbol{E}}(\boldsymbol{r},t) &= \underline{\boldsymbol{E}}(\boldsymbol{r})e^{j\omega t} = \boldsymbol{E}_m(x,y)e^{j(\omega t-\beta_m z)}, \\ \underline{\boldsymbol{H}}(\boldsymbol{r},t) &= \underline{\boldsymbol{H}}(\boldsymbol{r})e^{j\omega t} = \boldsymbol{H}_m(x,y)e^{j(\omega t-\beta_m z)}, \end{aligned} \tag{2.8}$$

where m is the mode label indicating the mode number and β_m is the propagation constant of the mode, which propagates in z direction. Although the glass window of a sunroof provides confinement in two dimensions, x and y as inferred from Fig. 2.11, only the confinement in x

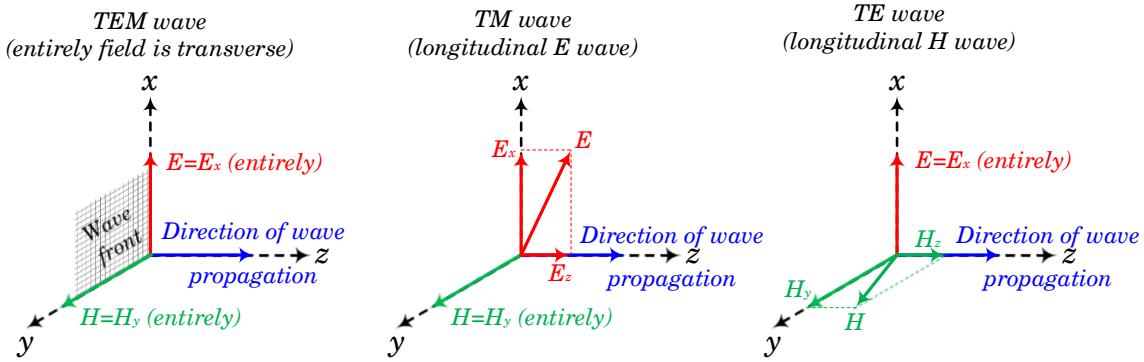

Figure 2.12: Graphical illustration of the field vectors for TEM, TM, and TE waves.

direction will be considered to simplify the analysis, since it is enough representative of the electromagnetic phenomena occuring in situations such as the one described in Fig. 2.11. This fact allows only one label m to be used for the mode number.

The general modal field solutions of equation (2.8) are inserted into Maxwell's equations to obtain the corresponding wave equations governing the two polarization mode types which can be supported by a planar dielectric waveguide (TE and TM). A graphical illustration of the field vectors for transversal electromagnetic (TEM), transversal magnetic (TM), and transversal electric (TE) waves can be seen in Fig. 2.12.

Since a planar glass film (with confinement only in the x direction) is considered, all field solutions are independent of the y-coordinate. The following analysis will be conducted for a TM mode, since the field of a monopole-type source corresponds to that of a TM mode. Its counterpart analysis, namely for TE modes, can be found in [66]. The fields for the TM modes are given by [66]

$$\begin{aligned} E_y &= H_x = H_z = 0, \\ E_x &= \left(\beta/\omega\varepsilon\right) H_y, \\ E_z &= -(j/\omega\varepsilon)\,\partial H_y/\partial x, \end{aligned} \tag{2.9}$$

with the H_y obeying the wave equation $(\Delta \underline{\boldsymbol{E}}(\boldsymbol{r}) + k^2 n^2(\boldsymbol{r})\underline{\boldsymbol{E}}(\boldsymbol{r}) = 0)$ given by [66]

$$\partial^2 H_y/\partial x^2 = \left(\beta^2 - n^2 k^2\right) H_y, \tag{2.10}$$

where the glass film is characterized by a dielectric constant $\varepsilon = \varepsilon_0 n^2(x,y)$ and $n(x,y) = n(x) = \sqrt{\varepsilon_r}$ is the refractive-index profile, which for confinement in the x-direction only and homogeneous materials as the case that concerns us is equal to the square root of the dielectric permittivity.

For dielectric waveguides, as the glass window of a sunroof or panorama glass roof, the field solutions can be of the form of guided modes (bound states), where the energy flow is confined near the propagation axis z; of radiation modes, where the energy associated to the wave spread

out through the air surrounding the glass window; and of the form of evanescent modes with imaginary propagation constants $\underline{\beta}_m = -j\gamma_m$, where the fields decay as $e^{-\gamma_m z}$.

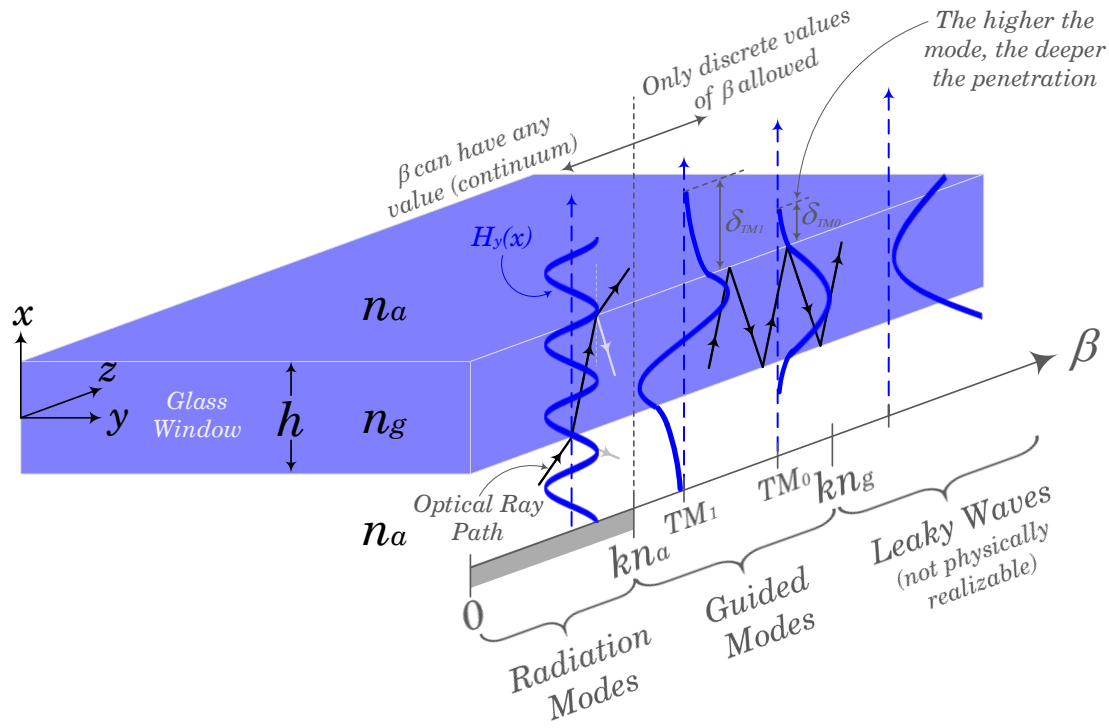

Figure 2.13: Propagation modes in a dielectric slab waveguide: Classification of the waveguide modes in a planar, symmetrical, three-layer dielectric slab waveguide, corresponding to a small piece of panorama glass roof with refractive index n_g and height h. The glass layer is sandwiched by air with a refractive index $n_a = 1$. Wave propagation occurs in the longitudinal $\hat{z}$-direction. The values of the propagation constant β for radiation modes form a continuum, and the field has a standing wave distribution outside the glass. For guided modes, only discrete values of β are allowed and the field decays exponentially outside the glass film. Inside the glass, harmonic variation of the field distribution is expected.

Fig. 2.13 shows a sketch of a planar approximation of a glass window of a sunroof with the classification of the modes present in a planar, symmetrical, three-layer dielectric slab waveguide as a function of the value of the propagation constant β. Ray-optical techniques with local plane wave approximation will be used here again to explain the electromagnetic phenomena that lead to distorted radiation patterns in the azimuth plane. Ray optics yields a graphical insight into the phenomena taking place in and around the glass window of a sunroof or panorama glass roof, which although it is not as complete as the mathematical description provided by the electromagnetic theory, it is much more appealing and intuitive for practical purposes. Full agreement with the equations derived from the electromagnetic theory is obtained, as will be shown hereafter.

As briefly commented before, the attenuation and ripple of the azimuth radiation pattern in

driving direction is due to the superposition of various waves with different phases as a result of different electromagnetic phenomena. The most important electromagnetic phenomena taking place in and around the glass window for sunroofs or panorama glass roofs are individually detailed as follows:

a) Surface waves (creeping waves for convex curved sunroofs) propagating on the surface of the glass coming from the source antenna. They create travelling waves in z direction with a wave vector $\boldsymbol{k}n_a$, where $n_a = 1$ and $k = 2\pi/\lambda$ is the propagation constant in the air, as shown in Fig. 2.14.

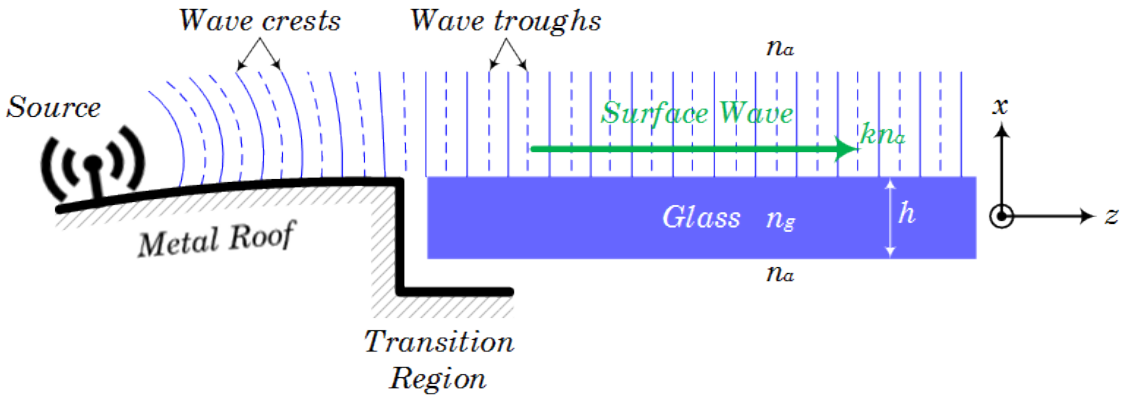

Figure 2.14: Sketch of the surface wave above the glass roof. The wave normal of the surface wave is indicated in green.

b) Guided wave inside the glass as a result of an incoming wave impinging the glass from the narrow side, as shown in Fig. 2.15. The incoming wave can be part of the travelling wave coming from the source antenna or as a result of the edge diffraction at the metal edge of the transition region.

According to Fig. 2.13, guided modes can only propagate at some discrete values of the propagation constant β, or more specifically, at some discrete values of the angle θ_i according to Fig. 2.15. Looking closer, the propagation constant β (related to the phase velocity v_p) is given by

$$\beta = \frac{\omega}{v_p} = kn_g \sin\theta_i, \tag{2.11}$$

which is the z-component of the wave vector $\boldsymbol{k}n_g$ [66].

Examining Fig. 2.15 in more detail by means of a ray-optical approach, the sum of all phase shifts in the zig-zag picture of the uniform plane wave normals from point A to B must be an integer m multiple of 2π. For a glass film of thickness h, this self-consistency condition leads to

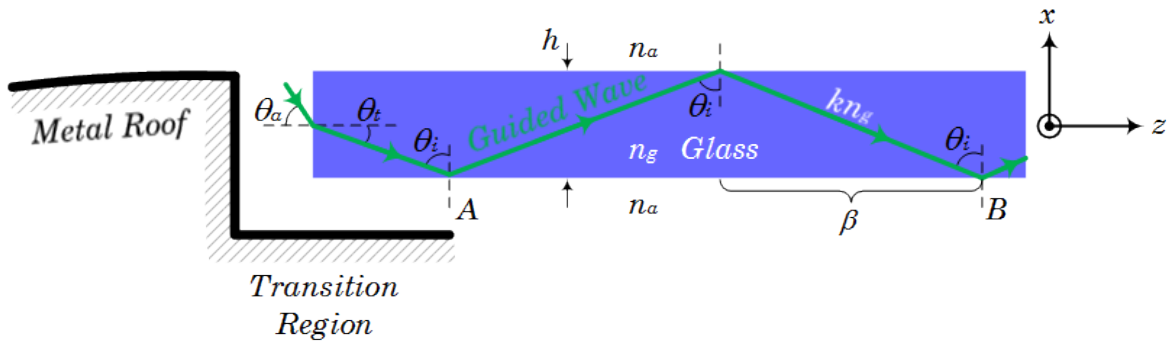

Figure 2.15: Sketch of the guided wave inside the glass window of a sunroof or panorama glass roof. The picture represents two superimposed uniform plane waves with wave normals which follow the zig-zag path indicated in green and which are totally reflected at the internal boundaries of the glass window.

the well-known *dispersion relation* or *transverse resonance condition* given by [66]

$$\underbrace{2kn_g h\cos\theta_i}_{\substack{\text{Phase shift for}\\ \text{transverse passage}\\ \text{through glass (up/down)}}} - \underbrace{2\phi_a}_{\substack{\text{Phase shift due to}\\ \text{total internal reflection}\\ \text{at upper interface}}} - \underbrace{2\phi_a}_{\substack{\text{Phase shift due to}\\ \text{total internal reflection}\\ \text{at lower interface}}} = 2m\pi \quad \text{for} \quad m = 0,1,2,\ldots, \tag{2.12}$$

where m is the mode number, ϕ_a is the phase shift associated with the total reflection at the glass-air boundary, θ_i is the angle of incidence at the internal boundaries of the glass-air interface, h the height of the glass slab, $n_g = \sqrt{\varepsilon_{r_g}}$ is the refractive index of the glass computed as the square root of the dielectric permittivity of the glass ε_{r_g}, and the wave number $k = 2\pi/\lambda$ denotes the absolute value of $\boldsymbol{k}$, considering that in the direction of the wave normals in Fig. 2.15 the uniform plane waves travel in zig-zag fashion with a wave vector $\boldsymbol{k}n_g$, whose fields vary as $e^{-jkn_g(\pm x\cos\theta_i + z\sin\theta_i)}$.

A graphical solution of the dispersion equation (2.12) can be seen in Fig. 2.16 for the fundamental mode $m = 0$ that propagates inside the glass window with a height h =6.76 mm and refractive index $n_g = \sqrt{\varepsilon_{r_g}} = \sqrt{6.9} = 2.63$. The figure shows, as a function of the incidence angle θ_i, both the phase shift in the transverse x-direction ($kn_g h\cos\theta_i$) and the sum of the phase shifts at the internal boundaries of the glass ($2\phi_a$). It can be inferred from Fig. 2.16 that there is always a solution for β (or θ_i) for the fundamental mode $m = 0$ satisfying the dispersion relation of equation (2.12), which means that unlike metal waveguides or asymmetric dielectric guides, for symmetrical dielectric waveguides as the glass window in sunroofs or panorama glass roofs, there is no cut-off for the fundamental mode. Increasing the glass height h or the frequency f (or decreasing λ_g), the glass window will also support higher modes.

Equation (2.12) yields, essentially, the propagation constant β as a function of the angular frequency ω and glass thickness h, whose general graphical sketch can be seen in Fig. 2.17. From the figure, showing the first three guided modes ($m = 0,1,2$), it can be inferred that the propagation constant β for guided modes is bounded from below by the plane-wave propagation

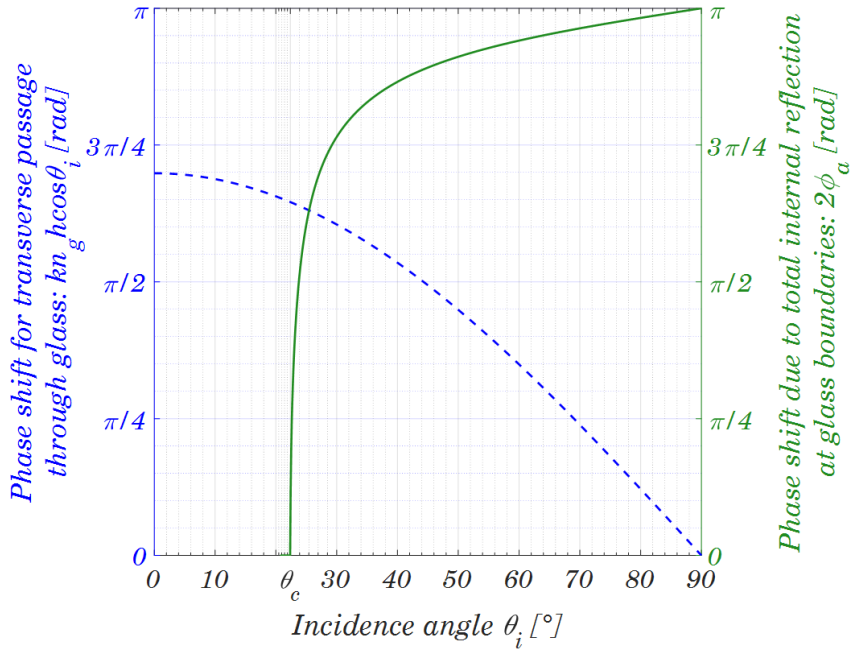

Figure 2.16: Graphical solution of the dispersion relation of equation (2.12) for the fundamental TM mode $m = 0$ of a glass window with height h =6.76 mm and dielectric permittivity $\varepsilon_{r_g} = 6.9$ in sunroofs or panorama glass roofs at 5.9 GHz. θ_c =22.38° denotes the critical angle. The intersection of both curves occurs at $\theta_i = 24.92°$.

constant of the air (kn_a), and from above by that of the glass (kn_g), so that $kn_a < \beta < kn_g$, which is often expressed as $n_a < N < n_g$, where

$$N = \beta/k = n_g \sin\theta_i \tag{2.13}$$

is a normalization factor called *effective guide index* N. As the angular frequency ω (or the glass height h) increases, more guided modes can propagate inside the glass. Together with the discrete values of β that lead to guided modes, the continuous spectrum of β up to the bound kn_a that lead to radiation modes is also shown in green.

For a more precise and universal ω-β diagram, equation (2.12) should be evaluated numerically after introducing some normalized values that combine several waveguide parameters [66]. The dispersion relation of equation (2.12) can be expressed more compactly as [67]

$$\underbrace{\kappa_g h}_{\substack{\text{Phase shift for}\\ \text{transverse passage}\\ \text{through glass}}} - \underbrace{2\phi_a}_{\substack{\text{Phase shift due to}\\ \text{total internal reflection}\\ \text{at internal boundary}}} = m\pi \quad \text{for} \quad m = 0, 1, 2, \ldots, \tag{2.14}$$

where κ_g is the *transverse propagation constant* in the glass given by

$$\kappa_g^2 = k^2\left(n_g^2 - N^2\right) = \varepsilon_{r_g} k^2 - \beta^2. \tag{2.15}$$

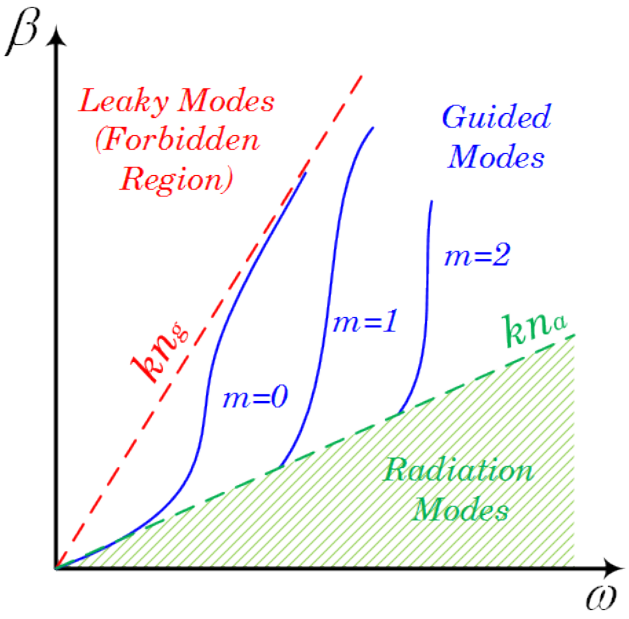

Figure 2.17: Sketch of a typical ω-β diagram of a dielectric waveguide. Shows the dispersion relation of equation (2.12) graphically.

The *transverse decay constant* in the air γ_a needed to determine the phase shift ϕ_a in the dispersion relation of equation (2.14), is given by [67]

$$\gamma_a^2 = k^2\left(N^2 - n_a^2\right) = -\kappa_a^2 = -\left(k^2 - \beta^2\right) \quad \text{for} \quad n_a = 1, \tag{2.16}$$

where κ_a is the transverse propagation constant in the air, and n_a is the refractive index of the air, so that $n_a = 1$.

The normalized frequency or glass thickness V is defined as [66, 67]

$$V = kh\sqrt{n_g^2 - n_a^2}. \tag{2.17}$$

Equations (2.13) to (2.17) are valid for TE and TM modes, but the phase shift ϕ_a depends on the propagation mode. The following analysis will be conducted for a TM mode, since the field of a monopole-type source corresponds to that of a TM mode. Its counterpart analysis, namely for TE modes, can be found for asymmetric, dielectric slab waveguides in [67]. The formula for the phase shift ϕ_a for TM modes at the interface glass-air is given by

$$\tan\phi_a = \left(\frac{n_g^2}{n_a^2}\right)\left(\frac{\gamma_a}{\kappa_g}\right). \tag{2.18}$$

A normalized guide index b as a function of the effective index N (and therefore β) is defined for TM modes as

$$b = \left(\frac{N^2 - n_a^2}{n_g^2 - n_a^2}\right)\left(\frac{n_g^2}{n_a^2 q_a}\right) \Rightarrow N^2 = \left[n_g^2(1-b) + n_a^2 b\right] q_a, \tag{2.19}$$

where the reduction factor q_a is given by

$$q_a = \frac{N^2}{n_g^2} + \frac{N^2}{n_a^2} - 1 = \frac{n_a^2/n_g^2}{(1-b) + b n_a^4/n_g^4}, \tag{2.20}$$

so that $b = 0$ at guide cut-off, and $b = 1$ far away from cut-off.

By means of the previously defined normalized frequency or thickness V, reduction factor q_a, and normalized guide index b, the normalized form of the dispersion relation of equation (2.14) becomes [67]

$$\underbrace{V\left[\sqrt{q_a}\left(\frac{n_g}{n_a}\right)\right]\sqrt{1-b}}_{\substack{\text{Normalized phase shift for}\\ \text{transverse passage}\\ \text{through glass}}} - \underbrace{2\arctan\sqrt{\frac{b}{1-b}}}_{\substack{\text{Normalized phase shift due to}\\ \text{total internal reflection}\\ \text{at internal boundary}}} = m\pi \quad \text{for} \quad m = 0,1,2,\ldots. \tag{2.21}$$

Equation (2.21) is solved numerically and plotted in Fig. 2.18 in the form of a universal chart. Substituting the height h =6.76 mm and the refractive index of the glass $n_g = \sqrt{\varepsilon_{r_g}} = \sqrt{6.9} \approx 2.63$ in equation (2.17) at 5.9 GHz, the normalized frequency or glass thickness V becomes $V = 2.029$ and from the universal chart of Fig. 2.18, the normalized guide index b can be found as $b \approx 0.69$. From Fig. 2.18 can also be inferred that only the fundamental mode $m = 0$ can propagate inside the glass window for the given thickness h at 5.9 GHz. Recall that there is no cut-off for the fundamental mode, as clearly seen in Fig. 2.18. The total number of allowed TM (it also applies to TE modes) guided modes in a symmetric guide is given by the relation [84]

$$m = \left\lceil \frac{V}{\pi} \right\rceil_{int} = \left\lceil \frac{2h}{\lambda}\sqrt{n_g^2 - n_a^2} \right\rceil_{int}, \tag{2.22}$$

where the symbol $\lceil \bullet \rceil_{int}$ denotes the integer immediately greater than the value of the number in brackets. For the case that concern us, the total number of allowed TM guided modes inside the glass window of the sunroof or panorama glass roof is $\lceil 0.65 \rceil_{int} = 1$. At 5.9 GHz, the next higher mode ($m = 1$) will only propagate if the height of the glass window $h \geq$1.05 cm.

To show that it is possible to couple into the glass from the narrow side of it with an angle θ_a (as depicted in Fig. 2.15) such that the wave travels inside the glass with an angle θ_i greater than the critical one θ_c for total internal reflection, the third Snell's law is used at the narrow side of the glass film where the incoming wave hits the glass window, and at the lower interface glass-air where the presumed guided wave should be totally internally reflected to be guided further inside the glass. It is worth noting that in this case the plane wave approach has been used for the ray picture even if the phase of the incoming wave changes according to the angle at which the wave hits the glass, since it does not matter with which phase the wave penetrates into the glass slab. Thus, according to Fig. 2.15 and the third Snell's law, it follows that

$$n_a \sin\theta_a = n_g \sin\theta_t = n_g \sin\left(\frac{\pi}{2} - \theta_i\right), \tag{2.23}$$

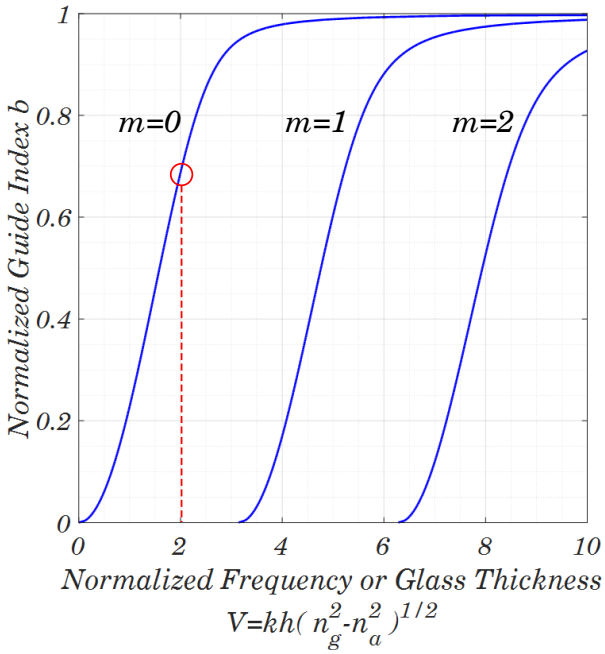

Figure 2.18: Normalized ω-β diagram: Graphical solution of the normalized dispersion relation of equation (2.21) for the normalized guide index b as a function of the normalized frequency V for the lowest three TM modes in a symmetric dielectric waveguide. The solution for the glass window with a height h =6.76 mm and $\varepsilon_{r_g} = 6.9$ has been marked in red, which leads to $V = 2.029$ and $b \approx 0.69$, so that only the fundamental mode $m = 0$ can propagate inside such a glass roof.

which leads to

$$\theta_i = \frac{\pi}{2} - \arcsin\left(\frac{n_a}{n_g}\sin\theta_a\right). \tag{2.24}$$

Fig. 2.19 shows the possible values for θ_i as a function of the incoming angles θ_a at the narrow side of the glass. It is worth noting that only angles $\theta_i \geq 67.624°$ are possible for a wave coupling into the glass from the narrow side of it with any possible angle $\theta_a \in [0°;90°]$. Since the critical angle for total internal reflection at the internal boundaries of the glass is given by the relation

$$\theta_c = \arcsin\left(\frac{n_a}{n_g}\right) = \arcsin\left(\frac{1}{\sqrt{6.9}}\right) = 22.38°, \tag{2.25}$$

which is also derived from the third Snell's law considering that the transmitted angle is greater than $\pi/2$, only incidence angles θ_i at the interface glass-air greater than the critical angle θ_c would lead to trapped waves inside the glass propagating in a zig-zag path with total internal reflection at the boundaries of the glass. For the case that concern us, the condition for total internal reflection for waves striking on the narrow side of glass is always ensured according to Fig. 2.19. However, as already seen in Figures 2.13 and 2.17, not all angles θ_i are allowed. Only a discrete set of them leads to a self-consistent zig-zag ray picture satisfying the dispersion relation of equation (2.12) illustrated in Fig. 2.16.

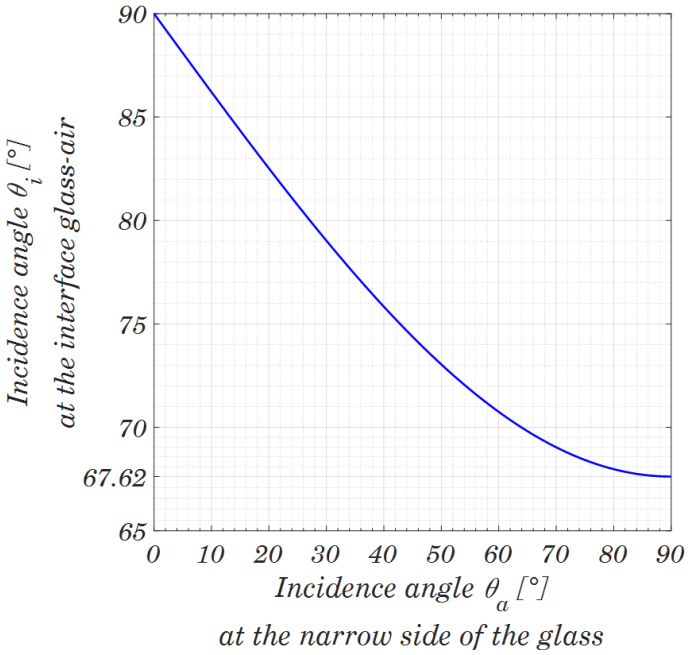

Figure 2.19: Incidence angle θ_i at the interface glass-air in Fig. 2.15 as a function of the incoming angle θ_a hitting the glass at its narrow side.

According to Fig. 2.16, the value of θ_i which is greater than the critical angle θ_c and satisfies at the same time the dispersion relation of equation (2.12) for the fundamental mode $m = 0$ is given by the intersection of the dashed blue line with the solid green one, and is equal to θ_i =24.92°. This is in disagreement with equations (2.23, 2.24), where it was derived that $\theta_i \geq$67.624° in order to couple into the glass with a real-valued angle θ_a.

This apparent contradiction is solved by means of the so-called *Goos-Hänchen shift*[8], which states that in order to obtain a zig-zag ray picture consistent with the energy flow, lateral shifts given by $2z_a$ at the upper and lower glass-air interfaces should be incorporated, as illustrated in the more detailed ray picture of Fig. 2.20.

These lateral shifts in z direction causes some part of the rays guided inside the glass to penetrate into the air with a penetration depth x_a. As a consequence, the glass appears to be higher than the physical height h, leading to consider an effective height h_{eff} defined by [67]

$$h_{eff} = h + 2x_a > h, \tag{2.26}$$

where the penetration depth x_a for TM modes is related to the decay constant in the air γ_a of equation (2.16) by the reduction factor q_a of equation (2.20) as follows [67]

$$x_a = \frac{1}{q_a \gamma_a}, \quad \text{so that} \quad h_{eff} = h + \frac{2}{q_a \gamma_a}. \tag{2.27}$$

[8]The incorporation of this effect into the ray model was first proposed by Burke in [26], the prediction of the ray lateral shift first pointed out by Newton in [91], and the name of Goos-Hänchen shift was given after the experimental demonstration performed by F. Goos and H. Hänchen in [44].

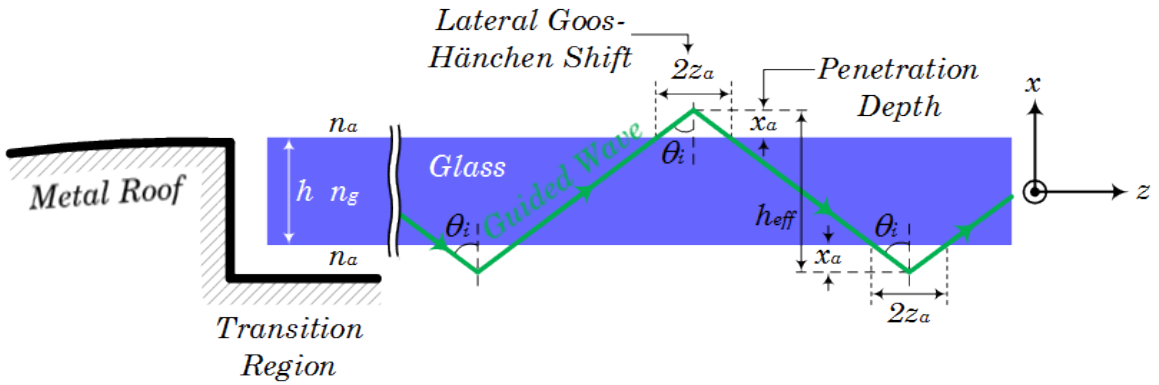

Figure 2.20: Refined ray picture of guided wave propagation inside the glass by means of the lateral Goos-Hänchen shift $2z_a$ and penetration depth x_a into the air, leading to a glass effective thickness h_{eff}.

An analogous normalization to that of V in equation (2.17) is done to define a normalized effective glass thickness W as follows

$$W = k h_{eff} \sqrt{n_g^2 - n_a^2}. \tag{2.28}$$

Combining equations (2.27) and (2.16), equation (2.26) can be written for TM modes in terms of the normalized effective glass thickness W as a function of the normalized frequency V as [67]

$$W \cdot \left[\sqrt{q_a}\left(\frac{n_g}{n_a}\right)\right] = V \cdot \left[\sqrt{q_a}\left(\frac{n_g}{n_a}\right)\right] + \frac{2}{\left[q_a \sqrt{b}\left(\frac{n_a}{n_g}\right)^2\right]}, \tag{2.29}$$

where its graphical solution is shown in Fig. 2.21 as a universal chart. The normalized effective glass thickness W has been marked in red for the corresponding normalized frequency V given by the physical height of the glass h =6.76 mm, refractive index $n_g \approx 2.63$, and frequency 5.9 GHz, which for $V = 2.029$, implies that $W \approx 22$. This means an effective height h_{eff} of roughly 7.3 cm.

The refined ray picture of Fig. 2.20 is changing the phase shift of the transverse passage through the glass in the dispersion relation comparing to Fig. 2.15, due to the larger height given by h_{eff}. Figure 2.22 illustrates graphically the new dispersion relation of equation (2.12) considering the effective height h_{eff}, instead of the physical height h, due to the Goos-Hänchen shift effect. It can be noted that now the discrete value of θ_i (and therefore β), for which a self-consistent ray picture leads to a guided wave, is given by the value of $\theta_i \approx 82.4°$. This value belongs to the interval $\theta_i \in [67.624°; 90°]$ derived in equation (2.24) by means of the third Snell's law, which corroborates the fact that a wave coupling into the glass from the narrow side of it (like ray 2 in Fig. 2.11) yields a guided mode inside the glass. According to Fig. 2.19, the angle of reflection for guided waves inside the glass given by $\theta_i \approx 82.4°$ implies a wave coupling into the narrow side of the glass with an angle $\theta_a \approx 20.3°$.

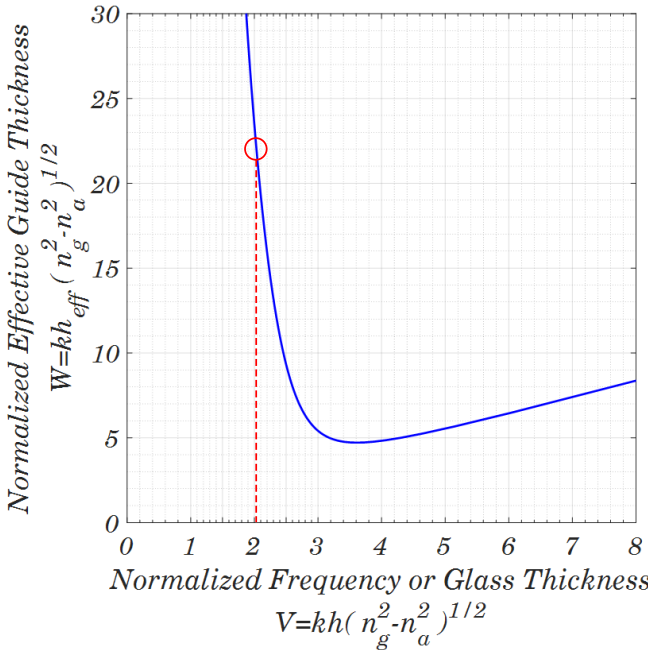

Figure 2.21: Normalized effective glass thickness W as a function of the normalized frequency V for the fundamental TM mode ($m = 0$). The value for the glass parameters under consideration has been marked in red.

Thus, once the electromagnetic wave couples into the glass, it propagates in zig-zag fashion through the dielectric glass window in z direction due to the total internal reflection produced at the glass boundaries, according to the ray picture of Fig. 2.20. The lateral shift of the Goos-Hänchen effect and the penetration of the rays in the air region surrounding the glass window can also be seen in the magnitude of the simulated Poynting vector of Fig. 2.23 for a flat panorama glass roof. It is worth noting that the rays of Fig. 2.20 are defined as the directions of the associated Poynting vectors or the energy flow of the waves, so that the depicted rays correspond to the axis of the narrow beams of the astigmatic ray tubes shown in Fig. 2.5. As already commented, unlike plane waves in a homogeneous, isotropic medium, for anisotropic mediums, the direction of the wave normal does not correspond to that of the ray picture. The same occurs when considering the Goos-Hänchen shift. Figure 2.23 shows how the energy flow is not only confined within the glass, but also in the vicinity of it, as predicted by the Goos-Hänchen shift.

The ray picture of Fig. 2.20 considering that the guided rays penetrate into the air region surrounding the glass is in perfect agreement with the description provided by electromagnetic theory, since the introduced penetration depth x_a is closely related to the exponential decay length of the evanescent wave in the air region surrounding the glass window, as will be seen in equation (2.30).

The field solutions for the fundamental TM mode $m = 0$ inside and surrounding the sunroof derived by means of electromagnetic theory using equations (2.9) and (2.10) are that of the

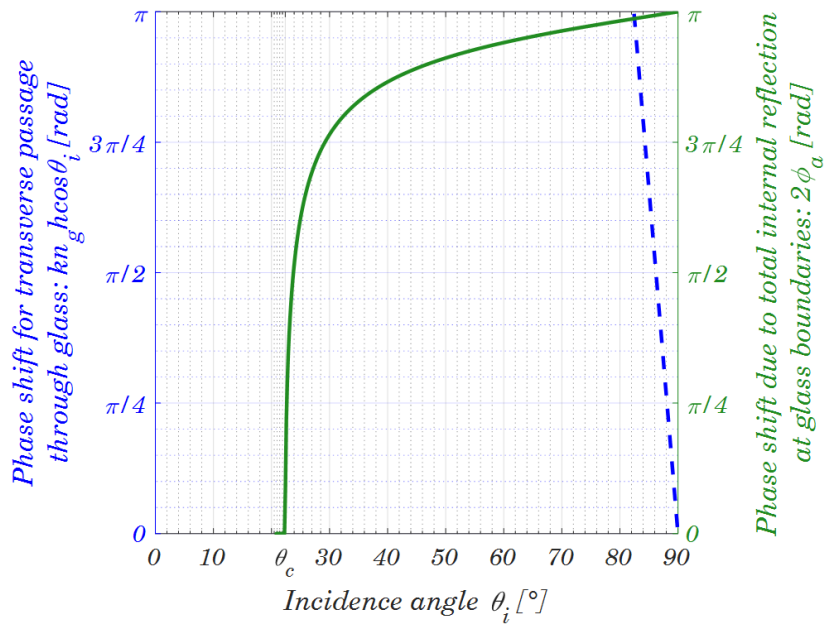

Figure 2.22: Graphical solution of the dispersion relation of equation (2.12) for the fundamental TM mode $m = 0$ considering the Goos-Hänchen shift effect in a glass window with effective height h_{eff} ≈7.3 cm and refractive index $n_g \approx 2.63$ at the frequency of 5.9 GHz. The intersection of both curves occurs at θ_i ≈82.4°.

symmetric slab waveguide [66]. They satisfy the boundary conditions at the interfaces glass-air, so that $H_y(x)$ (and therefore $E_x(x)$) and $\partial H_y(x)/\partial x$ (and therefore $E_z(x)$) are continuous at $x = -h/2$ and $x = h/2$. Thus, the field solutions take the form of the fields in equation (2.8), which are given by [66]

$$\text{(2.30)} \qquad \begin{cases} H_y(x) = H_a e^{-\gamma_a(x-h/2)} & \text{for} \quad x > h/2 \quad \Rightarrow \quad \textit{Exponential decay} \\ H_y(x) = H_g \cos\left(\kappa_g x\right) & \text{for} \quad |x| < h/2 \quad \Rightarrow \quad \textit{Harmonic variation} \\ H_y(x) = H_a e^{+\gamma_a(x+h/2)} & \text{for} \quad x < -h/2 \quad \Rightarrow \quad \textit{Exponential decay} \end{cases}$$

where H_a and H_g are the magnetic peak fields in the air and glass regions respectively, h the thickness (height) of the glass; propagation in z direction is assumed according to $e^{j(\omega t-\beta z)}$ and γ_a and κ_g are the decay factor in the air and the propagation constant in the glass, respectively, as defined in equations (2.15) and (2.16).

A snapshot in time of the magnetic field distribution located in the XZ plane is shown in Fig. 2.24 for the fundamental TM_0 mode traveling along the glass slab as a guided wave [24]. It can be clearly seen, for a region around the center of the glass roof, the harmonic variation within the glass in the form of a cosine function and the exponential distribution outside the glass, which agrees with the evanescent wave corresponding to the rays penetrating into the surrounding air region, as postulated by ray-optics theory with the Goos-Hänchen shift. The field profile in x

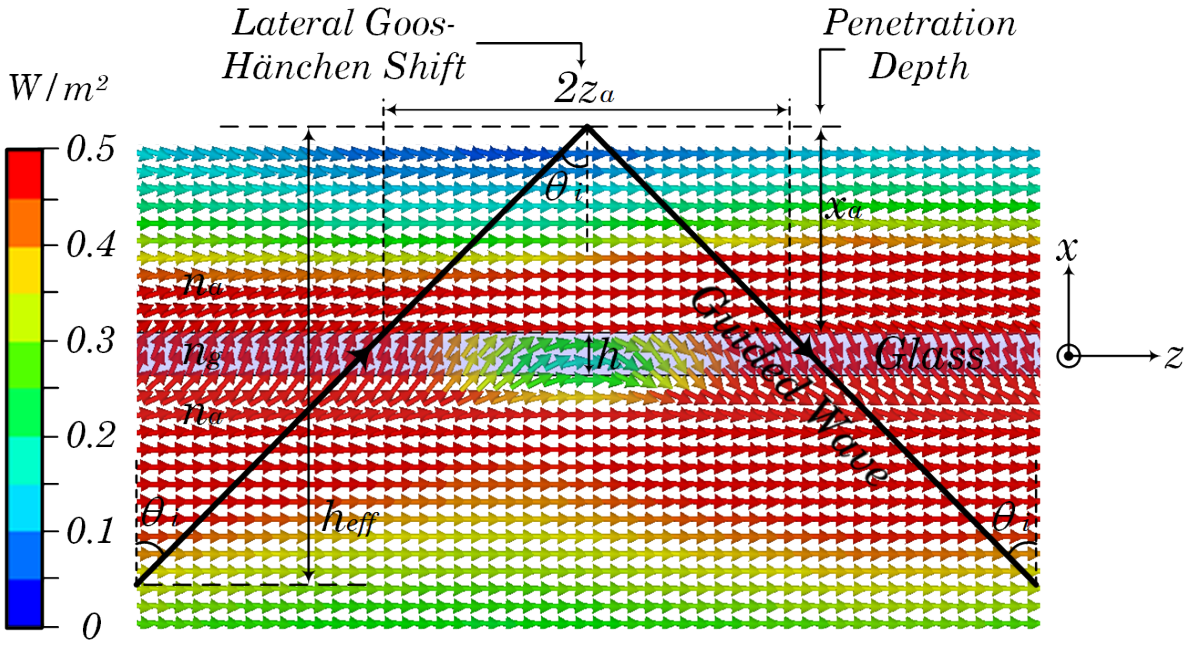

Figure 2.23: Snapshot in time of the Poynting vector in and around the glass window of a panorama glass roof to evaluate the energy flow. The Goos-Hänchen shift explains the lateral shift $2z_a$ seen in the ray picture, where the guided energy is not only confined within the glass, but penetrates with an exponential decay into the air surrounding the glass.

direction is computed both analytically by means of equation (2.30) and numerically by finite integration technique using a CAD model of a flat glass roof. The dark blue face represents the numerical solution and the red line the analytical solution for the first mode in the slab waveguide, indicating that only the fundamental mode TM_0 propagates inside the sunroof. There is no higher order mode at the operation frequency of 5.9 GHz and a glass thickness h =6.76 mm according to Fig. 2.18 and the magnetic field distribution obtained by means of numerical full wave methods.

As already seen, there are only a finite number of guided modes given by m in equation (2.22) satisfying the dispersion relation of equation (2.21). This fact means that other solutions of the Maxwell's equations which also satisfy the boundary conditions at the interfaces of the glass window must exist to provide a complete set of orthogonal modes. These solutions are the radiation modes, for which β can have any value, thus they form a continuum[9]. Such radiation modes correspond to the following electromagnetic effect that causes the attenuation of the azimuthal patterns in driving direction, which can be excited by (resuming the enumeration)

c) Waves hitting the glass from above (or below) the glass with any angle of incidence θ_a, leading to radiation modes.

[9]Radiation modes are sometimes referred as modes of the continuum.

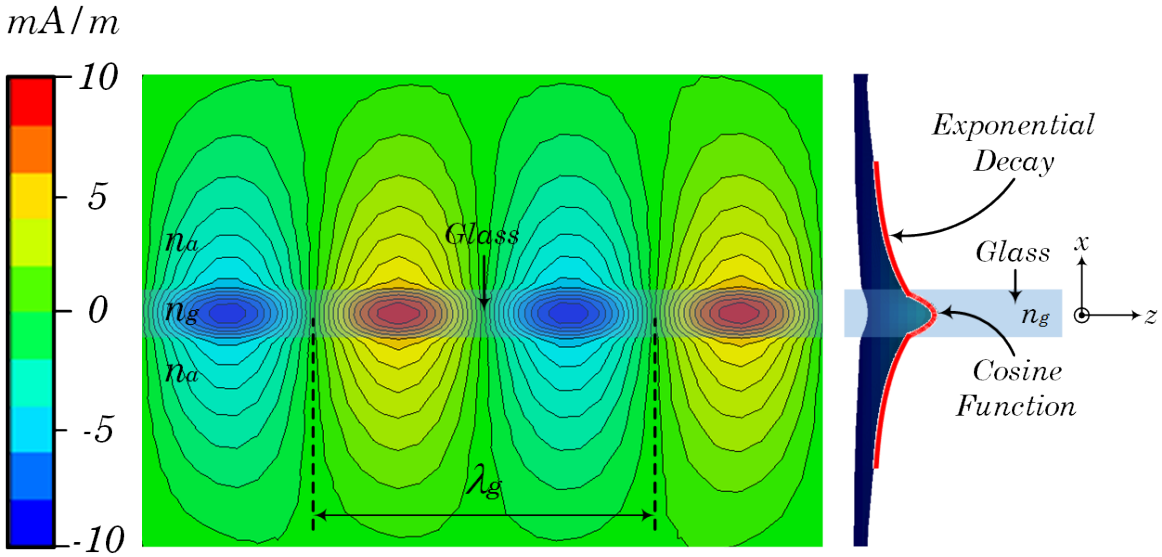

Figure 2.24: Fundamental mode TM_0 traveling along the glass slab: simulated magnetic field distribution (left); simulated (blue shade) and analytical (red curve) transversal $H_y(x)$ field profile (right). λ_g is the wavelength inside the glass.

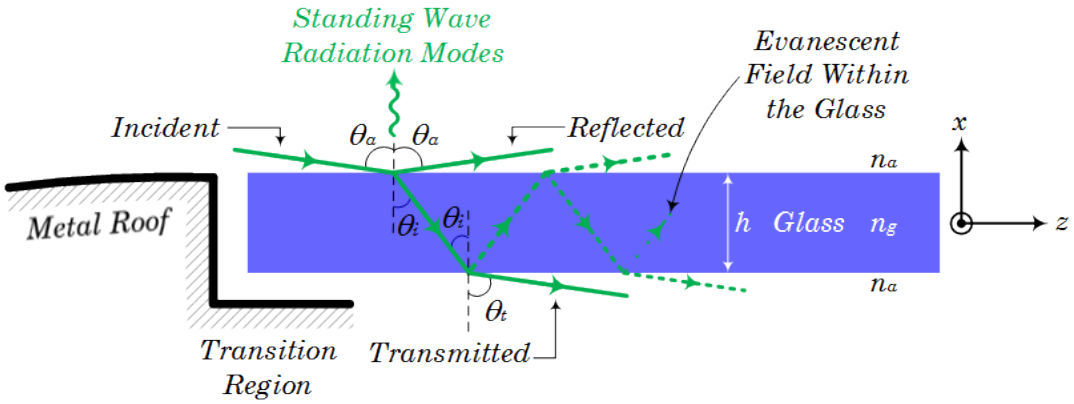

Figure 2.25: Sketch of a standing wave radiation mode hitting the glass window of a sunroof or panorama glass roof from above with an angle θ_a. The superposition of incident and reflected waves lead to a standing wave pattern in transverse x direction, while the mode travels along the z direction. The picture also represents two superimposed uniform plane waves with wave normals which follow a zig-zag path inside the glass reflecting at the glass boundaries with an angle θ_i smaller than the critical angle, so that some part of the ray is transmitted forward into the air surrounding the glass.

The field distributions in the transversal x direction show sinusoidal standing-wave patterns (harmonic variation) inside and outside the glass film, due to the interference between the incident and reflected waves. Their fields derived by means of electromagnetic theory for TM

modes are given for completeness and take the form of [66]

$$\left\{\begin{array}{lcll} H_y(x) & = & \overline{H}_a \cos\left[\kappa_a (x-h/2)+\overline{\phi}_a\right] & \text{for} \quad x > h/2 \quad \Rightarrow \quad \textit{Harmonic variation} \\ H_y(x) & = & \overline{H}_g \cos\left(\kappa_g x\right) & \text{for} \quad |x| < h/2 \quad \Rightarrow \quad \textit{Harmonic variation} \\ H_y(x) & = & \overline{H}_a \cos\left[\kappa_a (x+h/2)-\overline{\phi}_a\right] & \text{for} \quad x < -h/2 \quad \Rightarrow \quad \textit{Harmonic variation} \end{array}\right. \tag{2.31}$$

where $\overline{H}_a$ and $\overline{H}_g$ are the magnetic peak fields in the air and glass regions respectively, h the thickness (height) of the glass, κ_g is the transverse propagation constant in the glass as defined in equation (2.15), κ_a is the transverse propagation constant in the air, which is related to the transverse decay in the air γ_a as defined in equation (2.16), and the phase shift $\overline{\phi}_a$ is derived applying the boundary conditions and can be found in [66].

At this point, it is important to note that for a source of radiation placed outside the glass slab (see Fig. 2.11), and assuming a perfect, flat glass slab structure (that without dielectric losses and with infinite extension in the longitudinal ($\hat{z}$) and transversal ($\hat{y}$) directions, according to the axes shown in Fig. 2.11), none of its trapped energy inside the glass window can travel through the glass as a guided wave. This is because the incoming wave from the outside (ray 1 in Fig. 2.11) would require to hit the glass with imaginary incidence angles $\theta_a \in \mathbb{C}$ in Fig. 2.25, so that the wave would travel inside the glass as a guided wave with an angle θ_i according to the requirements previously discussed. Thus, rays hitting the glass from the top or bottom sides can only yield to radiation modes [84].

To illustrate this fact, the third Snell's law can be used, so that

$$n_a \sin\theta_a = n_g \sin\theta_i \quad \Rightarrow \quad \sin\theta_a = \frac{n_g}{n_a}\sin\theta_i. \tag{2.32}$$

For $\theta_a \in \mathbb{R}$, it must be fulfilled that

$$\frac{n_g}{n_a}\sin\theta_i \leq 1 \quad \Rightarrow \quad \theta_i \leq \arcsin\left(\frac{n_a}{n_g}\right) = \theta_c \equiv \textit{critical angle}. \tag{2.33}$$

However, it has already been shown that for total internal reflection at the internal boundaries of the glass, it must be accomplished that $\theta_i > \theta_c$. This shows that it is impossible to couple into the glass with a real-valued angle θ_a in such a way that the wave propagates inside the glass as a guided wave with total internal reflection at the interfaces glass-air. Thus, waves striking on the glass window from above or below can only excite radiation modes.

Unlike a perfect dielectric waveguide, where only the outgoing waves of radiation modes (those in Fig. 2.25 scaping the glass from below with an angle θ_t) contribute in proper phase to radiation, the glass window is no longer a perfect dielectric waveguide (it has finite longitudinal and transverse ($\hat{y}$) dimensions and losses), and the incoming and outgoing wave components fail to interfere constructively.

The next contribution to the destructive interference in driving direction is given by:

d) Diffracted waves at the edges of the metal-glass transition region.

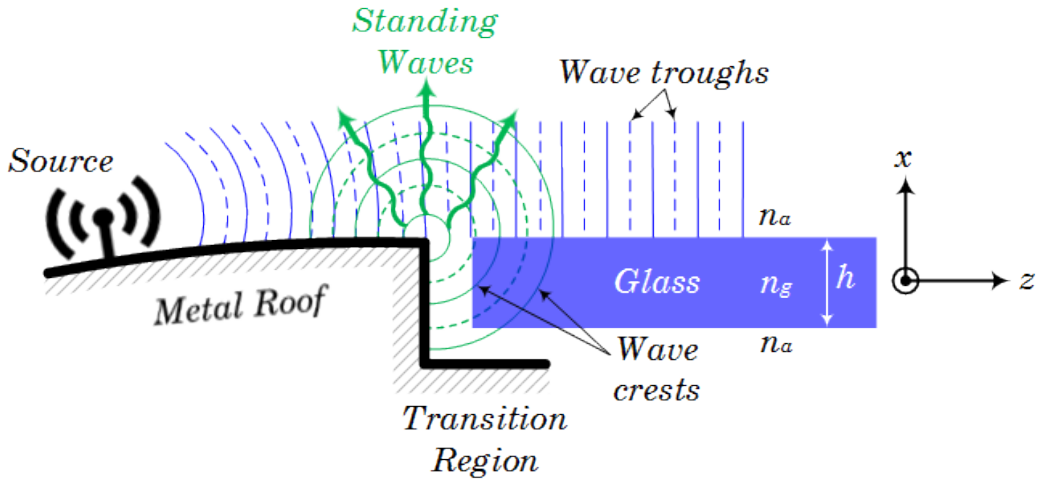

Figure 2.26: Sketch of diffraction effects at the edges of the transition region metal-glass. Standing waves are generated by superposition of the traveling waves from the source and the diffracted waves at the edge of the transition region.

This effect is analogous to that of Fig. 2.8 for diffraction at the edges of a metallic roof, and has been sketched in Fig. 2.26. The result is a standing wave pattern due to the superposition of the previously discussed phenomena and the diffracted (cylindrical) wave at the edges of the transition region. It is also responsible, together with the resultant standing waves of the radiation modes, for lifting upwards the main beam direction of the radiation pattern, which for a monopole-like antenna should be at elevation angles $\theta \approx 90°$. The effect can be clearly seen at the transition region far-away from the source antenna, as shown in Fig. 2.27. A comparison of different transition regions is shown in Fig. 2.28 to assess to what extent the shape of the transition region can be simplified [25]. Case A and B in Fig. 2.28 refer to the simplified structures, with and without a gap between metal and glass. Case C corresponds to the one built in a real sunroof. In this case, the standing waves (as illustrated in Fig. 2.26) are much more pronounced and the magnetic field under the metal roof much weaker than in the simplified cases.

e) Waves diffracted due to the curvature of the panorama glass roof.

The curvature of the glass roof can be treated as an imperfection of a perfect dielectric waveguide, which leads to some of the guided mode power to radiate outwards into the space surrounding the glass window in the form of traveling wave fields. If the curvature radius is small enough or the glass window large enough, a wave hitting from above can be trapped inside the glass with an angle such that excites a guided wave. However this phenomenon can only occur at large distances from the beginning of the glass, where the attenuation of the wave is high enough to cause minimal effects.

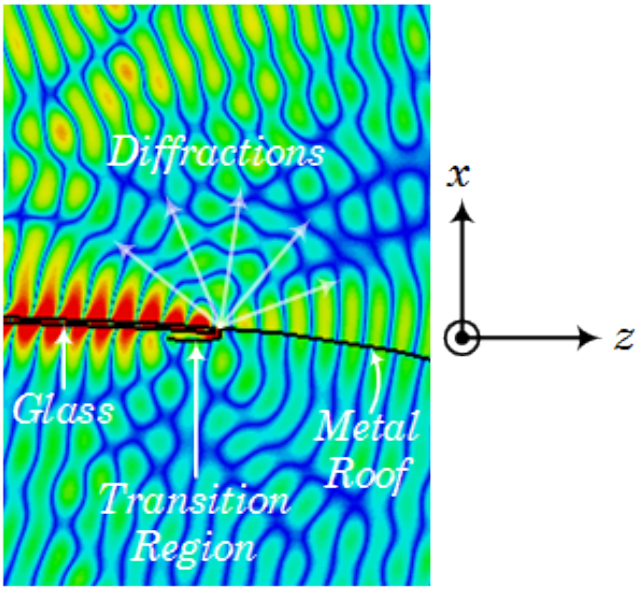

Figure 2.27: Zoom in at the diffractions caused by the transition region (case C in Fig. 2.28) glass-metal in a panorama glass roof.

The radiation excited by diffracted fields due to the curvature of the glass would always excite infinitely radiation modes, which would superimpose themselves in such a way that the incoming parts of the standing waves generated would be eliminated by destructive interference.

Considering all electromagnetic effects from a) to e) discussed in the previous paragraphs, the superposition of all of them leads to the power distribution (time-averaged Poynting vector) in and around the glass shown by case A in Fig. 2.29. The figure also shows the case of a sliding (glass) roof or folding roof (case B), where the sunroof has been left open; the standard metal roof for comparison purposes (case C), and the flat panorama sunroof considered for analysis purposes (case D). The values of all situations depicted in Fig. 2.29 have been normalized with regard to the maximum peak field value to allow for a fair comparison between them.

According to the different electromagnetic effects discussed in a) to e), the destructive interference pattern in driving direction (positive z direction) for elevation angles close to $\theta \approx 90^\circ$ for the case of a roof with a panorama glass window (case A in Fig. 2.29) is due to the superposition of the traveling wave from the source antenna with the edge diffracted fields at the transition region, the standing waves generated from the radiation modes of the waves impinging from above (or below) the glass film, and the traveling waves going out of the glass slab as a result of a guided mode power radiating away at the curvature points of the glass (waveguide imperfections). The same destructive interference can be seen in the case of a flat panorama glass roof (case E), which has been used to analyze the different electromagnetic effects that occur in real sunroofs. The picture corroborates thus the choice of a flat structure to model the effects in real sunroofs while reducing analytical complexity and computational simulation efforts and resources.

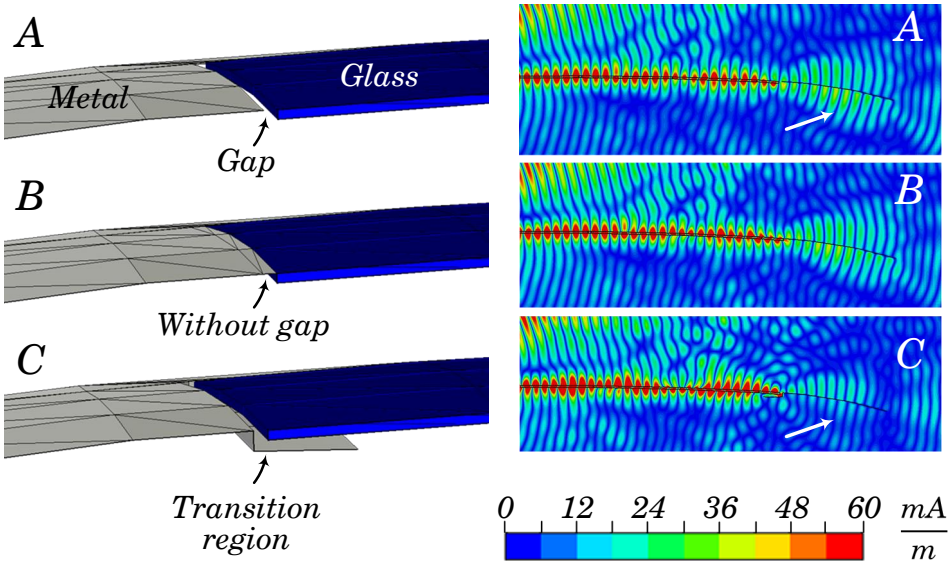

Figure 2.28: Effect of transition region shape on the field distribution in driving direction: Snapshot in time of the magnetic field distribution in mA/m for different transition regions to assess to what extent the structure can be simplified.

Fig. 2.30 shows a three-dimensional perspective of the propagation effects in the transverse x direction for the magnetic field distribution at different positions (A to D) along a flat panorama sunroof. The fields are evaluated by means of a hill plot with the height related to the field value at each point along the x coordinate. It can be clearly seen the exponential decay outside the glass slab and the standing wave patterns extending in the transverse x direction for positions B and C in the region of the glass. The destructive interference effects for elevation angles θ close to 90° are emphasized at position D outside the glass slab. Position A corresponds to the field distribution in the nearby of the antenna placed on the metallic part of the roof.

The standing waves generated at the edges of the transition region metal-glass as a result of diffraction, and that created from the interference of incident and reflected waves of radiation modes, also shift the main beam of the radiation pattern upwards. The disturbing effects in driving direction are more pronounced by curved structures, since the antennas are a little bit tilted up with regard to the horizontal plane and the convex shape of the sunroof guides the waves inside the glass and along the sunroof (surface waves) downwards regarding the horizon.

For the case B in Fig. 2.29, where no glass slab is present, the attenuation of the fields in driving direction is much less severe than in case A. In case B there are no guided waves or radiation modes interfering with the traveling wave coming from the source antenna, and only the diffractions at the edges are present, so that much more energy flows in driving direction compared with case A. Case C is the standard one for antennas on a metal roof, where only the diffractions at the edge of the transition region to the windshield are lifting the main beam upwards in driving direction. Replacing the glass slab in panorama sunroofs by energy saving

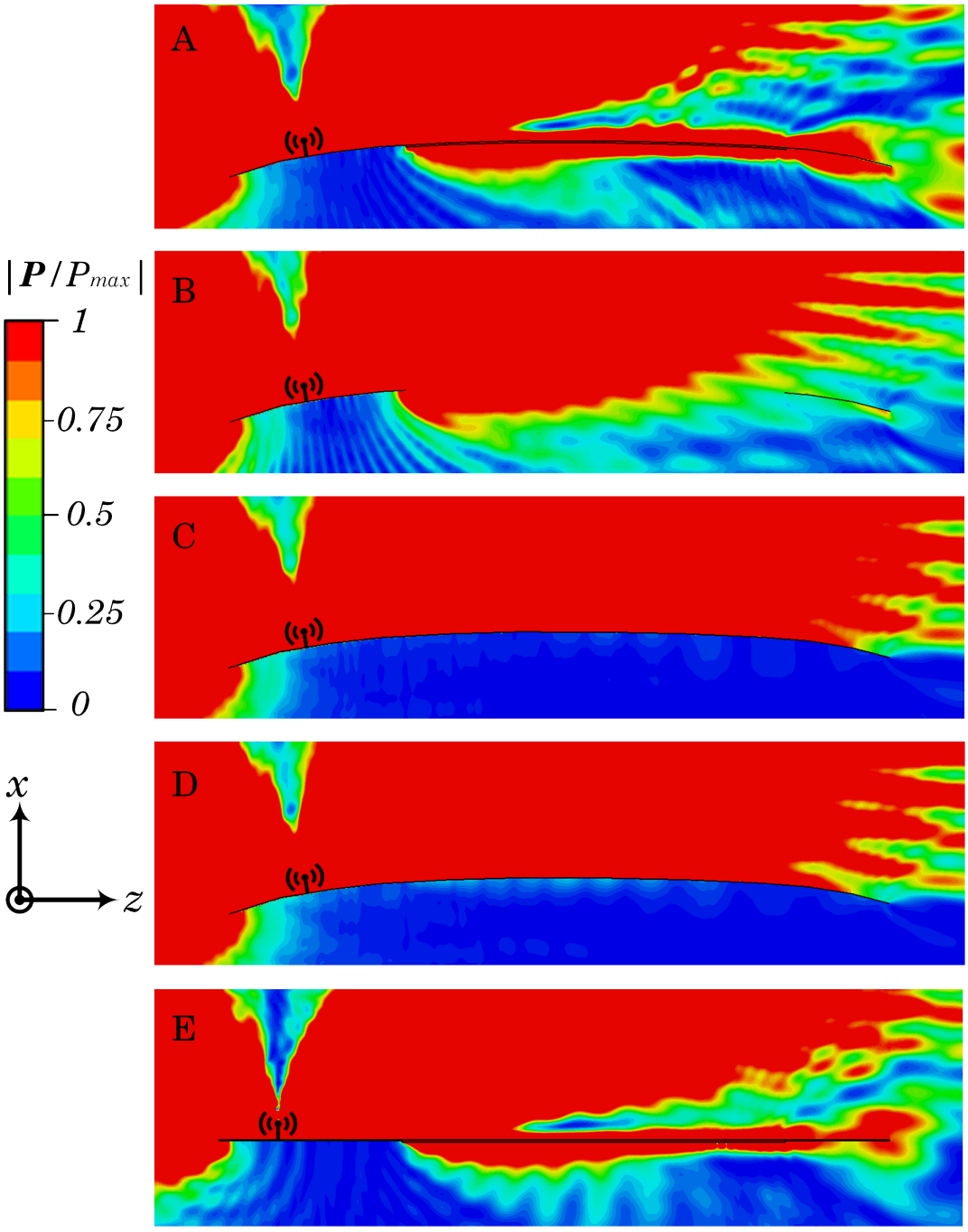

Figure 2.29: Magnitude of the normalized power distribution (time-averaged Poynting vector) in and around different car roof types. The normalization has been computed with regard to the maximum peak field value. Case A corresponds to that of a panorama glass roof with a guided wave inside the glass. Case B is the same as A but without glass (corresponding to sliding (glass) roofs or folding roofs with the sunroof open). Case C represents a full metal roof for comparison purposes. Case D is the same as A but with energy saving glass with a thin layer of metallic-oxide coating on top of the glass. Case E is the same as A but with a flat structure for analysis purposes, showing high similitude between them and corroborating the choice of using a flat panorama sunroof to explain the main electromagnetic effects.

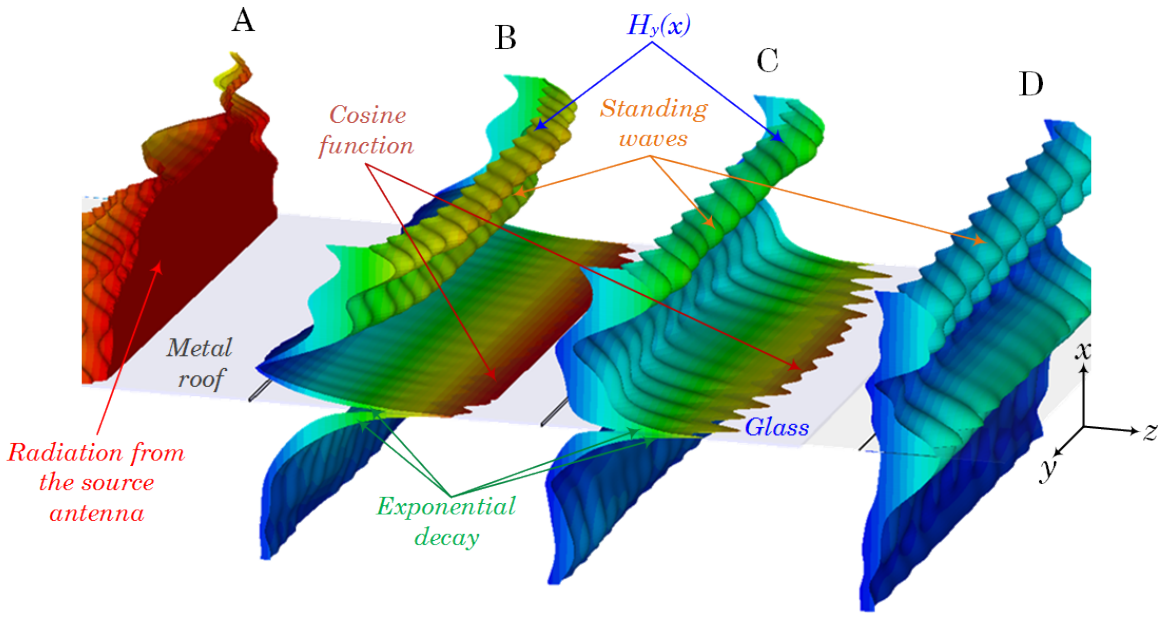

Figure 2.30: Three-dimensional view of the field profile in transverse direction x of the modes excited in and around a flat panorama sunroof and traveling along the z direction: snapshot in time of the magnetic field distribution $H_y(x)$ at different points (A to D) along the z axis of the sunroof. The results are evaluated by means of a hill plot with the height related to the field value at each point along the x coordinate.

glass, composed by a thin layer of metallic-oxide coating in the glass structure with surface resistance values of about 4 Ω/sq to 15 Ω/sq, almost the same field distribution than case C for full metal roofs is achieved.

Looking closer at cases A and E of Fig. 2.29, it is worth noting that the guided wave is not only confined to the physical height of the glass, as inferred from the magnitude of the Poynting vector which reaches the red zone along the whole glass slab and in the immediate vicinity of it. This phenomenon is directly related to the discussed Goos-Hänchen shift, where the guided wave is confined to an effective height h_{eff}, given approximately by the height of the red zone around the glass, which for the glass properties considered in this thesis, the effective height is a factor 11 higher than the physical height of the real glass, as inferred from Fig. 2.21 and qualitatively seen in Fig. 2.29.

To be able to identify the disturbing effects on the radiation patterns of antennas placed on panorama sunroofs, the magnetic field distribution in the horizontal plane (YZ plane) has been plotted in Fig. 2.31 for curved panorama glass (A) and full metal roofs (B) together with a circumference with reference angles [24]. The far-field radiation characteristics are the result of the interactions in the reactive and radiative (Fresnel zone) near-field of the source antenna. In such field distribution plots, the causes of the distortions in the radiation patterns can be directly attributed to certain parts of the car. Abrupt discontinuities, as the edges and corners of the roof,

or changes in material properties, as the metal-glass transition, modify the induced currents on the structure and therefore the radiation characteristics. Comparing the full metal roof of Fig. 2.31 (B) with the panorama glass roof (A) in the azimuth plane, attenuation and ripple effects in the radiation pattern of the latter in a sector of about 120° in driving direction are expected with regard to the former full metal roof, as inferred from the magnetic field distribution in the near-field region of the antenna.

Figure 2.32 shows three-dimensional radiation patterns (upper hemisphere, $(\theta \in [0°;90°], \varphi)$) in polar contour form for cases A-D of Fig. 2.29. The corresponding two-dimensional azimuth polar plots for the elevation angle $\theta = 90°$ are also illustrated at the bottom of Fig. 2.32.

Figure 2.33 corroborates the effects explained above by means of measurements in the anechoic chamber of the university. To perform the measurements, a flat metal roof prototype with a panorama glass window has been manufactured. The dimensions of the metal roof and glass areas are indicated in the picture showing the measurement setup at the top of Fig. 2.33 [25]. Measurements over azimuth and elevation with and without glass are compared with simulations showing good agreement between them. The only notable difference with respect to Fig. 2.32 is the greater gain obtained in the case of the flat roof in the driving direction. This is due to the lack of curvature of the roof, which avoids the shadowing effect previously discussed.

2.1.2.3 Antennas Placed Hidden Underneath the Roof

To illustrate the worsening of radiation patterns for hidden antennas, Fig. 2.34 shows the electric field distribution with the wave propagation effects highlighted for antennas hidden underneath the center of the roof [21]. Unlike antenna systems on the roof, or at positions where some LOS is ensured, the main radiation mechanism of antennas hidden underneath the roof is through diffraction at the boundaries of the roof from the whispering gallery wave propagating from the source antenna. The whispering gallery wave is the counterpart of the creeping wave for concave surfaces[10]. The interaction with the diffuse scattering from the inside of the car leads to a chaotic behavior of the patterns, which can only be analyzed by means of statistics and EDA.

2.1.3 Effects on Input Impedance of Antennas Installed in the Vehicle

Antennas installed in the car for V2X communication are usually of the monopole type when mounted on the roof, or dipole-like antennas when other positions like side mirrors or bumpers should be considered as the roof is no longer available (convertibles). For the former, the roof acts as a finite ground plane. For the latter, the vehicle acts as a reflector, which depending on the distance between the antenna and the chassis the change of the input impedance with regard to the dipole in free space is more or less severe.

[10]Recall that the antenna system is placed underneath the smoothly curved roof, so that the roof represents a concave surface.

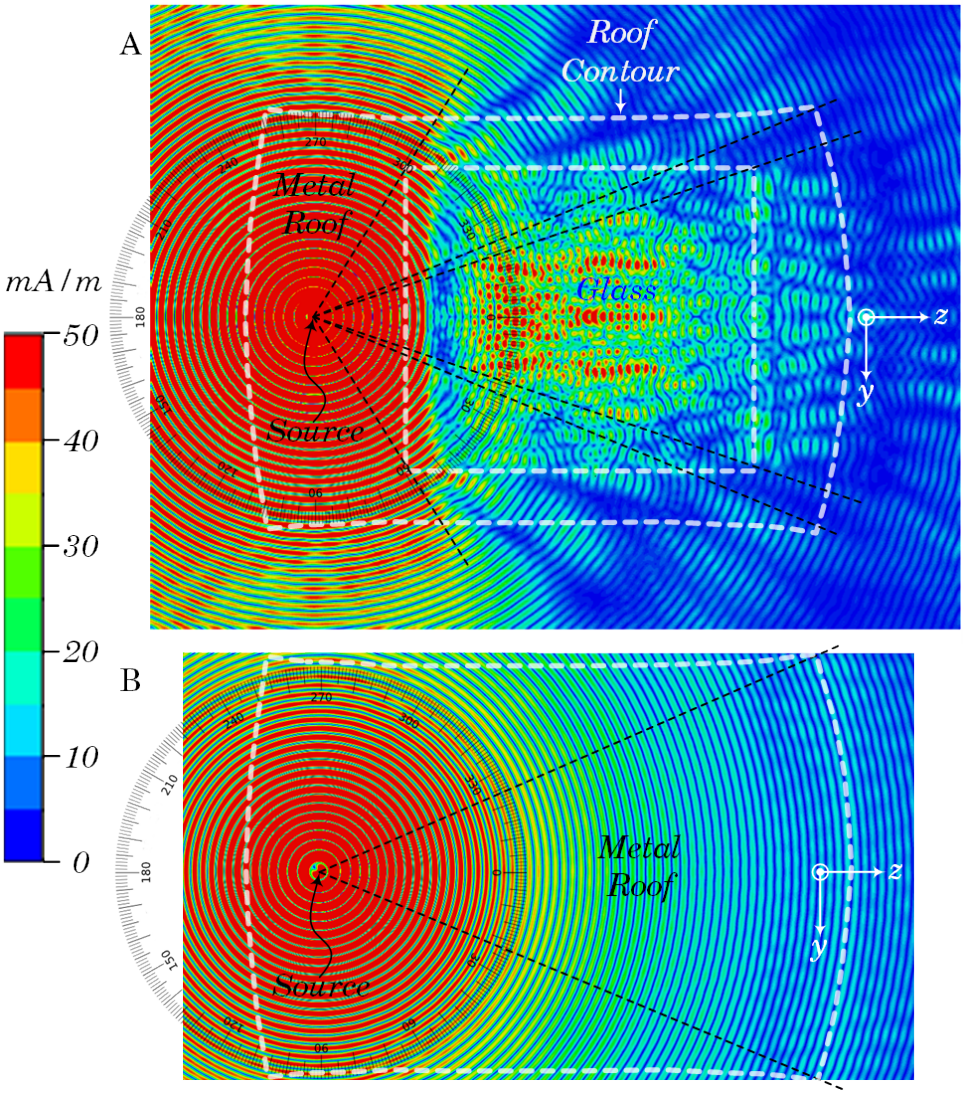

Figure 2.31: Top view comparison of the wave guidance and interference effects in curved panorama glass (top A) and full metal roofs (bottom B): magnetic field distribution H_y in the YZ-plane above the roof showing the effects of finite glass dimensions in y and z directions (A) and the uniform field of full metal roofs (B). The roof lies below the field plane as indicated with white dashed lines. A circumference with reference angles is also shown to be able to compare the propagation effects with the fadings in the radiation patterns. The relative angular positions of the corners of the glass and the metal roof with regard to the source antenna are highlighted, since they define angular sectors in the radiation patterns with similar radiation characteristics.

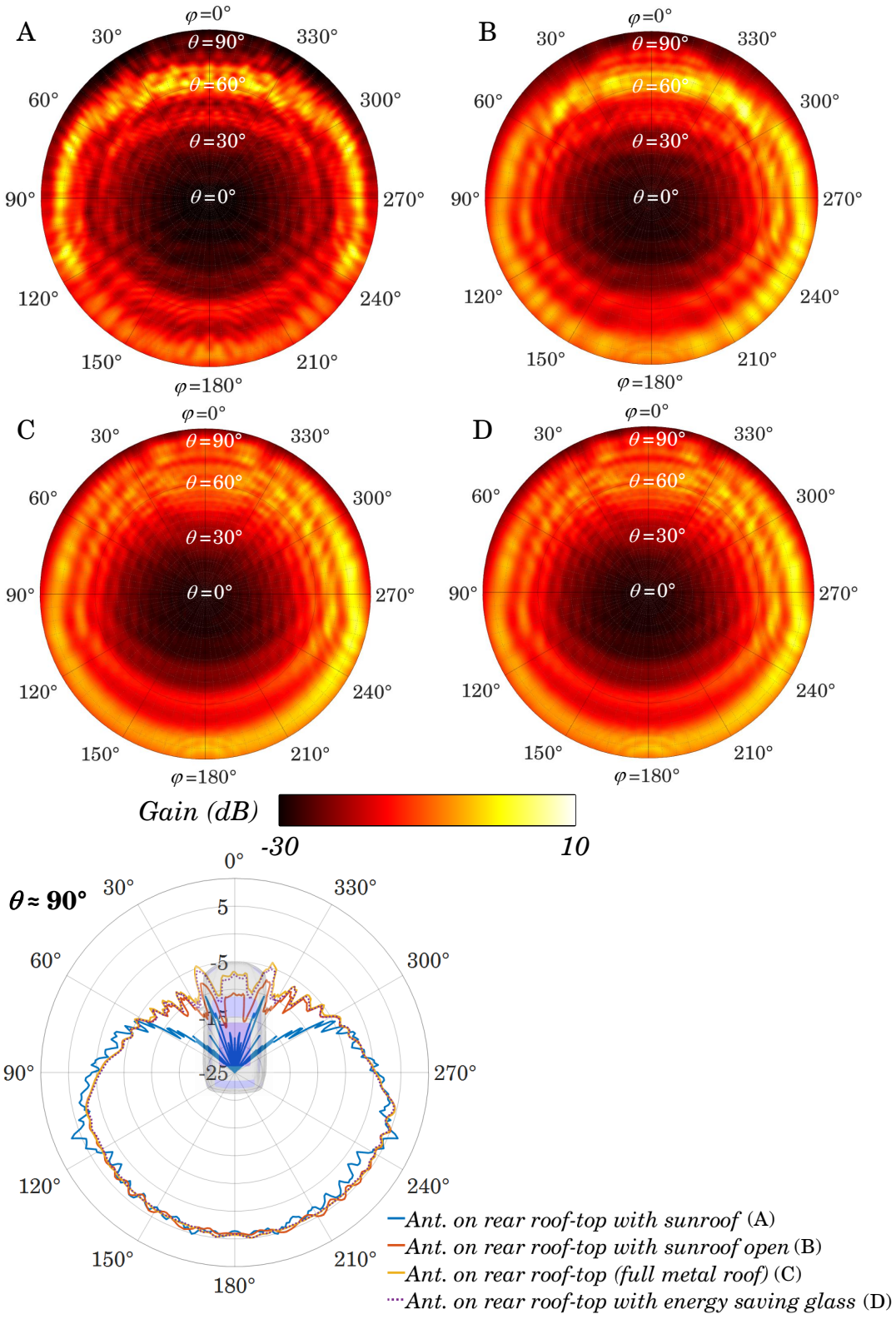

Figure 2.32: Effect of sunroofs on radiation patterns of antennas placed nearby: Antenna radiation patterns (realized gain) in polar contour form (upper hemisphere) and horizontal great circle cuts ($\theta = 90°, \varphi$) (bottom) for cases A-D of Fig. 2.29.

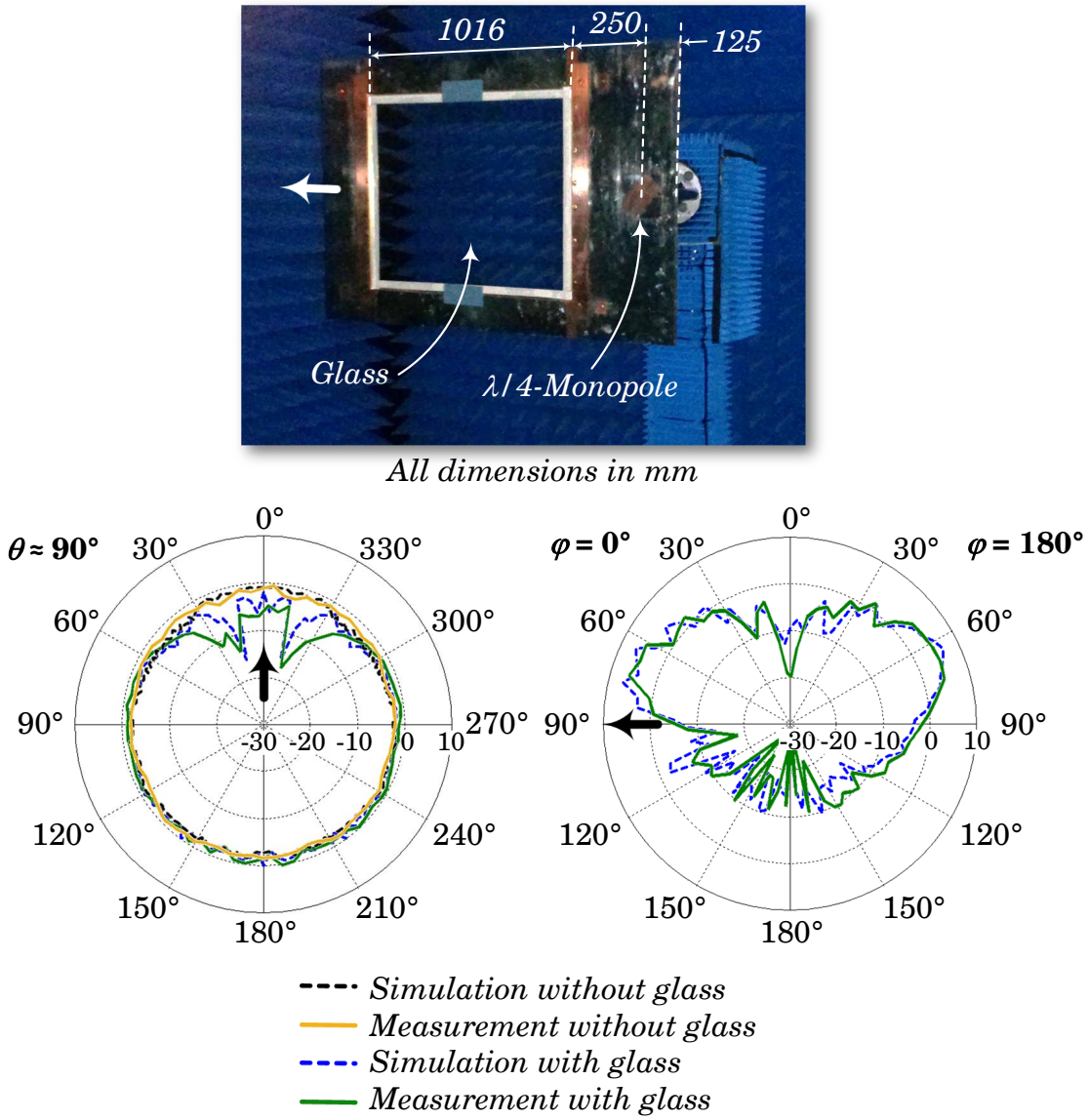

Figure 2.33: Validation of simulation approach under the presence of sunroofs through measurements with a flat sunroof prototype: Measurement setup (top) and antenna radiation patterns (realized gain) illustrated in polar horizontal (left) and vertical (right) great circle cuts for a simplified flat roof with a panorama sunroof of specified dimensions in mm. Thick lines correspond to measured values and dashed lines to simulated values. Resolution of 5°.

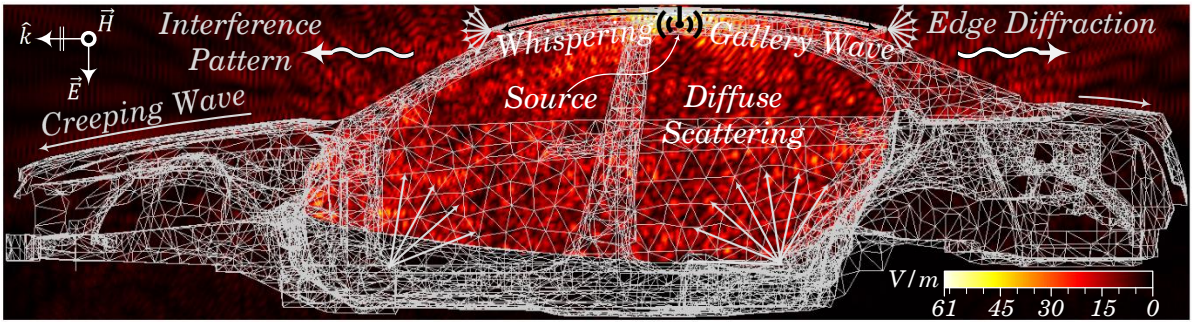

Figure 2.34: Wave propagation effects describing the electromagnetic radiation of antennas hidden underneath the roof of a car. Snapshot in time of the electric field distribution in V/m (longitudinal cross-section view of a wireframe CAD model of a car) of a $\lambda/4$-monopole antenna centered underneath the roof of a car.

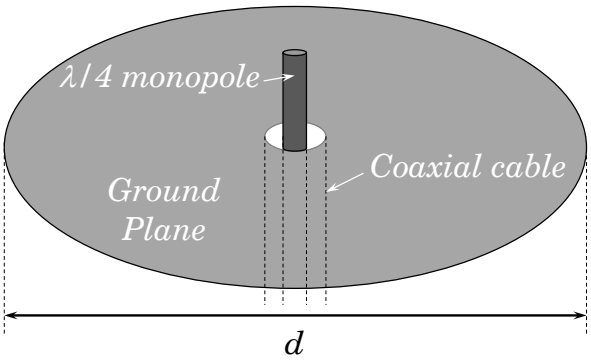

Figure 2.35: Sketch of a monopole antenna on a finite ground plane.

This section is devoted to quantify the change of the input impedance of monopole-like antennas for V2X communications at 5.9 GHz when mounted on the roof of a car. The effect of a large finite-size circular ground plane on the impedance of antennas of arbitrary length placed on it was investigated by Storer in [126], extending the work done by Bolljahn in [18], whose entire analysis can be found in [114].

To determine the change on input impedance introduced by a finite screen, a monopole-like antenna over a large circular metal ground plane as sketched in Fig. 2.35 has been considered. To obtain a formula for the change of the antenna impedance as a function of the electrical dimensions of the diameter of the circular ground plane d/λ, an integral equation obtained for the electric field in the plane of the circular metal plate outside the metal screen is solved approximately in [126] by means of a variational method. The formula for the change of antenna impedance is given by [126]

$$\Delta Z = Z - Z_0 = j\frac{60}{kd}e^{-jkd}\left|k\int_0^h \frac{I(z)}{I(0)}dz\right|^2 \tag{2.34}$$

where Z_0 denotes the impedance of a monopole antenna with regard to an infinite ground plane in Ω, d is the diameter of the circular metal ground plane, $k = 2\pi/\lambda$, h is the height of the monopole antenna, $I(z)$ is the current distribution function of the monopole, and $I(0)$ denotes the base current or input current at the feed point.

The universal curve for the change of antenna impedance as a function of the circular ground screen diameter in electrical dimensions d/λ found in [126] is reproduced here in Fig. 2.36 as an Argand diagram[11]. The curve plots the real and imaginary parts of the function $j(60/kd)e^{-jkd}$ in the X- and Y-axis, respectively. The curve is universal since the function $j(60/kd)e^{-jkd}$ is independent of the current distribution on the antenna. It has been assumed that $kd \gg 1$, $d^2 \gg h^2$, and $I(z) = I(0)\cos(kz)$ so that $\left| k\int_0^h \frac{I(z)}{I(0)} dz \right| \approx 1$ for a quarter-wave monopole antenna. Taking into account the assumptions, the universal curve of Fig. 2.36 is extended to smaller ground planes than those plotted in [126] to be able to analyze the change of input impedance of a monopole antenna at 5.9 GHz installed on the roof of a car near the rear rim with regard to its theoretical counterpart over an infinite ground plane.

Monopole-like antennas on the roof of the car are usually placed pretty close to the rear rim of the roof. A typical distance between the antenna and the rear rim of the roof is 12 cm, which at 5.9 GHz corresponds to 2.36λ. Although the roof extends several wavelengths in driving direction, the worst case change in the input impedance of the monopole antenna due to the rear edge of the roof can be approximated by the effect caused by placing a monopole on a metal disc of diameter 4.72λ. Looking at Fig. 2.36, and considering a matched monopole-like antenna with an input impedance of 50 Ω in an infinite ground plane, the change on input impedance due to the finite dimensions of the roof is expected to be lower than roughly 2 Ω. This means an impedance change of less than 4 % at 5.9 GHz. For the investigated application, this small variation in the input impedance can be neglected.

2.2 Effects of the Ground on Radiation Characteristics

The electric properties of the ground modify mainly the shape and absolute value of the radiation pattern in elevation for antennas placed somewhere in the car, as shown in Fig. 2.37. Although for terrestrial communications the most important plane is the horizontal one, where communication takes place, the effects of the ground in the vertical pattern are changing the absolute value of the radiation pattern in the horizontal plane. Therefore, such effects must be quantified with regard to the free-space case (with the influence of the car) discussed in section 2.1. The input impedance and efficiency of the antennas at 5.9 GHz remain almost unchanged since the ground is located several wavelengths apart from the feed point of the antenna.

[11] An Argand diagram [7] is a plot of complex numbers as points $z = x + jy$ in the complex plane using the x-axis as the real axis and y-axis as the imaginary axis.

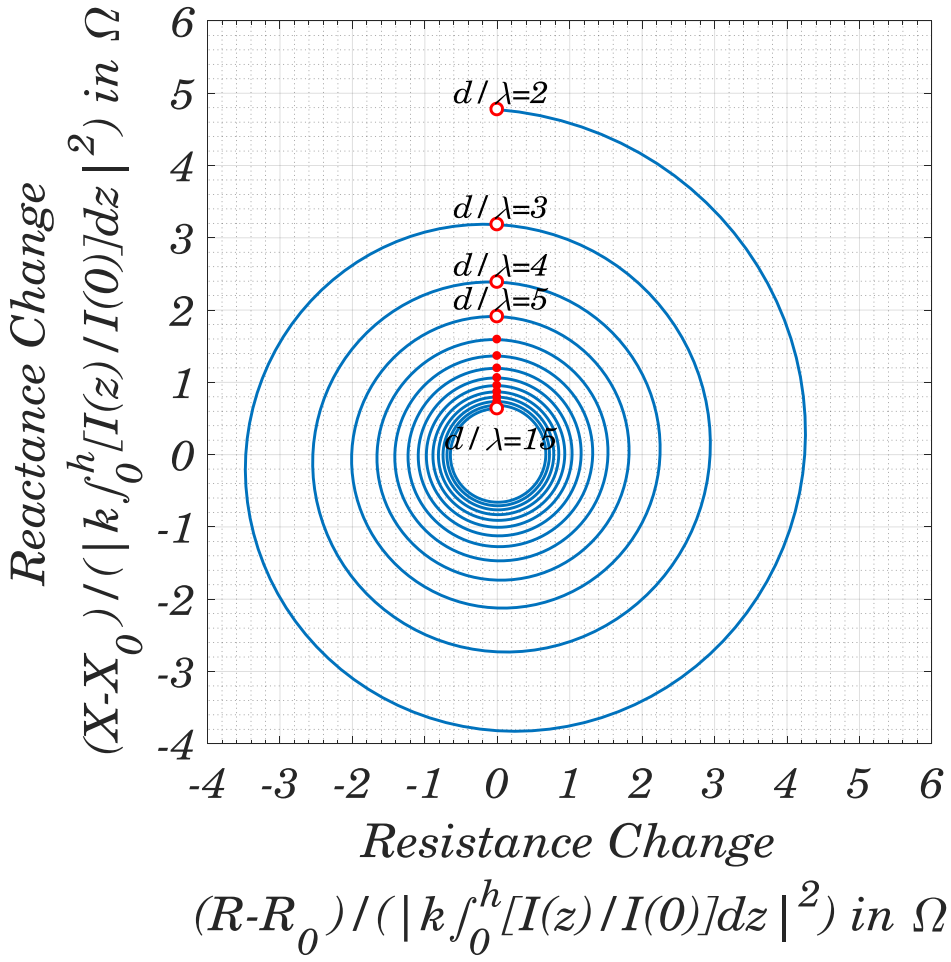

Figure 2.36: Impedance change of monopole-like antennas placed on a finite circular ground plane: Argand diagram showing the universal curve for the change of antenna impedance as a function of the electrical dimensions of the diameter of the circular ground plane.

2.2.1 Radiation Pattern Characteristics Under the Influence of the Ground

To understand the main effects on the radiation pattern of Fig. 2.37 under the influence of real lossy grounds, a high-frequency ray-optics approach can be used. The method is valid for high frequencies. For such cases, the wavelength is small enough to treat the spherical wave coming from the transmitting antenna installed in an elevated position (e.g. the car) as locally plane when striking the ground. Under such conditions, the two-ray method (direct and ground-reflected wave) can be used to analytically compute the far-field patterns. It should be noted that the two-ray method is an approximation, and although it yields very good results for stand-alone antennas above ground, some differences are seen for antennas installed in some kind of platform above ground, as the vehicle in this thesis. The interaction with the vehicle body leads to deviations from the approximated ray-optics computation, and to obtain a rigorous solution of the patterns,

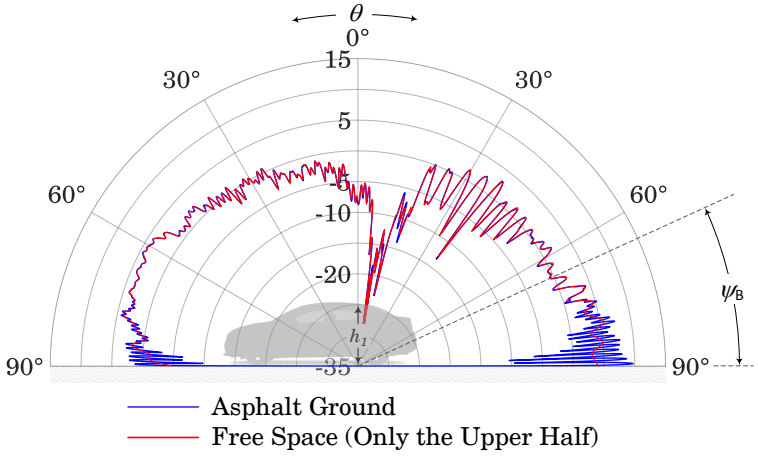

Figure 2.37: Effect of the electric properties of the ground at 5.9 GHz on the vertical gain (IEEE) pattern of a $\lambda/4$-monopole on the roof near the rear rim of a sedan-type car. ψ_B denotes the pseudo-Brewster angle, which corresponds to ≈25° for asphalt ground at 5.9 GHz according to the properties of table 2.1.

numerical methods should be used. However, the results are accurate enough near horizon, which is the most relevant angular sector in elevation for terrestrial communication.

For a vertically-polarized antenna above ground, image theory is used to add vectorially the ground-reflected field $\underline{E}^r_\theta$, equivalent to the electric field created by an image antenna acting as a virtual source, and the direct field $\underline{E}^d_\theta$, which is that obtained in free-space conditions. Referring to Fig. 2.38, the radiation pattern is obtained in the limit as r approaches infinity for the case where the total electric field is multiplied by r.

For the analysis is assumed that the transmitting antenna at point P_1 is high enough above ground (at a height h_1), that the wave striking on the surface of the ground is locally plane. The receiver, however, can be either elevated or close to the surface of the ground. By means of the reciprocity theorem, the validity of the complementary case is demonstrated.

Under such assumptions, the reflection factors (Fresnel coefficients) derived for general oblique incidence of plane waves in dielectric surfaces can be used. The real ground (e.g. asphalt, concrete) far away from being a good conductor (as the case at low frequencies), is by no means a perfect dielectric, and the losses from its real conductivity σ must be taken into account in the reflection coefficient in the form of a complex dielectric constant $\underline{\varepsilon}$ defined as[12]

$$\underline{\varepsilon} = \varepsilon_r - j\frac{\sigma}{\omega\varepsilon_0} \tag{2.35}$$

where ε_r is the dielectric permittivity of the medium, σ is the conductivity in S/m, $\omega = 2\pi f$ is the angular frequency in rad/s, and ε_0 =8.85 × 10^{-12} F/m is the vacuum permittivity.

[12]It can be derived from the Ampère-Maxwell's macroscopic differential equation $\nabla \times \underline{\boldsymbol{H}} = \varepsilon_0\varepsilon_r\frac{\partial \underline{\boldsymbol{E}}}{\partial t} + \sigma\underline{\boldsymbol{E}}$ for a lossy dielectric medium, considering $\underline{\boldsymbol{E}} = \underline{\boldsymbol{E}}_0 e^{j\omega t}$, so that $\frac{\partial \underline{\boldsymbol{E}}}{\partial t} = j\omega\underline{\boldsymbol{E}}$. Hence, $\nabla \times \underline{\boldsymbol{H}} = \left(\varepsilon_r + \frac{\sigma}{j\omega\varepsilon_0}\right)\frac{\partial \underline{\boldsymbol{E}}}{\partial t} = \underline{\varepsilon}\frac{\partial \underline{\boldsymbol{E}}}{\partial t}$.

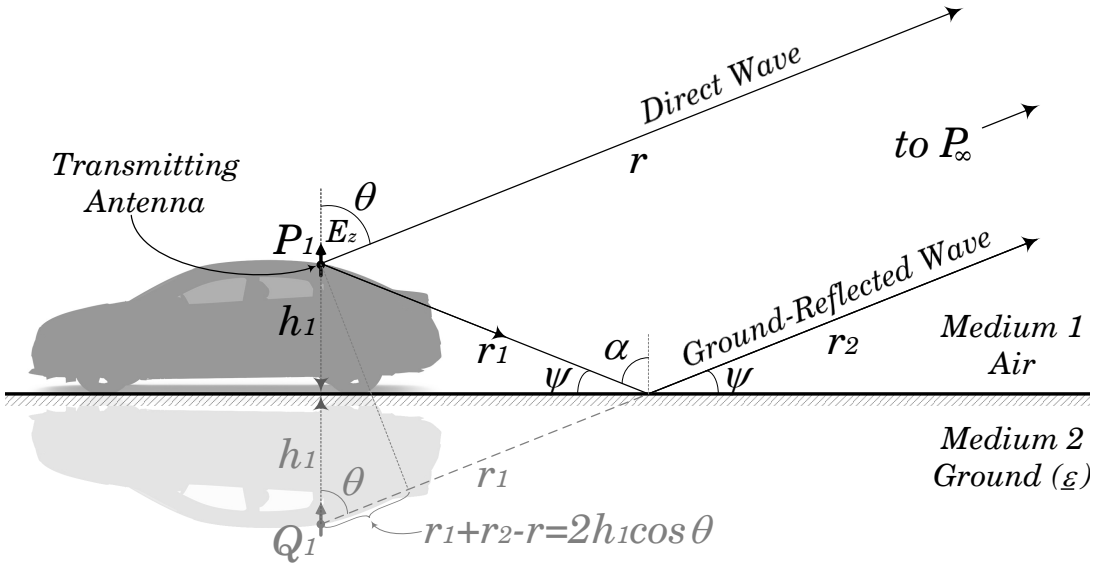

Figure 2.38: Computation of radiation patterns under the influence of real ground. Geometry for direct and ground-reflected wave in automotive scenarios. The image antenna at Q_1 acts as a virtual source for the reflected wave.

Table 2.1 summarizes the dielectric properties for various materials of which the ground is composed at different frequencies within the LTE-V2X bandwidth. They are relevant materials for wave propagation of automotive terrestrial services. The dielectric properties of asphalt pavement and concrete (40 years old) are measured values from [56] and [30, 51], respectively. The values for the other materials in table 2.1 are computed with dispersion models up to second order (e.g. Debye or Lorentz models) from [30] to characterize the frequency-dependent material behavior in a broadband frequency range.

Table 2.1: Dielectric Properties of Ground Materials at Different LTE-V2X Frequencies [30, 51, 56].

	Dielectric Permittivity ε_r			**Conductivity** σ (S/m)		
*Frequency (*MHz*)*	*800*	*2500*	*5900*	*800*	*2500*	*5900*
Asphalt	4.70	4.67	4.63	7.12×10^{-3}	2.24×10^{-2}	5.31×10^{-2}
Concrete	4.80	4.50	4.44	1.77×10^{-2}	3.06×10^{-2}	3.28×10^{-2}
Dry Soil	2.55	2.54	2.53	3.84×10^{-4}	1.23×10^{-3}	3.01×10^{-3}
Wet Soil	19.88	16.58	14.64	1.59×10^{-1}	5.08×10^{-1}	12.44×10^{-1}

Referring to Fig. 2.38, let us consider that the wave incident at the surface of the ground (medium (2) characterized by the complex dielectric constant $\underline{\varepsilon}$) comes from the source antenna at point P_1 in medium (1) (air). The reflection coefficient on dissipative media for vertical (parallel) polarization ($\underline{\boldsymbol{E}}$ is parallel to the plane of incidence, as depicted in Fig. 2.38, and $\underline{\boldsymbol{H}}$ is parallel to the reflecting surface, e.g. the ground) of a plane wave incident at an oblique angle of incidence α

(or elevation angle ψ =90°−α, so that $\cos\alpha = \sin\psi$ and $\sin\alpha = \cos\psi$) is a complex number given by[13] [88]

$$\underline{R}_v = \frac{\textit{Reflected field strength}}{\textit{Incident field strength}} = \frac{\underline{\varepsilon}\cos\alpha - \sqrt{\underline{\varepsilon} - \sin^2\alpha}}{\underline{\varepsilon}\cos\alpha + \sqrt{\underline{\varepsilon} - \sin^2\alpha}} \approx \frac{\sqrt{\underline{\varepsilon}}\cos\alpha - 1}{\sqrt{\underline{\varepsilon}}\cos\alpha + 1}, \quad \text{for} \quad |\underline{\varepsilon}| \gg 1. \tag{2.36}$$

Figure 2.39 shows the magnitude and phase of the plane-wave reflection coefficient for vertical polarization from equation (2.36) for various dielectric ground properties from table 2.1. For grazing incidence (ψ =0°) the magnitude of the reflection factor for vertical polarization equals 1 and its phase is 180°, so that $\underline{R}_v = -1$. This means that the electric field vector of the reflected wave is equal to that of the incident wave but 180° phase reversal. As the angle ψ increases, both the magnitude and phase of the reflected wave decrease quickly up to a critical angle ψ where a minimum of the magnitude is reached and the phase goes through φ =90°. This angle ψ corresponds to the pseudo-brewster's angle for a lossy dielectric material by analogy with the lossless case in optical systems (Brewster's angle[14]). For the perfect dielectric case $\sigma = 0$, the magnitude of the reflection coefficient at the Brewster angle is $|\underline{R}_v| = 0$ and the reflected wave completely disappears. This occurs when $\underline{\varepsilon}^2\cos^2\alpha = \underline{\varepsilon} - \sin^2\alpha$, or when $\psi = |\pi/2 - \arctan\left(\sqrt{\underline{\varepsilon}}\right)| \equiv \psi_B$. The abrupt phase change of the reflection coefficient near the pseudo-Brewster's angle is responsible for many of the propagation characteristics of vertically-polarized antennas. For a Perfect Electric Conductor (PEC), the conductivity $\sigma \to \infty$, and the reflection coefficient is $\underline{R}_v = 1$ for all angles of incidence.

Once the behavior of the reflected plane-wave at the boundary of a medium with finite conductivity is characterized, the total vertical electric field[15] considering the influence of the ground will be computed. Although the fields radiated from a vertical antenna above a plane earth with finite conductivity were first analyzed by Sommerfeld in 1909 [125], it was Norton in 1936 and 1937 [92, 93] who reduced the complexity of Sommerfeld's expressions to a form suitable for engineering computations.

According to Norton [93], the total electric field $\underline{E}_\theta$ at large distances from the antenna, so that the higher order terms may be neglected and the polar angles as observed from P_1 and Q_1

[13] The complex plane-wave reflection factor for horizontal polarization is given by $\underline{R}_h = \frac{\cos\alpha - \sqrt{\underline{\varepsilon} - \sin^2\alpha}}{\cos\alpha + \sqrt{\underline{\varepsilon} - \sin^2\alpha}} \approx \frac{\cos\alpha - \sqrt{\underline{\varepsilon}}}{\cos\alpha + \sqrt{\underline{\varepsilon}}}$, for $\underline{\varepsilon} \gg 1$ [88].

[14] Named after the Scottish physicist Sir David Brewster (1781 - 1868), is the angle of incidence at which polarized light is perfectly transmitted through a lossless dielectric surface, without reflection.

[15] It is important to note that only the vertical pattern is considerably affected by the dielectric properties of the ground (in shape and absolute value). The shape of the horizontal pattern will remain unchanged, although its absolute value changes depending on the ground properties.

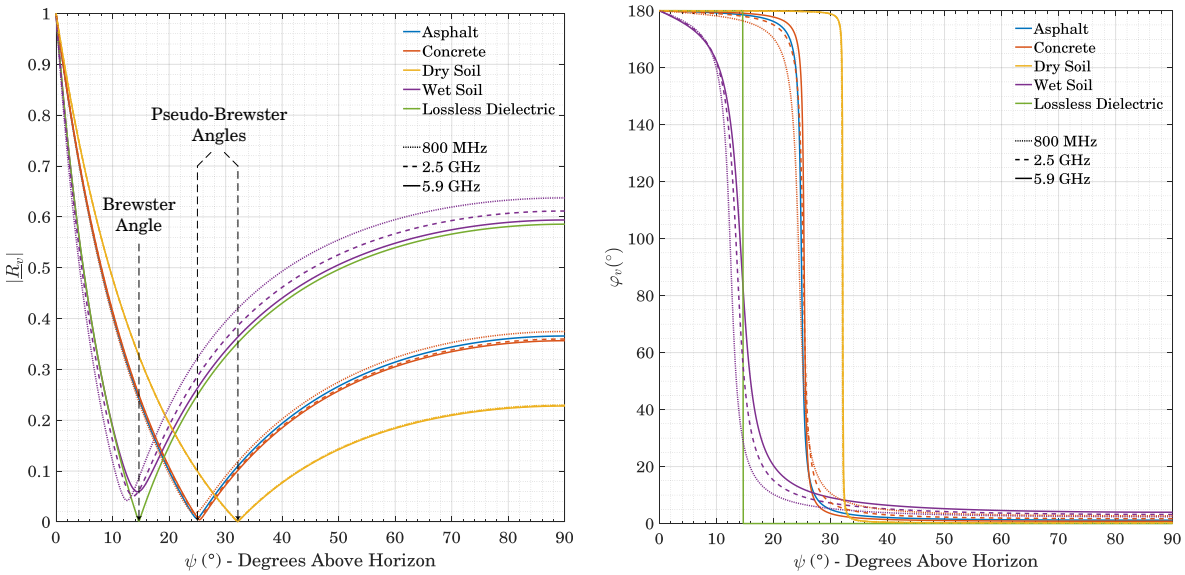

(a) Magnitude $|\underline{R}_v|$.

(b) Phase φ_v (°).

Figure 2.39: Magnitude and phase of the plane-wave reflection coefficient for vertical polarization.

in Fig. 2.38 are almost equal, is given by

(2.37)

$$\underline{E}_\theta = \underline{E}_\theta^d + \underline{E}_\theta^r + \underline{E}_\theta^s + \cdots = \underline{E}_\theta^d \Big[\underbrace{1}_{\substack{\text{Direct} \\ \text{Wave}}} + \underbrace{\underline{R}_v e^{-j\beta(r_1+r_2-r)}}_{\text{Reflected Wave}} + \underbrace{\left(1-\underline{R}_v\right) A e^{-j\beta(r_1+r_2-r)}}_{\text{Surface Wave}} + \underbrace{\ldots}_{\substack{\text{Induction Field,} \\ \text{Secondary Effects} \\ \text{of the Ground}}} \Big]$$

where $\underline{E}_\theta$ is the total electric field, $\underline{E}_\theta^d$ is the electric field due to the direct wave (free space), $\underline{E}_\theta^r$ is the field intensity from the ground-reflected wave calculated from the stationary properties of the energy rays by means of the Fermat's principle and the Snell's law, $\underline{E}_\theta^s$ is the electric field strength contribution from the surface wave[16], the ellipsis of the fourth addend $[\cdots]$ corresponds to the remaining terms representing the induction field and the secondary effects of the ground, $\underline{R}_v$ is the complex plane-wave reflection factor for vertical polarization[17], $\beta = 2\pi/\lambda$ is the phase constant, the angle $\beta(r_1 + r_2 - r)$ in the exponential terms is the phase difference in radians due to the path difference between direct and reflected rays, and A is the so-called *Sommerfeld's attenuation function*, which depends on the electric ground constants, the frequency, and the distance to the receiving point. A detailed mathematical expression for the surface wave can be found in [57, 125]. Due to the reasonably high frequency of V2X applications and the fact that

[16]Here the term surface wave is referred to the sometimes called *Norton surface wave* to distinguish from other connotations of this term as explained in [112]. Quoting James R. Wait in [134], "...surface waves are regarded as any wave which glides along an interface between dissimilar media".

[17]Equation (2.37) is also valid for horizontally polarized antennas, substituting $\underline{R}_v$ with the complex plane-wave reflection coefficient for horizontal polarization $\underline{R}_h$.

the effect of the surface wave is only relevant in a region a few wavelengths above the ground, the effect of the surface wave can be neglected in the following analysis.

The radiation pattern is obtained letting r approach infinity (far-field approximation), so that the path difference $r_1 + r_2 - r$ in Fig. 2.38 becomes equal to the projection of P_1Q_1 on Q_1P_∞. Neglecting the terms corresponding to the surface wave and the induction field and secondary effects of the ground in equation (2.37) due to the high frequency employed in this thesis, the field radiation pattern becomes

$$\underline{E}_\theta = \underline{E}_\theta^d \cdot \left(1 + \underline{R}_v e^{-2j\beta h_1 \cos\theta}\right). \tag{2.38}$$

For perfectly conducting grounds, the resultant field can be thought in terms of ray theory. The reflection coefficient of equation (2.36) becomes 1 for all incidence angles, and the exponential factor of equation (2.38) equals 1 at grazing incidence ($\theta = 90°$). This means that the total electric field at grazing incidence is twice as large as the direct field, which means that the maximum of radiation pattern for the vertical current element occurs at $\theta = 90°$. At this elevation angle, a theoretical increase in field strength of 6 dB over the free-space pattern is obtained. For finite conductivities, as in real ground, $\underline{R}_v = -1$ at grazing incidence, so that the total field vanishes and therefore, the radiation pattern has a null.

The computed vertical cut of the radiation pattern[18] by means of the two-ray method at 5.9 GHz of a quarter-wave monopole above the roof of a sedan-type car at about 21.5 cm from the rear rim is shown for real asphalt ground in Fig. 2.40 (solid green curve). The result is compared with the full-wave computation (solid blue curve), and its corresponding free-space pattern in solid red considering the antenna and the vehicle (only the upper half is plotted). The radiation pattern with the car above asphalt ground is computed as the decimal logarithm of the square of the absolute value of the total field $\underline{E}_\theta$ in equation (2.38). The direct field $\underline{E}_\theta^d$ and the reflection coefficient $\underline{R}_v$ of equation (2.38) have been replaced by the electric field strength in free space of a quarter-wave monopole on the roof of a whole car model of the sedan type and the electrical properties of the asphalt ground at 5.9 GHz, respectively.

According to Fig. 2.38, the incident wave always comes from a plane perpendicular to the horizontal one and therefore, only the vertical pattern is affected, as follows from equation (2.38). Hence, the shape of the radiation pattern in the horizontal plane remains unchanged, although its absolute value changes as inferred from the vertical pattern of Fig. 2.40. Unlike the patterns in free-space (those obtained from the direct wave and discussed in section 2.1 considering the vehicle body), only the upper half of the total vertical pattern actually exists for antennas in the presence of a ground.

As shown in Fig. 2.40, the two-ray approach yields very good results at elevation angles where the vehicle body is not obstructing the LOS of the ground-reflected wave, thus near horizon. The

[18] All values shown in the radiation patterns are *Gain (IEEE)* values in order to account for the power gain of the antenna in its environment (real lossy ground influence) [1]. The *realized gain* values are almost the same, since the antennas are well matched in the operating frequency band and the distance from the antenna to the ground is high enough to neglect the effects in the input impedance of the antenna.

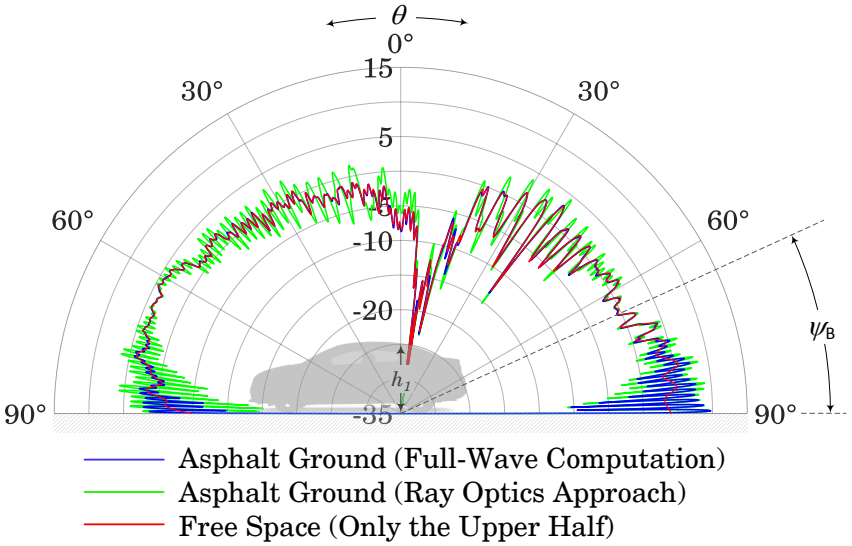

Figure 2.40: Comparison of vertical gain (IEEE) patterns computed with full-wave techniques and with the ray optics approach, both considering the electric properties of the ground at 5.9 GHz and a $\lambda/4$-monopole on the roof near the rear rim of a sedan-type car. ψ_B denotes the pseudo-Brewster angle, which corresponds to ≈25° for asphalt ground at 5.9 GHz according to the properties of table 2.1.

angles delimiting the boundary, where the ground-reflected wave is obstructed, are plotted in Fig. 2.41. The shadowing of the vehicle is also the reason why the pattern is more accurate in the direction opposite to the driving one than in driving direction for antennas placed on the roof near the rear rim, as the one in Fig. 2.40. Near horizon in driving direction the ground-reflected wave reaches the antenna on the roof of the car only by diffractions, which explains the attenuation of the ripple at angles δ near 0°.

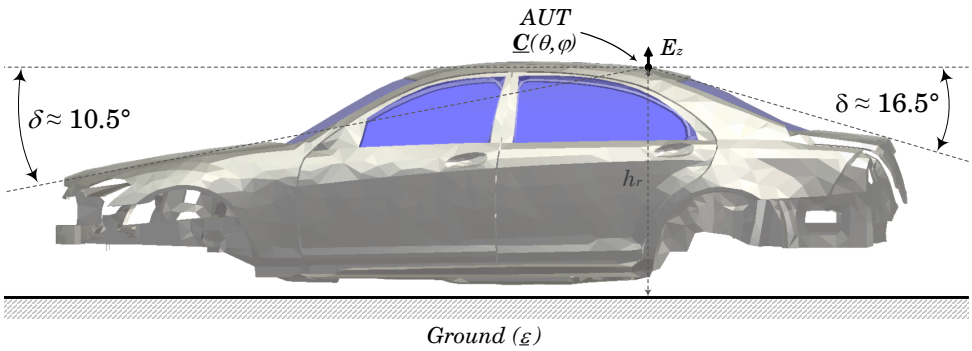

Figure 2.41: Relation between structure of the car and the elevation angles δ counting from horizon for which the ground-reflected wave is not completely obstructed.

Maybe the most significant characteristic of the radiation pattern under the influence of the

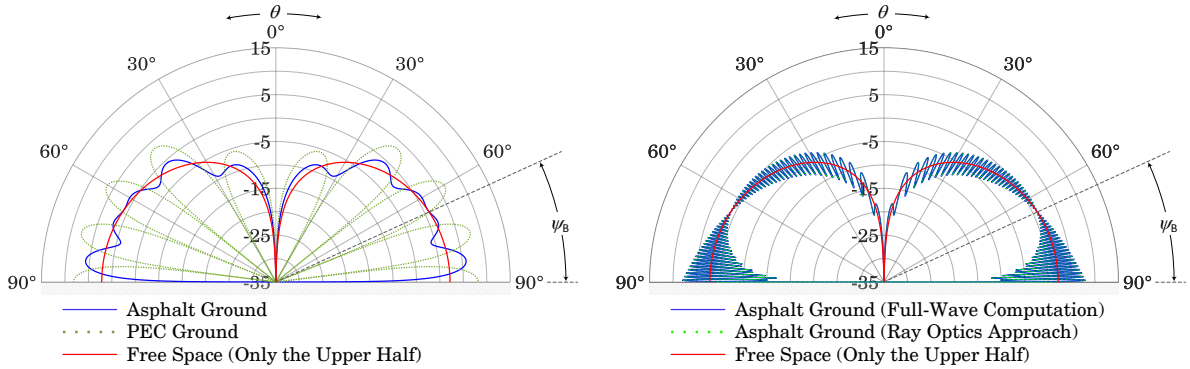

(a) $\lambda/2$-dipole at $h_1 = 2\lambda$.

(b) $\lambda/2$-dipole at $h_1 = 1.4\,\text{m} \approx 27.5\lambda$.

Figure 2.42: Effect of the electric properties of the ground at 5.9 GHz on the vertical gain (IEEE) radiation pattern of $\lambda/2$-dipole antennas at different heights. ψ_B denotes the pseudo-Brewster angle, which corresponds to ≈25° for asphalt ground at 5.9 GHz according to the properties of table 2.1.

ground is the null in the horizontal plane ($\theta = 90°$) of the vertical far-field pattern shown in Fig. 2.40 for the case of real lossy ground (here asphalt ground in solid blue). Since communication for LTE-V2X applications takes place mainly in the horizontal plane or at elevation angles near horizon, transmission at such elevation angles turns out to be a very important aspect, which will be discussed in the next section.

The other significant difference between the patterns in free space and the ones under the influence of the ground is the multiple lobes and nulls related to the electrical height h/λ (in terms of the wavelength) of the antenna above ground. This leads to the so-called *scalloping* effect due to the constructive and destructive interference of the direct and ground-reflected waves. The approximately number of lobes in the upper half space is given by the integer that is closest to $2[(2h/\lambda)+1]$ for vertically polarized antennas[19] [13]. This effect can be better understood in the simple case of a $\lambda/2$-dipole at a height h_1 above the ground, whose radiation pattern for various heights h_1 and different ground properties is illustrated in Fig. 2.42. The resultant effect is analogue to that of a monopole-like antenna placed on the roof of a car, at a height of $h_1 \approx 1.4$ m above ground, which corresponds to the typical height at which antennas are mounted on the roof of a sedan-type car with regard to the ground.

The *scalloping* effect can be realized in Fig. 2.42 (a) with a theoretical number of lobes for $h_1 = 2\lambda$ of 10, which is coincident with the computed patterns shown. The reduction in field strength of the patterns with regard to the PEC ground case is due to the losses of the real ground, in the form of an imaginary part of the complex dielectric constant $\underline{\varepsilon}$ of equation (2.35). This reduction can also be clearly seen in Fig. 2.42 (a) for constructive interference when comparing the PEC ground (dashed green) and the asphalt ground curve (solid blue). Increasing the height

[19] For horizontally polarized antennas the number of lobes is given approximately by the most closely integer to $2(2h/\lambda)$ [13].

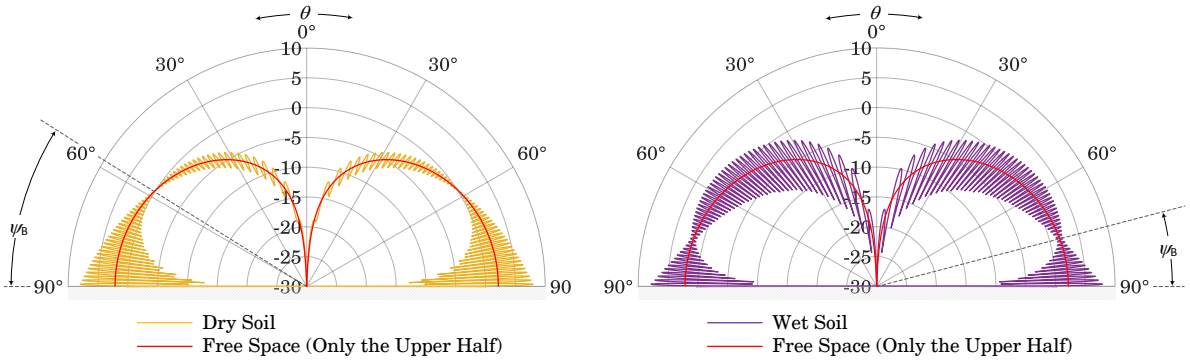

(a) Dry soil. $|\underline{\varepsilon}| = 2.53$.

(b) Wet soil. $|\underline{\varepsilon}| = 15.12$.

Figure 2.43: Effect of a change in the absolute value of the complex dielectric permittivity or, equivalently, various humidity values of the ground at 5.9 GHz on the vertical gain (IEEE) radiation pattern of a $\lambda/2$-dipole antenna at a height h_1 =1.4 m above the ground. ψ_B denotes the pseudo-Brewster angle, which corresponds to ≈32° for dry soil and ≈14.5° for wet soil at 5.9 GHz according to the properties of table 2.1.

of the antenna above ground grows the number of lobes and nulls, as depicted in Fig. 2.42 (b), filling up the funnel-shaped hole near grazing angles ($\theta \approx 90°$). The pseudo-Brewster angle ψ_B is easy to recognize in the far-field pattern when the antenna is placed several wavelengths above ground, as in Fig. 2.42 (b). Recalling Fig. 2.39, the phase of the reflection coefficient equals 90° at the pseudo-Brewster's angle ψ_B and its magnitude is almost zero, so that almost only the contribution of the direct wave affects the total field according to equation (2.38). Thus, in the vicinity of ψ_B the ripple of the *scalloping* effect decreases and exactly at ψ_B the curve of the far-field pattern considering the ground almost equals the one in free-space conditions.

Figure 2.43 shows the effect on radiation pattern of a change in the absolute value of the complex dielectric permittivity $|\underline{\varepsilon}|$ or equivalently, the effect of the relative humidity of the ground. In agreement with Fig. 2.39, the pseudo-Brewster angle ψ_B increases as the absolute value of the complex dielectric permittivity $|\underline{\varepsilon}|$ decreases and vice versa.

2.2.2 Theoretical Far-Field Patterns vs. Measured Patterns

The null in the horizontal plane ($\theta = 90°$) of the radiation patterns of Fig. 2.37, 2.40 and 2.42 for asphalt ground (and in general for lossy grounds) does not mean that the electric field intensity is identically zero [113]. Radiation patterns represent angular field distributions of the main component of the electric field when r approaches infinity. When approaching the limit, the terms varying inversely as the square of the distance vanish, causing a null at infinite distances from the transmitting antenna located at P_1 [29].

As occurs in a real scenarios like the one sketched in Fig. 2.44 for V2V-communication, at finite distances and in the vicinity of the funnel-shaped nulls of the theoretical far-field pattern,

it is impossible to plot only a single pattern independent of the distance from the transmitter, since the absolute value changes with regard to the finite distance d_{tr} from the RF source. From Fig. 2.44 it can be inferred that for finite distances between transmitting and receiving antennas, with at least one of them in an elevated position, the incidence angle of the ground-reflected wave α never reaches 90°. This means that even for elevation angles θ =90° and real lossy grounds, the direct wave does not cancel with the ground-reflected wave and the null seen in Fig. 2.37 or 2.40 it is not actually a null anymore.

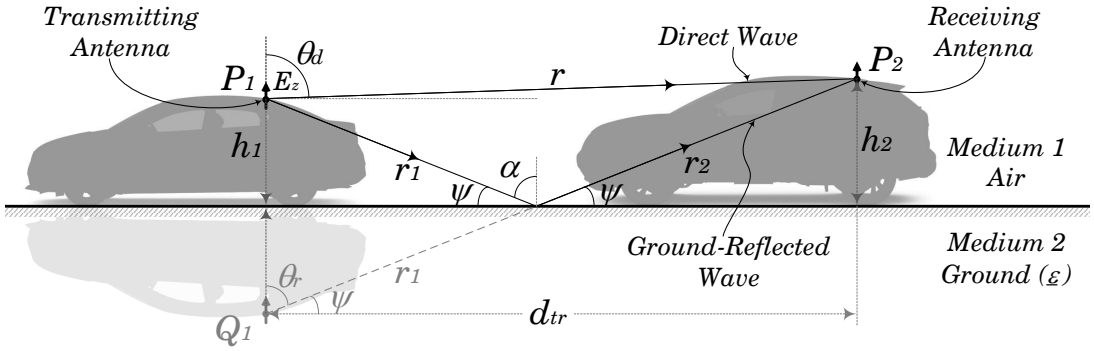

Figure 2.44: Geometry for direct and ground-reflected wave in a real V2X scenario. The image antenna at Q_1 acts as a virtual source for the reflected wave.

To accurate represent the radiation diagrams measured in a real V2X-scenario[20] and to be able to fairly compare simulations and measurements performed in a radome or in an open area test site (OATS), equation (2.38) should be more precisely expressed for finite distances from the transmitting antenna.

Referring to Fig. 2.45, which shows a sketch of a radome facility capable of measuring radiation patterns in azimuth and elevation of antennas installed in a car, and considering a spherical scan in elevation, the height of the transmitting antenna h_t at each position along a quarter sphere can be given as a function of the radius of the sphere d and the elevation angle counting from horizon δ as

$$h_t = d \sin\delta \quad \text{for} \quad \delta \in [0°;90°] \quad \Rightarrow \quad h_t \in [0,d], \tag{2.39}$$

and the distance between transmitting and receiving antenna d_{tr} as

$$d_{tr} = \sqrt{d^2 - h_t^2} \quad \text{for} \quad h_t \in [0;d] \quad \Rightarrow \quad d_{tr} \in [d,0]. \tag{2.40}$$

The paths r and $r_1 + r_2$ that follow the direct and ground-reflected wave respectively, as well as the angles γ_1 and γ_2 can be computed with trigonometry as a function of the antenna heights

[20]The scenario depicted in Fig. 2.45 corresponds to that of a rural or highway environment, where the ground-reflected wave plays an important role on the received signal. The radome itself distorts also the azimuthal patterns due to reflections and diffractions on the surfaces of the radome. In urban scenarios more distorted patterns are expected due to multiple reflections from trees, man-made structures, and other moving vehicles and pedestrians.

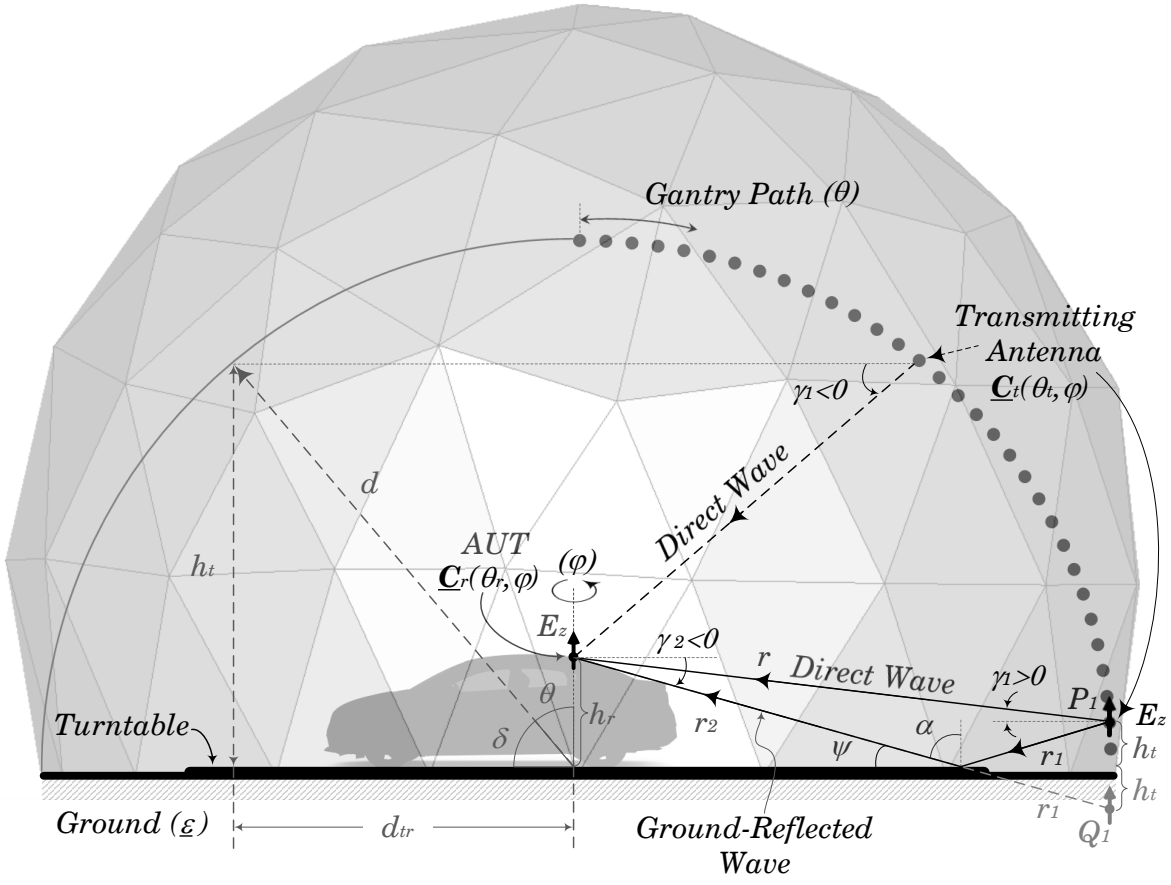

Figure 2.45: Sketch of a radome facility capable of measuring radiation patterns in azimuth and elevation. The image antenna at Q_1 acts as a virtual source for the reflected wave.

and distance between transmitting and receiving (AUT) antennas[21]. This leads to

$$r = \sqrt{d_{tr}^2 + (h_t - h_r)^2} \quad \text{and} \quad r_1 + r_2 = \sqrt{d_{tr}^2 + (h_t + h_r)^2} \tag{2.41}$$

$$\gamma_1 = \arctan\left(\frac{h_t - h_r}{d_{tr}}\right) \quad \text{and} \quad \gamma_2 = -\arctan\left(\frac{h_t + h_r}{d_{tr}}\right), \tag{2.42}$$

where h_r is the height of the receiving antenna (AUT), which is known and for a sedan-type car corresponds to about 1.4 m.

The angles required to calculate the corresponding antenna patterns in the direction of the propagation paths are also defined as

$$\theta_t^d = \frac{\pi}{2} - \gamma_1 \quad \text{and} \quad \theta_t^r = \frac{\pi}{2} - \gamma_2 \tag{2.43}$$

[21]For measurement purposes, the receiving antenna is the Antenna Under Test (AUT) and the transmitting antenna is a fully characterized and well known log-periodic or horn antenna, which is rotated 90° to measure both vertical and horizontal polarizations. For satellite antennas a reference circularly-polarized antenna can also be used. By means of the reciprocity theorem, the same patterns are obtained for the AUT when used as a transmitting antenna.

(2.44) $$\theta_r^d = \frac{\pi}{2} + \gamma_1 \quad \text{and} \quad \theta_r^r = \frac{\pi}{2} - \gamma_2,$$

where θ_t^d is the elevation angle in the direction of the direct wave for the radiation pattern of the transmitting antenna, θ_t^r is the elevation angle in the direction of the ground-reflected wave for the radiation pattern of the transmitting antenna, and θ_r^d and θ_r^r the corresponding elevation angles for the direct and reflected wave, respectively, for the radiation pattern of the receiving antenna.

The measured power at the AUT, P_r, for vertical polarization is thus, according to [41]

(2.45)
$$P_r = \left(\frac{\lambda}{4\pi}\right)^2 P_t G_t G_r \left| \underline{C}_{r\theta}\left(\theta_r^d, \varphi\right) \underline{C}_{t\theta}\left(\theta_t^d, \varphi\right) \frac{e^{-j\beta r}}{r} + \underline{R}_v\left(\alpha = \frac{\pi}{2} + \gamma_2\right) \underline{C}_{r\theta}\left(\theta_r^r, \varphi\right) \underline{C}_{t\theta}\left(\theta_t^r, \varphi\right) \frac{e^{-j\beta(r_1+r_2)}}{r_1+r_2} \right|^2,$$

where λ is the operating wavelength, P_t is the transmitted power, G_t is the gain of the transmitting antenna, G_r is the gain of the receiving antenna, $\underline{C}_{r\theta}\left(\theta_r^d, \varphi\right)$ is the vertically-polarized radiation pattern of the receiving antenna at the elevation angle θ_r^d defined in equation (2.44), $\underline{C}_{t\theta}\left(\theta_t^d, \varphi\right)$ is the vertically-polarized radiation pattern of the transmitting antenna at the elevation angle θ_t^d defined in equation (2.43), $\beta = 2\pi/\lambda$ is the phase constant, $\underline{R}_v\left(\alpha = \pi/2 + \gamma_2\right)$ is the plane-wave reflection coefficient at the incidence angle $\alpha = \pi/2 + \gamma_2$, $\underline{C}_{r\theta}\left(\theta_r^r, \varphi\right)$ is the vertically-polarized radiation pattern of the receiving antenna at the elevation angle θ_r^r defined in equation (2.44), and $\underline{C}_{t\theta}\left(\theta_t^r, \varphi\right)$ is the vertically-polarized radiation pattern of the transmitting antenna at the elevation angle θ_t^r defined in equation (2.43).

Looking closer at equation (2.45), the incidence angle α in the reflection coefficient $\underline{R}_v$ is always less than 90° for finite distances and at least one elevated antenna (recall that the angle γ_2 is defined negative, as shown in Fig. 2.45). This can also be inferred from Fig. 2.45 and means that the direct and reflected wave would never completely cancel each other near grazing incidence as occurs when $r \to \infty$ in the theoretical far-field patterns.

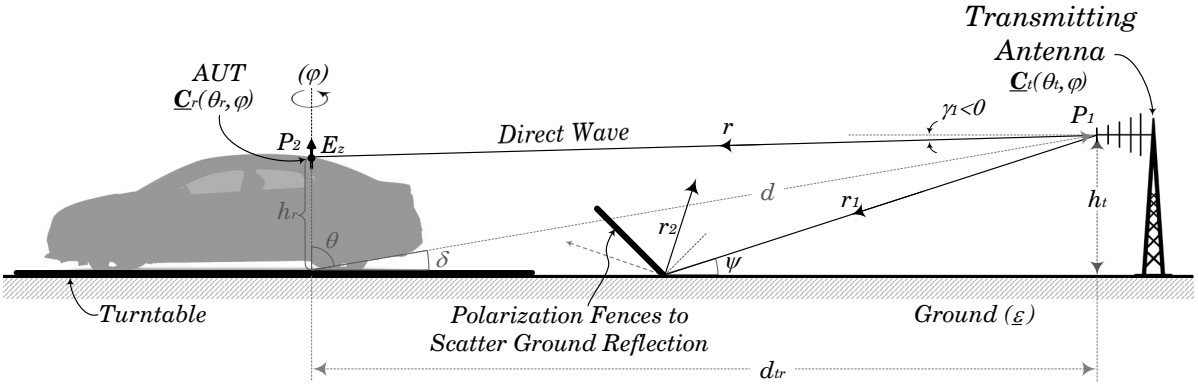

Figure 2.46: Sketch of an Open Area Test Site (OATS) with polarization fences to scatter ground reflection. Measurements of azimuthal conical cuts can be performed.

Unlike the case of the radome, in an OATS, as the one depicted in Fig. 2.46, the influence of

the vehicle body on the radiation pattern of the AUT can be largely isolated from the effects of the ground. This is accomplished by means of polarization fences situated exactly at the point where the ground-reflected wave hits the ground relative to the position of the transmitting antenna and the phase center of the AUT[22]. The metal fences scatter the reflected wave in the specular direction with regard to the angle formed with the normal vector of the fences, so that only the direct wave reaches the AUT in the vehicle. This is the reason why the results of the AUT installed in the vehicle simulated in free space (without considering the ground effects), can be directly compared with the ones measured in an OATS equipped with polarization fences.

Unlike for LTE or terrestrial broadcast services, where a mobile-unit antenna installed in the car at heights ranging from about 1.3 m to roughly 3 m receives the signal transmitted from a base-station antenna situated higher than most of its surroundings, for V2X, bi-directional communication between mobile-unit antennas at roughly the same height also occurs (V2V case). Although in both cases holds the reciprocity principle in terms of signal field strength (because propagation takes place in a homogeneous medium), for V2V communication, the signal-to-noise ratio (SNR), correlation separation between antennas (in case of MIMO applications), and antenna radiation patterns, are also reciprocal at both sites of the communication chain. This is due to the fact that the noise received at both ends can be considered to be similar. For LTE or broadcast services the reciprocity principle only holds in terms of signal field strength. Due to the measurement setup, the antennas under test (AUT) investigated in this thesis have been characterized in reception mode, but the same results are expected in transmission mode for V2V scenarios.

[22]The exact point where the polarization fences must be situated is given by finding the reflection point in the considered terrain by means of the Snell's law and image theory [71].

CHAPTER 3

SHARK-FIN ANTENNAS ON THE VEHICLE'S ROOF

As already discussed in the previous chapter, the electrical dimensions of the vehicle's roof at each frequency band of the microwave spectrum differently affect the radiation pattern and input impedance of the antennas installed on the car. Antenna performance degradation is expected for aerials placed on curved roofs and close to glass sunroofs. At 5.9 GHz the dimensions of the roof are on the order of tens of wavelengths, being the metallic roof large enough to act as a good ground plane for the monopole-like antennas placed on it. The main disturbance at such rather high frequencies is actually the shadowing effect due to the curvature of the roof. Although the curvature effect is rather small because of a large curvature radius on the order of hundreds of wavelengths at 5.9 GHz, the fields originated at the antenna and following a geodesic path along the curved roof, diffract energy at each point where the tangential fields change direction, resulting in a shadowing effect on the antenna pattern in driving direction. Adding the effect of a finite ground plane (real roof in a car) and the fact that the antenna is sometimes a little bit tilted to be settled correctly above the roof, the main beam of the antenna in driving direction is tilted upwards. This effect yields to a range reduction in forward direction. Against driving direction, the effects are alleviated by the inclination of the antenna, where the main beam direction tilts down heading towards the horizontal plane.

The goal of this chapter is to analyze the performance degradation of antennas on the commonly used rear roof-top mounted position, considering the whole vehicle body, and to investigate solutions to counteract the deviation from omnidirectional far-field patterns. Antennas within a shark-fin cover are highly demanded in modern automobiles and they offer a privileged position to get the best radiation properties from the antennas, given their high position with respect to the ground or asphalt. However, the space within the shark-fin is rather reduced to arrange all the antennas for the high demand of different wireless services. Hence, goal of

this chapter is also to investigate broadband antenna geometries, capable of covering various wireless services offered in modern automobiles with a single antenna and a single feeding and soldering point to also reduce costs. The designed antenna may be suitable to be placed inside the shark-fin cover. As a special feature, the antenna should counteract the radiation pattern deformation caused by the curvature of the roof and the geometry of the vehicle, especially in the V2X frequency band around 5.9 GHz. Due to the safety-related nature of V2X communication services, more stringent requirements on the performance of the antennas are foreseen. The antenna should preferably be made of metal to reduce dielectric losses present in the substrates of cheap printed circuit board (PCB) materials. The antenna should also be shaped in a form that allows for easy fabrication to minimize costs.

3.1 Radiation Pattern Improvement of V2X Roof Antennas

As already seen in Chapter 2, the omnidirectionality of the radiation pattern of a quarter-wave monopole antenna at 5.9 GHz placed on the typical rear roof-top mounted position is severly affected by the curved geometry of the vehicle's roof. Roughly 5 dB gain are lost in the whole angular sector corresponding to the front of the car. This front angular sector is of utmost importance for safety-related systems such as in the case of V2X communication. Although the system has to be able to send and receive messages, the reception of safety-relevant messages for the occupants of the car occurs to a large extent and in most situations through the front of the car, as this is the one that follows the driving direction. This means that gain values as high as possible in driving direction are a key factor for the proper operation of the V2X communication antenna system.

Figure 3.1 shows the degradation of the radiation patterns for antennas placed on the rear roof-top mounting position. It also highlights schematically the loss of gain in driving direction due to the curvature of the roof in a transparent blue color. About 5 dB loss in gain patterns is attributed to the curved geometry of the car's roof. On the right side of Fig. 3.1, the cumulative distribution function (CDF) of the horizontal patterns shown on the left side is plotted to clearly see the deviation from an omnidirectional pattern of more than 6 dB in driving direction.

Statistically, the histogram of antennas placed on the middle of the roof can be fitted with a Rician distribution, since full line of sight (LOS) is ensured. However, for antennas installed on the rear roof-top mounting position, the histogram is composed of a mixture distribution with roughly 50 % of the pattern in LOS conditions and the other 50 % in non line of sight (NLOS) conditions. This behaviour is shown in Fig. 3.2, where the left side of the figure shows the characteristic histogram of an antenna above the middle of the roof obtained after a demeaning operation to an antenna placed on the rear roof-top mounting position to remove the shadowing effect of the curved roof. The histogram can be perfectly fitted by a Rician distribution, showing that only LOS exists. On the right side of Fig. 3.2, the histogram of an antenna installed on

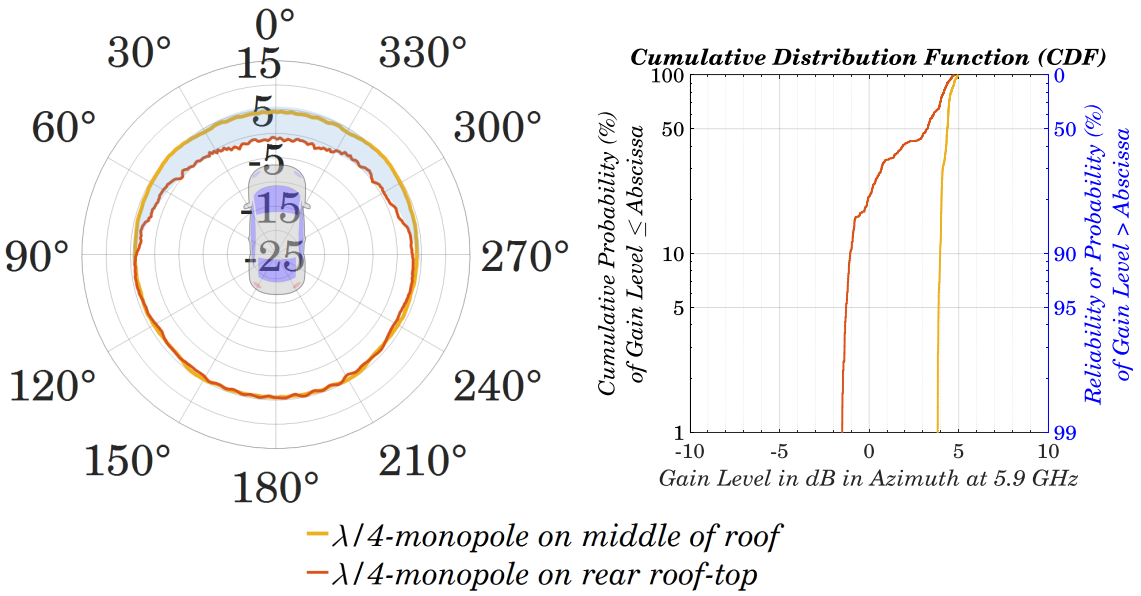

Figure 3.1: Radiation pattern degradation at 5.9 GHz for antennas placed on the rear roof-top mounting position: Conical cuts at $\theta = 90°$ for a quarter-wave monopole on the middle of the roof and on the rear roof-top mounting position (left) highlighting the gain degradation in driving direction in a transparent blue color, and cumulative distribution function (CDF) of the horizontal radiation patterns (right).

the typical rear roof-top mounting position is shown. As can be clearly seen, the shadowing effects of the geometry of the roof are causing the statistical distribution to become a mixture distribution with an almost 50 % of the values lying under NLOS conditions. These values are those corresponding to the front of the car, as inferred from Fig. 3.1.

Several techniques to counteract the effects of the vehicle's roof at 5.9 GHz have been investigated. Among the different techniques investigated, those of a monopole in a higher position or an array of collinear antennas in the form of a Marconi-Franklin antenna [70, 88] do not produce an omnidirectional radiation pattern when the antenna is placed on the rear roof-top mounting position. They can only achieve more gain due to their elevated position or due to the array gain, but they do not modify the shape of the radiation pattern in the horizontal plane. Hence, in order to counteract the shadowing effects caused by the curvature of the roof for V2X antennas placed on the roof near the rear edge, a certain directivity must be given to the antenna. Fig. 3.3 shows the normalized (to 0 dBi) horizontal radiation pattern of a monopole-like antenna in red, and the green line shows the desired directive radiation pattern of the monopole-like antenna on an infinite flat ground plane to achieve an omnidirectional pattern when the antenna is placed on the roof near the rear edge.

The blue striped area in Fig. 3.3 shows how many dB should be added to the directivity of the antenna in driving direction; the orange striped area shows the dB that can be lost relative

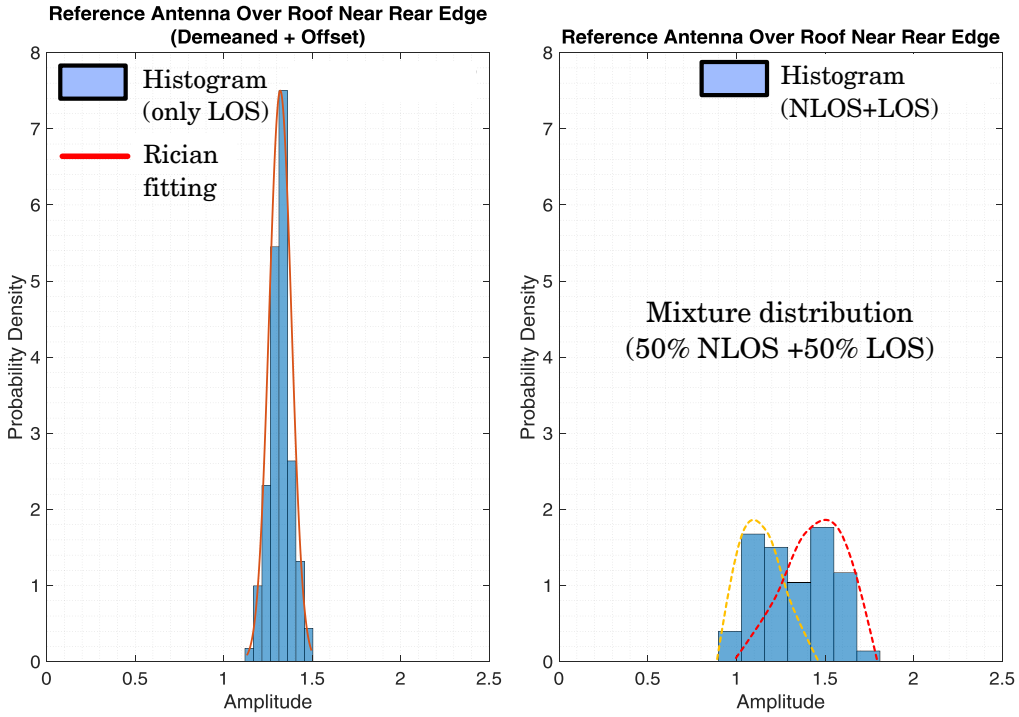

Figure 3.2: Histogram of the radiation pattern at 5.9 GHz for antennas placed on the rear roof-top mounting position: Histogram of the radiation pattern of an antenna placed on the rear roof-top mounting position after a demeaning operation to show the equivalence with the histogram of an antenna on the middle of the roof with full line of sight (LOS) (left), and histogram of the radiation pattern of an antenna placed on the rear roof-top mounting position as a mixture distribution due to the combination of a non line of sight (NLOS) and a LOS part (right).

to the omnidirectional pattern normalized to 0 dBi over an infinite ground plane to obtain an omnidirectional pattern when the antenna is placed on the roof of the car near the rear edge.

The only investigated configurations that modify the far-field pattern in the horizontal plane are the directive array by means of parasitic or driven elements, as shown in Fig. 3.4. The length and spacing between the elements can be adjusted to produce the required pattern. An example of directive pattern required to obtain an omnidirectional diagram on the roof of the car is shown in a three-dimensional view in Fig. 3.4.

The following sections deal with the research conducted to design an antenna geometry capable of producing an omnidirectional radiation pattern in the horizontal plane when the antenna is placed on the typical rear roof-top mounting position. The technique shown on the left side of Fig. 3.4 with a directive array of driven elements will be used to obtain the desired patterns for V2X communication at 5.9 GHz.

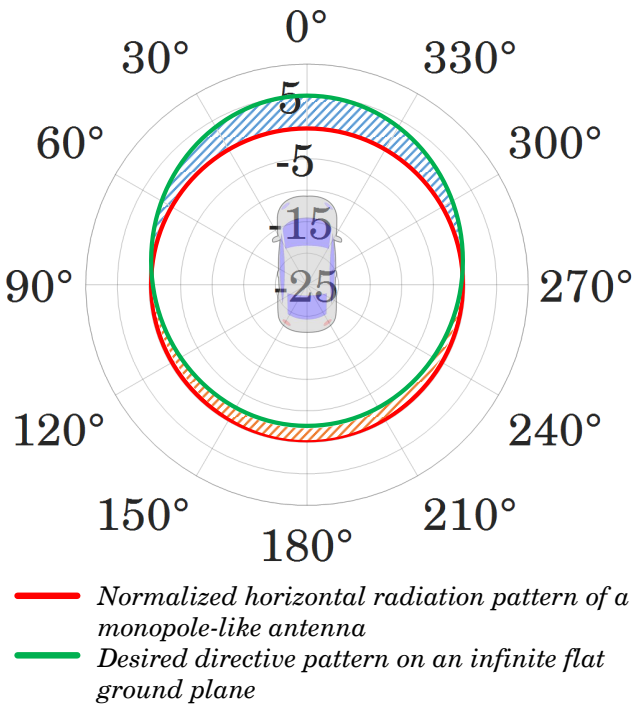

Figure 3.3: Omnidirectionality improvement for antennas on the car's roof near the rear edge: Desired patterns for monopole-like antennas on an infinite ground plane to achieve omnidirectional patterns when placed on the roof the car near the rear edge. The blue striped area shows how many dB should be added to the directivity of the antenna in driving direction; the orange striped area shows the dB that can be lost relative to an omnidirectional pattern normalized to 0 dBi over an infinite ground plane to obtain an omnidirectional pattern when the antenna is placed on the roof of the car near the rear edge.

3.2 LTE - V2X Antenna Structures

3.2.1 Antenna Specifications

The LTE-V2X antenna structures investigated in this chapter are based on the *Nefer-Antenna* principle, previously reported in [43] for LTE coverage only. In order to enlarge the impedance bandwidth of the antenna to cover the 5.9 GHz frequency range with the desired radiation pattern, some modifications on the original structure have to be done. Such changes on the previous structure reported in [43] modify at the same time the current distribution on the antenna at LTE frequencies and therefore, its impedance and radiation properties.

The antenna should cover a wide spectrum in the decimeter and centimeter-wave bands between 698 MHz and 5.9 GHz in blocks separated by frequency gaps. LTE comprises the bands between 698 MHz and 960 MHz, called low LTE band, and 1460 MHz and 2700 MHz, called middle/upper LTE band. V2X communication covers the frequency band between 5.85 GHz and

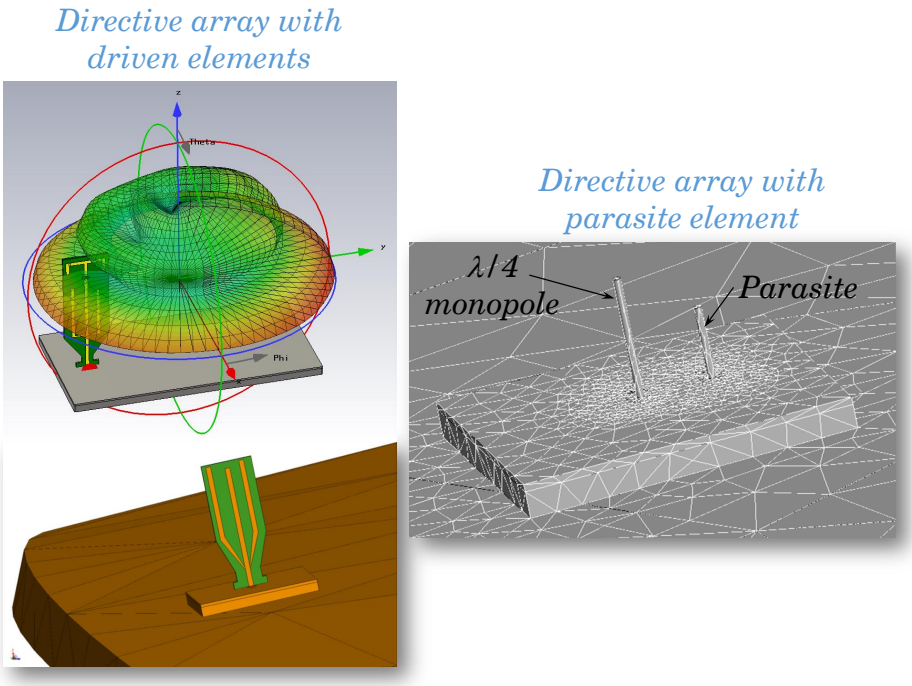

Figure 3.4: Techniques to counteract the shadowing effects due to the curvature of the car's roof: Directive arrays composed of driven elements with proper length and spacing (left), and array with a parasite element (right).

5.925 GHz. According to typical specifications for LTE-V2X automotive antennas, reflection coefficient values $|S_{ii}| \leq -6$ dB are required in the previously specified frequency range, since it is the minimum value required for proper operation of automotive LTE receivers. This threshold corresponds to a Voltage Standing Wave Ratio (VSWR)[1] close to 3, and therefore, 25% of the power delivered to the antenna is reflected. Reflection coefficient values of $|S_{ii}| \leq -10$ dB are, however, highly desired. The -10 dB threshold for the reflection coefficient corresponds to a VSWR of roughly 2, which means that only about 11.1% of the power is reflected.

Matching values of $VSWR \leq 2$ in the whole frequency range can be difficult to achieve for non-resonant antennas with a broadband partial realized gain, as the ones usually implemented in shark-fin covers for LTE coverage. Thus, $VSWR \leq 3$ is considered a good trade-off value to optimize the antenna. Additionally, it is usually desired to achieve an impedance bandwidth a little bit greater than that of the specified channel bandwidth in order to minimize the detuning effects that may occur in the environment of the antenna.

For LTE services, an omnidirectional pattern at all frequencies is required. For V2X communication, omnidirectional or elliptical patterns, with the largest semi-axis oriented in driving

[1] If the magnitude of the reflection coefficient $|S_{ii}|$ is given in dB, the VSWR is calculated as follows: $VSWR = \left(1+10^{(|S_{ii}|/20)}\right)/\left(1-10^{(|S_{ii}|/20)}\right)$.

direction, are desired. Omnidirectional patterns, which are optimal for mobile broadcasting services, may be advantageous for covering intersections with NLOS at V2X frequencies. However, due to the so-called canyon effect in urban environments, elliptical patterns have shown to provide better down-range coverage, which can be of interest for most of the V2X applications that should be covered. Average realized gain values as high as possible are advantageous to maximize the range of the antenna. Total mean gains for elevation angles between 70° and 90° of at least -2 dB must be fulfilled. Ripples and fadings in the radiation pattern should be avoided as far as possible.

The LTE-V2X radiator is intended to be placed inside a shark-fin cover close to other antennas for Global Navigation Satellite System (GNSS). GPS, GLONASS, Galileo, and BeiDou, are typical positioning systems found inside a shark-fin and covering, with more or less narrow bandwidths, the frequency range between 1.164 GHz and 1.592 GHz. Antennas for Satellite Digital Audio Radio Services (SDARS) operated by Sirius-XM with 25 MHz bandwidth around 2.3325 GHz are usually found in the U.S. and Canada. LTE-V2X MIMO configurations are also possible inside the shark-fin, where another antenna for LTE-V2X services (typically at the front part of the shark-fin) can be found. Low cross-talk values of at least $\left|S_{ji}\right| \leq -15$ dB for all $j \neq i$ between different services are required in order to reduce interferences for communication services working at the same frequency band.

3.2.2 Theoretical Background and Constraints in the Antenna Structure

The proposed structure is based on the well known conical antenna over ground plane (the unipole version of a balanced biconical antenna). Since the antenna structure performs as an impedance transformer from the 50 Ω-system reference impedance to the spherical-mode wave impedance that propagates through the air ($\approx 377\,\Omega$), a linearly tapered geometry would provide broadband characteristics and can be a good starting point [2,3].

Such conical geometry of finite height (finite aperture dimensions) shows extremely large bandwidth because it exploits efficiently the available volume within a sphere of radius a enclosing the antenna. The upper bound of the impedance bandwidth would be unbounded if the apex of the cone ends in a pointed way, leading to a high-pass frequency response, typical of UWB geometries. Moreover, a conical structure with an infinite extent would have a constant input impedance independent of frequency, since the structure remains the same when scaling by a factor k, being a self-similar structure and, in this special case, showing constant radiation properties (e.g. constant realized gain) and being a frequency-independent antenna [12]. If the antenna is fed from its apex, the fundamental spherical mode TM_{01}, which provides the

[2] To quote Ben A. Munk: "To match to an UWB antenna begin with a well-matched antenna" [111].

[3] For applications where the height is restricted and the antenna is small in terms of ka, where k is the wave number in free space and a the radius of the circumscribing sphere, starting with a well-known self-resonant structure could not be the optimal strategy. For such small antenna cases, the use of computer-aided algorithms can be advantageous to compute the optimal current distribution that leads to the best matched structure within the smallest volume possible [45]

minimum radiation Q-factor, is strongly excited, and dominates the overall antenna performance. Excitation of higher order modes, would increase the effective Q-factor of the antenna, reducing its bandwidth.

Each variation of the original smoothly tapered geometry with infinite extent will affect the performance of the antenna at some frequencies. Therefore, the challenge is to meet the requirements imposed by the automotive industry on size, input impedance, and radiation properties for lightweight LTE-V2X antennas in an easy and cheap manufacturing process.

Due to manufacturing constraints of a shell conical antenna and the heavy weight of a solid one, unacceptable for automotive applications, a geometrical simplification should be done. As starting point, an unbalanced triangular metal sheet over ground (derived from the balanced bow-tie antenna) is chosen to maintain most of the broadband electrical and radiation characteristics of the solid conical structure. To efficiently use the whole available volume, a three-dimensional structure with a form resembling that of a wire-cage conical structure will be investigated. The final three-dimensional antenna is fabricated with a punch and bent technique after milling the metal sheet with the appropriate shape.

The fact that the antenna must fit inside the shark-fin imposes a height requirement for the antenna, which typically must be smaller than 55 mm. Due to the shape of the shark-fin, the available width to design the antenna is restricted as well. Moreover, the available width is further limited since other antennas for different services must fit in the same shark-fin. The maximum dimensions on height and width are limiting the onset of the lowest frequency of operation and the achievable bandwidth of the structure. The highest frequency of operation, which is in theory not limited if the apex of the cone ends in a pointed way, is in practice limited by the dimensions of the transmission line feeding structure.

Losses as low as possible are required to optimize the efficiency of the antenna, so that self-matched antennas to commonly used 50 Ω-systems without additional matching networks are desired. The antenna is usually fed by means of FAKRA (SMB)[4] automotive RF connectors, but other types of connectors compatible with the previously specified frequencies (like SMA) can be used for prototypes and measurement purposes.

It is straightforward that antennas can be impedance matched using an external matching network based on lossy reactive components without modifying the antenna structure. The main drawback of such approach is that the loss resistances of the discrete components often exceed the radiation resistance of the antenna itself, leading to low efficiency values. This may be the case at the low-LTE band, where the antenna can be considered as a small antenna and the radiation resistance of the input impedance can be very small. Better performance would be obtained by modifying somehow the antenna's structure. This will be the approach followed in this thesis in order to avoid the use of external matching networks. This can be accomplished by capacitive (in the form of top-hat loading) or inductive loading (in the form of meander lines), showing the

[4]FAKRA (Fachkreis Automobil - Automobile Expert Group) SMB (SubMiniature version B) RF connectors are specified from DC to 6 GHz [108]

former for many practical applications better performance than the latter [15]. Other techniques like folding the arms of a wire-cage structure, using multiple arms electromagnetically coupled, or including shunt or parallel matching stubs in the geometry of the antenna can also be used to achieve impedance matching without the need of an external matching network. Investigations on how to design self-matched antennas to avoid the use of additional matching networks would be one of the main focus on this chapter.

On the other hand, the reduction on the overall efficiency due to losses up to a certain value can be somehow advantageous because it increases the operating bandwidth of the antenna. This small increase in bandwidth can be used as a guard band for possible detuning effects. This effect will be considered at the low-LTE band.

3.2.3 Description of the Antenna Geometry and its Electromagnetic Performance

The final structure of the LTE-V2X antenna [20] is shown in Fig. 3.5, comparing the simulation model with the manufactured prototype within the Electrostatic Discharge (ESD) dielectric protection cover.

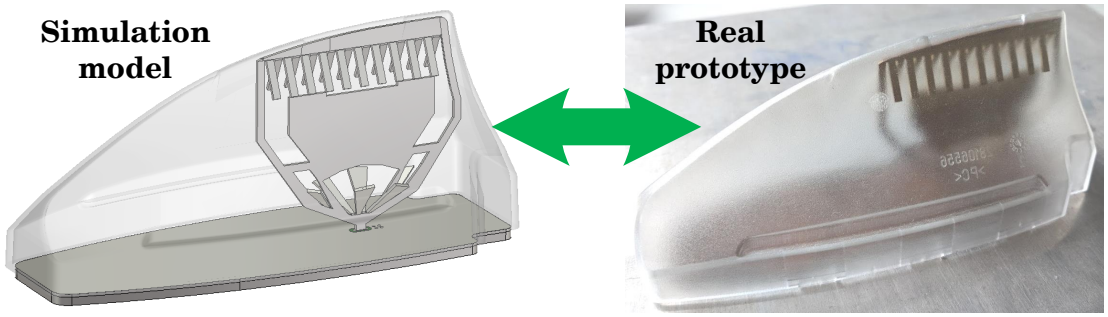

Figure 3.5: Simulation and prototype model of the LTE-V2X shark-fin antenna final geometry: Simulation model (left) and manufactured prototype (right) within the ESD dielectric protection cover.

Figure 3.6 shows the optimized LTE-V2X structure in perspective, in profile and from above to get a better idea of its three-dimensional shape. The top of the figure highlights, with a picture of the manufactured prototype, the parts of the antenna that are mainly responsible for the low frequency behaviour of the antenna (left side), and the parts that mostly radiate at mid-high frequencies (right side). In a similar way, a semi-transparent grey colour shows the model used in the simulations to put in the background the parts that contribute less to the radiation in the respective frequency bands.

Adding together the two parts shown at the top of Fig. 3.6, leads to the final structure of the manufactured prototype, which is shown at the middle of Fig. 3.6 in perspective view. At the

bottom of the figure, the profile and top view of the simulation model are shown for completeness.

For the low frequency band, a tapered structure in the form of a mono-cone bow-tie planar antenna capacitively loaded has been chosen to maximize the bandwidth at the low-frequency end. Following the principle that the current concentrates at the edges of the antenna geometry, the planar cone has been designed with two inductive strips connected together at the upper end by a fan of metal strips. The inductive strips interconnecting the inverted pyramid at the bottom with the fan of metal strips at the top of the geometry helps to separate the low- and mid-frequency bands by blocking the higher frequencies to flow into the upper part of the antenna. The fan of metal strips at the top of the antenna, loads the structure capacitively to be able to reduce the overall height and to keep a good impedance matching at the low-frequency extreme. The capacitive loading extends the current path in a virtual way, increasing thus the effective length of the antenna. The fan shape of the capacitive loading, alternating the metal strips from one side to the other, has been adopted to minimize coupling effects with a possible satellite antenna in the form of a loop surrounding the LTE-V2X antenna. A full-metal capacitive roof may cause shadowing effects to the radiation pattern of the satellite antenna, whose main beam points upwards.

The inverted "U" profiles in the form of a slot between each part of the antenna create an anti resonance or parallel resonance that divide the frequency spectrum in three bands (low, mid and high), as will be shown in the voltage standing wave ratio curve. The slot separating the low and mid frequencies, with an antiresonance at roughly 1.2 GHz, also helps to shift the bandwidth of the low frequency band to even lower frequencies, further improving the impedance matching at the lower end of the antenna frequency range of operation. The frequency, at which the slot separating the mid and high frequency bands has dimensions of about $\lambda/2$, is tuned to a frequency of $\approx$ 3.6 GHz, to be far away enough from both upper end of the mid-frequency range and lower end of the high-frequency band.

At low frequencies, a planar structure is enough to obtain omnidirectional patterns with very good circularity values with a ripple below $\pm$ 3 dB. This is due to the fact that both width and length of the antenna in the direction of the X and Y-axis, as denoted in Fig. 3.6, are roughly equal and small in terms of electrical dimensions. As the frequency increases, however, the dimensions of the antenna along the X-axis (referring to Fig. 3.6) become comparable to the wavelength or even greater, and the difference between length and width is very large. In this case, the conical cut in azimuth around $\theta \approx 90°$ (the pattern in the horizontal plane) and at other elevation angles, differs significantly from a characteristic pattern of an omnidirectional antenna, with a ripple significantly exceeding the $\pm$ 3 dB threshold.

In order to avoid this deformation of the radiation patterns at high frequencies, an oval-shaped inverted conical structure made of metal fan-shaped strips has been optimized to yield omnidirectional patterns at the high-frequency band around 5.9 GHz. The oval-shaped inverted

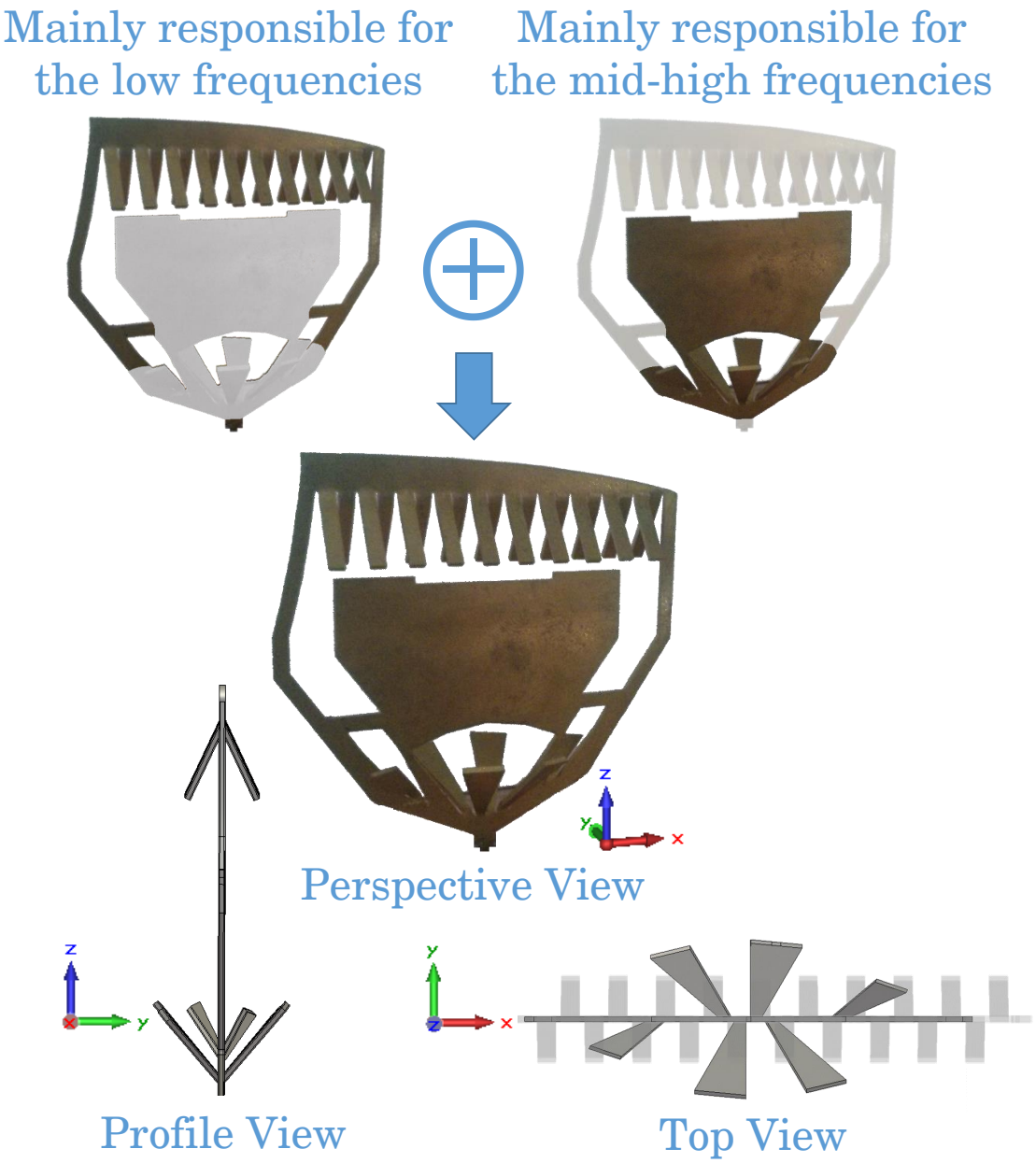

Figure 3.6: LTE-V2X shark-fin antenna final geometry: The top of the figure shows with a picture of the manufactured prototype the parts which are mainly responsible for the low frequency radiation (top left) and the ones that are mainly responsible for the mid-high frequency radiation (top right). With the CAD simulation model, the parts that contribute less to radiation at each frequency band are shown in transparent grey colour. At the middle of the figure, the final geometry of the manufactured prototype in perspective view. At the bottom of the figure, the profile (left) and top (right) view of the CAD simulation model of the antenna.

conical structure for the V2X frequency band can be easily recognized in the top view of Fig. 3.6. It is preferred to that of an inverted cone in a circular fashion when the antenna is intended to be installed on the roof of a car near the rear edge within a shark-fin cover. This is due to the curved shape of the roof, which causes shadowing effects in driving direction and diffractions shedding energy along the roof, as explained in Chapter 2. The oval-shaped inverted conical structure produces an oval-shaped radiation pattern on an infinite ground plane with the major axis of the ellipse oriented in parallel to the driving direction axis. The greater directivity obtained in driving direction counteracts the shadowing effects caused by the curved roof, yielding an almost omnidirectional pattern when the antenna is installed on the roof of the car.

A horizontal small metal strip joins the part mainly responsible for the low frequency radiation and the one for the mid-high frequency radiation. It provides on one side mechanical stability and on the other side improves the impedance matching of the antenna at the upper end of the low frequency range as well as the lower end of the mid-frequency range. This is due to the fact that the strip controls the electrical length of the inverted "U"-shaped slot, and therefore the antiresonance of the antenna between the low- and mid-frequency bands. The small slit at the top edge of the planar inverted pyramid also controls the electrical length of the slot and thus, the parallel resonance at $\approx 1.2\,\text{GHz}$.

Figure 3.7 shows a variety of LTE-V2X multiband structures with various form factors optimized to different commercially available shark-fin covers. At the top of the figure, the V2X-LTE multiband antenna discussed in Fig. 3.6 is shown within the dielectric shark-fin covers with the overall height and length dimensions in millimeters [20]. At the middle of Fig. 3.7, two prototype variations of the antenna geometry previously discussed are shown above a finite ground plane. The model shown on the left side allows it to be placed in very thin shark-fin covers. Unlike the antenna geometry shown in Fig. 3.6, these both models have only one notch frequency gap around 1.3 GHz, induced by the horizontally onriented embedded slot (left model), and the inverted "U"-shaped slot created between the planar inverted conical structure for the low frequencies and the inverted pyramid for mid-high frequencies (right model). At the bottom of Fig. 3.7, the low-cost fabrication technique for such antennas is illustrated. After milling the antenna in a single metal sheet, the volume is easily given by means of a punch and bent technique. In all cases, the shape and length of the metal fan-shaped strips conforming the inner inverted pyramid are optimized to obtain almost omnidirectional patterns when the antenna is installed above the roof near the rear edge.

The antenna is first covered with an Electrostatic Discharge (ESD) dielectric suppression cover for RF antenna protection, as shown at the top of Fig. 3.7. Due to the external position of the antenna above the roof of the car, it can capture and transmit ESD strikes, which are high-frequency signals that flow into the RF components below the shark-fin antenna, damaging the RF circuits and performance of the overall antenna system. Due to aesthetics reasons, the antenna may also be covered with a dielectric design cover. These dielectric covers have been

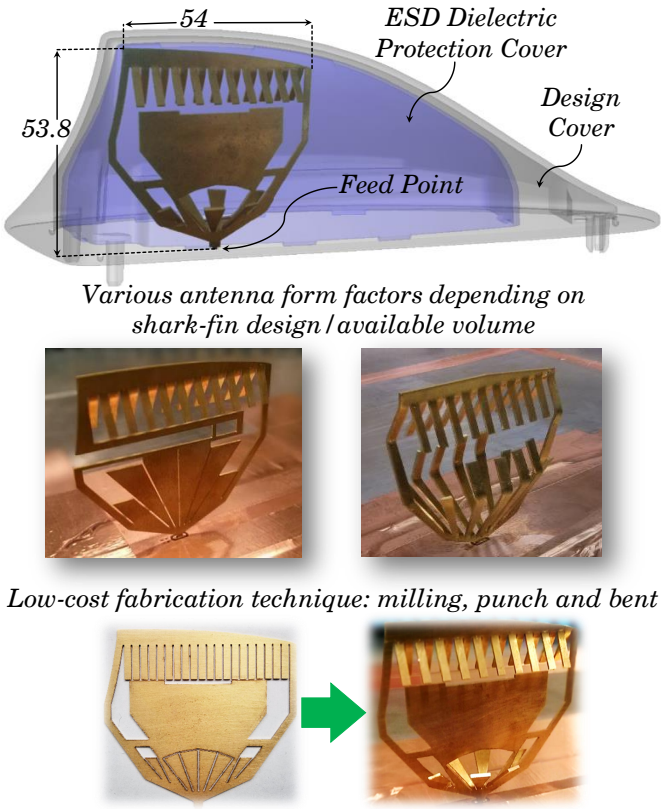

Figure 3.7: V2X/WLAN/LTE multiband shark-fin antennas to mitigate the shadowing effects for antennas placed on the rear roof-top position. Prototype inside a shark-fin cover (top) with overall height and length dimensions in millimeters. Antenna prototypes with various form factors (middle). Low-cost fabrication technique from a single metal panel (bottom).

shown to have a noticeable effect on the radiation pattern of the antennas, specially at the high-frequency end, as discussed in [34]. This is due to the fact that the dielectric cover is usually shaped in a shark-fin fashion, whose walls are not completely perpendicular to the poynting vector of the fields radiated by the antenna at all angles. Hence, in most cases the wave impinges on the dielectric wall of the shark-fin cover with angles that differ significantly from the normal incidence case, leading to an attenuation of the radiated wave and increasing reflections that modify the radiation pattern of the original antenna without the cover. The effects are more pronounced at the nose of the shark-fin, as shown in [34], in the same way as occurs in tangent ogive shaped radomes.

All designs shown in Fig. 3.7, have an aspect ratio close to $h/L \approx 2$ according to Fig. 3.8 and as can be inferred from the dimensions of Fig. 3.7, which has already been shown to yield the best impedance matching results. As already discussed, this aspect ratio tends to maximize the volume occupied by the antenna within the minimum spherical volume circumscribing the antenna geometry. Further improvement in impedance matching is also obtained by adjusting

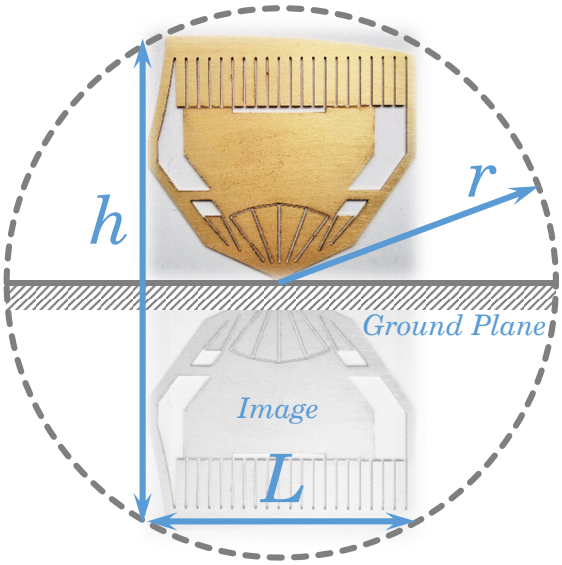

Figure 3.8: Aspect ratio of LTE-V2X antenna geometries for optimum performance: Antenna and its electric image below the electric ground plane circumscribed by the minimum spherical volume of radius r. The height and length of the antenna and its image are denoted by the letters h and L, respectively. An aspect ratio of ≈ 2, as can be inferred from the figure, yields the best results in terms of impedance matching.

the beveling angle that extends from the feed point of the antenna. The same way it happens in the case of fat dipoles, the ultimate goal of such fat inverted conical structures is to minimize the reactive energy around the feed point of the antenna, which does not contribute to the radiation process.

Figure 3.9 shows the measurement setup used for input impedance measurements and for radiation pattern measurements inside the anechoic chamber of the university. For input impedance measurements, a metal round dish with a diameter larger than 1 m is used with the edges covered with absorber material to avoid diffractions, as shown on the left side of Fig. 3.9. The S-parameters are measured by means of a vector network analyzer, and the results are plotted in Fig. 3.10 in the form of Smith chart and with the corresponding voltage standing wave ratio over frequency. For radiation pattern measurements in the anechoic chamber of the university, a metal round dish with a diameter of ≈ 1.2 m is also used with bent edges to prevent from unwanted edge diffractions. The anechoic chamber is provided with a two-axis spherical near-field system in far-field mode of operation. The distance between the transmitting double ridged waveguide horn antenna and the AUT has been set to 5.45 m, ensuring enough farfield conditions at all frequencies of operation. Since phase measurements are not important for the application under investigation, a small error in the measured phase, due to the distance separating the antennas, can be tolerated. This small phase error is not affecting the magnitude of the radiation patterns, which are already well formed in the Fraunhofer region. The antenna

Input impedance measurement setup

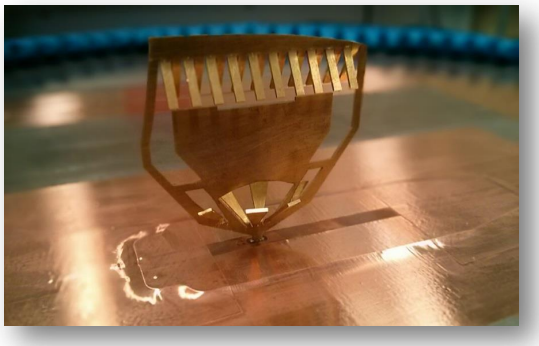

Radiation patterns measurement setup

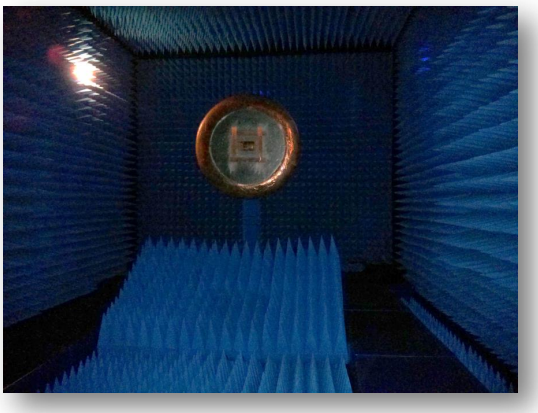

The antenna is placed in both cases on a metal round dish with bent edges or with the edges covered with absorbers to avoid diffractions

Figure 3.9: Impedance matching and radiation pattern measurement setup: AUT placed on a metal round dish with a diameter larger than 1 m and with the edges covered with absorbers to avoid diffractions (left) for impedance matching measurements with the aid of a network analyzer, and the AUT placed on a metal round dish with bent edges in the anechoic chamber of the university, at a distance of 5.45 m from the transmitting double ridged waveguide horn antenna.

is placed centered with the feed point coincident with the coordinate origin of the measurement system, so that the axis of the AUT is aligned with the axis of rotation of the measurement system. Hence, no further offset correction is needed.

Figure 3.10, shows the input impedance matching of the LTE-V2X antenna structure of Fig. 3.6 [20]. On the left side of the figure, the Voltage Standing Wave Ratio (VSWR) achieved by the antenna has been computed. It usually yields a better representation for broadband antennas than the reflection coefficient in dB, since the focus lies on achieving an impedance matching over the whole frequency band of operation below some threshold, usually VSWR = 2 or 3. For narrowband antennas, the reflection coefficient gives a more accurate representation of how good is the impedance matching of the antenna at a specific frequency. The VSWR diagram depicts the results of different configurations sketched with a small picture at the bottom of the figure. The different curves correspond to the simulation and measurement results for the stand-alone antenna (dashed black and solid green lines, respectively), the measured results for the antenna with the ESD protection cover (solid red), and the measured results with the ESD and design covers (solid blue). As inferred from the figure, all the curves overlap to a large extent, showing that the effect of the dielectric shark-fin covers on the impedance matching of the antenna can be neglected. At the low-frequency end, the dielectric covers help to shift the curves to lower frequencies, improving the matching at the low-frequency extreme in exchange

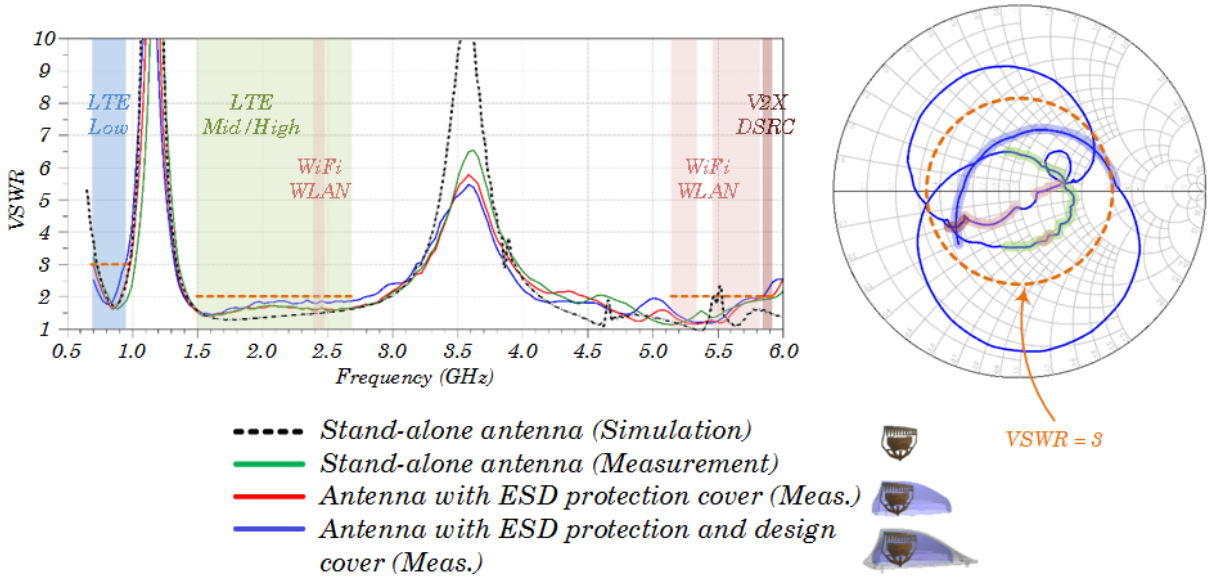

Figure 3.10: Broadband impedance matching (referred to 50 Ω) of V2X/WLAN/LTE multiband shark-fin antennas without the need of external matching networks. Comparison of Voltage Standing Wave Ratio (VSWR) between simulation and measurement results of the stand-alone antenna, and the measured lossy effects of the shark-fin covers (left). Input impedance behavior in the Smith chart for the stand-alone antenna (right). The limit of $VSWR = 3$ has been drawn as a reference in form of an orange dashed line and circle.

for increased dielectric losses. At the high-frequency end more differences in the ripple of the curves are observed, since the electrical thickness of the dielectric walls begins to be relevant to the frequencies of interest. It is worth noting the two notch frequency gaps at ≈ 1.2 GHz and 3.6 GHz due to the embedded slots in the antenna geometry. The different LTE, WiFi/WLAN, and V2X/DSRC frequency bands are also highlighted with different colours to clearly show the frequency bands where the antenna should work properly. The VSWR= 3 line for the low LTE frequency band, and VSWR= 2 line for the other bands (dashed orange), show that the input impedance of the AUT is well matched over the entire frequency bands of operation. The input impedance behaviour is also shown in Smith chart form on the right side of Fig. 3.10 for the measured stand-alone antenna. The different frequency bands are also highlighted along the curve with the same colours used on the VSWR plot of the left side of the figure to easily recognize the frequency bands and how the impedance curve is rolled up. The reference circle corresponding to a VSWR= 3 is shown in dashed orange.

Simulations have been performed by means of full-wave methods. First a simulation in time domain based on the Finite Integration Technique (FIT) has been done by means of a commercially available electromagnetic software [30]. This solver is particularly suitable for simulating broadband and ultrawide-band antennas, as the one discussed here. In time domain, and after specifying the frequency range of interest, a Gaussian signal $X(f)$ covering the whole

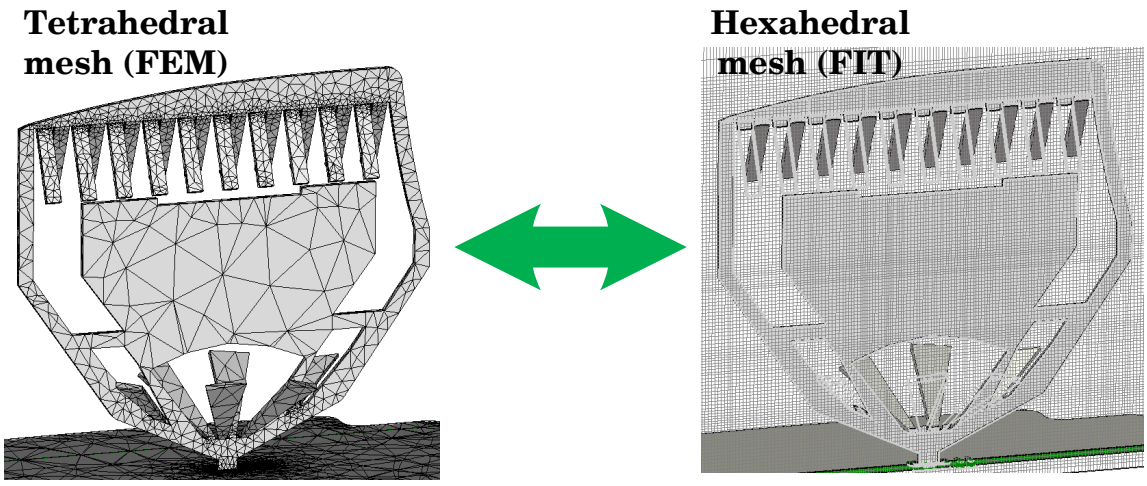

Figure 3.11: Mesh view used in frequency and time domain simulations for the LTE-V2X multi-band antenna: Tetrahedral mesh used in frequency domain simulations based on the Finite Element Method (FEM) solver (left), and hexahedral mesh used in time domain simulations based on the Finite Integration Technique (FIT) solver (right).

frequency band is defined. The spectrum of the Gaussian signal is transformed into time domain by means of an inverse Fourier transformation, yielding the time signal $x(t)$ with Gaussian envelope. This Gaussian pulse excites the specified mode pattern at the input port of the antenna and it propagates through the antenna geometry until the energy of the pulse decays below a given threshold. The lower the energy threshold the higher the precision of the results but the longer the simulation time. During the propagation of the pulse through the structure, the reflected and transmitted signals $y(t)$ are monitored. The S-parameters over the entire frequency range are calculated by means of the Fourier transform applied to the resultant time signal $y(t)$, leading to the corresponding signal in frequency domain $Y(f)$. Hence, in one single run, all frequencies can be calculated, so that fast results can be obtained for broadband structures. The mesh used for time domain computations using FIT is the hexahedral mesh, which is shown on the right side of Fig. 3.11.

In order to corroborate the simulated results, a good practice is usually to simulate the structure with a different solver based on a different simulation technique. If both solvers are properly configured and the reality of the problem is properly captured in the model geometry and the boundary conditions, the solutions will converge to the same results. Unlike time domain solvers, the frequency domain solvers are more suitable to simulate resonant narrowband antennas, since a single simulation run is performed at each single frequency. So that for simulations of antennas with broadband behaviour, lots of simulations have to be performed to calculate the S-parameters in a wide frequency range. The commercially available software used throughout this thesis [30] implements hexahedral mesh corrections in its time domain FIT solver to conform the mesh to rounded structures (Perfect Boundary Approximation - PBA),

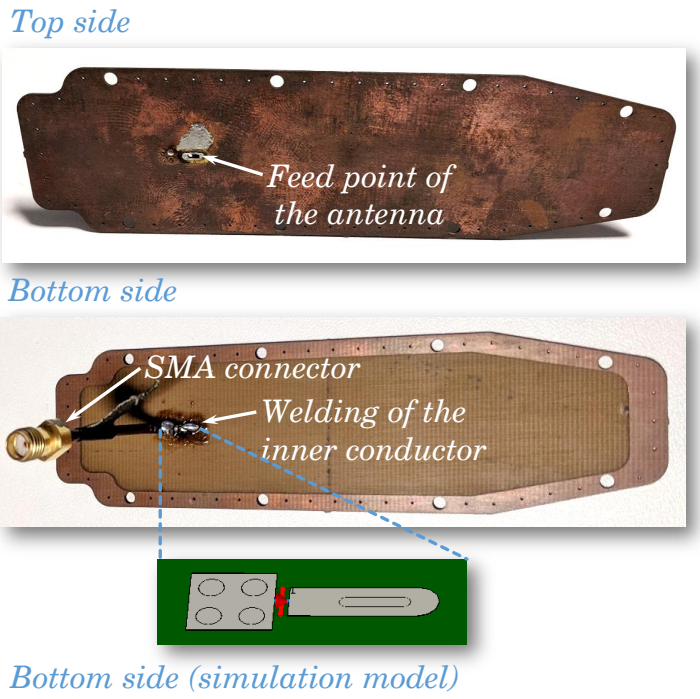

Figure 3.12: LTE-V2X antenna feed: Top side of the manufactured PCB where the antenna is welded (top), and bottom side of the PCB with the SMA connector and the RF cable with its inner conductor welded to the feed point of the antenna and the outer conductor to the ground plane of the PCB, which has been connected through vias to the ground plane on the top side of the PCB (middle). Feed point with the discrete face port used in simulations (bottom).

and to allow more than one material in one hexahedral mesh cell (Thin Sheet Technique - TST). However, by nature, the tetrahedral mesh used by the frequency domain FEM solver adapts much better to the real geometry volumes that define the three-dimensional antennas. The tetrahedral mesh used in frequency domain simulations by the FEM solver is shown on the right side of Fig. 3.11. The antenna is fed with a discrete face port from the bottom side of the ground plane. The feeding point of the manufactured prototype is shown in Fig. 3.12. The discrete face port in the simulations is placed at the bottom side of the PCB, where the weld is displayed. Enough distance has been maintained between the port and the vertex where the antenna structure begins to ensure that the port mode has been generated correctly. Even better accuracy is usually obtained with waveguide ports attached to the cross-section of a coaxial cable, but the modeling of the coaxial geometry can lead to slightly increase the number of mesh cells. As a compromise solution and given the good accuracy of the results, the antenna has been excited with discrete face ports. Similar results are obtained with both solvers and very good agreement is obtained between simulation and measurement results, as shown in Fig. 3.10 in dashed black.

Figure 3.13 shows the measured radiation patterns obtained in the LTE band with the

multiband antenna of Fig. 3.6 under investigation [20]. Realized gain values are shown to demonstrate the efficiency of the antenna. At the top of the figure, the conical cuts at an elevation angle θ corresponding to the main beam direction at each frequency (horizontal cuts) of the vertically polarized LTE-V2X antenna are shown for various frequencies within the bandwidth of interest. The diagrams are omnidirectional at all frequency bands with a circularity better than 3 dB.

At the bottom of Fig. 3.13, measured vertical patterns of the AUT at various frequencies within the LTE bandwidth are shown in solid colored lines. Again, realized gain values are displayed. These vertical patterns are computed after averaging great circle cuts at various azimuth angles φ = 0°, 45°, 90°, and 135°. This offers a good representation of the measured data, as long as the far-field patterns of the antenna are omnidirectional. The plot also shows in dashed colored lines the vertical patterns of a set of reference quarter-wave monopoles tuned at each resonance frequency. The patterns are again averaged over various great circle cuts at the same azimuth angles as with the AUT in order to be able to compare them. Almost the same results are obtained with the LTE-V2X multiband antenna as would be obtained with a reference quarter-wave monopole antenna. But the substantial difference that makes the LTE-V2X antenna special is that it yields almost the same results with roughly half the dimensions of the quarter-wave monopole at the lowest frequency of operation and with a significantly higher impedance bandwidth and pattern stability over frequency than that obtained with a thin quarter-wave monopole antenna.

To show how efficient the antenna is, the simulated vertical radiation pattern averaged over various azimuth angles of a reference quarter-wave monopole above an infinite ground plane is displayed in a dashed black line. It is worth noting that although the main beam direction of the LTE-V2X antenna tilts upwards to lower θ angles due to diffraction effects at the edges of the finite ground plane where the antenna is measured, the realized gain value in main beam direction is the same as the one obtained with the quarter-wave monopole tuned at each resonance frequency at θ = 90°.

As discussed before, the radiation patterns within the V2X frequency band have been designed to be elliptical when the antenna is placed above a flat ground plane. As already shown, this is accomplished with the inverted pyramid at the bottom of the antenna. The measured patterns are shown in Fig. 3.14 in the same form as those shown in Fig. 3.13. It can be clearly seen the oval-shaped form of the conical cuts (horizontal patterns) in main beam direction when the antenna is measured above a flat, finite, rounded metal dish with bent edges. As in the LTE case before, and due to the finite dimensions of the ground plane, the measured patterns in elevation shown after averaging the great circle cuts at various azimuth angles, are tilted upwards. Due to the higher frequency of operation comparing with LTE frequencies, the main beam direction is located at higher θ angles, closer to θ = 90°.

It is also worth noting that a remarkable amount of radiation is directed towards low θ

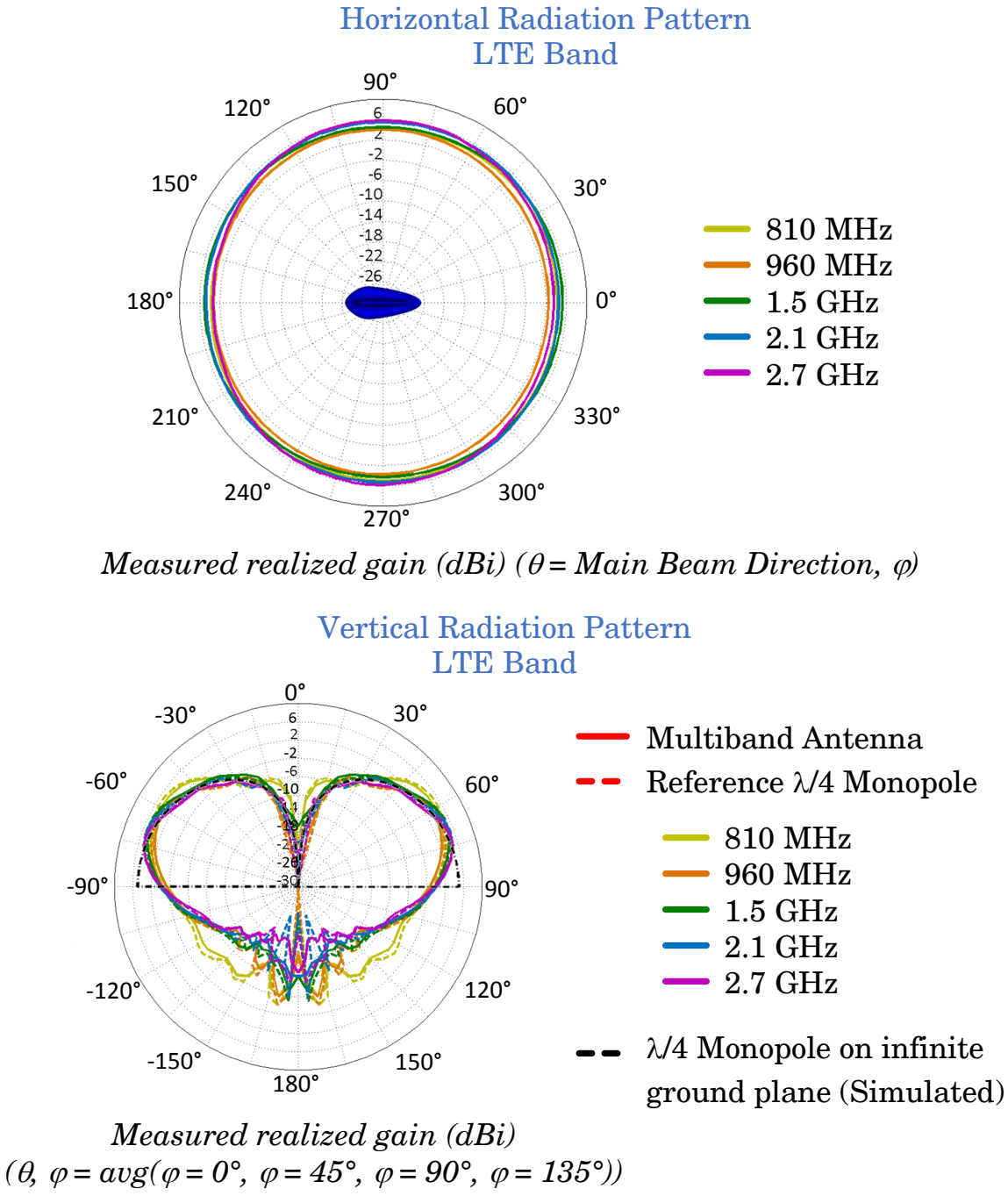

Figure 3.13: Measured radiation patterns of the LTE-V2X antenna for the LTE band: Conical cuts in main beam direction (horizontal patterns) at various frequencies within the LTE bandwidth (top). Great circle cuts (vertical patterns) averaged over various azimuth angles $\varphi = 0°$, 45°, 90°, and 135° at various frequencies within the LTE bandwidth (bottom). At the bottom the measured patterns of a set of reference quarter-wave monopoles tuned at each resonance frequency are shown (dashed colored lines). A simulated quarter-wave monopole above an infinite ground plane is also shown in a dashed black line.

angles, as shown at the bottom of Fig. 3.14. This is due to the spurious current that flows into the upper part of the antenna and leads to radiation (the antenna structure is effectively larger than a quarter wavelength). Although this current distribution is largely blocked by means of the inductive metal strips that connect the capacitive cap to the feeding point of the antenna, it cannot be completely suppressed.

This special oval-shaped form given to the antenna radiation patterns above a flat ground plane is intended to become omnidirectional whith the antenna placed on the roof of the car, near the rear edge. To demonstrate this behaviour, the antenna is installed on the roof of a sedan car with an angle of inclination of about 12°. The simulated results are shown in Fig. 3.15. On the left side of the figure, a three-dimensional view of the far-field pattern at 5.9 GHz is shown with a sketch of the CAD model of the car. Comparing with the great circle cuts in elevation shown at the bottom of Fig. 3.14, the patterns are completely deformed. The half power beamwidth is significantly reduced and the main beam direction changes over azimuth due to the inclination angle of the roof. A severe ripple is shown at low θ angles. However, the conical cut at $\theta = 90°$ looks almost round, with circularity values of $\pm$ 2 dB, as shown on the middle side of Fig. 3.15. Although radiation patterns are affected by different car geometries in different ways, keeping the radiation diagram in driving direction with as little alteration as possible is an important aspect of this type of safety-related systems. Moreover, the directivity of the LTE-V2X antenna in driving direction yields $\approx$ 5 dB more gain than a quarter-wave monopole tuned at 5.9 GHz in the same position on the roof of the car.

On the right side of Fig. 3.15, the cumulative distribution function (CDF) of the gain level values over azimuth is shown. The CDF compares the curves depicted in the upper right of Fig. 3.15. It can be inferred that the V2X-LTE multiband antenna at 5.9 GHz performs better than a quarter-wave monopole in the same rear roof-top position for almost all cumulative probability values. Moreover, in median (50% cumulative probability), the investigated multiband antenna differs only $\approx$ 1 dB from a tuned quarter-wave monopole on the middle of the roof and surpasses the performance of the ideal placed monopole for cumulative probability values greater than $\approx$ 90%.

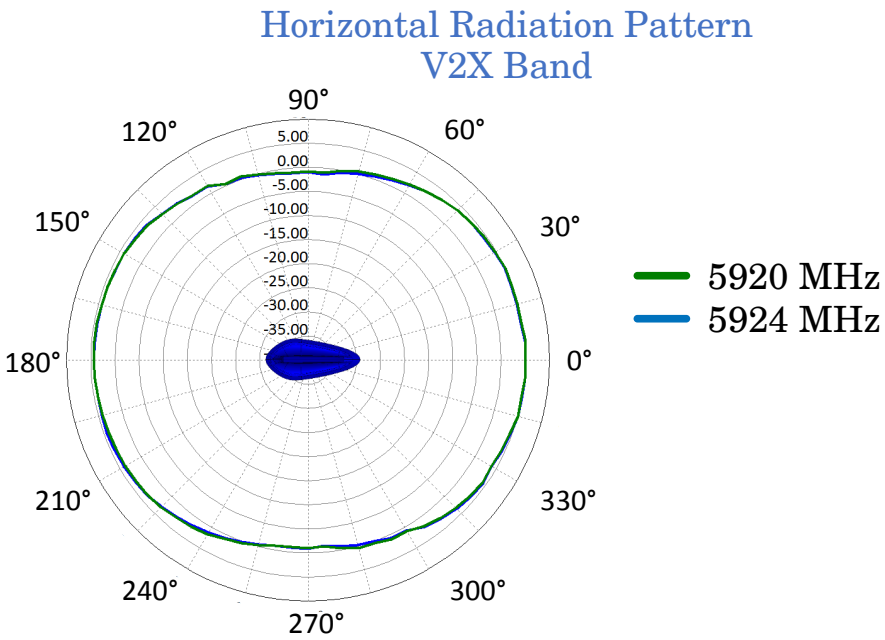

Measured realized gain (dBi) (θ = Main Beam Direction, φ)

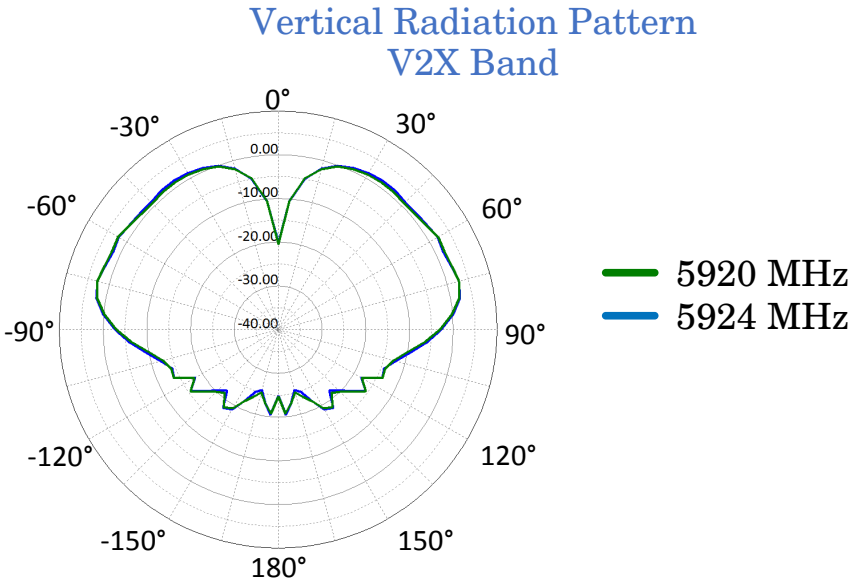

Measured realized gain (dBi)
(θ, φ = avg(φ = 0°, φ = 45°, φ = 90°, φ = 135°))

Figure 3.14: Measured radiation patterns of the LTE-V2X antenna for the V2X band: Conical cuts in main beam direction (horizontal patterns) at two frequencies within the V2X bandwidth (top). Great circle cuts (vertical patterns) averaged over various azimuth angles φ = 0°, 45°, 90°, and 135° at two frequencies within the V2X bandwidth (bottom).

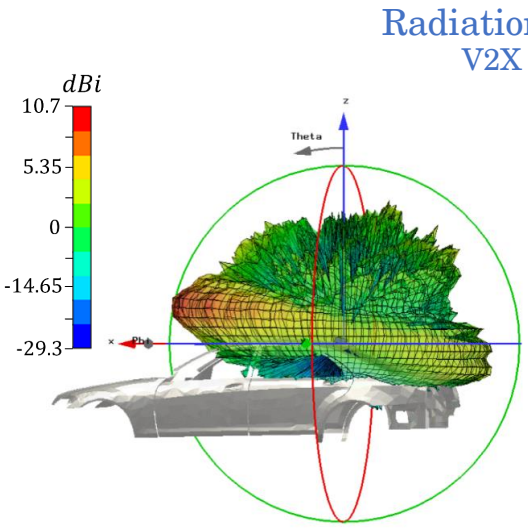

3D – (Simulated) Radiation pattern of the multiband antenna at f = 5.9 GHz

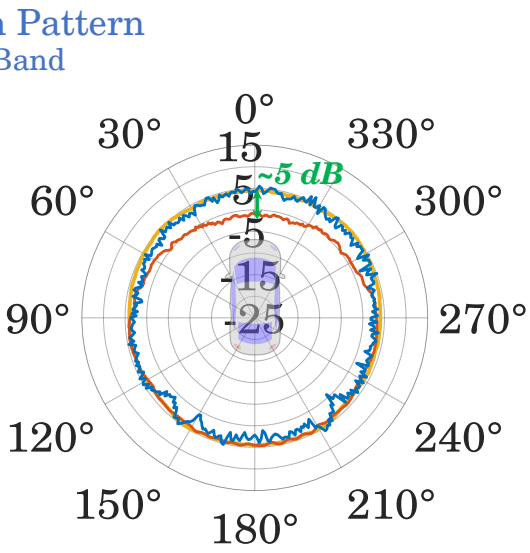

(Simulated) Horizontal cuts of the radiation pattern at f = 5.9 GHz (θ = 90°, φ)

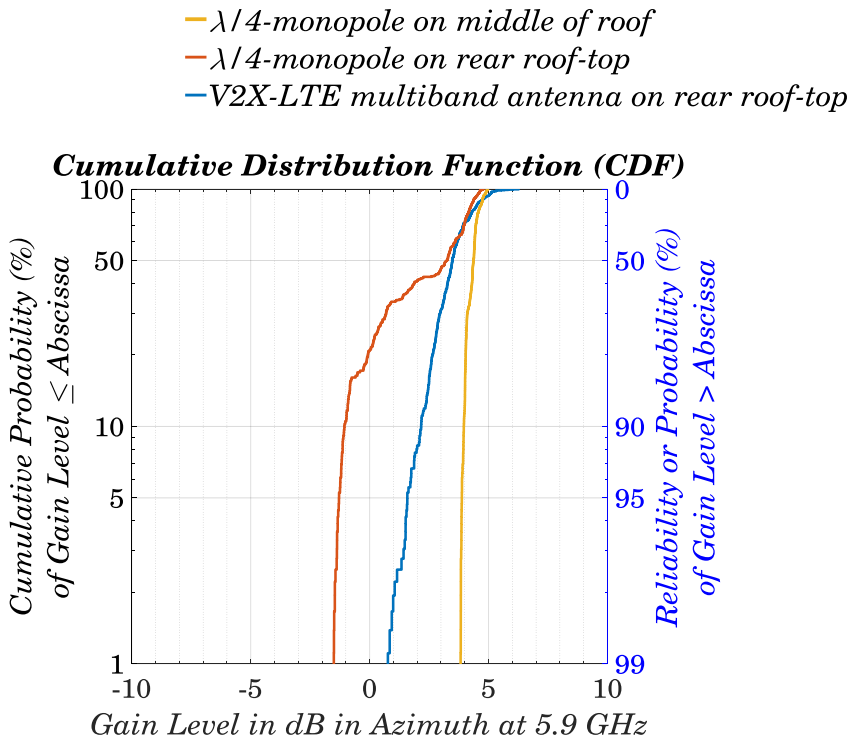

Figure 3.15: Radiation patterns of the LTE-V2X antenna mounted on the vehicle's roof: Three-dimensional view along driving direction of the far-field pattern at 5.9 GHz (top left), conical cut at $\theta = 90°$ comparing with the pattern obtained with a quarter-wave monopole on the middle of the roof and on the rear roof-top position (top right), and cumulative distribution function (CDF) derived from the horizontal radiation patterns (bottom).

CHAPTER 4

DECENTRALIZED MACRO-DIVERSITY SYSTEMS: MOUNTING POSITIONS

Wireless communication systems suffer from multipath fading, polarization mismatch, and interference due to the mobile radio-frequency channel where the electromagnetic waves propagate. The complex signals received by automotive antennas have random amplitudes and phases associated with the superposition of the multiple reflected and diffracted signals from the channel scenario traveling different paths and adding to the direct signal in the best case of Line of Sight (LOS). The random phase associated to the antenna is also varying as the vehicle moves. High data rate and reliable systems are of the utmost importance when it comes to safety applications like V2X communication. The increasing trend towards hidden and compact automotive antennas increases the challenge to achieve reliable systems, since antenna patterns suffer from ripples and shadowing effects as a result of the interaction between antennas and their mounting positions.

Combinations of various antenna mounting positions in the form of decentralized antenna arrays can conform the resulting radiation pattern in an optimal shape to improve the overall capacity and the reliability of the V2X system by means of diversity techniques and adaptive beamforming. Diversity algorithms select or combine dynamically the multiple replicas of the signal-fading channels (completely uncorrelated and with the same mean power in the ideal case) carrying the same message at each antenna of the array to mitigate multipath fading and increase the channel capacity or outage capacity C_{out}, which is directly related to the SNR at the outage probability level P_{out}, denoted by SNR_{out}[1], by means of Shannon's formula $C_{out} = B \cdot$

[1]To ensure reliable wireless communication systems in fading environments, it should be guaranteed that the received SNR only falls below a specified threshold level during a short period of time with a so-called outage probability P_{out}, so that a minimum SNR value given by SNR_{out} can be guaranteed with probability $(1 - P_{out})$.

$\log_2(1+SNR_{out})$. In case of diversity combining or adaptive beamforming, the ergodic capacity[2] is also improved. Diversity combining or adaptive beamforming techniques simultaneously combine the weighted signals of more than one antenna (in phase and sometimes also in amplitude to match with the spatial characteristics of the fading channel and minimize the mean-squared error), and dynamically selects at each instant of time (or point in space) the combination that yields the best *SNR*. This can only be accomplished by combining simultaneously the signals of more than one antenna, which means increasing the average Signal-to-Noise ratio (*SNR*), i.e. the array gain.

Diversity systems require more than one signal with approximately the same mean power (power imbalance $P_{imb} \approx 0$) carrying the same message but experiencing independent fading statistics (uncorrelated signals at each branch or antenna element in the array). Continuous selection or coherent combination[3] at each instant of time of the random signals received from each array element yields a resultant diversity signal with much less severe fading and, therefore, improved reliability. The statistically independent (uncorrelated) signals in a multipath-fading environment[4] can be obtained by means of different alternatives, namely spatial, polarization, angle or pattern, field component, frequency, or time diversity.

Spacing the antenna elements by a distance $d \geq 0.175\lambda$ in a spatially white channel (uniform angular distribution of wave arrival), yields to almost uncorrelated signals, technique which is called spatial diversity. The spatial correlation coefficients ρ between two electric or magnetic fields received at the respectively antenna elements placed on the vehicle are computed by means of the Bessel function of first kind and zero order $J_0(\cdot)$. Correlation factors of $\rho(d) = J_0(\beta d) \leq 0.707$ or envelope correlation coefficients $\rho_e = |\rho|^2 \leq 0.5$, which lead to antenna separations $d \geq 0.175\lambda$, have been shown to yield values of diversity gain for antenna arrays installed in the car reasonably close to those obtained with correlation factors equal to zero (which implies an antenna separation $d \geq 0.38\lambda$) [55, 72]. Since in real channels the direction of arrival of the incoming waves is not uniformly distributed, the required antenna separation d, for which the correlation factor is exactly zero, is a little bit larger than that of spatially white channels. Differences on antenna separation that yield uncorrelated signals have been shown between urban, suburban, and rural areas, due to the different spatial channel characteristics.

[2]The ergodic capacity is a long term mean value depending on the average *SNR* gain or array gain, an thus not affected by an increased reliability.

[3]Coherent combination is referred here to the sum of complex quantities with the same phase.

[4]Diversity only makes sense in a multipath-fading environment, namely a radio-frequency channel where the signal arrives from multiple directions, much more than elements in the array. In the extreme case where the signal arrives from all directions evenly likely (large angular spread), so that on average all directions of arrival (DoA) yield the same amount of power, the channel is called *spatially white* (it has no directivity). In this case, the phase relation between adjacent antenna elements at each instant of time is completely random distributed, leading to completely uncorrelated signals. This ideal situation corresponds to the one where the maximum benefit of diversity can be exploited. The opposite spatial structure of the radio channel where the received replicas are fully correlated (directive channel) corresponds to that where signals arrive at the antenna array from only one direction, so that the phase and amplitude relations between elements in the array remain constant over time. Real channels are somewhere in between both extremes, and the degree of channel directivity together with the temporal fading statistics and the required level of outage probability will determine the level of improvement in terms of diversity and array gain.

Usually, separations of $d \approx 0.5\lambda$ are used in the praxis to cover all possible scenarios in a V2X communication system. Although there is no limitation on the number of antennas used for spatial diversity, the amount of improvement in diversity gain by adding more antenna elements decreases as the number of antennas grows.

Polarization diversity achieves uncorrelated signals by means of antennas with orthogonal polarizations. The diversity order is thus limited to two, since there are only two orthogonal polarizations. The advantage is that both antennas can be placed together, since the decorrelation of signals does not depend on the antenna separation.

Angle or pattern diversity yields independent fading signals by means of multiple directive antennas with main beams pointing in different directions according with the direction of arrival of the scattered waves. The average signal power strength received in spatially white channels, where the density function of incoming waves is uniform distributed in all incident angles from 0 to 2π, is independent of the antenna radiation pattern. This means that the average received power with a directive antenna should be equal to that of an ideal isotropic antenna. As far as receiving maximum average signal strength is concerned, and since real channels differ from the idealized spatially white channel, directive antennas with radiation patterns confined to the solid angles, where the scattered waves are expected to arrive, would maximize the received average signal strength [55]. As far as the amount of reduction of fading is concerned, which is the main goal of diversity, the angle or pattern diversity technique takes advantage of the less severe fading characteristics (directly related to the reduced level crossing rate[5]) of directive antennas in channels where it is reasonably to assume a uniform arrival angle in all directions.

Field component diversity takes advantage of the different reflection coefficients of the electric and magnetic fields in a multipath environment, which after superposition of the multiple paths leads to uncorrelated electromagnetic field components.

Frequency diversity can be used in frequency-selective channels, where the fading signals on different frequencies separated by the so-called coherence bandwidth B_c are uncorrelated. However, it requires much more frequency spectrum and separate transmitters for each branch.

Time diversity takes advantage of the low degree of correlation of a randomly fading signal at sufficiently separated instants of time. However, for stationary vehicles, the time diversity technique would not yield to any improvement in the amount of fading, since the minimum time separation between samples is inversely proportional to the speed of the vehicle [55].

The diversity techniques used in this chapter are based on spatial and angle diversity, since combining antenna elements at different mounting positions lead to antenna separations much greater than the wavelength at 5.9 GHz, and due to shadowing effects from the vehicle body, directive radiation patterns are obtained.

[5]The level crossing rate is defined as the expected ratio at which the envelope of the received signal crosses a specified threshold level at its positive slope [72].

4.1 Commonly Used Mounting Positions for Decentralized Macro-Diversity Systems

Taking the roof-top mounting position as a reference, this section is intended to analyze the radiation characteristics of other antenna placements on the vehicle for cases where the roof position is not available, as in the case of convertibles or when it is required to hide the antennas for aesthetic reasons.

4.1.1 Radiation Characteristics and Reduction of Computational Effort

The state-of-the-art of simulation of antennas placed on any large and complex environment like the car is first carried out using a very simplistic CAD model to which can be added various details that better represent the actual real structure where the antenna should be placed. This is accomplished by taking the most characteristic and bulky structures first and progressively adding more parts and details until the computed results converge to the measured ones or to some reference values. This allows not only a better evaluation of the results, but also a better intuitive understanding of the physical phenomena involved. Unfortunately, this preliminary model investigation often requires many trial-and-error attempts and some kind of asymptotic computational method to speed up the simulation process.

In order to obtain accurate results in an efficient way, the feasibility of a new method has been investigated in terms of antenna pattern accuracy and computational effort. The method consists of considering only the relevant parts of the car illuminated by a large electromagnetic field strength. This dramatically reduces the number of cells, while reducing simulation time and computational resources without compromising accuracy. With just one simulation, the electromagnetically relevant parts can be identified by plotting the field distributions along the vehicle body, and the tedious trial-and-error method can be avoided. Moreover, the details of the complex environment in the vicinity of the antenna can be kept intact without compromising the simulation time and maintaining the accuracy of the results. Thus, full-wave volume discretization methods can still be used, offering high accuracy with reasonable simulation times.

The method takes advantage of the reasonable high frequency of operation (5.9 GHz). Unlike other low-frequency automotive applications, like audio broadcast services, the electromagnetically significant environment for far-field diagrams considering the car and which must be enclosed by a sphere of radius D_{car} is much smaller for frequencies inside the V2X bandwidth than for audio broadcast frequencies. These electromagnetically relevant parts are related to the maximum antenna-and-structure extent D_{car} used in the approximated formula to calculate the range at which the far field can be measured[6], which for antennas placed on or near large and

[6]The range, from which the far-field of an antenna in free space can be measured with a reasonable phase error smaller than $\pi/8$, is given by $r \geq \frac{2D^2}{\lambda}$, where D is the maximum extent of the antenna or antenna and structure, and λ is the wavelength [41].

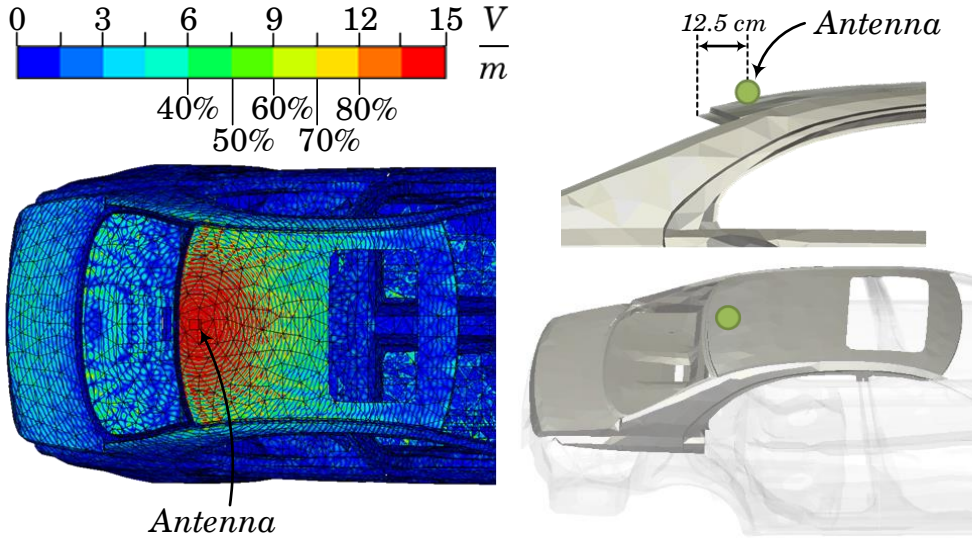

Figure 4.1: Roof-top mounting position: Snapshot in time of the electric field distribution along the chassis of the car (left) of a quarter-wave monopole antenna placed above the roof near the rear rim (right, top), to evaluate the complexity reduction of the CAD model (right, bottom) through the electromagnetic field strength.

complex structures is larger than the maximum extent of the stand-alone antenna D for far-field computations in free space.

Starting with the roof-top mounting position and considering a quarter-wave monopole placed about 12.5 cm away from the rear edge of the roof, which corresponds to 2.46 wavelengths at 5.9 GHz, the electric field distribution considering the whole chassis has been analyzed. A snapshot in time of the electric field strength along the chassis of the car is shown in Fig. 4.1 [25]. It is worth noting that only the roof of the car has an electric field concentration greater than 60 % to 70 %, while the rear shelf and trunk do not exceed the 40 % to 50 %. On the rest of the car the field is lower than 40 %. Fig. 4.1 also shows the exact antenna position (right, top), and the electromagnetically significant parts are highlighted (right, bottom) to assess the reduction in complexity of the problem.

To evaluate the accuracy of the method, Fig. 4.2 shows the polar plots of radiation patterns of a quarter-wave monopole placed as shown in Fig. 4.1 considering the electromagnetically significant parts and comparing with the whole vehicle body as a reference. Three patterns have been computed with different degrees of simplification. First, only the parts of the vehicle inside the Fraunhofer region of the antenna in free space have been considered. For a quarter-wave monopole at 5.9 GHz in free space, the Fraunhofer boundary is only $2D^2/\lambda$ =6.36 mm from the antenna structure. As expected and discussed before, this distance is not enough to account for the effects of the large and complex environment where the antenna is placed. Therefore, an omnidirectional pattern in the horizontal plane with less gain than a monopole on an infinite

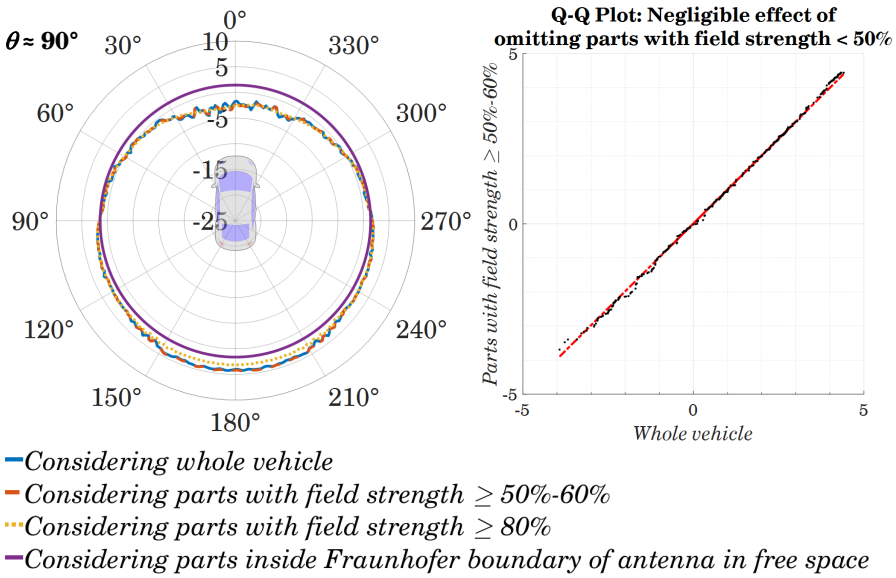

Figure 4.2: Accuracy of the radiation patterns through simplification and complexity reduction of the CAD model: Horizontal great circle cut of the radiation pattern of a quarter-wave monopole placed as shown in Fig. 4.1 for various complexity simplification levels (left). Quantile-quantile (Q-Q) plot (right) to evaluate the accuracy of the investigated method to reduce the computational effort. Points along the 45° inclined line denote a high level of coincidence.

ground plane at $\theta = 90^\circ$ (due to the small finite dimensions of the ground plane) is obtained. Adding the parts of the car illuminated by the antenna with electric field strengths greater or equal than 80 %, a radiation pattern almost equal to that considering the whole vehicle is obtained. Considering the parts of the car with an electric field strength of 50 % to 60 %, the resultant pattern converges to that obtained considering the whole vehicle, omitting more than 3/4 of the complete vehicle structure and reducing the simulation time in a factor of 4.6[7].

On the right side of Fig. 4.2, a quantile-quantile plot (Q-Q plot) to assess the negligible effect of omitting the parts of the car with field strengths lower than 50 % is computed. The Q-Q plot compares the gain values over azimuth considering only the significant parts with field strengths greater than or equal to 50 % to 60 % with the gain values considering the whole vehicle. Since the black points follow the red straight line inclined 45°, both set of values come from the same statistical distribution with a high correlation factor of 0.9987 between both set of values at each azimuth angle.

The same process has been used to evaluate the method at typical mounting positions in convertible cars, namely the front and rear bumpers and the right and left side mirrors. Figures 4.3 and 4.5 show the electric field distribution (left) for antennas placed in the position indicated on the right side of the same figures for the rear bumper and the left side mirror cases, respectively

[7]Simulations performed on a workstation equipped with eight-core Intel® Xeon processors (E5 series) at a clock rate of 2.90 GHz, 64 GB of RAM and 2 NVIDIA Tesla C2075 GPUs.

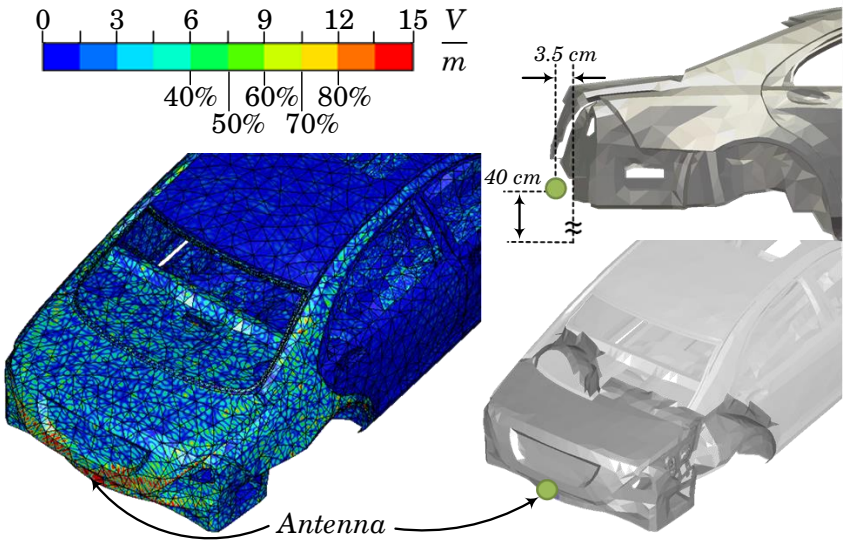

Figure 4.3: Rear bumper mounting position: Snapshot in time of the electric field distribution along the chassis of the car (left) of a half-wave dipole antenna placed in the rear bumper (right, top). Significant parts after applying the method to reduce the computational effort (right, bottom).

[25]. According to the electric field distributions, the most significant parts have been extracted and simulations have been performed to assess the validity of the discussed method. Figures 4.4 and 4.6 illustrate the success of the method in form of polar plots of the respective radiation patterns and in form of Q-Q plot as a matter of proof. High correlation factors greater than 0.98 are obtained for both cases.

It is worth noting from Figures 4.4 and 4.6, that the greatest discrepancy between results is obtained in the opposite directions to those of the main antenna beams. Anyway, it should be noticed that for a single antenna placed on the rear bumper or in a side mirror, the front of the car or the other lateral side, respectively, is meaningless.

4.1.2 Optimization of Radiation Characteristics

When dealing with antenna placement problems in complex environments like the car, it is difficult to make statements that are valid in all situations. Depending on the type of car, its characteristic shape in the vicinity where the antenna should be placed, and the relative position of the antenna with regard to the chassis and other metallic parts, can shape the radiation pattern by directing the main beam into a particular region or producing unwanted ripple, as already seen in the radiation patterns of the section before.

Once the relevant parts and details affecting the antenna radiation pattern have been identified, an optimization process can be carried out. As seen before, a single antenna is not

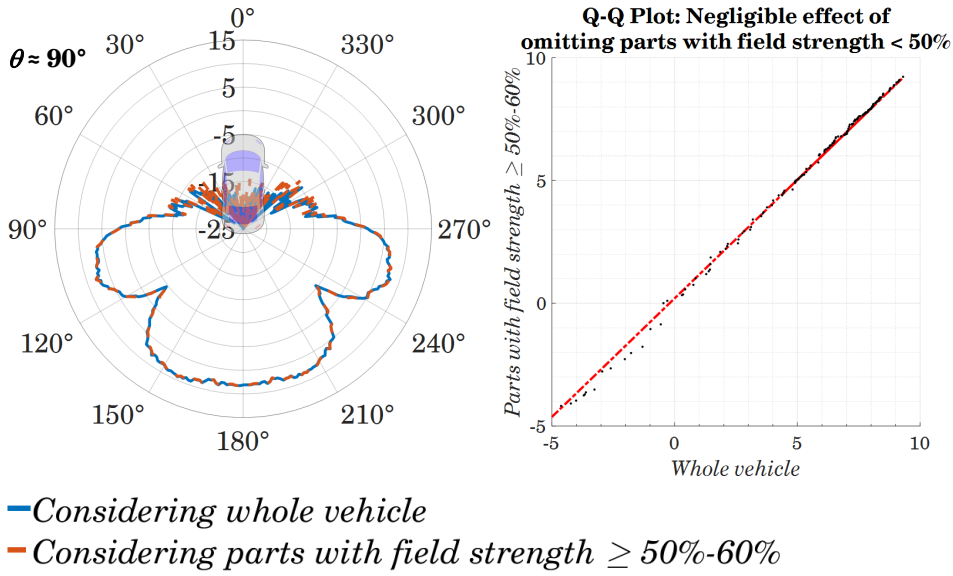

Figure 4.4: Accuracy of the radiation patterns for the rear bumper position: Horizontal great circle cut of the radiation pattern of a half-wave dipole placed as shown in Fig. 4.3 for the whole vehicle and considering only the parts with high electric field strength (left). Quantile-quantile (Q-Q) plot (right) to evaluate the accuracy of the investigated method to reduce the computational effort.

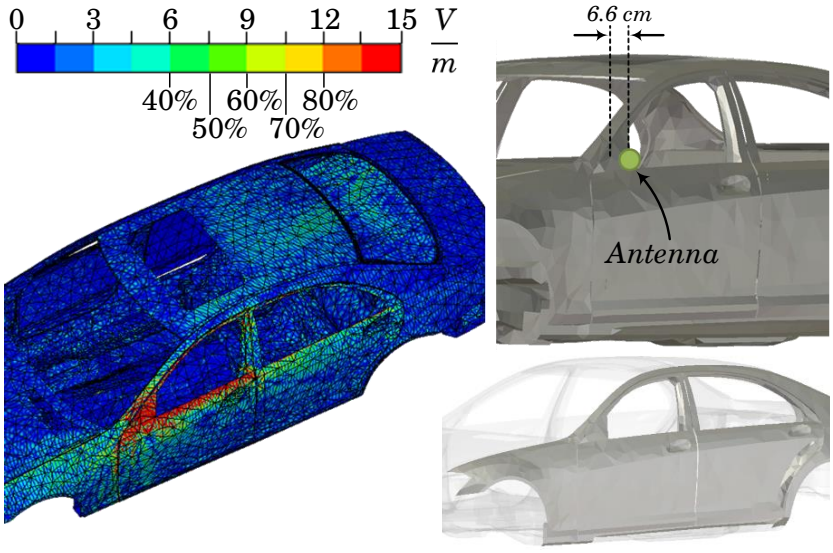

Figure 4.5: Side mirror mounting position: Snapshot in time of the electric field distribution along the chassis of the car (left) of a half-wave dipole antenna placed in the left side mirror at the driver side (right, top). Significant parts after applying the method to reduce the computational effort (right, bottom).

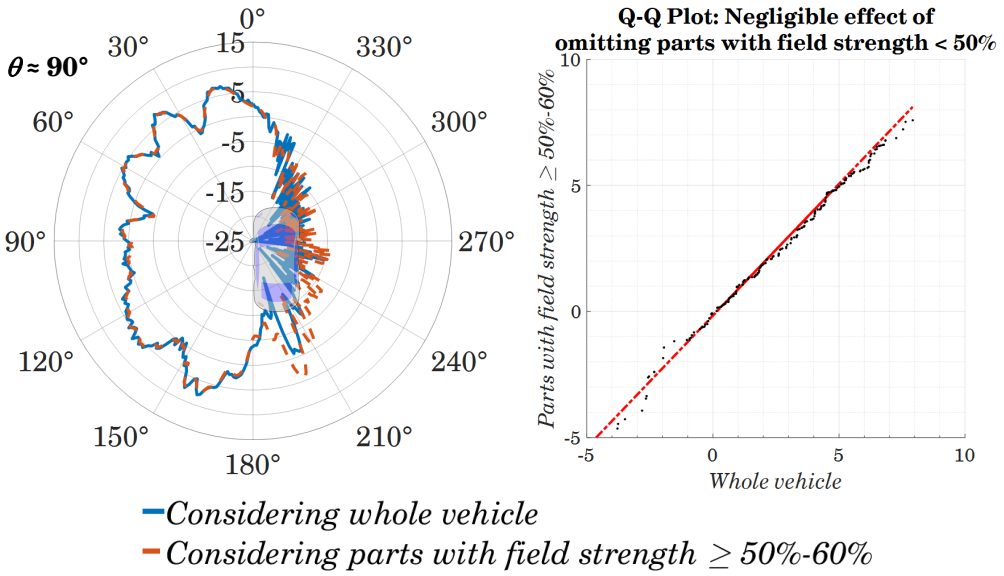

Figure 4.6: Accuracy of the radiation patterns for the left side mirror position: Horizontal great circle cut of the radiation pattern of a half-wave dipole placed as shown in Fig. 4.5 for the whole vehicle and considering only the parts with high electric field strength (left). Quantile-quantile (Q-Q) plot (right) to evaluate the accuracy of the investigated method to reduce the computational effort.

enough to completely cover the horizontal plane, due to blockage effects from the chassis of the car. Therefore, the optimization process will be carried out so that the combination of several antennas will result in an omnidirectional pattern. Since one single antenna in the front/rear bumper or right/left side mirror can only cover a sector of about 120° with adequate gain levels, combinations of at least two antennas become mandatory for safety-related applications like V2X communication. Two antenna combinations would also suffer from shadowing effects in two opposite angular sectors of 60°. The antenna patterns can be smoothed in main beam direction and deep fadings caused by the relative position of the antenna and the vehicle body can be avoided. The antennas should be placed close to the chassis, at distances of less than 0.5λ with optimums at about 0.3λ, in accordance with the theoretical patterns of dipole antennas over a conducting plane [69]. Fig. 4.7 shows the resultant radiation patterns to obtain the best coverage by means of macro-diversity techniques.

As seen in Fig. 4.7, a smoothed pattern where the main beam is directed in the horizontal plane has been obtained. The superposition of all four patterns from the corresponding single antennas in their mounting positions in one figure, reveals perfect omnidirectional coverage at all azimuth angles if the four antennas are combined. For low-end cars, the combination of front and rear bumper would yield enough gain in the critical directions to be covered for V2X safety-related systems, namely the driving direction and the opposite one.

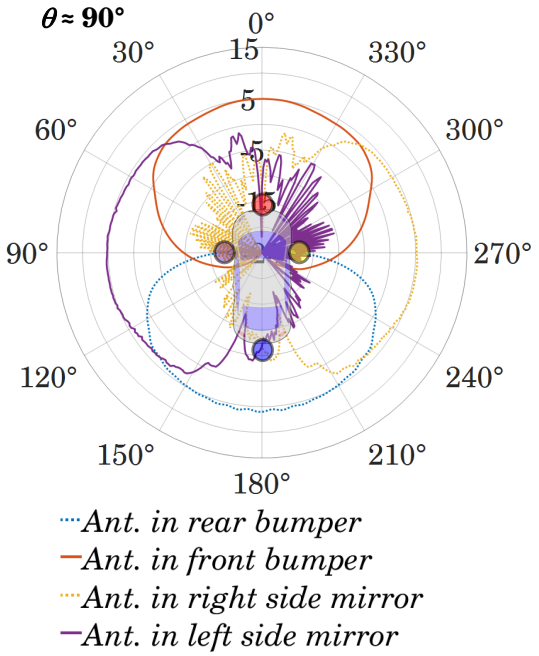

Figure 4.7: Radiation pattern optimization depending on antenna mounting position to achieve a smooth omnidirectional coverage by means of macro-diversity: Horizontal great circle cut of the radiation pattern of a half-wave dipole in the front, rear bumper and right, left side mirrors, as indicated by the colored dots.

4.2 System's Reliability Improvement Through Macro-Diversity

The commonly used hidden mounting positions discussed in the previous section do not ensure good coverage in the whole azimuth plane, except for the ideal position on the top of the roof. This fact leads to a worsening of the antenna system's performance in a real V2X scenario, where omnidirectional or elliptical radiation patterns are required. An improvement of the radiation characteristics for hidden antennas in various mounting positions in the car to ensure the reliability of the V2X antenna system in a real multipath scenario is accomplished by means of antenna diversity. With such an smart antenna array of at least two antennas, not only it is possible to conform the radiation pattern in an omnidirectional or elliptical shape increasing the gain of the overall antenna system, but it is also possible to reduce the signal fading and time delay spread due to the multipath fading of the V2X mobile communication scenario.

A distinction should be made between micro-diversity, which applies on co-located antenna sites, and macro-diversity, which applies on separated antenna sites. The former uses a small inter-element spacing between adjacent elements in the antenna array, typically in the order of classic fixed beamforming arrays, namely $d/\lambda \leq 1$; while the latter uses larger spacings, namely $d/\lambda \gg 1$. Although both diversity antenna arrangements are intended to mitigate the fading in a multipath environment, not both of them are useful for reducing the two kinds of fading existing

in a multipath channel, namely the long-term fading and the short-term fading.

The long-term fading is associated to the variation of the local means of the received envelope signal due to shadowing effects through different terrain contours and human-made structures as the vehicle moves. It follows a log-normal distribution, and can only be mitigated by means of macro-diversity systems.

Short-term fading is associated to the multipath reflections by local human-built scatterers or natural obstacles such as forests surrounding the vehicle (short-term fading can not be caused by natural obstructions such as mountains, they only cause long-term fading), which superimpose together with different amplitudes and phases. This fact leads to a fading signal which is usually characterized by a Rayleigh statistical distribution in space (or over time) for NLOS scenarios, whose envelope shows amplitude dynamic variations of about 40 dB with regard to the local mean. In case of superposition of only two waves, a standing-wave pattern would be achieved, but this situation does not correspond to the V2X spatial channel and more than two waves are present. As long as more than two waves are added together, fading received envelope signals as the ones depicted in Fig. 4.8 for different multipath environments are achieved. The short-term fading can be reduced by means of macro- or micro-diversity.

Figure 4.8 shows a theoretical comparison of the maximum reliability improvement that can be achieved by means of diversity in different scenarios, namely NLOS, indoor, and LOS. Such environments are usually modeled by Rayleigh, Nakagami, and Rice statistical distributions, respectively. They have been generated with the aid of a computer matrix-based software with a common seed to achieve almost completely uncorrelated signals $\rho \approx 0$ that are also repeatable[8]. This way, every time the random generator is initialized with the same seed, same pseudo-random results are obtained and the maximum improvement when combining four antennas with the well-known linear combining techniques in different scenarios can be better evaluated.

As can be seen in the inset of the plots in Fig. 4.8, the maximum correlation factor between a pair of pseudo-random signals is $\rho = 0.008$. In the figures on the top and on the bottom at the left side, the received signals in the different three environments considered are shown as a function of the sampled point (corresponding to different positions or instants of time where the signal is sampled). The SNR of the received signals normalized to the mean SNR of the best single antenna (which corresponds to the antenna with the highest mean level depicted as a solid black line) is plotted. The different diversity combinations, namely Switch/Selection Combining (SC), Equal Gain Combining (EGC), and Maximum-Ratio Combining (MRC) are shown in green, blue, and red, respectively. The straight lines indicate the 1 % value of the best antenna in black, and the 1 % value of the MRC combination in red, which correspond to the 1 % cumulative probability value or 99 % reliability value. As shown in the inset of the plots in Fig. 4.8, maximum diversity gains at the 99 % reliability of 9.5 dB, 6.4 dB, and 4.9 dB, are achieved for SC, EGC, and MRC, respectively. This shows that better improvement can be obtained for worst case scenarios where

[8] $\rho = 0$ is not possible to achieve with computers, since they are deterministic machines and they can not generate completely random sequences, but only pseudo-random numbers.

the signal suffers many fades, as in the case of Rayleigh-distributed signals. The inset of the figures also shows the maximum difference between the MRC combination and the best single antenna at each sample point, which for $N = 4$ ideal antennas completely uncorrelated, it yields a maximum difference of $10\log_{10}(N) \approx 6$ dB. It is worth noting that even for almost completely uncorrelated ideal signals, the maximum difference yields sometimes 5.9 dB, as shown in the NLOS and indoor environments. With practical real antennas, this value is not attainable.

At the bottom, on the right side of Fig. 4.8, the Probability Density Functions (PDF) of the best single antennas in each scenario and the PDF of the corresponding resultant diversity MRC combination is shown to see how the curves of the single antennas move to the right when combined following the mentioned linear techniques and change in some cases the statistical distribution that best fits the envelope. It can be concluded that the Nakagami distribution, which is related to the gamma distribution and is often used in communications theory to model scattered signals that reach a receiving antenna by multiple paths, yields a good model to characterize the diversity combinations. The Nakagami distribution[9] is characterized by the following density function

$$f(x) = 2\left(\frac{\mu}{\omega}\right)^{\mu} \frac{1}{\Gamma(\mu)} x^{(2\mu-1)} e^{-\frac{\mu}{\omega}x^2}, \quad \forall x \geq 0 \quad \text{and for} \quad \mu \geq \frac{1}{2} \quad \text{and} \quad \omega > 0; \tag{4.1}$$

where μ denotes the shape parameter, ω is the scale parameter controlling the spread of the curve, and $\Gamma(\cdot)$ is the gamma function[10]. Moreover, the Nakagami distribution gives more control over the extent of the fading than the Rayleigh or Rician distributions, so that Rayleigh and Rician can be modeled by modifying the shape and scale parameters of the Nakagami distribution.

[9]The Matlab® function *makedist('Nakagami')* is used to create a Nakagami distribution object.

[10]The gamma function is defined by the integral $\Gamma(x) = \int_0^{\infty} e^{-t} t^{x-1} dt, \quad \forall x \in \mathbb{R}_{\geq 0}$, and is computed in Matlab® by invoking the function *gamma*.

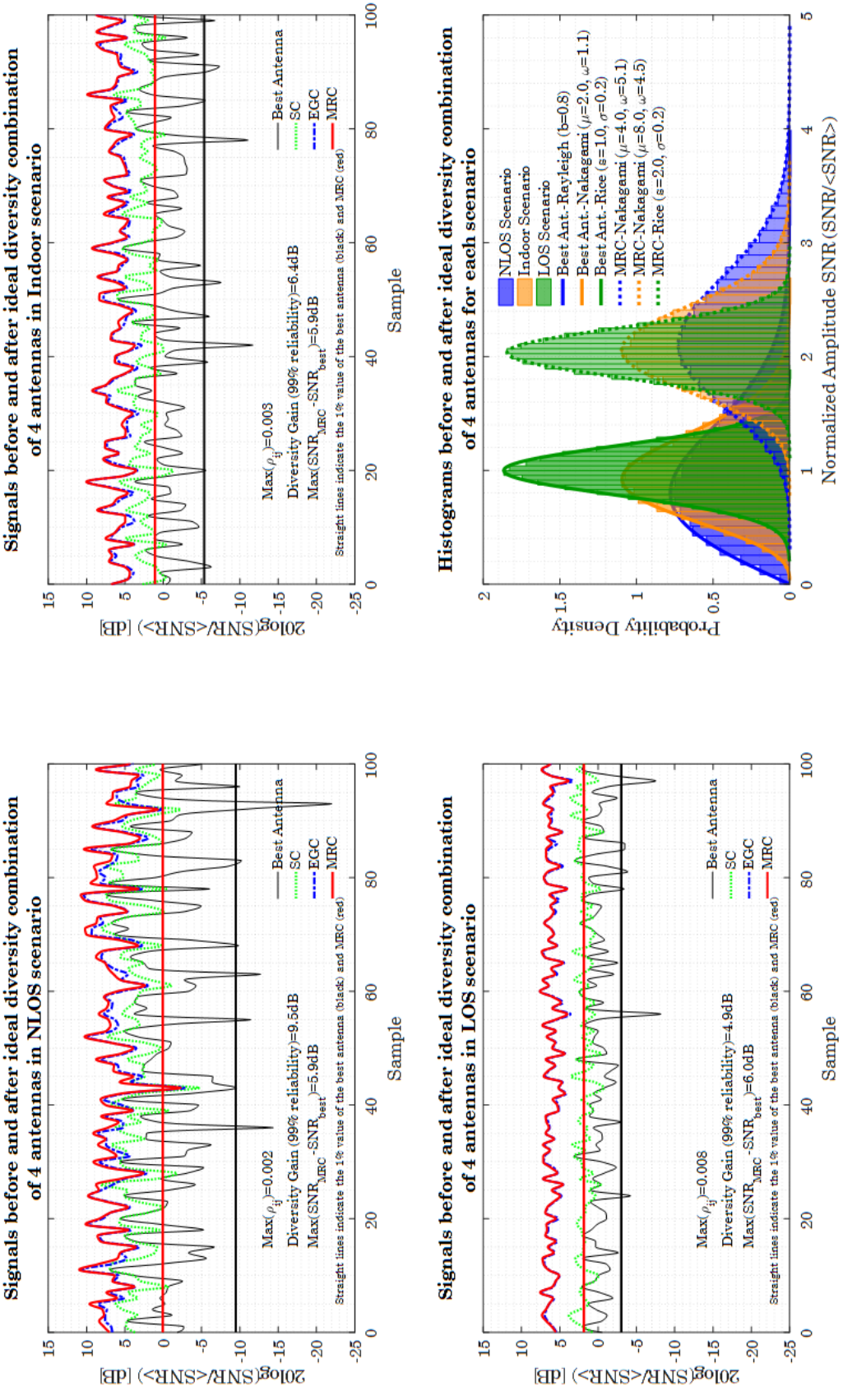

Figure 4.8: Reliability improvement of received signals through linear diversity combining techniques in different scenarios: Computer-generated characteristic statistical received signals in NLOS (top, left), indoor (top, right), and LOS (bottom, left) scenarios, and their combinations through diversity techniques. Greater improvement is obtained for worst case Rayleigh-distributed NLOS scenarios (top, left). The PDF functions shift to the right by means of diversity (bottom, right), and the resultant curves can be fitted with a Nakagami distribution.

Figure 4.9 shows the cumulative distribution function of the received signals after applying linear diversity combining techniques in the different scenarios illustrated in Fig. 4.8. The graph clearly shows the concepts of *diversity gain* vs. *array gain* (also called *beamforming gain*), and how the improvement in the reliability of the radio link, given by the diversity gain value, is most significant in NLOS scenarios. Both concepts, diversity and array gain, are fundamentally different in nature. The diversity gain represents the increase in SNR at a specified outage level and is only defined between two fading statistics with the same mean power. It is also limited to the degree of spatial diversity offered by the radio channel. In contrast, the array gain is constant, and depends on the number of antennas used. The CDF denotes the probability that the received SNR is above the value of the abscissa, which in practice can be read as the more to the right the better. If we look at the curves in Fig. 4.9 after the diversity combination, we see that they do not take the same value as the curves that represent a single antenna for a 100% cumulative probability. This shift to the right illustrates the array gain. If the mean powers of the single antenna and the diversity combination are now equalized by shifting the MRC curve to the left exactly by the array gain value, the effect of diversity can be isolated. The diversity gain at a given probability value can be read from the CDF graph by measuring the SNR difference at that given value of outage probability. Thus, it strongly depends on the given cumulative probability level, the linear combining technique used (SC, EGC, MRC) and the characteristics of the radio channel (LOS, NLOS).

When combining various mounting positions of the type described in the previous section (e.g., one antenna at each side mirror, or one antenna at the front bumper and one at the rear bumper), macro-diversity is implemented, since the spacing between the antennas are much greater than the wavelength at 5.9 GHz. Chapter 5 will deal with micro-diversity systems with compact antenna arrangements hidden underneath the roof of the car. There, the mitigation of long-term fading has been sacrified in favour of a reduction in costs and losses compared to the long cables required in macro-diversity systems. On the other side, a compact antenna set completely hidden underneath the roof suitable for installation next to the electronic control unit (ECU) is proposed and investigated.

4.2.1 Smart or Adaptive MIMO Antenna Array Systems

Classic MIMO systems were originally conceived for radar applications to enhance reception of weak signals, enable direction finding, and reduce interference by means of phased arrays (progressive phase weighting) or beamformers (amplitude and phase weighting) steering the main narrow beam towards the direction of the wanted signal (small angular spread) and forcing a minimum in the radiation pattern to suppress the undesired directions in interference limited scenarios, namely where the number of interferers N_{int} is lower than the number of antenna elements in the array N_{ant}. This assumption does not hold for mobile communications scenarios like LTE or V2X, where the spatial properties of the channel are more similar to that of a spatially

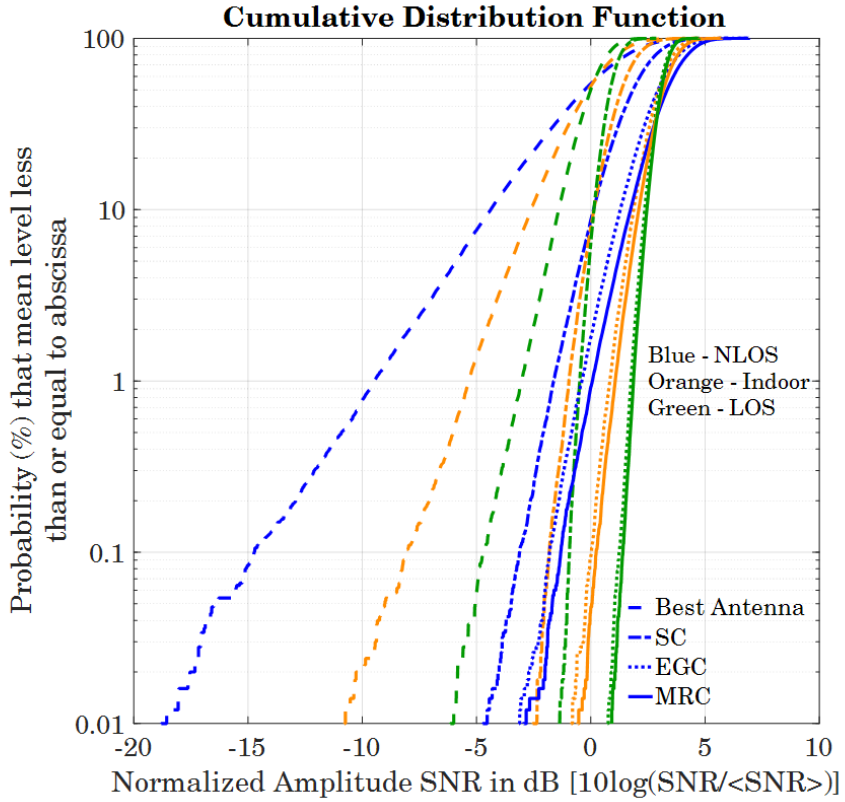

Figure 4.9: Reliability improvement of received signals through linear diversity combining techniques in different scenarios: CDF's of the computer-generated characteristic statistical received signals shown in Fig. 4.8. Greater diversity gain values are obtained for NLOS Rayleigh-distributed scenarios.

white channel than that of a channel with the incoming signals arriving at the array from a single direction of arrival (DoA).

To mitigate the fading and shadowing effects on the radiation patterns discussed on the previous section and shown together in Fig. 4.7, spatial macro-diversity is proposed and investigated. The antennas are placed in the front/rear bumpers and in both side mirrors around the center of the car, at azimuthal angles $\varphi = 0°$ (Ant. 1, front bumper), 90° (Ant. 2, left mirror), 180° (Ant. 3, rear bumper), and 270° (Ant. 4, right mirror), with respect to the driving direction ($\varphi = 0°$). The multiple replicas of the received signal at the sufficiently separated antennas are amplified, co-phased and added according to the commonly known predetection diversity linear combining techniques as described in [19], namely, Selection/Switch Combining (SC), Equal-Gain Combining (EGC), and Maximal-Ratio Combining (MRC). In contrast to a single antenna, the occurrence of deep fadings in the combined signal is considerably reduced by means of diversity, specially for those cases where there are simultaneous fadings at all antennas. Assuming that all amplifiers add the same complex Additive White and Gaussian Noise (AWGN) $\underline{n}(t)$, and that it is

uncorrelated between amplifiers and with any of the input signals, the noisy signals at any time received at each antenna terminal $\underline{r}_j(t) = \underline{V}_{r_j}(t) + \underline{n}_j(t)$ are amplified and added together after cophasing as a linear combination, whose envelope is given by [19]

$$\left|\underline{r}(t)\right| = \sum_{j=1}^{M} \left|\underline{g}_j \underline{r}_j(t)\right| = \sum_{j=1}^{M} \left|\underline{g}_j \left(\underline{V}_{r_j}(t) + \underline{n}_j(t)\right)\right|. \tag{4.2}$$

Each $\underline{r}_j$ can be weighted by a complex coefficient $\underline{g}_j$, which is proportional to the amplifier gain and can vary according to the fluctuations of the local statistics of the signal.

The signals $\underline{V}_{r_j}$ are assumed to vary much slower than the noise in a short period of time, where the former is relatively constant and the latter undergoes several fluctuations. Thus, the noise can be described as a stochastic process which follows the central limit theorem and can be modeled as a normal distribution with zero mean and a variance or noise power $E\left\{\underline{n}_j^2\right\} = N_j = N_0$, for $j = 1,\ldots,M$, where $E\{\bullet\}$ denotes the expected value [32]. The voltage gain values $\underline{g}_j$ depend on the combining technique. In SC, $\underline{g}_j = 1$ for the antenna $j = k$ that yields the largest S/N and $\underline{g}_j = 0$, for all $j \neq k$ and $j = 1,\ldots,M$. In EGC, all branch gains $\underline{g}_j = 1$, for $j = 1,\ldots,M$. And in MRC, the gains of each branch are adaptively adjusted to their instantaneous signal voltage to noise power ratios, so that $\underline{g}_j = \underline{V}_{r_j}^*/N_j$, for $j = 1,\ldots,M$, where $(^*)$ denotes conjugate [19].

According to equation (4.2) and the voltage gain values $\underline{g}_j$ for each combining technique, the instantaneous signal-to-noise power ratio S/N at the output of the system can be written as

$$S/N \approx \begin{cases} \left|\underline{V}_{r_k}\right|^2/N_0, & \text{for SC} \\ \left(\sum_{j=1}^{M}\left|\underline{V}_{r_j}\right|\right)^2/MN_0, & \text{for EGC} \\ \sum_{j=1}^{M}\left|\underline{V}_{r_j}\right|^2/N_0, & \text{for MRC .} \end{cases} \tag{4.3}$$

The value of the average noise power N_0 is considered to be constant and will be set to unity throughout this contribution. This assumption does not imply any loss on information since N_0 does not change the shape of the Probability Density Function (PDF) of S/N. It only contributes to the variance, determining how wide the form is stretched. The effect of the average noise power N_0 in the CDF is only a shift of all curves to the left or to the right, since it is only a multiplicative constant as shown in equation (4.3) [32].

To compute the diversity patterns, the envelopes of the gain patterns in dB of each antenna in the array are transformed to linear voltage ratios by means of the square root of the antilogarithm of the recorded values. Such values are obtained from measurements and/or simulations with all other antennas terminated with 50 Ω. In a computer-aided post-processing step, the envelope voltage ratios (equivalent to $\left|\underline{V}_{r_j}\right|$, for $j = 1,\ldots,M$) are combined according to equation (4.3) with $N_0 = 1$.

The computed radiation patterns after macro-diversity combinations for two and four antennas are shown in Fig. 4.10. The radiation patterns of the single antennas are displayed in grey, the SC-combination in green, the EGC-combination in red, and the MRC-combination in blue.

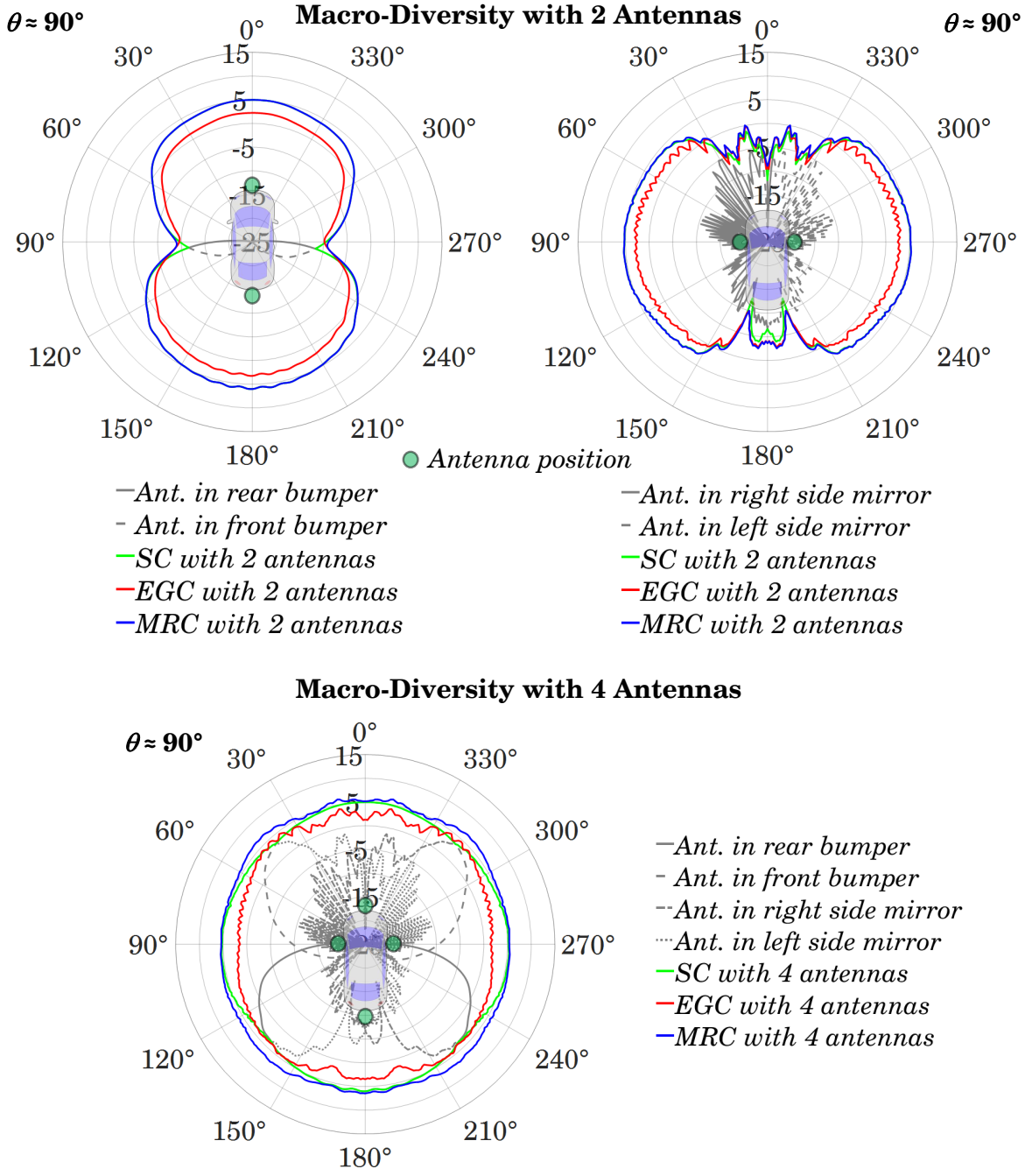

Figure 4.10: Radiation pattern improvement through linear macro-diversity combinations: Horizontal great circle cut of the radiation patterns for two-antenna combinations (top), and four-antenna combinations (bottom). The antenna positions are indicated by a green dot and the patterns of the single antennas with grey lines. SC means switch/selection combining. EGC means equal gain combining, and MRC means maximum-ratio combining.

The position of the antennas is depicted with a small green circle on the top view of a car. It can be observed that with two antennas eight-shaped patterns can be achieved. Only the macro-diversity combination of antennas in the front and rear bumpers yields acceptable results, emphasizing the coverage in driving and opposite to driving directions. As discussed earlier, this can be advantageous in urban scenarios, where the so-called canyon effect occurs. The combination of right and left side mirrors does not lead to a great improvement for V2X communication scenarios. In contrast, the four-antenna macro-diversity combinations yield almost omnidirectional patterns for all combination techniques, due to the balanced distribution of the antennas around the car.

It is also worth noting how in this case the SC-combination leads to much better results than the EGC-combination. This is because if the average power value of any of the antennas differs greatly from the rest of the antennas, the use of equal gain combining actually deteriorates the SNR when compared to just selecting the strongest branch (SC). It can be seen that if the magnitude of a signal r_2 at t_0 fulfills that $r_2(t_0) < \left(\sqrt{2}-1\right) r_1(t_0) \approx 0.414 r_1(t_0)$, the output SNR after EGC is less than the SNR received from the signal r_1 of the single antenna 1 [32]. Thus, this deterioration effect on the SNR of the combined EGC signal occurs when the mean power of the signal r_2 is weaker than that of antenna 1 with a difference greater than $\approx 7.66\,\mathrm{dB}$ (which corresponds to $20\log_{10}(0.414)$). For such decentralized antenna placements, there are always shadowing regions due to the chassis of the car, so that in many cases, using EGC is meaningless, as clearly shown in Fig. 4.10.

To better illustrate how crucial is the use of diversity in decentralized systems, Fig. 4.11 clearly shows, by means of statistical evaluation, the radiation pattern improvement achieved through linear macro-diversity combining techniques (colored lines) with regard to the single antennas (depicted in grey). Diversity and array gain is achieved by properly combining all decentralized antennas. Moreover, the verticality of the CDF curves after applying linear diversity combining techniques indicates that the radiation patterns are much more omnidirectional than for single antennas. Diversity gain values of roughly 15 to 16 dB can be read from the graph for SC-combinations with two antennas for an outage probability level of 10%, and up to 24 dB for the same cumulative probability level with four antennas. The fact that EGC performs worse than SC can be clearly corroborated in this figure, given that EGC curves (red) are more to the left than SC curves (green) for most outage probability values. This means that for some azimuth angles, the difference in mean power between the various single antennas is greater than 7.66 dB.

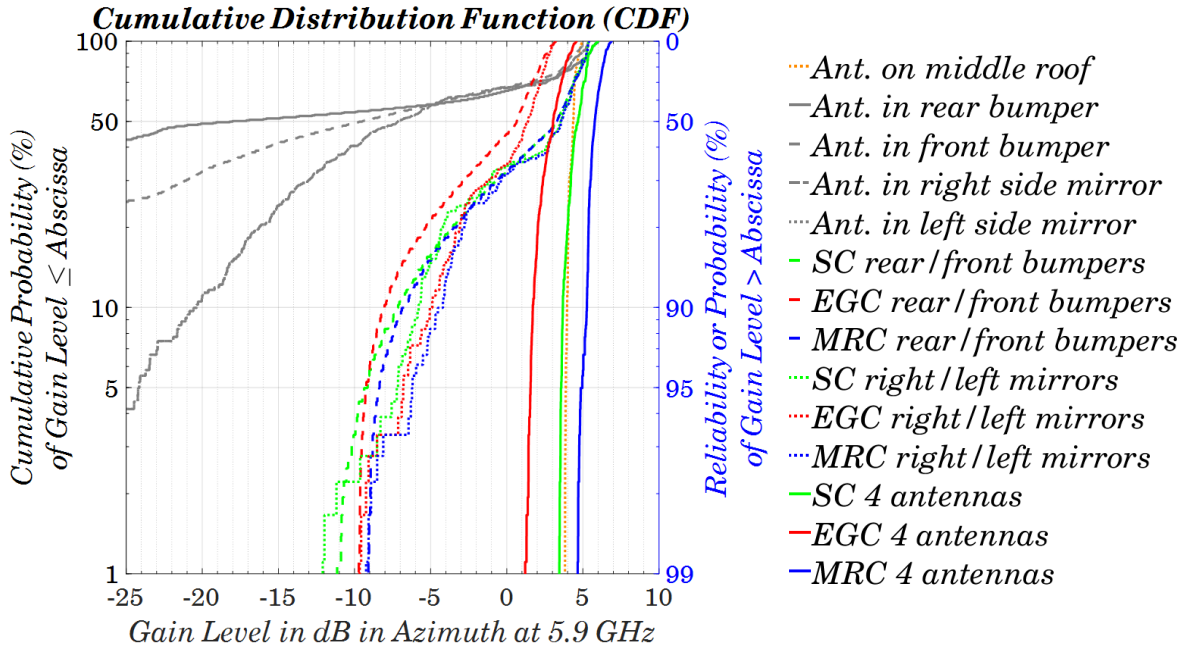

Figure 4.11: Statistical performance evaluation of radiation pattern improvement through linear macro-diversity combining techniques: Cumulative Distribution Function (CDF) (left axis) and reliability (right axis), both in a logarithmic scale, of the gain levels over azimuth for various diversity combinations with two and four antennas. The single antennas have also been included as a reference for assessing diversity gain.

CHAPTER 5

HIDDEN MICRO-DIVERSITY SYSTEMS

Looking back at the evolution of automotive antennas, there was always the need to design them as small as possible or embedded in some parts of the vehicle body in order not to disturb so much the aesthetics of the car. Examples of antenna size reduction are the radio broadcasting rod antennas discussed in [17, 104], where telescope rod antennas of 80 mm are actually replaced by small helical ones (operating in normal mode) of up to 14 mm in combination with the high-impedance amplifier. Embedded antennas in the front and rear window panes are typical examples of the historic trend to make antennas unobtrusive to the aesthetic design of the vehicle.

Nowadays, and with the increasing number of wireless services in modern automobiles and the reduced space to place their respective antennas, completely hidden locations are demanded by the automotive industry while keeping high the specifications to be fulfilled. This may sound contradictory, since hiding the antennas somewhere in the chassis of the car means worsening their performance due to shadowing effects, reflections, diffractions, and coupling effects with other metal and dielectric parts in close proximity to the source of radiation. Therefore, new concepts should be investigated to preserve the aesthetics of the car while ensuring good performance of the overall antenna systems.

To compensate the disturbing effects of hidden antennas, micro-diversity systems placed underneath the roof are proposed and their feasibility for V2X communication is investigated. Such diversity systems not only counteract the worsening effects on radiation pattern due to the hidden position, but also serve for improving the Signal-to-Noise Ratio (SNR) in real V2X fading scenarios. Unlike the macro-diversity or decentralized systems discussed in Chapter 4, micro-diversity systems in the form of spatial or polarization diversity avoid the long cables needed to interconnect the antenna diversity system with the control unit. They yield a compact

and unobtrusive solution. Moreover, they also reduce the heavy weight of the wiring in the car, which can be more than 50 kg in modern automobiles.

For other wireless services offered in modern cars, such as LTE or GPS/SDARS, different solutions based on cavity-like molds shaped on the roof have been proposed [9]. For V2X services, the investigated diversity system underneath the roof shows some advantages with regard to the common cavity solution investigated in the literature. Since V2X antennas are intended to communicate not only with other cars but also with road infrastructure and with electronic devices carried by humans, radiation patterns should also point toward low elevation angles with an acceptable level. Such low elevation angles are better covered with antennas placed underneath the roof than with those placed inside a cavity on the roof, because diffractions at the edges of the cavity tilt up the radiation pattern and reduce the coverage near the azimuth plane. Note the difference from LTE antennas, which should only communicate with cell-phone towers, thus requiring an omnidirectional coverage in the upper hemisphere.

Hidden positions underneath the roof present however some challenges, since the antenna is immersed within an environment of great reflections (car's cabin) and the electromagnetic waves must escape through the windows of the car, which are the unique apertures for microwave radiation to go through. The windows of the car are usually coated with metal resistive sheets to maintain a constant temperature inside the car reducing fuel consumption. In this chapter, it has also been investigated frequency selective surfaces on the windshield or rear pane of the car to let the waves pass through. Another challenge when sitting the antenna underneath the roof is to keep controlled the radiated energy in order to complain with human electromagnetic exposure. This point will also be addressed in this chapter.

5.1 Performance of Single Antennas Under the Roof

The scenario under consideration is depicted in Fig. 5.1. At 5.9 GHz, an antenna placed inside the chassis of a car can be treated as a radiator inside an overmoded electrically large, lossy cavity (metal chassis) with electrically large apertures (windows). Dimensions of the car body-shell are typically several tens of wavelengths at 5.9 GHz, leading to a complex resonant structure. Therefore, the electromagnetic field distribution is nonuniform in space (see Fig. 5.7) and change when the frequency (inside the bandwidth of interest) or the volume of the car cabin is varied (different types of cars: sedan, hatchback, SUV, etc.). That yields to severe changes in the shape of the radiation pattern even for adjacent frequency points within the impedance bandwidth of interest. However, and as shown in Fig. 5.2, the coherence bandwidth for an antenna placed underneath the roof of the car lies within the accepted values according to [71], since the correlation factor between the patterns within the operational bandwidth is greater than 0.5. To compute the curve of Fig. 5.2, a cross-correlation between the radiation pattern at the center frequency of 5.890 GHz and all radiation patterns at the adjacent frequencies within the V2X

bandwidth has been performed.

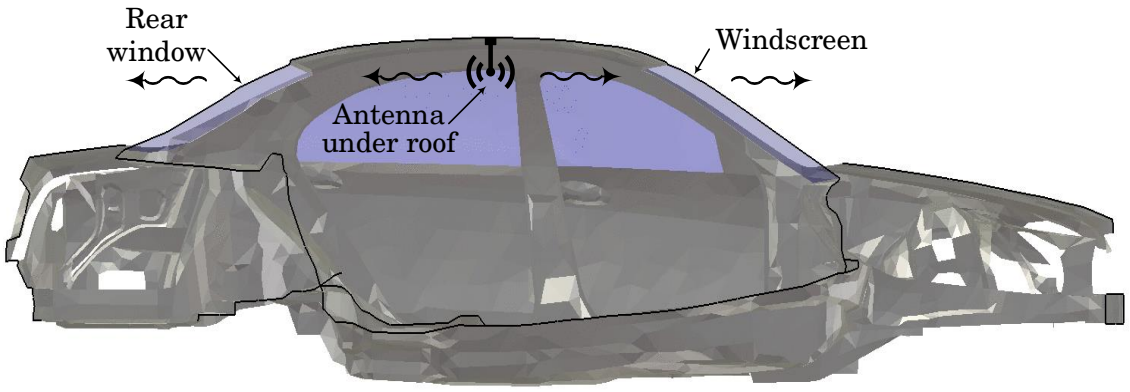

Figure 5.1: Hidden antenna under the roof of a car. Longitudinal cross-section view of a *NASTRAN* car model with an antenna centered under the roof. Electromagnetic waves in the microwave band radiate outwards through the windows of the car.

5.1.1 Radiated Fields of the Single Antenna

Hiding the antennas underneath the roof requires compact and concealed antennas to be fitted between the roof's metal chassis and the roof lining usually made of fibre, fabric or black lining with relative dielectric permittivities close to one and low loss tangent values [109]. A basic structure as the inverted-L monopole depicted in Fig. 5.3 with vertical and horizontal arm lengths given by l_v =9.9 mm and l_h =4 mm, respectively, and wire radius a =1.5 mm has been chosen as a single antenna element [21, 22]. Its small height dimensions (smaller than the λ/4-monopole due to the capacitive top-loading effect of the horizontal arm), the ability of the antenna to match with vertically and horizontally polarized waves (due to the fields related to the vertical and horizontal arms) in a multipath scenario where depolarization of the incoming waves occurs, and the versatility of such a simple structure to generate radiation patterns associated to more complex geometries (monopole-type, half isotropic, or patch-type radiation patterns) depending on the aspect ratio between vertical and horizontal arms [6], make the inverted-L monopole a promising candidate for a single element of a more complex adaptive diversity antenna array.

According to Fig. 5.3 and considering the current distributions I_1 and I_2 associated to the vertical and horizontal arms, respectively, the radiated fields derived in [6] applying image theory are given for both *E-theta* (E_θ) and *E-phi* (E_φ) components by

$$E_\theta = -j30\frac{e^{-jkr}}{r}\left(I_2\cos\theta\frac{e^{jk_x\frac{l_h}{2}}}{\sin\theta}\sin\left(k_x\frac{l_h}{2}\right)4j\sin(k_z l_v) - I_1\sin\theta\frac{2\sin(k_z l_v)}{\cos\theta}\right), \tag{5.1}$$

$$E_\varphi = -j30\frac{e^{-jkr}}{r}\left(-I_2\sin\varphi\frac{e^{jk_x\frac{l_h}{2}}}{\sin\theta\cos\varphi}\sin\left(k_x\frac{l_h}{2}\right)4j\sin(k_z l_v)\right), \tag{5.2}$$

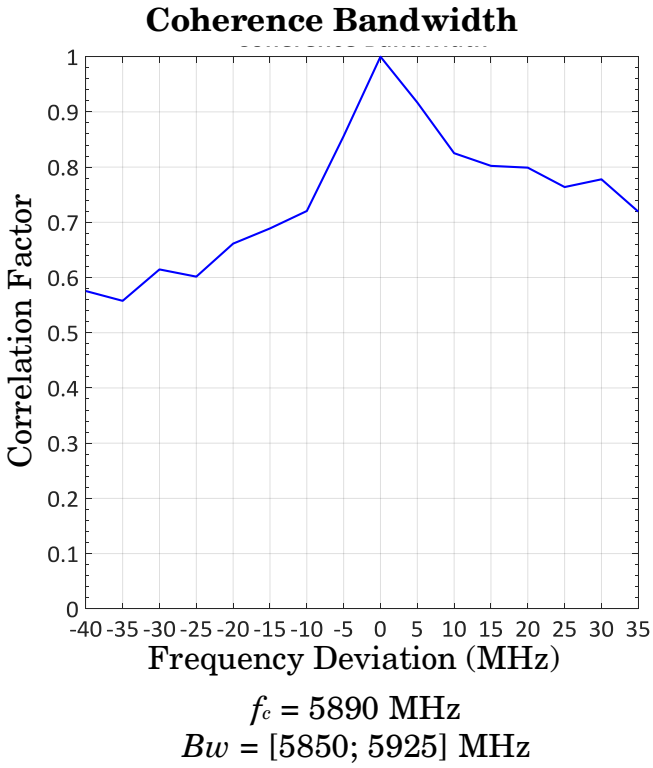

Figure 5.2: Coherence bandwidth for an antenna placed underneath the roof of the car.

where l_v is the length of the vertical arm, l_h the length of the horizontal arm, $k_z = k\cos\theta$ the vertical component of the wave vector $\boldsymbol{k}$, $k_x = k\sin\theta\cos\varphi$ the horizontal component of the wave vector $\boldsymbol{k}$, and (r,θ,φ) the spherical coordinates. Although the currents flowing in both arms are contributing to radiation in the *theta* polarization, only the current distribution I_2 in the horizontal arm is radiating a *phi*-polarized field.

Since monopole-type radiation patterns are required for V2X communication, an inverted-L monopole with an aspect ratio $l_v/l_h \approx 2.5$ and overall dimensions $L = l_v + l_h = 13.9\,\text{mm}$ has been used, whose different great circle and conical cuts of its radiation pattern are shown in Figures 5.4 and 5.5. Simulations considering an infinite ground plane made of perfect electric conductor (PEC) have been performed by means of a commercial electromagnetic software [30] using a solver based on the method of moments (MoM). The theoretical curves depicted with points in Figures 5.4 (left) and 5.5 are obtained by means of a matrix-based numerical computing environment [86] after evaluating equations (5.1) and (5.2).

It is worth noting from Fig. 5.4 the non-zero phi-component E_φ plotted in red in the great circle cut for an azimuth angle $\varphi = 90°$, which can be advantageous for channels with strong depolarization of waves, as expected for antennas placed inside the cabin of the car. Monopole-type

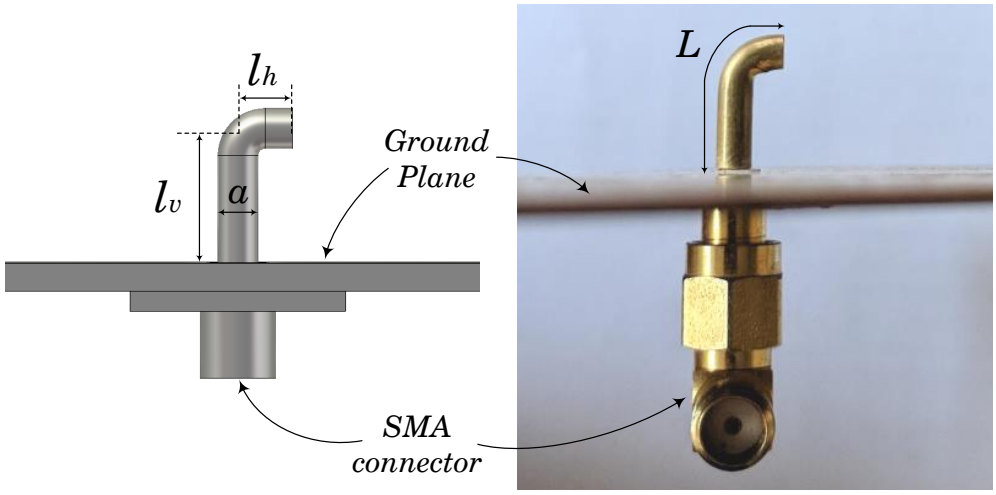

Figure 5.3: Side view of the inverted-L monopole antenna resonant at 5.9 GHz, with vertical and horizontal arm lengths given by l_v and l_h, respectively, and wire radius a. The ground plane and the SMA connector for measurement purposes are also shown. Simulation model (left) and built prototype (right).

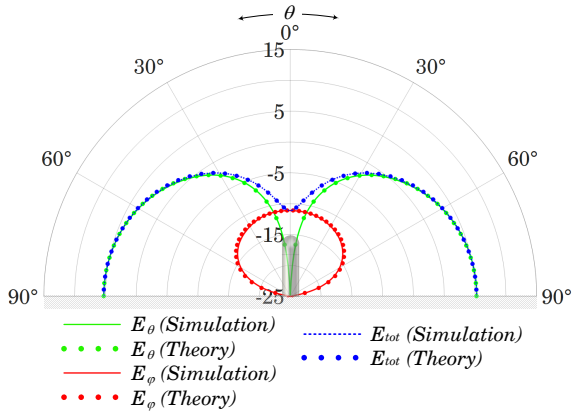

(a) Great circle cut ($\theta, \varphi = 90°$).

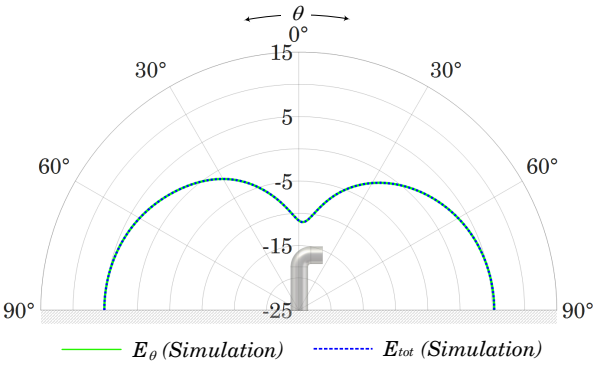

(b) Great circle cut ($\theta, \varphi = 0°$).

Figure 5.4: Great circle cuts in elevation ($\theta, \varphi = 0°, 90°$) (realized gain) of the radiation pattern of the inverted-L monopole antenna at 5.9 GHz.

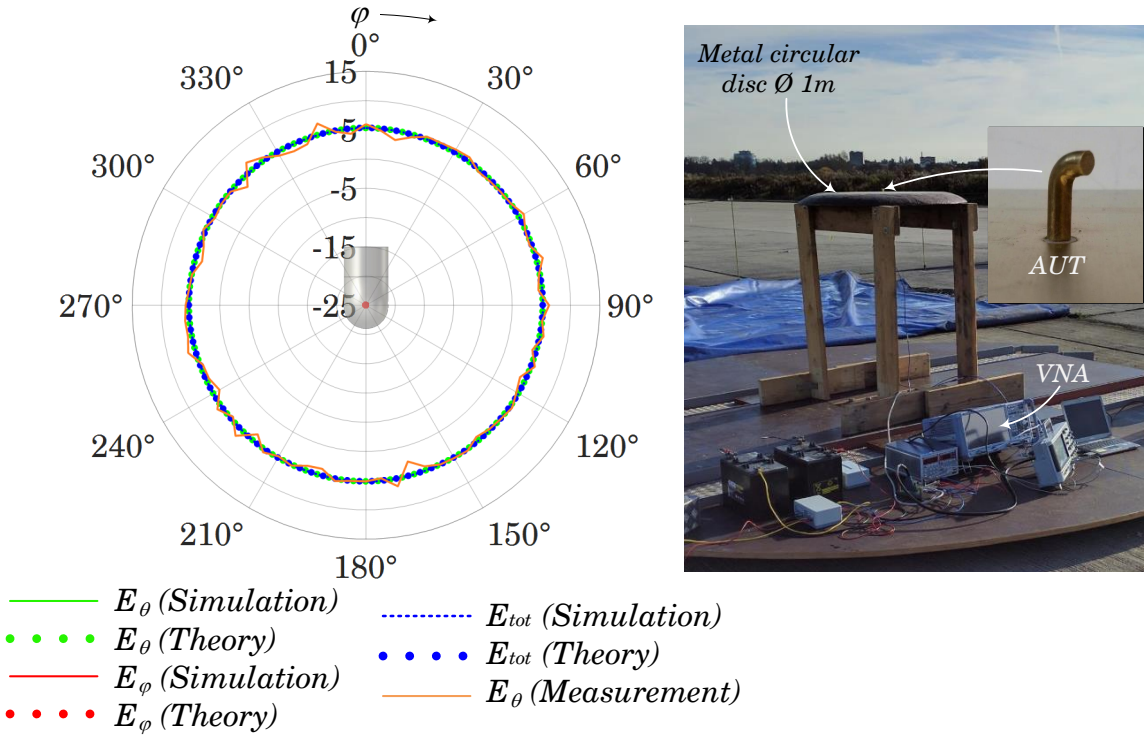

Figure 5.5: Conical cut or horizontal great circle cut ($\theta = 90°, \varphi$) (realized gain) of the radiation pattern of the inverted-L monopole antenna at 5.9 GHz (left). Setup for radiation pattern and return loss measurements at the open area test site (OATS) (right).

radiation patterns are shown with maximum realized gains of about 5.3 dB at 5.9 GHz. A small asymmetry is observed in the elevation pattern of the great circle cut at $\varphi = 0°$, on the right side of Fig. 5.4, due to the asymmetrical L-shaped geometry of the inverted-L monopole. Conical cuts with omnidirectional radiation characteristics are achieved with main beam direction in the horizontal plane corresponding to the horizontal great circle cut or conical cut at $\theta = 90°$ and depicted in Fig. 5.5. Very good agreement between theory (equations (5.1) and (5.2)) and simulations is obtained, as inferred from Figures 5.4 (left) and 5.5, as well as for the measured conical cut in main beam direction($\theta \approx 90°, \varphi$) in the open area test site (OATS), as shown in Fig. 5.5 (orange solid line). For the radiation pattern measurement, the gain transfer method has been used.

The return loss of the investigated inverted-L monopole antenna is shown in Fig. 5.6. Very good agreement has been obtained between simulation (blue solid line) and measurement (red solid line with red point markers). For the measurement, a metal circular disc with a diameter of approximately 1 m has been used.

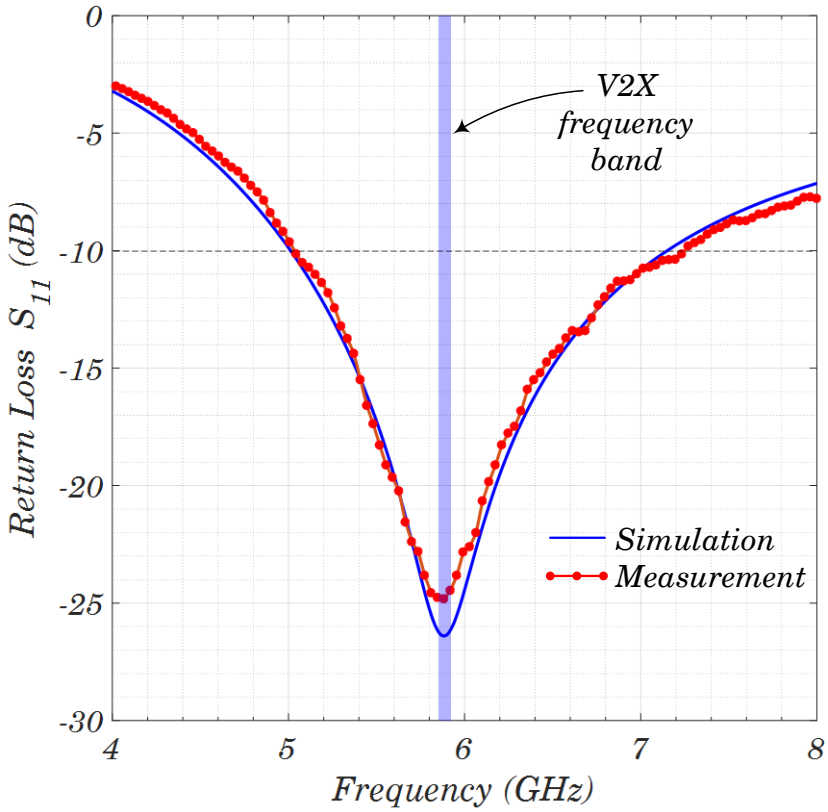

Figure 5.6: Return loss in dB of the input impedance of the inverted-L monopole antenna. Simulations in solid blue line and measurement in solid red with red point markers. The V2X frequency band is highlighted in transparent blue. The −10 dB reference return loss value is marked with a dashed line.

5.1.2 Wave Propagation Effects and Statistical Electromagnetic Approach

The cabin of a car, as an electrically large cavity, is not intended to behave as an specific radio-frequency device, such as a microwave resonator for which the cavity details are well known. Conversely, the irregular shape of a chassis and the complexity and variability of its interior loading, make it difficult to mathematically model all the electromagnetic phenomena occurring inside the car in a deterministic mode.

Sometimes the lack of accurate models regarding geometry and electromagnetic properties of materials found within an automobile makes it difficult to compare simulations and measurements directly at each point in space. The number of people occupying the vehicle on each trip, or even if a passenger were holding a metallic object like a cola can [99], can also change the electromagnetic fields inside the car at the 5.9 GHz band. Parametric studies, where a parameter, e.g. the antenna position, is varied to investigate the influence on radiation pattern, require very long simulation times. In such cases, deterministic approaches are thus inadequate.

However, what makes the statistical approach most interesting is the fact that the statistical

distributions characterizing the fields inside such large cavities, where the mode density becomes large, do not depend on small changes or details of the cavity [99].

5.1.2.1 Electromagnetic Fields Generated by Antennas Placed Inside the Car

To show how sensitive are the electromagnetic fields at the 5.9 GHz band to a change in frequency or volume inside the car's cabin, in [50], approximate equations for large cavities are derived to quantify such phenomena. The relative frequency change between adjacent modes in a cavity is given by:

$$\frac{\Delta f}{f} \cong \frac{\lambda^3}{8\pi V} \tag{5.3}$$

and the relative change in volume is given by:

$$\frac{\Delta V}{V} \cong \frac{3\lambda^3}{8\pi V} \tag{5.4}$$

where V is the cavity volume and λ is the free-space wavelength.

Considering a real hatchback car geometry and approximating the car's cabin to a rectangular one with dimensions $2.21 \times 1.77 \times 1.32$ m^3, at the frequency of 5.9 GHz, the relative frequency change is in the order of $\Delta f/f \approx 10^{-6}$. This small relative frequency change yields to a completely different field structure inside the body shell. The same behavior is observed by a relative change of cavity volume of roughly 3×10^{-6}. Although numerical simulations can predict with reasonably accuracy the electromagnetic field structure at each point in space within the body shell, as seen in Fig. 5.7, the physical interpretation would be difficult and is generally meaningless. From a practical point of view, the goal is to quantify what is the probability that the performance of an antenna for a given position is degraded. Such questions are only affordable with a statistical approach.

As pointed before and shown in [105], the interior of the vehicle behaves as an electrically large, multimoded lossy cavity, also known as a mode-stirred chamber. If a large number of modes are simultaneously excited within the cavity, the amplitude probability density function (PDF) of the magnitude of the field component (electric or magnetic) in each orthogonal direction of the orthonormal basis follows a chi distribution with two degrees of freedom ([48]), and according to [94], has a Rayleigh distribution given by:

$$f\left(\left|E_{x,y,z}\right|\right) = \frac{\left|E_{x,y,z}\right|}{b^2} e^{\left[-\frac{|E_{x,y,z}|^2}{2b^2}\right]} \tag{5.5}$$

where the parameter b corresponds to the mode or most probable value of the Rayleigh distribution, which equals the standard deviation σ (square root of the variance) of the real and imaginary parts of any of the electric field components.

The magnitude of the power field components (squared magnitude) is, thus, chi-square distributed with two degrees of freedom. This corresponds to an exponential distribution, whose

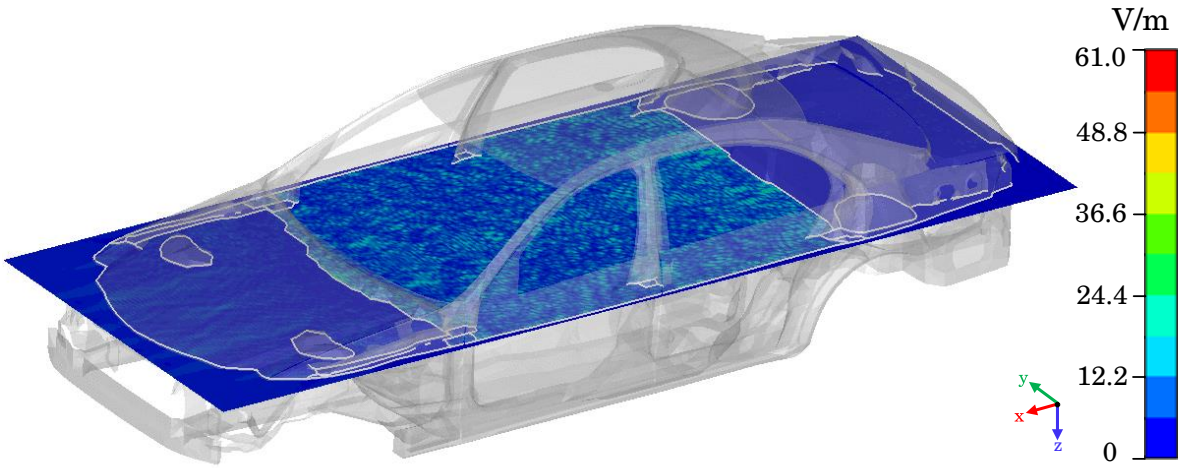

Figure 5.7: Statistical nature of electromagnetic fields inside a complex electrically large cavity for antennas placed under the roof. RMS electric field distribution of the $|E_z|$ component in a horizontal plane at half height inside the car shell.

PDF is given by [94]:

$$f\left(\left|E_{x,y,z}\right|^2\right) = \frac{1}{\mu} e^{\left[-\frac{|E_{x,y,z}|^2}{\mu}\right]} \tag{5.6}$$

where the parameter μ is the mean of an exponential distribution, and is related to the variance of the real and imaginary parts of any of the electric field components as $\mu = 2\sigma^2$.

The amplitude of the total electric field is, therefore, chi distributed with six degrees of freedom, since each of the three components of the field is chi distributed with two degrees of freedom. The PDF is given by [94]:

$$f\left(\left|\vec{E}\right|\right) = \frac{\left|\vec{E}\right|^5}{8\sigma^6} e^{\left[-\frac{|\vec{E}|^2}{2\sigma^2}\right]} \tag{5.7}$$

A chi-square distribution with six degrees of freedom is obtained for the squared magnitude of the total electric field, whose PDF can be written as follows [94]:

$$f\left(\left|\vec{E}\right|^2\right) = \frac{\left|\vec{E}\right|^4}{16\sigma^6} e^{\left[-\frac{|\vec{E}|^2}{2\sigma^2}\right]} \tag{5.8}$$

If the cavity is not electrically large enough, the insufficient modes excited change the statistical distribution of the amplitude fields from Rayleigh to a compound exponential distribution, as shown in [8].

As shown in Fig. 5.8, a normal distribution with zero mean and standard deviation $\sigma = 0.3$ is obtained for the real and imaginary parts of the E_x component. A uniform Rayleigh distribution with parameter $b = 0.3$ is obtained for the amplitude of the electric field magnitude of E_x, and

exponential distribution with parameter $\mu \approx 0.2$ for its squared magnitude. The distribution of the magnitude of the total electric field follows, as expected, a chi distribution with six degrees of freedom, being its squared magnitude chi-square distributed with six degrees of freedom. Such statistical analysis proofs that at 5.9 GHz, the body-shell of a car can be regarded as an electrically large cavity where the distributions characterizing the electromagnetic phenomena become independent of the car's details.

To compute the statistics, the electric and magnetic field was sampled in a horizontal plane inside the car shell, as illustrated in Fig. 5.7. Real and imaginary parts of the amplitude of the electric field for each component obtained from a numerical simulation performed in frequency domain were exported to Matlab® and normalized to the maximum value. The histograms were computed by means of the so-called function using a PDF normalization, where the sum of the bar areas, each of them relative to the number of observations, is less than or equal to one. In order to fit the simulated data with a suitable probability distribution, a function based on maximum likelihood estimation was used.

A centered region at half height of the car has been considered to illustrate the fields, excluding a margin of at least $\sim \lambda/4$ from the metallic enclosure of the chassis. This is due to the electromagnetic boundary conditions at the metallic walls, where tangential electric field and normal magnetic field components equal zero. In this region the statistical predictions cannot be validated, since outliers can be found, distorting the uniformity of the statistical distribution. The same statistical behavior of the field can be observed at any point inside the cabin of the car at the frequencies of interest, independently of position.

Measurements of the spatial distribution of electromagnetic fields inside the car body can be difficult to perform due to probe disturbances when scanning the fields. Numerical simulation techniques can be used to obtain detailed field distributions. As a drawback, they consume a significant amount of computational resources and the use of acceleration devices as graphical processing units (GPU) or by means of Message Passing Interface (MPI) become almost mandatory.

Other scenarios which resembles that of an inside of a car, where statistical theory has been used successfully, are buildings and aircrafts where wireless communications are required, as those described in [99, 132]. Alternative approaches like the power balance method [49] could also be used to make statistics of the electromagnetic phenomena taking place inside such complex cavities.

5.1.2.2 Wave Propagation Through the Windows. Effect of Laminated Glass

Referring to Fig. 5.1, the only way that have the electromagnetic wave to radiate outwards is through the windows of the car. Although many apertures can be found in the metal chassis of a car, most of them are electrically small, so that the wave can not pass through. Typical electrical dimensions at 5.9 GHz of windscreens of passenger cars are on the order of 18x24 λ^2, about

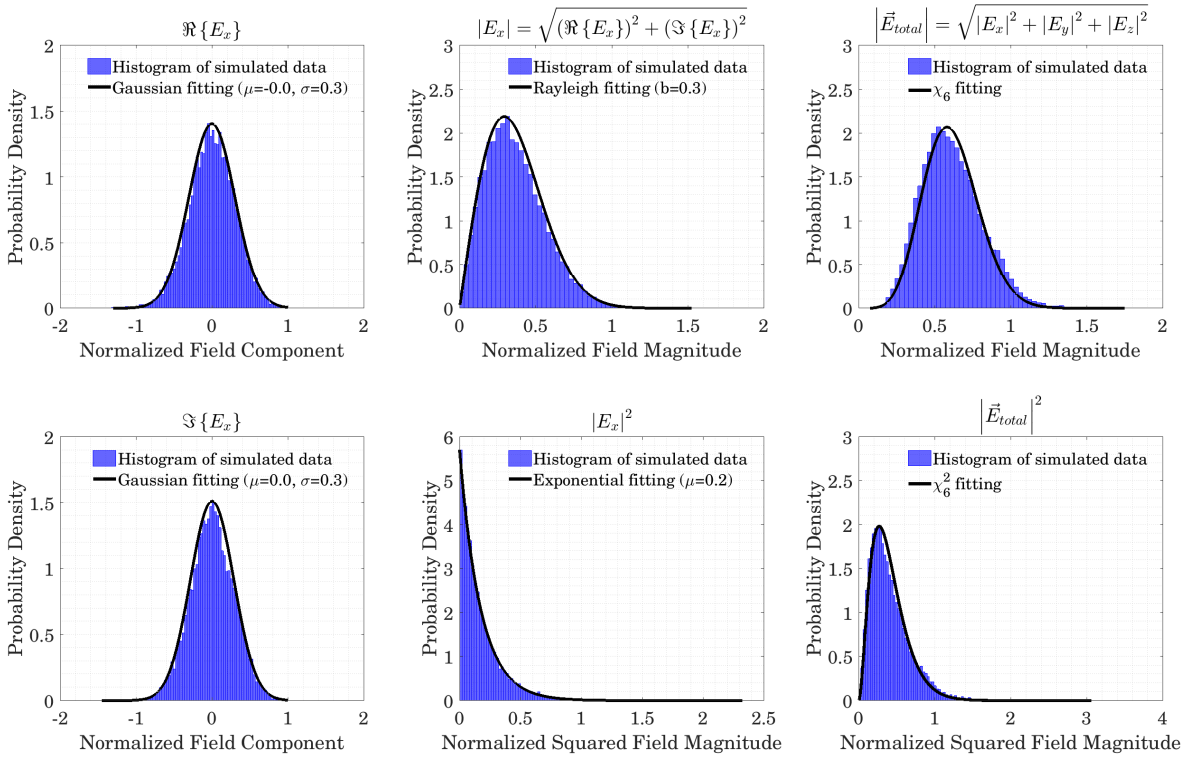

Figure 5.8: Statistical distributions of normalized electric fields inside the body shell of a car. PDF of the real and imaginary parts of the normalized electric field E_x component (top and bottom left) are Gaussian distributed. PDF of the magnitude of the electric field component E_x (top, middle) is Rayleigh distributed. PDF of the squared magnitude of the electric field component E_x (bottom, middle) is exponential distributed. PDF of the magnitude of the total electric field (top, right) is chi distributed with 6 degrees of freedom. PDF of the squared magnitude of the total electric field (bottom, right) is chi-square distributed with 6 degrees of freedom.

14x23 λ^2 for the rear screen, and roughly 9x17 λ^2 for each side window. Since the aperture theory categorizes the cases depending on the aperture dimensions compared to the wavelength, it has been first determined if the car windows can be treated as electrically large apertures for the frequencies of interest.

The total power transmitted through the windows can be computed as the product of the power density per unit area of the incoming wave, the area of the window aperture, and the transmission coefficient of the aperture:

$$P_t(f) = T_{aperture}(f) \cdot S_i(f) \cdot A \tag{5.9}$$

Solving the equation for the transmission coefficient:

$$T_{aperture}(f) = \frac{P_t(f)}{S_i(f) \cdot A} \tag{5.10}$$

where it can be seen its dependence with frequency, aperture geometry, angle of incidence and polarization of the incoming wave. Although car windows can take arbitrary shapes, even slightly curved, a good approximation could be a flat rectangular aperture, for which a transmission coefficient of electromagnetic waves is well known. In [65] a formula to estimate the transmission coefficient of a rectangular aperture under uniform and normal incidence is given. The formula is derived by means of Kirchhoff's boundary values and the diffraction pattern as a function of the spherical coordinates of a plane wave impinging normally on a rectangular aperture with sides a and b:

$$T_{aperture}\left(\frac{a}{\lambda},\frac{b}{\lambda}\right)=\frac{4ab}{\lambda^2}\int_0^{\frac{\pi}{2}}\int_0^{\frac{\pi}{2}}\left[\frac{\sin\left(\frac{a\pi}{\lambda}\cdot\sin\theta\cdot\cos\phi\right)}{\frac{a\pi}{\lambda}\cdot\sin\theta\cdot\cos\phi}\cdot\frac{\sin\left(\frac{b\pi}{\lambda}\cdot\sin\theta\cdot\sin\phi\right)}{\frac{b\pi}{\lambda}\cdot\sin\theta\cdot\sin\phi}\right]^2\cdot\sin\theta d\theta d\phi \tag{5.11}$$

In Figure 5.9 the transmission coefficient according to equation 5.11 as a function of the electrical dimensions of the window is computed in two- and three-dimensional form, showing the convergence to unity as the electrical dimensions increase.

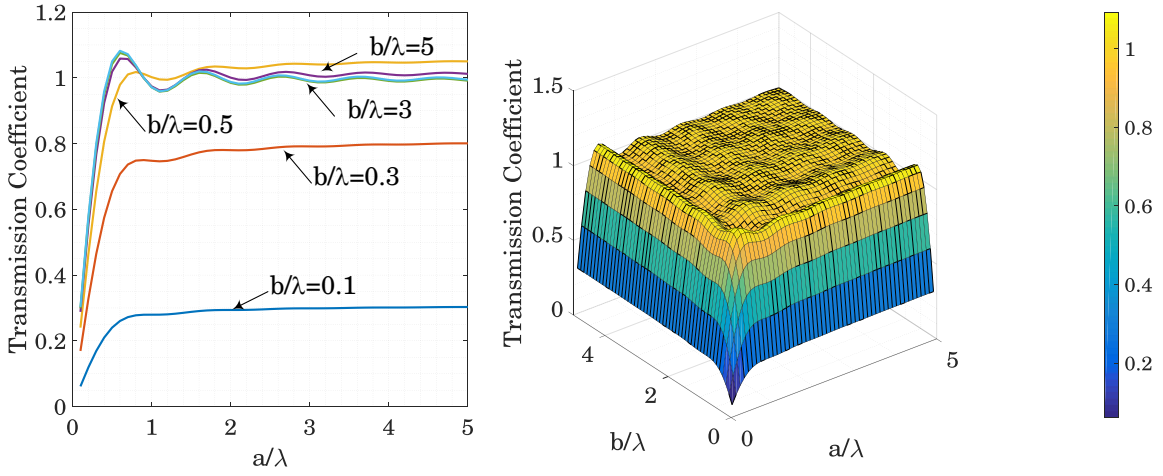

Figure 5.9: The transmission coefficient through the windows of the car, approximated by a rectangular large aperture computed from equation 5.11 in a cartesian plot (left) as a function of the electrical dimensions of the aperture (a/λ, b/λ), and in the form of a surface three-dimensional plot (right).

Writing equation 5.11 as a function of frequency ($f = c/\lambda$) and plotting the rectangular aperture transmission coefficient over frequency, it can be inferred the convergence to unity as the frequency increases, indicating that the windows of the car can be treated as electrically large apertures in the V2X frequency range. Thus, the power transmitted through the windows depends only on the power density S_i incident on the aperture, the angle of incidence θ^i, and the window area A. Using the geometrical optics approximation, the power transmitted through the car windows can be written as:

$$P_t=\sigma_t\cdot S_i=A\cdot\cos\theta^i\cdot S_i \tag{5.12}$$

showing that the transmission coefficient is now independent of frequency, polarization, and azimuth angle of the incident field.

The windshield and/or rear window of a car is of the laminate window type, as shown in Fig. 5.10. They are composed of an external layer of glass with 3 mm thickness, dielectric permittivity ε_r=6.9, and electrical conductivity σ=5 × 10^{-4} S m^{-1}, an intermediate layer of 0.76 mm thickness, which is a thermoplastic adhesive of the polyvinyl butyryl (PVB) type with ε_r=2.9 and tanδ=0.05, and an internal sheet of glass with the same dielectric properties as the external one and again with 3 mm thickness [63], whose normal component points through the inside of the vehicle. The side windows are composed of a layer of glass with 3 mm thickness and the same dielectric properties as in the windshield or rear window.

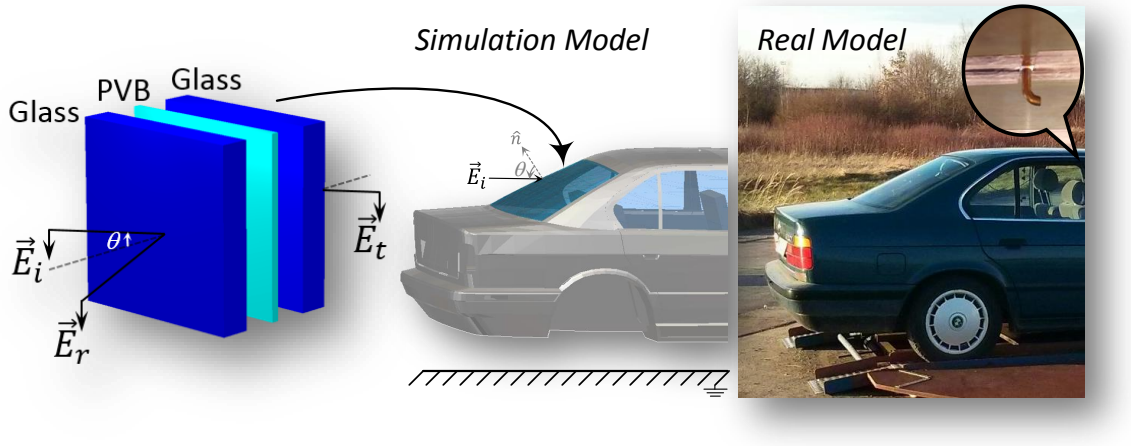

Figure 5.10: Exploded view of a laminate window of a car (left), the simulation model of a car (middle), and its corresponding real prototype (right) with a zoom in at the antenna positioned underneath the roof of the car.

The laminated glass let be modeled by multiple cascaded equivalent transmission lines, with their respective propagation constants and characteristic impedances, due to the affinity of the transverse field components in low loss media to the transmission line equations.

It has been considered N=3 dielectric slabs, corresponding to the external and internal glass and the PVB intermediate layer, $N+1$ interfaces, and $N+2$ dielectric media, including the semi-infinite media of the interior and exterior of the car n_0 and n_{N+1}, both assumed to be air (n_0=n_{N+1}=1). Since the antenna inside the car is operating in a linear medium with linear materials, the reciprocity theorem can be applied. From this point on, it is considered the case where the wave, coming from the antenna placed inside the car, hits the interior of the glass. Referring to the windscreen of Fig. 5.1, the incident and reflected fields are considered at the left of each interface. There are no incident fields from the exterior of the car, so that the outer half space is assumed to be matched.

The overall transmission and reflection coefficients of the lossy multilayer structure can be computed with the aid of the transmission line transfer matrix method. Unlike a single interface, in a stratified medium the reflection in each layer is also partially transmitted and again partially reflected inside the same layer. The method makes use of the Fresnel equations for a single interface and the continuity condition for the electric field across boundaries, to compute in a 2×2 matrix expansion the infinite number of reflections (matching matrix) while taking into account the propagation path length (propagation matrix), as will be discussed later.

Fields Across a Single Glass Slab (Side Windows)

In order to characterize the nature of the wave impinging at the internal glass of the car (interface i=1), the Fresnel equations in the specific situation where the radiator is hidden under the middle of the car's roof have been derived. Referring to Fig. 5.1, and considering that the electrical distance between the antenna and the glass at 5.9 GHz is large enough, so that farfield conditions can be assumed, a linearly polarized plane wave travelling through the air (with wavenumber k_0) parallel to the incident plane (oblique incidence) impinges on a no magnetic dielectric medium (glass, with wavenumber k_1). The electric and magnetic field related to the incident, reflected and transmitted wave is given by:

$$\vec{E}_i(\vec{r}) = E_{0i}(\cos\theta_i \hat{y} - \sin\theta_i \hat{z}) e^{-jk_0(\sin\theta_i y + \cos\theta_i z)} \tag{5.13a}$$

$$\vec{E}_r(\vec{r}) = E_{0r}(\cos\theta_r \hat{y} + \sin\theta_r \hat{z}) e^{-jk_0(\sin\theta_r y - \cos\theta_r z)} \tag{5.13b}$$

$$\vec{E}_t(\vec{r}) = E_{0t}(\cos\theta_t \hat{y} - \sin\theta_t \hat{z}) e^{-jk_1(\sin\theta_t y + \cos\theta_t z)} \tag{5.13c}$$

and for the magnetic field

$$\vec{H}_i(\vec{r}) = \frac{1}{\eta_0}\hat{k}_i \times \vec{E}_i = -\frac{E_{0i}}{\eta_0}\hat{x} e^{-jk_0(\sin\theta_i y + \cos\theta_i z)} \tag{5.14a}$$

$$\vec{H}_r(\vec{r}) = \frac{1}{\eta_0}\hat{k}_r \times \vec{E}_r = \frac{E_{0r}}{\eta_0}\hat{x} e^{-jk_0(\sin\theta_r y - \cos\theta_r z)} \tag{5.14b}$$

$$\vec{H}_t(\vec{r}) = \frac{1}{\eta_1}\hat{k}_t \times \vec{E}_t = -\frac{E_{0t}}{\eta_1}\hat{x} e^{-jk_1(\sin\theta_t y + \cos\theta_t z)} \tag{5.14c}$$

The tangential components for the electric and magnetic fields at the interface between air and glass are the component along the Y axis and X axis respectively. If the appropriate boundary conditions for the tangential components at the interface (plane Z=0) are applied (continuity across the two sides of the interface), and taking into account that there are no free charges in a dielectric medium:

$$\hat{n} \times \left(\vec{E}_1 - \vec{E}_0\right)_{|S} = 0 \Rightarrow \left(E_{iy} + E_{ry}\right)_{|z=0} = E_{ty}{}_{|z=0} \tag{5.15a}$$

$$\hat{n} \times \left(\vec{H}_1 - \vec{H}_0\right)_{|S} = 0 \Rightarrow \left(H_{ix} + H_{rx}\right)_{|z=0} = H_{tx}{}_{|z=0} \tag{5.15b}$$

applying the boundary conditions to the electric field

$$E_{0i}\cos\theta_i e^{-jk_0\sin\theta_i y} + E_{0r}\cos\theta_r e^{-jk_0\sin\theta_r y} = E_{0t}\cos\theta_t e^{-jk_1\sin\theta_t y} \tag{5.16a}$$

as well as for the magnetic field

$$-\frac{E_{0i}}{\eta_0}e^{-jk_0\sin\theta_i y}+\frac{E_{0r}}{\eta_0}e^{-jk_0\sin\theta_r y}=-\frac{E_{0t}}{\eta_1}e^{-jk_1\sin\theta_t y} \tag{5.16b}$$

The exponential terms can be removed with the aid of the second and third Snell's laws:

$$\theta_r=\theta_i \tag{5.17}$$

$$k_0\sin\theta_i=k_1\sin\theta_t\equiv n_0\sin\theta_i=n_1\sin\theta_t \tag{5.18}$$

leading to the following linear system of equations

$$\begin{cases}(E_{0i}+E_{0r})\cos\theta_i=E_{0t}\cos\theta_t\\ \dfrac{E_{0i}-E_{0r}}{\eta_0}=\dfrac{E_{0t}}{\eta_1}\end{cases} \tag{5.19}$$

Solving the system of equations in terms of E_{0i} the Fresnel equations of reflection and refraction are obtained:

$$E_{0r}=\frac{\eta_1\cos\theta_t-\eta_0\cos\theta_i}{\eta_1\cos\theta_t+\eta_0\cos\theta_i}E_{0i} \tag{5.20}$$

$$E_{0t}=\frac{2\eta_1\cos\theta_i}{\eta_1\cos\theta_t+\eta_0\cos\theta_i}E_{0i} \tag{5.21}$$

Writing (5.20) and (5.21) as a function of the reflection and transmission coefficients:

$$E_{0r}=\rho E_{0i} \tag{5.22}$$

$$E_{0t}=\tau E_{0i} \tag{5.23}$$

so that,

$$\rho=\frac{\eta_1\cos\theta_t-\eta_0\cos\theta_i}{\eta_1\cos\theta_t+\eta_0\cos\theta_i} \tag{5.24}$$

$$\tau=\frac{2\eta_1\cos\theta_i}{\eta_1\cos\theta_t+\eta_0\cos\theta_i} \tag{5.25}$$

Fields in a Laminated Glass (Windscreen)

The transmission line transfer matrix method is used to derive the transmittance and reflectance through a windscreen consisting of a laminated glass as decribed at the beginning of this section. Referring to Fig. 5.11, the tangential components of the total fields from the left

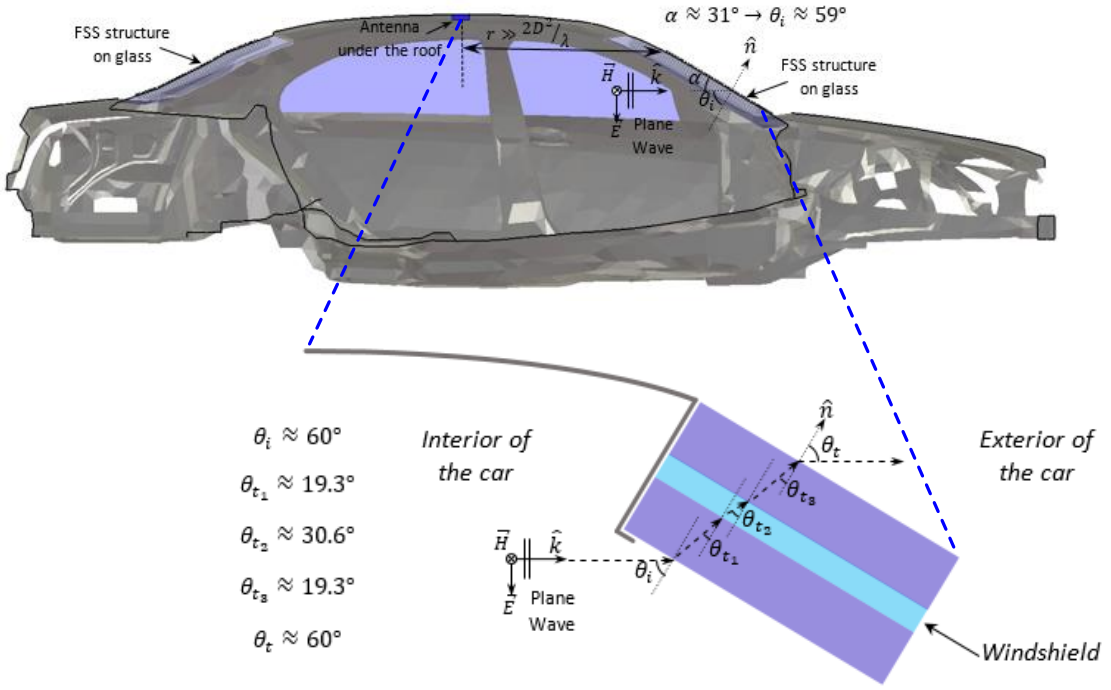

Figure 5.11: Definition of angles for computing the transmittance and reflectance through a windscreen of a car.

of the interface can be expressed in terms of the corresponding forward (+) and backward (−) electric fields at the boundary between two different mediums (plane Z=0):

$$\vec{E}(\vec{r}) = E_{0+}\cos\theta_+ \hat{y} e^{-jk\sin\theta_+ y} + E_{0-}\cos\theta_- \hat{y} e^{-jk\sin\theta_- y} \tag{5.26}$$

$$\vec{H}(\vec{r}) = -\frac{E_{0+}}{\eta}\hat{x} e^{-jk\sin\theta_+ y} + \frac{E_{0-}}{\eta}\hat{x} e^{-jk\sin\theta_- y} \tag{5.27}$$

Applying the second Snell's law ($\theta_- = \theta_+$) and taking the absolute value

$$E = (E_{0+} + E_{0-})\cos\theta_+ \tag{5.28}$$

$$H = \frac{E_{0+} - E_{0-}}{\eta} \tag{5.29}$$

and now expressed in matrix form

$$\begin{pmatrix} E \\ H \end{pmatrix} = \begin{pmatrix} \cos\theta_+ & \cos\theta_+ \\ \frac{1}{\eta} & -\frac{1}{\eta} \end{pmatrix} \cdot \begin{pmatrix} E_{0+} \\ E_{0-} \end{pmatrix} \tag{5.30}$$

To find the matching matrix, which relates the fields on either sides of the interface to each other, is more convinient to express (5.30) in terms of E and H

$$\begin{pmatrix} E_{0+} \\ E_{0-} \end{pmatrix} = \frac{1}{2}\begin{pmatrix} \frac{1}{\cos\theta_+} & \eta \\ \frac{1}{\cos\theta_+} & -\eta \end{pmatrix} \cdot \begin{pmatrix} E \\ H \end{pmatrix} \tag{5.31}$$

and then apply the continuity boundary condition of the tangential fields across the interface

$$\begin{pmatrix} E \\ H \end{pmatrix} = \begin{pmatrix} E' \\ H' \end{pmatrix} \tag{5.32}$$

leading to

$$\begin{pmatrix} E_{0+} \\ E_{0-} \end{pmatrix} = \frac{1}{2} \begin{pmatrix} \frac{1}{\cos\theta_+} & \eta \\ \frac{1}{\cos\theta_+} & -\eta \end{pmatrix} \cdot \begin{pmatrix} \cos\theta'_+ & \cos\theta'_+ \\ \frac{1}{\eta'} & -\frac{1}{\eta'} \end{pmatrix} \cdot \begin{pmatrix} E'_{0+} \\ E'_{0-} \end{pmatrix} \tag{5.33}$$

Multiplying the matrices and using (5.24) and (5.25), the matching matrix at the interface k is obtained as a function of the reflection (ρ) and transmission (τ) coefficients

$$\begin{pmatrix} E_{0+} \\ E_{0-} \end{pmatrix} = \frac{1}{\tau_k} \begin{pmatrix} 1 & \rho_k \\ \rho_k & 1 \end{pmatrix} \cdot \begin{pmatrix} E'_{0+} \\ E'_{0-} \end{pmatrix} \tag{5.34}$$

where

$$\rho_k = \frac{n_{k-1}\cos\theta_k - n_k\cos\theta_{k-1}}{n_{k-1}\cos\theta_k + n_k\cos\theta_{k-1}} \tag{5.35}$$

$$\tau_k = \left(1+\rho_k\right)\frac{\cos\theta_{k-1}}{\cos\theta_k} \tag{5.36}$$

being $1 \le k \le N+1$ the interface's number.

Now the fields at the right of an interface have been related to the fields at the left of the next interface, to account for the propagation of the wave through a given medium of thickness l_i, being $0 \le i \le N+1$ the medium's number. For the forward and backward waves in medium $i = 1$

$$E'_{0+} = e^{jk_{z1}l_1}E_{1+} \tag{5.37}$$

$$E'_{0-} = e^{-jk_{z1}l_1}E_{1-} \tag{5.38}$$

which expressed in matrix form yields to

$$\begin{pmatrix} E'_{0+} \\ E'_{0-} \end{pmatrix} = \begin{pmatrix} e^{jk_{z1}l_1} & 0 \\ 0 & e^{-jk_{z1}l_1} \end{pmatrix} \cdot \begin{pmatrix} E_{1+} \\ E_{1-} \end{pmatrix} \tag{5.39}$$

known as the propagation matrix, where the complex phase thickness is given by

$$k_{zi}l_i = k_0 n_i \cos\theta_i l_i \tag{5.40}$$

being

$$k_0 = \frac{\omega}{c_0} = \frac{2\pi f}{c_0} \tag{5.41}$$

the free-space wavenumber.

Rewriting the term $\cos\theta_i$ with the aid of the third Snell's law, for $0 \le i \le N+1$

$$\cos\theta_i = \sqrt{1-\sin^2\theta_i} = \sqrt{1-\frac{n_0^2\sin^2\theta_0}{n_i^2}} \tag{5.42}$$

so that:

$$k_{zi}l_i = \frac{2\pi f}{c_0} l_i n_i \sqrt{1-\frac{n_0^2\sin^2\theta_0}{n_i^2}} \tag{5.43}$$

Writing $c_0 = f_0\lambda_0$, the complex phase thickness $k_{zi}l_i$ can be expressed in terms of the normalized frequency f/f_0 and physical length l_i/λ_0

$$k_{zi}l_i = 2\pi\frac{f}{f_0}\frac{l_i}{\lambda_0}\sqrt{n_i^2 - n_0^2\sin^2\theta_0}, \qquad \text{for } 0 \le i \le N+1 \tag{5.44}$$

where the refractive index n_i is generally a complex number given by

$$n_i = \sqrt{\varepsilon_i(\omega)} = \sqrt{\varepsilon'_i(\omega) - j\varepsilon''_i(\omega)} = \sqrt{\varepsilon'_i(\omega)[1-j\tan(\delta_i(\omega))]} = \sqrt{\varepsilon_r - j\frac{\sigma}{\omega\varepsilon_0}} \tag{5.45}$$

being ε_r the dielectric permittivity, and where the losses can be expressed with a loss tangent $\tan(\delta_i)$ or an electrical conductivity σ.

The combination of a matching and a propagation matrix leads to the well known transfer matrix, relating the fields across different interfaces and mediums. Considering now a laminated glass of a car as decribed before, with $N = 3$ layers, the equation relating the fields inside and outside the car can be obtained. Assuming that the outer half space is matched ($E'_{5-} = 0$), and generalizing (5.34) and (5.39):

$$\begin{pmatrix} E_{1+} \\ E_{1-} \end{pmatrix} = \left[\prod_{i=1}^{i=N+1} \frac{1}{\tau_i} \cdot \begin{pmatrix} 1 & \rho_i \\ \rho_i & 1 \end{pmatrix} \cdot \begin{pmatrix} e^{jk_{zi}l_i} & 0 \\ 0 & e^{-jk_{zi}l_i} \end{pmatrix} \right] \cdot \begin{pmatrix} E'_{5+} \\ 0 \end{pmatrix} \tag{5.46}$$

The reflection and transmission coefficient respectively can now be computed from (5.46) as follows:

$$\rho = \frac{E_{1-}}{E_{1+}} \tag{5.47}$$

$$\tau = \frac{E'_{5+}}{E_{1+}} \tag{5.48}$$

which can be expressed more convinient as a reflectance R and transmittance T respectively as follows:

$$R = |\rho|^2 \tag{5.49}$$

$$T = 1 - |\rho|^2 = \frac{n_{N+1}}{n_0}|\tau|^2 \tag{5.50}$$

In order to corroborate the theory results, the equations are programmed in Matlab® and compared with the results provided from a full wave simulation using the Finite Element Method (FEM), periodic boundary conditions and Floquet-mode ports to account for the polarization and the mode type of the incoming wave. Figure 5.12 shows the simulated results (points) together with the theoretical computations (solid lines) obtained from the above equations. As can be seen, an excellent agreement is obtained, validating thus simulations and the theoretical hypothesis to explain the wave propagation phenomena through the laminated glass of a windshield of a car.

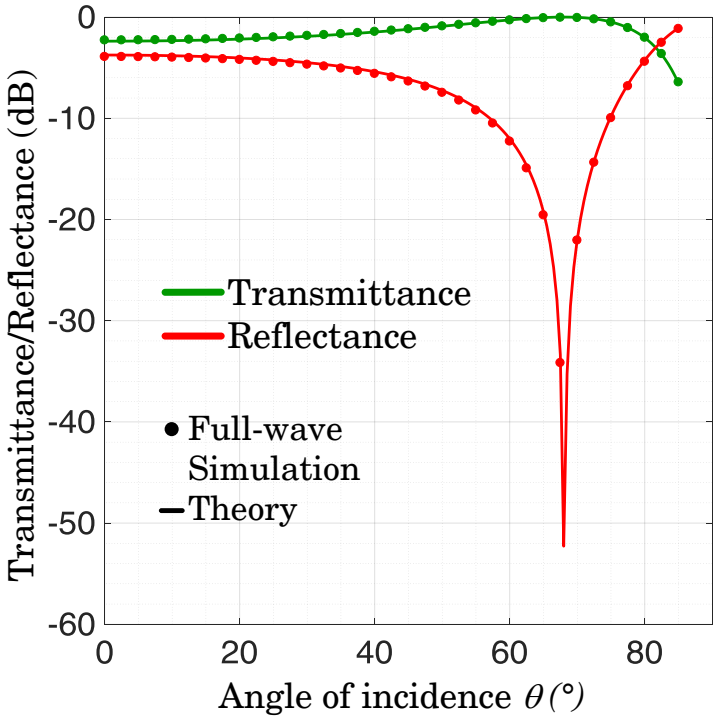

Figure 5.12: Transmittance (green) and reflectance (red) through a windscreen of a car computed by means of full-wave simulations (points) and theoretical equations (solid line) based on the transmission line transfer matrix method.

The angle α formed by the windscreen with respect to the roof of the car can be extracted from the CAD model and it is found to be $\alpha \simeq 31°$ (see Fig. 5.11), which means an incoming angle for the main beam of $\theta_i \simeq 59°$. Assuming that the distance between the source of radiation and the windscreen is large enough ($> 2D^2/\lambda$), the wave hitting the windscreen can be treated as a plane wave.

As can be inferred from Fig. 5.12, very good transmission properties are obtained close to an incidence angle θ_i of approximately 68°, which according to Fig. 5.11, this angle would be close to the angle of incidence of a plane wave coming from an antenna placed underneath the roof. Looking closer, the losses introduced by the laminated glass for a plane wave with an angle of incidence $\theta_i \simeq 68°$ are less than 1 dB. This angle with specially good transmission

properties corresponds to the Brewster's angle given by $\theta_i = \arctan(n_2/n_1)$, where n_1 and n_2 are the refractive index of air ($n_1 = 1$) and glass ($n_2 = \sqrt{\varepsilon_{r_{glass}}}$), respectively. However, inside the cabin of a car the situation is more complex. Multipath propagation yields to incident rays on the glass coming from all angles. The laminated glass reflects a significant part of the transmitted power at angles of incidence smaller than 55° and greater than 75°.

Nowadays, an ever-increasing number of automobiles are equipped with solar control or energy saving glasses, which add a transparent electrically conducting layer to the commonly used laminated glass to selectively reflect the heat-causing infrared (IR) radiation (wavelengths between 780 and 2500 nm), block the ultraviolet (UV) rays present in sunlight (wavelengths between 100 and 380 nm), while making possible viewing through the window. Such metal-coated glasses keep a constant temperature in the inside of the car both in summer and in winter, reducing the fuel consumption to maintain a desired temperature, but they have the main drawback that they not allow microwave radiation to pass through.

A transparent metal-coated sheet with a relatively small electrical resistance of typically 4 Ω is attached to the laminated glass, between layers as shown in Fig. 5.13 or at the outside part of the glass, making possible to reflect the IR radiation while keeping a clear visibility. Actually, the car's manufacturers leave always a margin uncoated around the windscreen and rear window, the so-called frit, which is a black painted enamel band. It is usually used to place other antennas or electronic sensors which need electromagnetically transparent visibility to let the waves pass through.

Figure 5.13 shows how the microwave propagation properties deteriorate in the presence of energy saving glasses with regard to the properties of the laminated glass windows shown in Fig. 5.12. An example of radiation pattern in azimuth of an antenna placed underneath the middle of the car's roof equipped with laminated glass and energy saving glass with an uncoated area surrounding the window (frit) is shown in Fig. 5.14. It can be seen how deep nulls of up to about 15 dB appear in driving and opposite direction with regard to the case without metal coating. This fact would prevent the antennas from being placed under the roof of the car without modifying the energy saving glass in any way.

In order to improve the transmission properties of such electrical insulation at microwave frequencies without overly compromising the thermal and visual characteristics, a frequency selective surface (FSS) in the metal coating in the form of thin slots is proposed. The radiation coming from or going to the antenna hidden inside the car is absorbed by the metal coating and retransmitted by the slots which act as antennas. This concept will be dealt with in detail later on.

5.1.3 Statistical Nature of Radiation Pattern of Antennas Under the Roof

As shown in section 5.1.2, antenna systems placed within the car's cabin should be evaluated in a statistical manner, since complex cavity geometries, like the chassis of a car, can generate

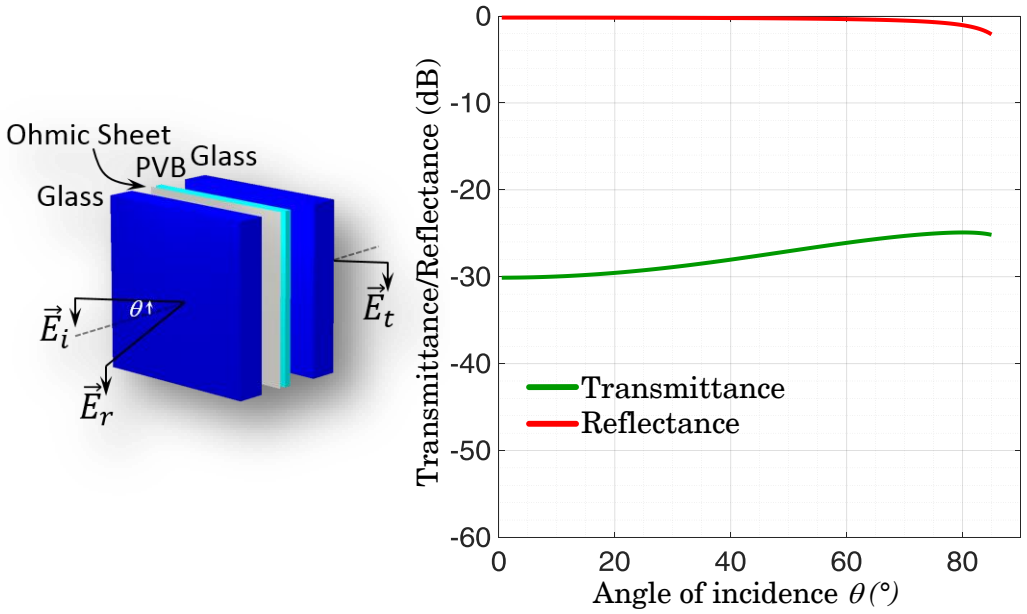

Figure 5.13: Transmittance (green) and reflectance (red) through a windscreen of a car provided with energy saving glass. Computations are performed by means of full-wave methods considering a resistive sheet of about $4\Omega/sq$.

ray chaos. Although one does not expect a chaotic behavior from antennas placed inside a linear medium, where Maxwell's equations are still linear equations, even with homogeneous refractive index, chaotic behavior can be visualized through reflections at the boundaries of the vehicle body at the limit where the frequency approaches infinity (zero wavelength). As long as the dimensions of the car are large with regard to the wavelength (high operating frequency), ray chaos is observed as suggested by the sensitivity of the electromagnetic fields to a small change in frequency or volume of the car.

5.1.3.1 Open Circuit Voltage at Antenna Terminals and Power Received by Antennas Within the Car

Inside an automobile, a vast amount of scatterers can be found in the form of sharp edges, corners, curved and rough surfaces, and single and multi-layered materials with different dielectric properties. Thus, the electromagnetic wave must overcome different propagation phenomena before reaching the receiving antenna[1], leading to multipath propagation, shadowing effects, and depolarization of the incoming wave. Propagation phenomena like reflections on the metal chassis, coated and layered glass; refractions through the glass windows; diffractions on sharp

[1]In the following, the AUT is considered in receiving mode. However, from the principle of reciprocity for antennas operating in a linear medium made of linear materials, in its transmitting mode, the same properties are expected than considering the antenna in its receiving mode.

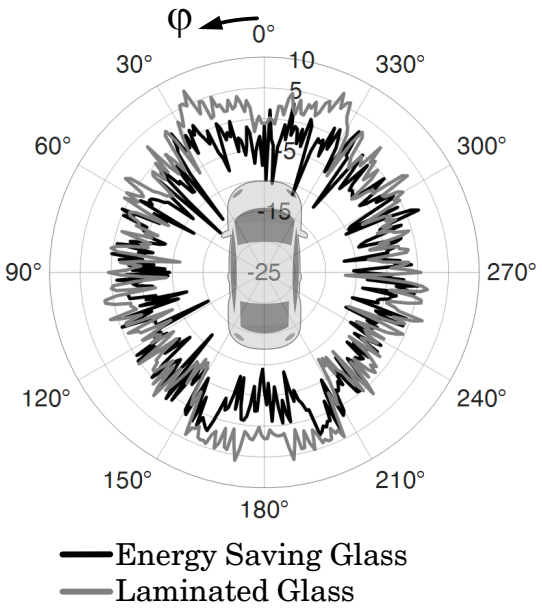

Figure 5.14: Radiation pattern in azimuth (θ =90°, φ) at 5.9 GHz showing the range degradation with a windscreen and rear window provided with energy saving glass with an uncoated area surrounding the window (frit).

edges, corners and curved surfaces; and scattering from rough and complex-shaped surfaces can be found. At each azimuth angle at the receiving antenna, the resulting radiation pattern is the combination of several waves with different amplitudes, phases and polarizations weighted with the radiation pattern produced by the same antenna in free space. The scenario can be addressed with the random plane wave model, which is based on the superposition of a large number of plane waves with random arrival directions, phases, and polarizations, and agrees with the ray chaos theory that characterize the interior of the body-shell of a vehicle.

It is not intended to exactly analyze the multipath problem inside the car, which although it is an awesome and challenging task, lacks practical interest. Conversely, the goal is to get a statistical description of the propagation phenomena by reducing the problem to a simple form, in order to get understanding of the radiation characteristics of antennas placed underneath the roof of the car.

To characterize the radiation pattern in a hidden position underneath the roof of the car, let us first consider a single vertically polarized quarter-wave monopole on a finite curved perfectly conducting concave surface, which represents a first order approximation of locating the antenna underneath the finite roof of the car. In Chapter 2, where antennas were placed on top of the roof, a first order approximation was given by a radiator on a curved perfectly conducting convex surface terminated abruptly due to its finite dimensions. Besides the launching coefficients for the creeping waves (CW) following geodesic paths along the convex surface according to Fermat's

principle and losing energy at each diffraction point, the diffraction coefficients for edge-diffracted rays at the boundaries of the roof were also considered. Contrary to Chapters 2 and 3, the actual problem deals with a curved conducting concave surface, and the whispering gallery (WG) modes should be considered. At the edges of the roof, the incident whispering gallery mode undergoes diffraction, whose coefficients can be calculated according to [52]. The asymptotic approximation in the high frequency limit $ka \gg 1$, where $k = 2\pi/\lambda$ is the wave number (λ is the operating wavelength) and a the radius of curvature reduces to the classical coefficients given by GTD and previously derived in Chapter 2.

Let us denote the normalized complex vector radiation pattern by $\underline{\mathbf{C}}$ in a spherical coordinate system (r,θ,φ) defined in the conventional way relative to the cartesian system. According to [41], $\underline{\mathbf{C}}$ is thus given by

$$\underline{\mathbf{C}}(\theta,\varphi) = \left.\frac{\underline{\mathbf{E}}(r,\theta,\varphi)\, e^{jkr}}{\left|\underline{\mathbf{E}}(r,\theta,\varphi)\right|_{max}}\right|_{r=cte\to\infty} = \underline{C}_{\theta}(\theta,\varphi)\,\mathbf{e}_{\theta} + \underline{C}_{\varphi}(\theta,\varphi)\,\mathbf{e}_{\varphi} \tag{5.51}$$

where

$$\underline{C}_{\theta,\varphi}(\theta,\varphi) = \left.\frac{\underline{E}_{\theta,\varphi}(r,\theta,\varphi)\, e^{jkr}}{\left|\underline{\mathbf{E}}(r,\theta,\varphi)\right|_{max}}\right|_{r=cte\to\infty} \in \mathbb{C}. \tag{5.52}$$

In equation (5.51), $\underline{\mathbf{E}}(r,\theta,\varphi)$ is the radiated electric field complex vector, $\left|\underline{\mathbf{E}}(r,\theta,\varphi)\right|_{max}$ the maximum absolute value of the radiated electric field vector, k the wave number, $\mathbf{e}_{\theta}$ and $\mathbf{e}_{\varphi}$ are the spherical unit basis vectors, and $\underline{C}_{\theta,\varphi}(\theta,\varphi)$ the θ- or φ-component of the normalized complex radiation pattern. In equation (5.52), $\underline{E}_{\theta,\varphi}(r,\theta,\varphi)$ are the θ- or φ-component of the radiated complex electric field. The reference phase at the antenna port is set to zero without loss of generality. Both, absolute value and phase of the normalized far-field radiation pattern $\underline{\mathbf{C}}(\theta,\varphi)$ are independent of the distance r from the antenna for $r \geq 2D^2/\lambda$, where D is the largest dimension of the antenna[2].

The normalized complex vector radiation pattern $\underline{\mathbf{C}}(\theta,\varphi)$ defined in equation (5.51) contains all the information regarding absolute value, phase, and polarization considering far-field conditions. From equation (5.51), the scalar normalized radiation pattern can be written as

$$C(\theta,\varphi) = \left|\underline{\mathbf{C}}(\theta,\varphi)\right| = \sqrt{\left|\underline{C}_{\theta}(\theta,\varphi)\right|^2 + \left|\underline{C}_{\varphi}(\theta,\varphi)\right|^2} \in \mathbb{R}. \tag{5.53}$$

Usually, the gain is a more useful parameter describing the performance of the antenna. It is defined as the ratio of the intensity in a given direction (θ,φ), to the radiation intensity obtained if the accepted power by the antenna were radiated isotropically, which according to equation (5.53) can be written as

$$G(\theta,\varphi) = G_{\theta}(\theta,\varphi) + G_{\varphi}(\theta,\varphi) = C^2(\theta,\varphi)\cdot G \tag{5.54}$$

[2]The value $r = 2D^2/\lambda$ corresponds to the boundary between the radiating near-field (Fresnel) region and the far-field (Fraunhofer) region of the antenna to obtain a maximum phase error of $\pi/8$. To be valid, D must also be large compared to the wavelength λ. Thus, the radiation pattern in the far-field region depends only on the angles θ and φ, since the radial field component can be neglected and the radiated field components are essentially transverse [12].

where

$$G_{\theta,\varphi}(\theta,\varphi) = \left|\underline{C}_{\theta,\varphi}(\theta,\varphi)\right|^2 \cdot G \tag{5.55}$$

are the linearly polarized orthogonal θ- and φ-components, and G is the maximum gain related to the far-zone electric field of the antenna by

$$G = \epsilon_{rad} \cdot 4\pi r^2 \cdot \left.\frac{\left|\underline{\mathbf{E}}(r,\theta,\varphi)\right|^2_{max}}{2\eta P_{rad}}\right|_{r=cte\to\infty} \in \mathbb{R}. \tag{5.56}$$

In equation (5.56), ϵ_{rad} (dimensionless) $\in [0,1]$ is the radiation efficiency of the antenna considering only the conduction and dielectric efficiency but not the reflection (mismatch) efficiency, according to the IEEE definition of gain[3] [1], η the characteristic or intrinsic impedance of vacuum ($\eta = 120\pi\ \Omega$), and P_{rad} the total radiated power by the antenna.

The roof of a typical sedan-type car at V2X frequencies involves dimensions of the roof which are much greater than the wavelength. At 5.9 GHz, the operating wavelength λ is about 5 cm, so that the roof is equivalent to a surface of about $30 \times 23\lambda^2$. Therefore, high-frequency asymptotic techniques based on ray-tracing theory can be used to give an expression of the fields. The radiated fields $\underline{E}_{\theta,\varphi}$ considering far-field conditions can be expressed in analytical form by means of the Geometrical/Uniform Theory of Diffraction (GTD/UTD) [96]. GTD takes into account the diffracted fields at the edges of the finite conducting surface and UTD obtains accurate enough results at the shadow boundaries present in curved surfaces, as already discussed in Chapter 2.

Considering the centered location of the monopole, the divergence of rays in azimuth can be neglected and only a ripple can be observed in elevation, keeping almost unchanged the round shape diagram in the azimuth plane typical of a monopole over an infinitely large ground plane.

As long as the pillars and other parts of the car are added, the radiation pattern of the antenna is being distorted due to shadowing effects and multiple reflections and diffractions, spreading out the radiated fields in elevation to a great extent, even at low elevation angles where the amplitude of radiation pattern is no longer negligible.

The whole vehicle body acts as an overmoded electrically large metal cavity (lossy) with electrically large apertures (windows), leading to a complex resonant structure which diffuses the radiated field in all directions, as inferred from Fig. 5.15 [21]. The strong ripple induced in the far-field pattern and the randomness of the problem make it suitable to be treated with a statistical approach, where the radiation pattern at a given time t is a stochastic process as a function of θ and φ. From a practical point of view, the goal is to quantify the probability that the performance of an antenna system at a given position inside the car is being degraded.

Thus, the open-circuit voltage $\underline{V}_r$ induced at the receiving antenna terminal takes into account all the fields summed by the antenna in the multipath scenario. It can be expressed as

[3] According to [1], to take also into account the losses from impedance mismatches, the so-called realized gain should be considered. It includes all antenna efficiencies given by the overall efficiency $\epsilon_{tot} = \epsilon_{ref} \cdot \epsilon_{rad}$ (dimensionless), where ϵ_{ref} is the reflection (mismatch) efficiency and is given by $\epsilon_{ref} = 1 - |S_{11}|^2$ (S_{11} denoting the reflection coefficient at the input terminals of the antenna by means of the scattering parameter).

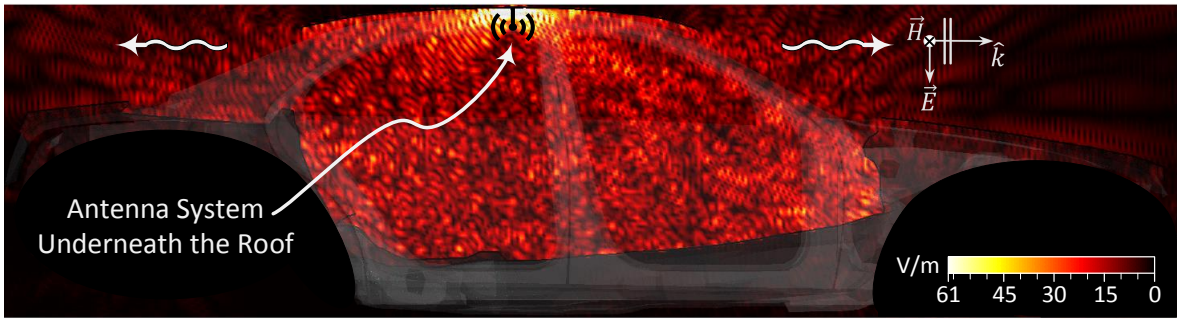

Figure 5.15: Longitudinal cross-section view of a CAD model of a car with a snapshot in time of the electric field distribution in V/m from a $\lambda/4$-monopole hidden underneath the center of the car's roof and radiating outwards through the car's windows.

a function of the spatial incident fields and the properties of the antenna itself defined in the effective antenna height. $\underline{V}_r$ is thus given by [41, 132]

$$\underline{V}_r = \sum_{i=1}^{N} \left(\underline{\mathbf{E}}_i^{inc} \cdot \underline{\mathbf{h}}_{eff} \right) = \sqrt{4 \frac{R_{rad}}{\eta} \frac{\lambda^2}{4\pi} G} \sum_{i=1}^{N} \left(\underline{\mathbf{C}}(\theta_i, \varphi_i) \cdot \underline{\mathbf{E}}_i^{inc} \right) \tag{5.57}$$

where $\underline{\mathbf{E}}_i^{inc}$ is the i-th incident electric field (considering a multipath scenario with N plane waves impinging on the antenna), $\underline{\mathbf{h}}_{eff}$ is the vector effective height of the antenna, which contains all far field properties of the antenna including its polarization characteristics[4], R_{rad} is the radiation resistance of the antenna, which is equivalent to the real part of the input impedance, η is the characteristic impedance of vacuum ($\eta = 120\pi\ \Omega$), and G is the maximum gain of the antenna.

Since it is intended to analyze the far-field patterns, equation (5.57) can be transformed to compute the received power at the feed point of the antenna resulting in (considering matching conditions) [41]

$$P_r = \frac{|\underline{V}_r|^2}{8R_{rad}} = \frac{1}{\eta} \frac{\lambda^2}{8\pi} G \left| \sum_{i=1}^{N} \left(\underline{\mathbf{C}}(\theta_i, \varphi_i) \cdot \underline{\mathbf{E}}_i^{inc} \right) \right|^2 . \tag{5.58}$$

Radiation pattern measurements of the AUT as a receiving antenna are performed using the comparison method with a reference antenna in the outdoor far-field test range shown in Fig. 5.16. It is equipped with a broadband log-periodic transmitting antenna placed 20 m away from the turntable where the vehicle rotates in azimuth to record the horizontal cut of the antenna pattern with a resolution of 5° in azimuth. More than 40 dB of dynamic range is ensured with a previously amplified transmitting antenna, to allow the measurement of the deep nulls common in such mounting positions without distorting the pattern.

Since this chapter deals with antennas underneath the roof, the antennas show deep nulls and chaotic behavior in their radiation characteristics. Therefore, it is very important to ensure a

[4] $\underline{\mathbf{h}}_{eff}$ would have to be conjugated in equation (5.53) if the transmitting instead of receiving antenna were considered [132]. The conjugate comes from a convention to refer the antenna polarization to the same axis direction as the incoming wave polarization.

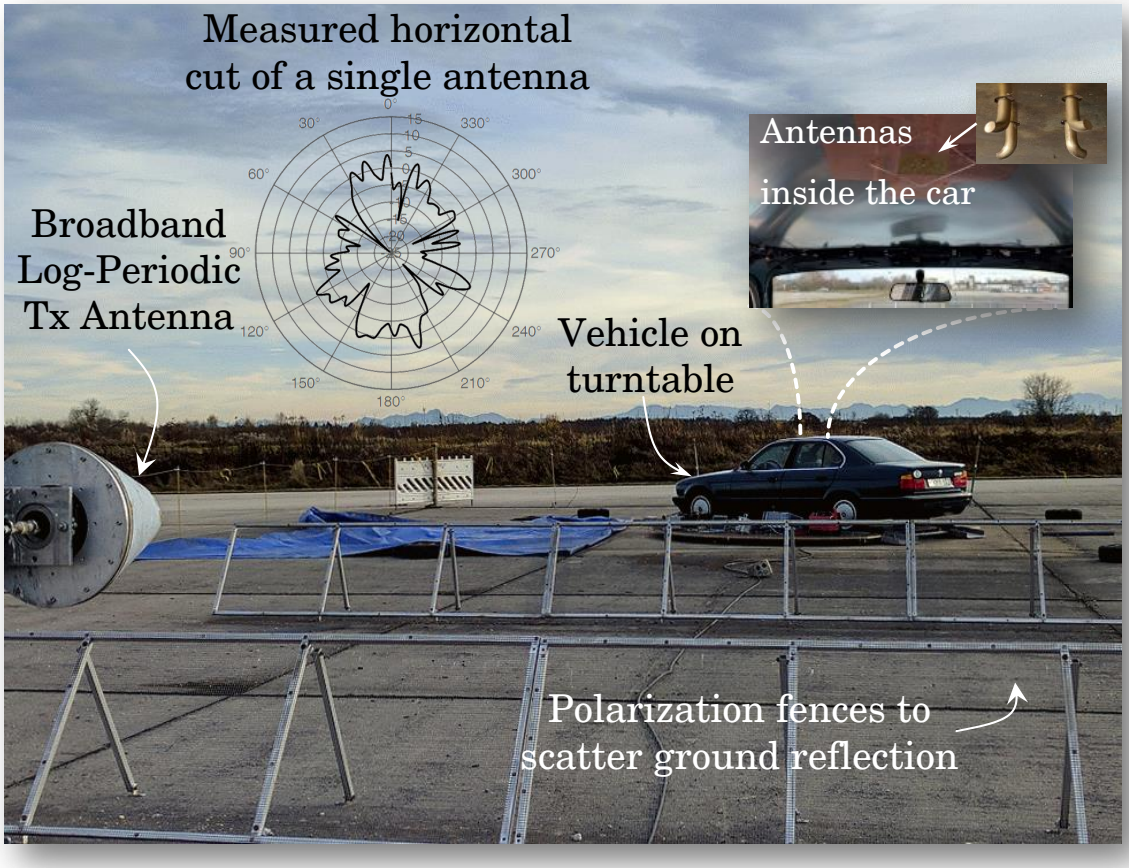

Figure 5.16: Open Area Test Site (OATS) at the University of the Bundeswehr in Munich, Germany, with a detailed view of the antenna diversity set underneath the roof in the inset and an example of measured radiation pattern in azimuth.

wide dynamic range in the measurement setup in order to be able to account for all amplitude variations in the radiation pattern. A study to evaluate the effect of noise in the measurements has been performed by adding Additive White Gaussian Noise (AWGN) to the useful signal and computing the Signal-to-Noise Ratio (SNR). As shown in Fig. 5.17, for a SNR value greater than 20 dB the pearson correlation factor between the clean and noisy signals is greater than 0.9, being the correlation factor for a SNR of 40 dB almost one.

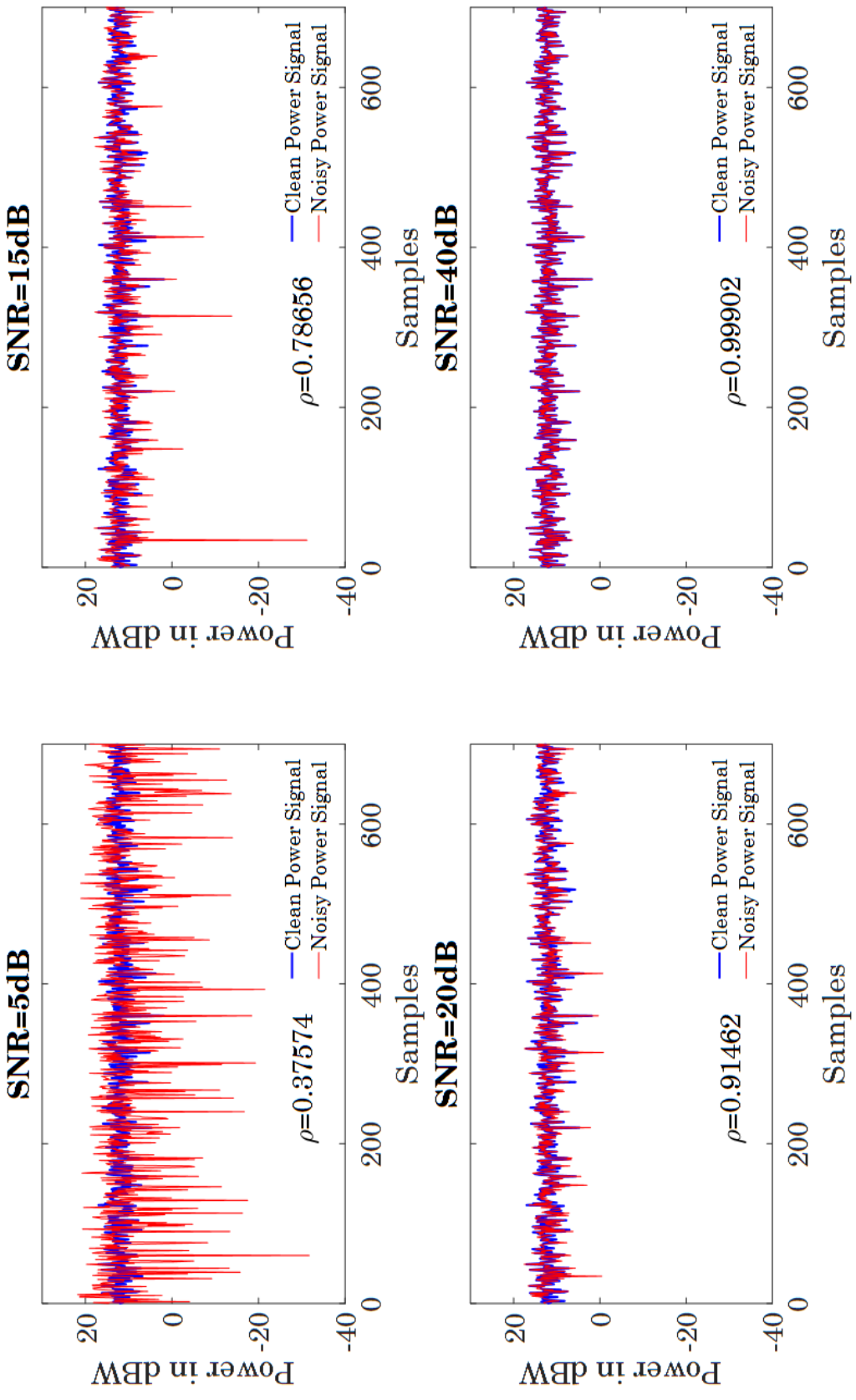

Figure 5.17: Noise effect on the received signal: Received power for various SNR ratios. For $SNR \geq 20$ dB the pearson correlation factor between the clean and the noisy signals is greater than 0.9, as shown in the inset of the figures.

A comparison of a measured and a simulated (using Method of Moments (MoM)) radiation pattern for a single antenna placed centered underneath the roof is shown in Fig. 5.18 [21]. Measured and simulated results show an excellent agreement. It is worth noting the deep nulls in the horizontal plane caused by the shadowing from the pillars of the car, which could be greater than 20 dB.

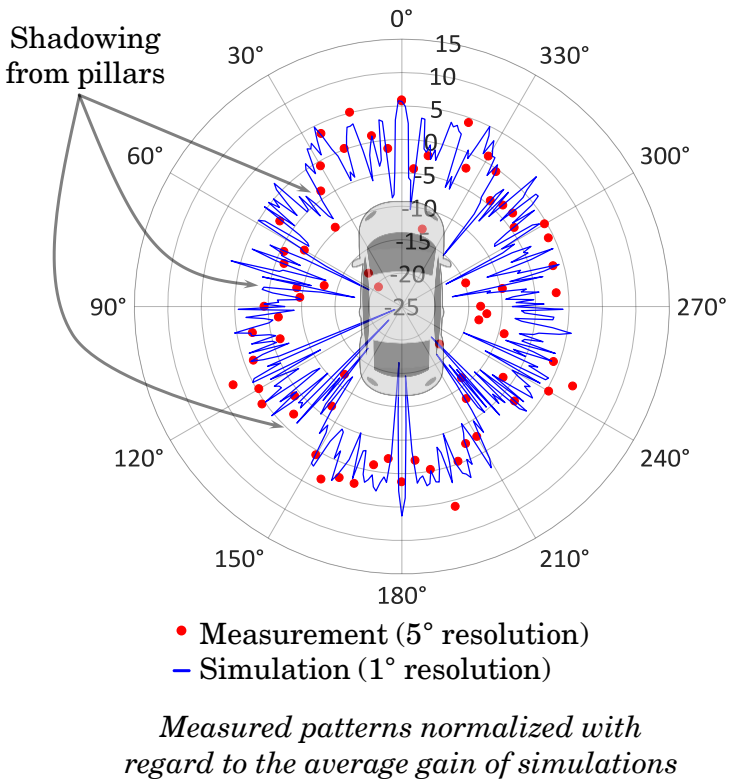

Figure 5.18: Horizontal-cut ($\theta \approx 90°, \varphi$) of the measured (red dots) and simulated (blue solid curve) radiation pattern of a $\lambda/4$-monopole centered underneath the car roof. The measured pattern is normalized to the average gain of the reference antenna obtained from simulations based on MoM.

As a matter of proof, a two-sample Kolmogorov-Smirnov test (two-sided) has been applied to validate the agreement (see Fig. 5.19) [132].

Given the random variables $\mathbf{X} = (X_1, \ldots, X_m)$, with $m = 72$, and $\mathbf{Y} = (Y_1, \ldots, Y_s)$, with $s = 360$, corresponding to the gain levels over azimuth of the measured (every 5°) and simulated (every 1°) radiation patterns at $\theta \approx 90°$, respectively. Let $F_m(x)$ and $G_s(x)$ denote the empirical Cumulative Distribution Functions (CDF) derived from $\mathbf{X}$ and $\mathbf{Y}$, respectively. The statistic $D = max_x |F_m(x) - G_s(x)|$ is used for testing the null hypothesis $\boldsymbol{H}_0$ that $F_m(x)$ comes from the same distribution than $G_s(x)$ at the α =1% significance level against all of the possible alternative hypothesis $\boldsymbol{H}_1 : F_m(x) \neq G_s(x)$. Both measurements and simulations are in good agreement if

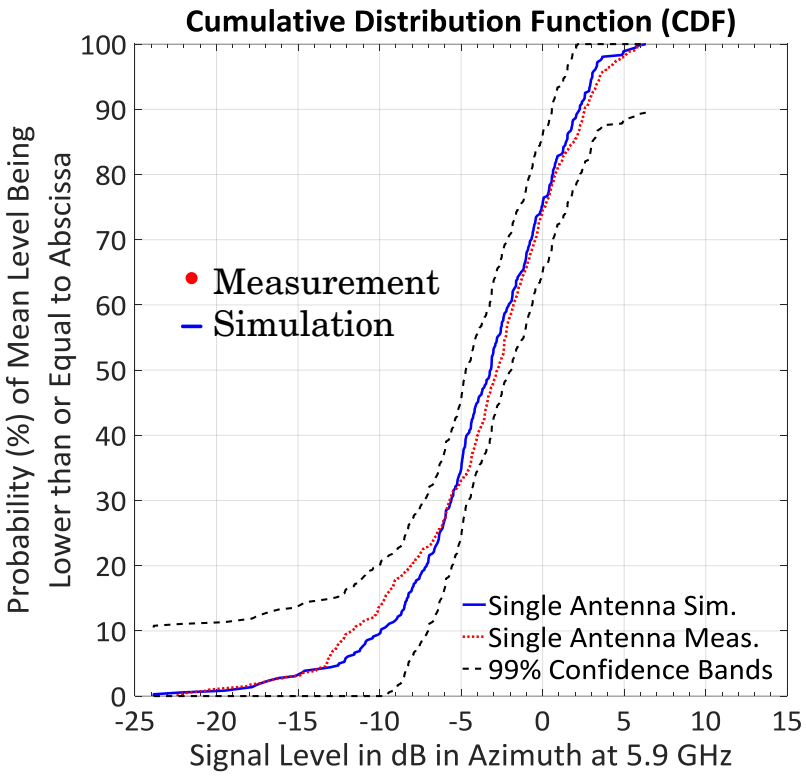

Figure 5.19: Cumulative Distribution Functions (CDFs) comparing simulated (MoM) and measured results in the OATS for a single antenna centered underneath the roof. The confidence bands derived by means of the Kolmogorov-Smirnov test have also been plotted to corroborate the good agreement between measurements and simulations.

they do not reject the null hypothesis, that is, if $D \leq c$, where c is a critical value so that $Prob(D \leq c) = 1 - \alpha$. The critical value c is tabulated in the literature for various significance levels α and sample sizes. Hence, it can be concluded that the curves in Fig. 5.18 are in good agreement, since they do not reject $\boldsymbol{H}_0$ at α =1%.

Figure 5.18 shows once again the random and chaotic nature of the radiation patterns underneath the roof, so that only a statistical analysis of the diagrams makes it possible to evaluate the system in an objective way. Looking closer at Fig. 5.19, it can be noted that with a cumulative probability of 75 %, the values of the radiation pattern for a single antenna underneath the roof lie below the threshold of 0 dB. This means that the system offers only 25 % reliability considering that a good communication link requires at least 0 dB. These values may not be sufficient when it comes to safety systems.

Moreover, Fig. 5.19 also shows that in the interquartile range, which is the difference between the upper and lower quartiles, the circularity of the patterns is about ±3.25 dB. If the difference between the percentile 90 and 10 is observed, the circularity of the patterns worsens to values of

about ± 6.75 dB, which cannot be considered anymore as an omnidirectional antenna as required for V2X-communication.

Hence, the electromagnetic phenomena taking place inside the car, difficult an omnidirectional coverage or even an elliptical one, which is required for proper operation of V2X systems. As will be discussed in the next section, a solution based on a new micro-diversity concept to be placed hidden underneath the roof of the car can improve such impairments and outperform the operation of single antennas in such unsuitable positions from an electromagnetic point of view. As will be shown, the diversity system not only enables smoothed radiation patterns with a unique compact antenna arrangement with a size of less than $10 \times 48 \times 48$ mm^3 completely hidden underneath the roof of a car, but also combats signal fluctuations inside the car and mitigates Rayleigh-fading in a real V2X scenario.

Comparing with the decentralized macro-diversity systems discussed in Chapter 4, the micro-diversity systems that will be discussed in the next section allow to preserve the aesthetics of the car hiding the system of antennas in a very reduced space of the car without affecting the performance of the system. Additionally, they allow to reduce the length of the cables needed to interconnect the antennas with the front-end, making possible compact configurations.

5.2 Improvement of the Radiation Pattern Through Antenna Diversity

5.2.1 The Antenna Array

A spatial micro-diversity smart antenna system in the form of a uniform circular array as shown in Fig. 5.20 is investigated as a measure to improve the performance of antennas hidden underneath the roof [21, 22], the same way was done in Chapter 4 for a macro-diversity system based on antennas placed on different mounting positions.

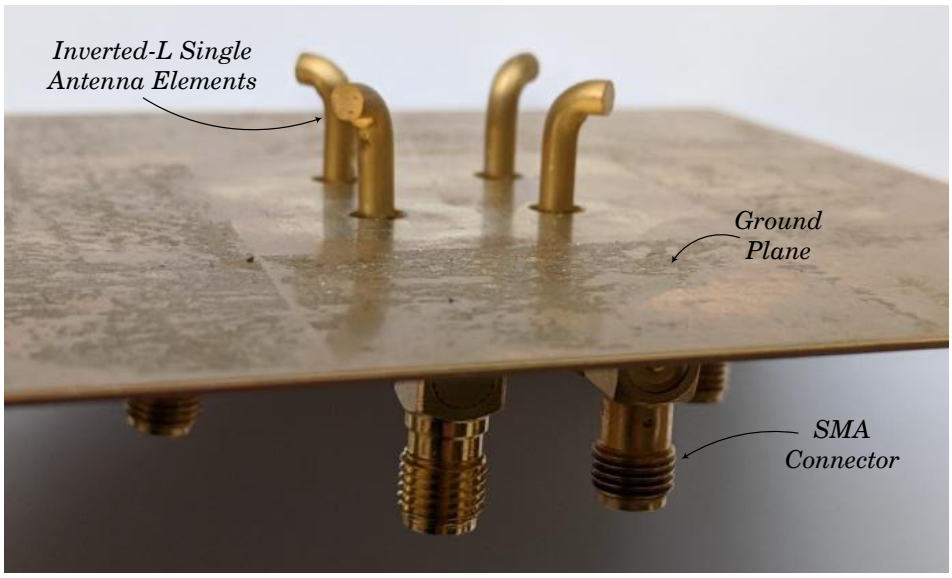

Figure 5.20: Prototype of the circular array investigated. The goal is the improvement of the radiation pattern by means of spatial micro-diversity.

The uniform circular array has been chosen due to its versatility to generate omnidirectional or directive patterns depending on the configuration of the amplitudes and phases of the feeding network and the radiation patterns of the single elements of which the array is composed. The small and compact dimensions, where all elements are placed along a circle of radius d, and the capacity to cover arbitrary azimuth angles without compromising the sharpness of the main beams, as occurs in uniform linear arrays, are promising properties to achieve good performance by means of micro-diversity adaptive antenna systems in multipath environments.

Referring to Fig. 5.21, $N = 4$ single inverted-L monopole antenna elements, of the type discussed in section 5.1.1 and assumed to be identical and omnidirectional in the horizontal plane, have been uniformly distributed along a circle of radius d (arranged on the end points of the circumscribed square). The circular array is located on the XY-plane and illuminated by a planar wavefront tangent to an observation point $P(\theta, \varphi)$ referring to a spherical coordinate system, whose origin is located at the center of the circular array. The angular position of the nth

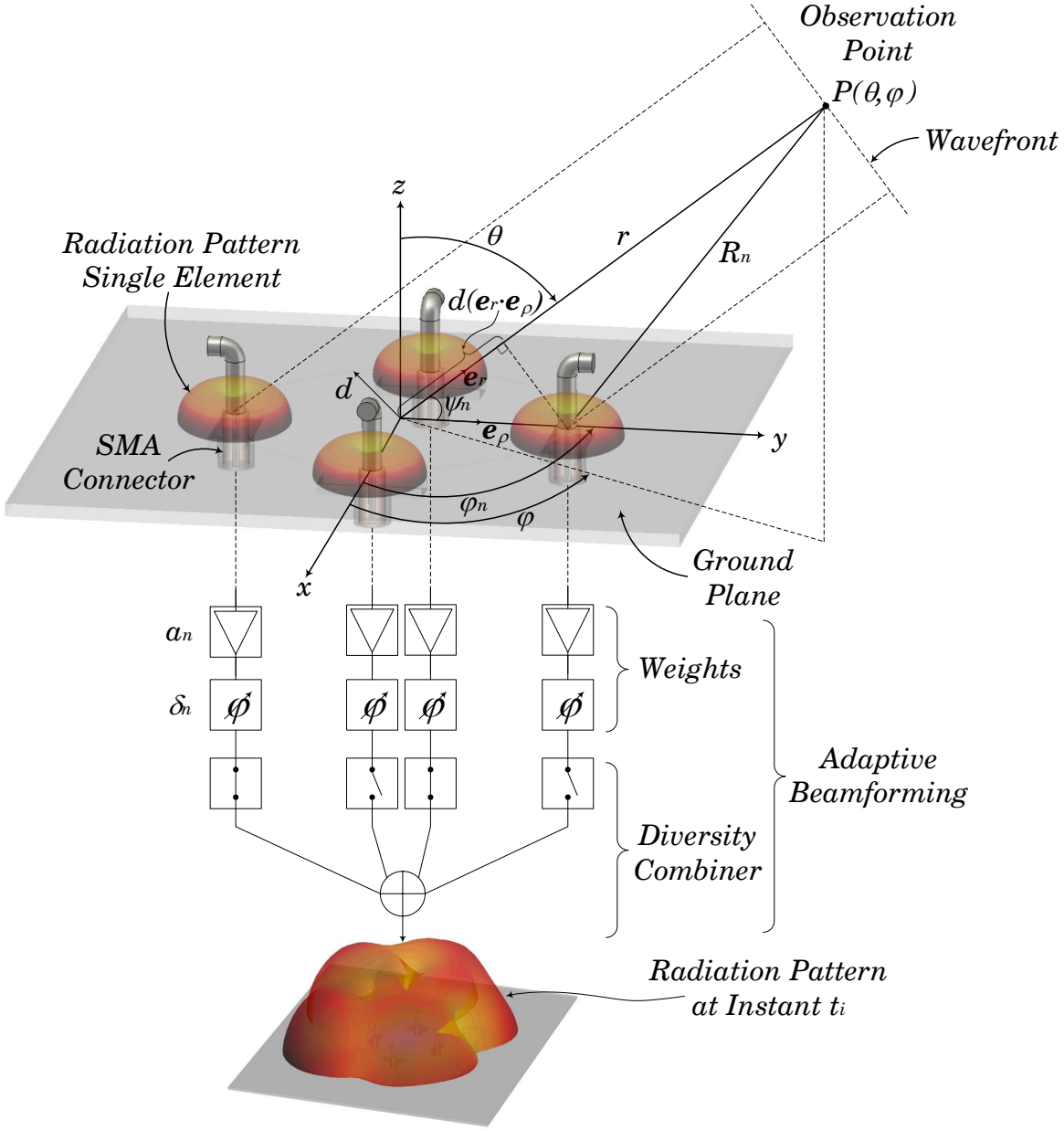

Figure 5.21: Geometry of the CAD model of the circular array investigated, with radius d and $N = 4$ equally spaced inverted-L antenna elements.

element of the array is given by

$$\varphi_n = (n-1)\frac{2\pi}{N} \quad \text{for} \quad n = 1 \ldots N = 4. \tag{5.59}$$

The normalized electric field generated by the circular array consisting of $N = 4$ identical and

omnidirectional antennas at the observation point $P(\theta,\varphi)$ is given by

$$\underline{\boldsymbol{E}}_n(r,\theta,\varphi) = \underline{\boldsymbol{C}}_0(\theta,\varphi)\cdot\sum_{n=1}^{N}\underline{I}_n\frac{e^{-jkR_n}}{R_n}, \tag{5.60}$$

where $\underline{\boldsymbol{C}}_0$ is the normalized complex vector radiation pattern as defined in 5.51 with the subindex zero referring to the reference single element in the array. $\underline{I}_n$ is the excitation coefficient of the nth element, which can be written as $\underline{I}_n = a_n e^{-j\delta_n}$, for $n = 1\ldots N = 4$, where a_n is the amplitude excitation of the nth element and δ_n the phase excitation of the nth element relative to the array center. R_n is the distance from the nth element to the observation point $P(\theta,\varphi)$, which considering the angle ψ_n formed between the unit vectors $\boldsymbol{e}_\rho$ and $\boldsymbol{e}_r$ as indicated in Fig. 5.21, R_n is given by

$$R_n = \sqrt{r^2 + d^2 - 2dr\cos\psi_n}\,. \tag{5.61}$$

Under far-field conditions ($r \gg d$), the distance R_n is approximately r reduced by the projection of $\boldsymbol{e}_\rho$ on $\boldsymbol{e}_r$, so that equation (5.61) asymptotically reduces to

$$R_n \simeq r - d\cos\psi_n = r - d\left(\boldsymbol{e}_\rho\cdot\boldsymbol{e}_r\right) = r - d\sin\theta\cos\left(\varphi-\varphi_n\right), \tag{5.62}$$

where $\boldsymbol{e}_\rho\cdot\boldsymbol{e}_r$ denotes the inner product given by

$$\boldsymbol{e}_\rho\cdot\boldsymbol{e}_r = \left(\cos\varphi_n\boldsymbol{e}_x + \sin\varphi_n\boldsymbol{e}_y\right)\cdot\left(\sin\theta\cos\varphi\boldsymbol{e}_x + \sin\theta\sin\varphi\boldsymbol{e}_y + \cos\theta\boldsymbol{e}_z\right) = \sin\theta\cos\left(\varphi-\varphi_n\right). \tag{5.63}$$

The asymptotic approximation of equation (5.62) is used for the phase factor e^{-jkR_n} of equation (5.60) under far-field conditions, while for amplitude variations $R_n \simeq r$.

Thus, the general mathematical expression for the normalized electric field of a circular array given by equation (5.60) reduces to

$$\underline{\boldsymbol{E}}_n(r,\theta,\varphi) = \underbrace{\underline{\boldsymbol{C}}_0(\theta,\varphi)\frac{e^{-jkr}}{r}}_{\substack{\text{Radiation pattern}\\ \text{single element}}}\cdot\underbrace{\sum_{n=1}^{N}a_n e^{j[kd\sin\theta\cos(\varphi-\varphi_n)-\delta_n]}}_{\substack{\underline{M}(\theta,\varphi)\equiv\text{Array factor}\\ \text{circular array}}}, \tag{5.64}$$

where the far-zone field $\underline{\boldsymbol{E}}_n(r,\theta,\varphi)$ is obtained by means of pattern multiplication of the single element at the reference point (center of the array) with the field pattern of the array factor $\underline{M}(\theta,\varphi)$ corresponding to the term containing the summation.

Directive radiation patterns can be obtained for beamforming applications with the main beam directed in the (θ_i,φ_i) direction by means of proper configuration of the phase shifters depicted in Fig. 5.21, where the theoretical value for the progressive phase excitation of the nth element is given by

$$\delta_n = -kd\sin\theta_i\cos\left(\varphi_i-\varphi_n\right). \tag{5.65}$$

Omnidirectional patterns can also be conformed when all antenna elements are excited with equal currents in amplitude and phase and the number of elements of the array N meets the following requirement [88]

$$N \geq kd + 2. \tag{5.66}$$

In this case, due to symmetry reasons in circular arrays and the fact that the cosine is an even function ($\cos\left(-\psi_n\right) = \cos\psi_n$), equation (5.64) reduces to [88]

$$\underline{\boldsymbol{E}}_n\left(r,\theta,\varphi\right) = \underline{\boldsymbol{C}}_0\left(\theta,\varphi\right)\frac{e^{-jkr}}{r}\cdot 2\sum_{n=1}^{N/2}\cos\left(kd\sin\theta\cos\left(\varphi-\varphi_n\right)\right), \tag{5.67}$$

where the array factor $\underline{M}\left(\theta,\varphi\right)$ can be derived using the relation of equation (5.63) as

$$\begin{aligned}\underline{M}\left(\theta,\varphi\right) &= \sum_{n=1}^{N} e^{-jkd\cos\psi_n} = \sum_{n=1}^{N/2}\left(e^{-jkd\cos\psi_n} + e^{-jkd\cos\left(\pi-\psi_n\right)}\right) = \\ &= 2\sum_{n=1}^{N/2}\cos\left(kd\cos\psi_n\right) = 2\sum_{n=1}^{N/2}\cos\left(kd\sin\theta\cos\left(\varphi-\varphi_n\right)\right)\end{aligned} \tag{5.68}$$

Since an adaptive or smart antenna arrangement in the form of a micro-diversity system is intended to mitigate the multipath scenario of antennas underneath the roof, patterns with arbitrary lobes constantly adapted to the multipath channel response at each instant of time (or position in space) should be generated. Therefore, the phase excitations change randomly in a channel with spatial properties close to that of a spatially white one, according to the phases on each antenna element at each instant or time. This is done in order to add the replicas of each branch constructively (co-phasing). Meaningless patterns at each instant of time (in the sense that there is any differentiated main lobe usually associated to a specific direction in a LOS environment, as occurs in classical beamforming) are thus obtained. An example of a radiation pattern obtained after coherently combining the random incoming signals at the four antennas at a specific instant of time is shown in Fig. 5.21.

Figure 5.22 shows the measured complex input impedances over frequency for a diversity system composed of 4 antennas placed underneath the roof of the car. The complex impedances are plotted in form of smith chart for a pair of antennas and as S-parameters representation to evaluate the mutual coupling between the antennas ($S_{j,i}$) for various antenna separations d, namely $d = 0.3\lambda$ and $d = 0.7\lambda$. It is noticeable the not negligible mutual coupling between the antennas for a separation between them of about 0.3λ. This will lead to higher values of envelope correlation coefficient, as will be shown in the next subsection, degrading the diversity performance of the system.

5.2.2 Power Imbalance and Envelope Correlation Coefficient

In order to evaluate how good the diversity system will perform in a multipath fading environment, two conditions must be met primarily in the antenna's development stage. First, the

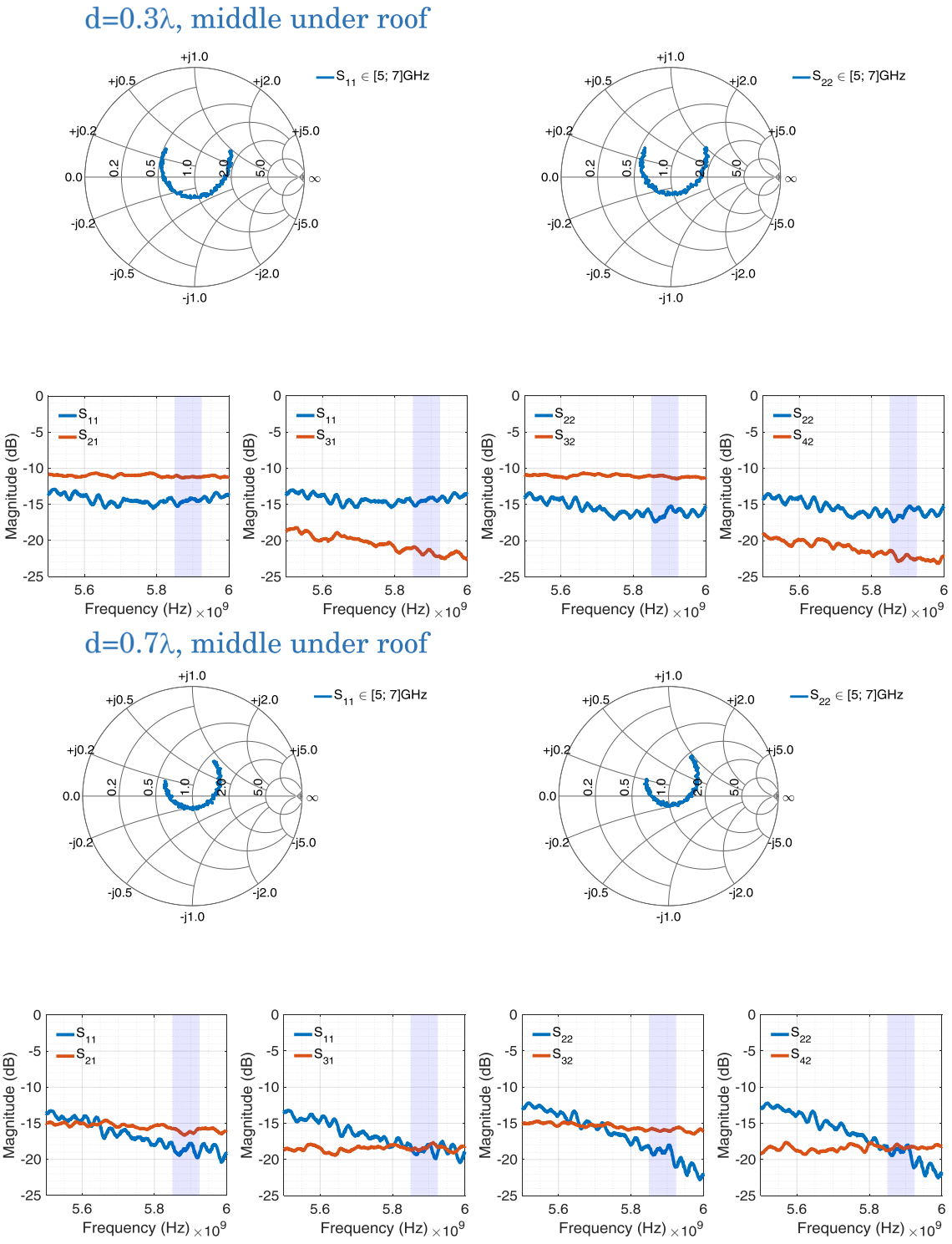

Figure 5.22: Complex input impedances over frequency in form of smith chart and S-parameters representation to evaluate the mutual coupling between the antennas in a diversity set of 4 antennas placed underneath the roof and separated by a distance of $d = 0.3\lambda$ (top) and $d = 0.7\lambda$ (bottom).

average envelope power imbalance (or just *power imbalance*), which is defined as the difference in the average distribution of the signal-to-noise ratio (SNR) in dB between two diversity branches [32], should be as small as possible. Second, the *envelope correlation coefficient*, defined as a measure of the resemblance between the signals received at two different branches, should be smaller than 0.5 to be able to improve the signal reliability by means of diversity [72]. That is, all antennas of the array should have almost the same time-averaged power and the envelopes of the received signals at each instant of time should be as different as possible (uncorrelated).

Intuitively, if there are antennas in the array which receive signals with much larger mean SNR than others, the weaker ones will not contribute much to the resultant diversity signal. Diversity means variety, diversification, difference. If the different received signals by the various antennas in the array have all of them at a each instant of time the same envelope, the received signals are completely correlated and there is no improvement of the reliability of the resultant signal by means of diversity.

Considering that the noise powers in each branch are equal, the power imbalance can be mathematically defined as

$$P_{imb}(dB) = 10\log_{10}(\max[P_1,\ldots,P_N]) - 10\log_{10}(\min[P_1,\ldots,P_N]), \tag{5.69}$$

where $\max[\bullet]$ and $\min[\bullet]$ returns the maximum and minimum element of the array inside the brackets, respectively, and P_n (for $n = 1,\ldots,N$) denotes the average envelope power received at each of the N branches of the diversity system. P_n can be computed from the statistical distribution of the envelope at each of the individual branches $n \in [1,N]$ as follows [32]:

$$P_n = E\left[r_n^2\right] = \int_0^\infty r_n^2 f_{R_n}(r_n)\,dr_n, \quad \text{for} \quad n = 1,\ldots,N, \tag{5.70}$$

where r_n is the envelope of the received signal at the branch n, $f_{R_n}(r_n)$ is the probability density function of the received envelope r_n, and $E[\bullet]$ is the expected value of the term in brackets, so that $E\left[r_n^2\right]$ is the second order moment of the stochastic variable r_n.

Figure 5.23 shows the measured levels of an antenna diversity set composed of 4 antennas separated by a distance of $d \approx 0.6\lambda$ and placed centered underneath the roof of the car. The levels are normalized to a reference antenna placed above the roof. It is worth noting the level difference caused by hiding the antennas underneath the roof, which can be as much as 8 dB in average. The figure also shows the power imbalance between the antennas, as previously defined. Low values of about 1 dB in average are obtained, which is a necessary condition for proper diversity operation.

A general form of the envelope correlation coefficient $\rho_{e_{i,j}}$ is computed using the far-field patterns of the antennas in the array, and is given by

$$\rho_{e_{i,j}} = \frac{\left|\iint_{4\pi}\left[\underline{\boldsymbol{C}}_i(\theta,\varphi)\cdot\underline{\boldsymbol{C}}_j^{\dagger}(\theta,\varphi)\right]d\Omega\right|^2}{\iint_{4\pi}\left|\underline{\boldsymbol{C}}_i(\theta,\varphi)\right|^2 d\Omega\cdot\iint_{4\pi}\left|\underline{\boldsymbol{C}}_j(\theta,\varphi)\right|^2 d\Omega}, \tag{5.71}$$

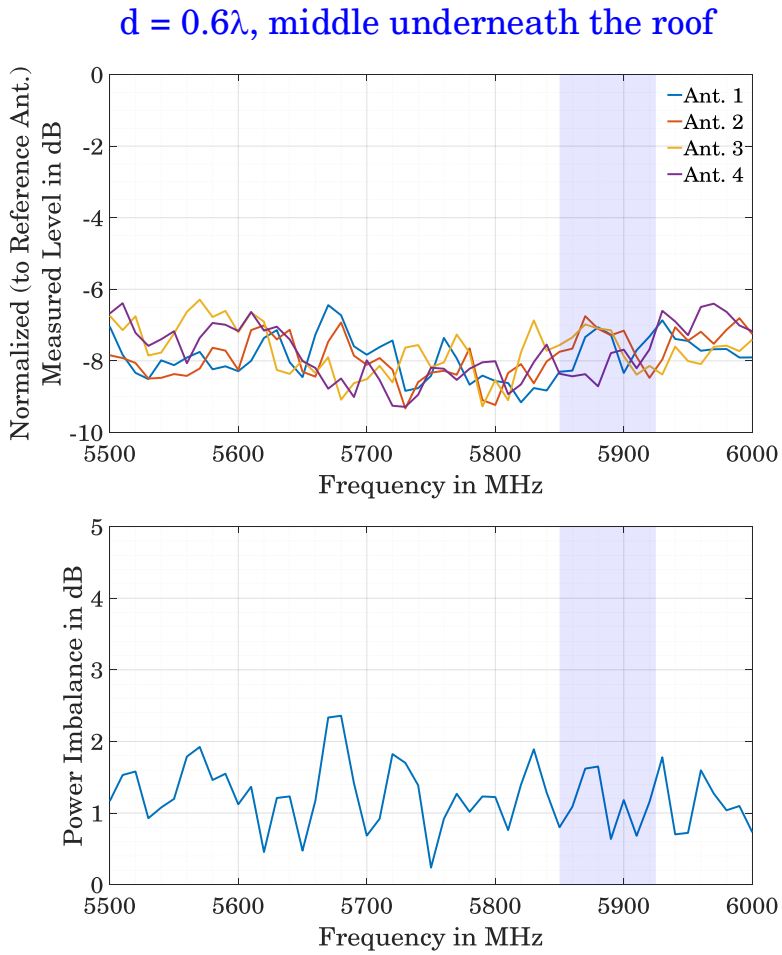

Figure 5.23: Measured levels over frequency for antennas centered underneath the roof with a separation of $d = 0.6\lambda$ normalized to a reference antenna over the roof (top), and power imbalance defined as the difference in power in decibels between the antenna receiving the highest level and the one receiving the lowest power level (bottom)

where $\underline{\boldsymbol{C}}_{i,j}(\theta,\varphi)$ is the normalized complex voltage radiation pattern as defined in 5.51, which includes the effect of the other antennas terminated by the reference impedance Z_0; the dagger † denotes the conjugate transpose, so that an inner product in the complex space $\{\mathbb{C}^3\}$, also known as the hermitian form of the inner product, is performed in the integrand of the numerator; and $d\Omega = dA/r^2 = \sin\theta d\theta d\varphi$ denotes the element of solid angle of a sphere, where dA represents the infinitesimal area on the surface of a sphere of radius r.

The most general form of the envelope correlation factor is obtained considering the spatial characteristics of the communication channel in which the diversity system is intended to be implemented. This means some knowledge of the eigenvalues of the channel and its temporal fading statistics. Following the notation introduced in equation (5.57), and according to [133], the

correlation coefficient for the open circuit ith and jth signals is

$$\rho_{e_{i,j}} = \frac{\left[E\left\{\left(\underline{V}_{r_i} - \overline{V}_{r_i}\right)\left(\underline{V}_{r_j} - \overline{V}_{r_j}\right)^*\right\}\right]^2}{E\left\{\left(\underline{V}_{r_i} - \overline{V}_{r_i}\right)^2\right\} E\left\{\left(\underline{V}_{r_j} - \overline{V}_{r_j}\right)^{2*}\right\}}, \tag{5.72}$$

where $\underline{V}_{r_{i,j}}$ is the open-circuit voltage induced at each of the receiving ith, jth antenna terminals taking into account all the fields summed by the antennas in the multipath scenario. $E\{\bullet\}$ denotes the expectation operator, which is taken over the same interval as in the biased time average (demeaning) denoted by the swung dash ($\overline{V}_{r_{i,j}}$). The formula compares two received signals ith, jth, after a demeaning process to be able to compare the same magnitudes. After all, a normalization is performed to give a correlation factor ≤ 1.

Equation (5.72) can be more conveniently written as a function of the complex electric field, power distributions and cross-correlation ratio. If two complex terms $\underline{A}_\theta^{i,j}$ and $\underline{A}_\varphi^{i,j}$ are defined as a function of the θ- or φ-component of the complex electric field and power distributions, as expressed by

$$\underline{A}_\theta^{i,j} = \underline{E}_{\theta_i}(\theta,\varphi) \cdot \underline{E}^*_{\theta_j}(\theta,\varphi) \cdot P_\theta(\theta,\varphi), \text{ and} \tag{5.73}$$

$$\underline{A}_\varphi^{i,j} = \underline{E}_{\varphi_i}(\theta,\varphi) \cdot \underline{E}^*_{\varphi_j}(\theta,\varphi) \cdot P_\varphi(\theta,\varphi), \tag{5.74}$$

then, the envelope correlation coefficient according to [127, 132] is thus given by:

$$\rho_{e_{i,j}} = \frac{\left|\int_0^{2\pi}\int_0^{\pi}\left[XPR \cdot \underline{A}_\theta^{i,j} + \underline{A}_\varphi^{i,j}\right]\sin\theta d\theta d\varphi\right|^2}{\int_0^{2\pi}\int_0^{\pi}\left[XPR \cdot \underline{A}_\theta^{i,i} + \underline{A}_\varphi^{i,i}\right]\sin\theta d\theta d\varphi \cdot \int_0^{2\pi}\int_0^{\pi}\left[XPR \cdot \underline{A}_\theta^{j,j} + \underline{A}_\varphi^{j,j}\right]\sin\theta d\theta d\varphi}, \tag{5.75}$$

where the model takes into account that an isotropic power distribution over all angles (Clarke's model scenario [28]) is an unlikely model for ground based mobile communications, and instead, another statistical distribution over the elevation angle is assumed. The power distributions are given by $P_\theta(\theta,\varphi)$ and $P_\varphi(\theta,\varphi)$ for the vertical and horizontal components respectively. The cross polarization ratio (XPR) between the vertical and the horizontal component is defined as follows:

$$XPR\,(dB) = 10 \cdot \log_{10}\left(\frac{E\left\{\left|\underline{E}_\theta(\theta,\varphi)\right|^2\right\}}{E\left\{\left|\underline{E}_\varphi(\theta,\varphi)\right|^2\right\}}\right) = 10 \cdot \log_{10}\left(\frac{P_\theta(\theta,\varphi)}{P_\varphi(\theta,\varphi)}\right), \tag{5.76}$$

where $E\{\bullet\}$ denotes the expectation operator, $\underline{E}_{\theta,\varphi}(\theta,\varphi)$ are the θ- or φ-component of the complex electric field, and P_θ and P_φ are the power distributions for the vertical and horizontal components, respectively.

Since the antenna's engineer is only concerned on the antenna's part, some assumptions should be made on the spatial characteristics of the channel, since they are affecting the degree of performance of the diversity system. If only the antenna is considered, without taking into account

the real spatial conditions of the channel, an angle of arrival of the incoming signals uniformly distributed in all θ and φ angles referring to spherical coordinates is assumed ($P_\theta(\theta,\varphi) = P_\varphi(\theta,\varphi) = 1$), which corresponds to the case of a spatially white channel. This ideal channel does not exist in a real fading environment, so that the values achieved by considering only the antenna array are upper bounds or maximum values achieved under ideal conditions.

Under such conditions, and considering no cross polarization ratio (XPR =0 dB), and a lossless structure, the envelope correlation coefficient $\rho_{e_{i,j}}$ can also be computed from the S-parameter characterization of the antenna array, which has the advantage that it is not necessary to know the radiation patterns of the antennas in the array considering the corresponding mutual coupling between them and saves time and costs associated with the measurements or numerical computations of the radiation patterns. As derived in [16], it takes the form of

$$\rho_{e_{i,j}} = \frac{\left|S_{ii}^* S_{ij} + S_{ji}^* S_{jj}\right|^2}{\left(1-\left(|S_{ii}|^2 + |S_{ji}|^2\right)\right)\left(1-\left(|S_{jj}|^2 + |S_{ij}|^2\right)\right)}, \tag{5.77}$$

where S_{ii}, S_{jj} denote the return loss of the antenna i, j, respectively, S_{ij}, S_{ji} the crosstalk between antenna pairs, and * denotes complex conjugate. In the ideal case of incoming waves with directions of arrival statistically uniformly distributed in the whole sphere, equations (5.71) and (5.77) give the same results [16]. As mentioned above, equations (5.75) and (5.77), give also the same results if an isotropic power distribution ($P_\theta(\theta,\varphi) = P_\varphi(\theta,\varphi) = 1$), no cross polarization ratio (XPR =0 dB) and a lossless structure is considered, and the double integrals in equation (5.75) are computed over the whole sphere.

In case of an omnidirectional scenario in the horizontal plane as defined in the Clarke's model scenario [28], no cross polarization ratio (XPR =0 dB) and a lossless structure, the formulas given in equations (5.71), (5.72), (5.75), and (5.77) for the envelope correlation coefficient reduce to

$$\rho_{e_{i,j}} = \left[\int_0^{2\pi} e^{jkd\cos\theta} d\varphi\right]^2 = J_0^2(kd), \tag{5.78}$$

where $k = 2\pi/\lambda$ is the wave number, d is the separation between antennas, and $J_0(\bullet)$ is the Bessel function of the first kind and zeroth order.

Figure 5.24 shows the envelope correlation coefficient computed from far-field results in the horizontal plane (red and pink curves) by means of equation (5.71) and comparing with the results obtained with the S-parameters (blue and green curves) by means of equation (5.77).

Two substantial differences can be noticed. The first one is the difference in magnitude between the two computations. It is due to the fact that in the computation using the radiation patterns, only the horizontal plane has been considered instead of the whole sphere, violating thus one of the requirements discussed above to be equal. Of course, the other idealizations given by XPR =0 dB and a lossless structure are also not fulfilled. It is also worth noting that it is meaningless to consider the whole spherical range in V2X communication systems, because it

should be ensured good diversity performance only where communication takes place, hence, around the horizontal plane. Although worse results are obtained, these can be considered as worst case and to be representative for a proper operation of the whole system. The second difference is the position of the first local minimum, which appears earlier in the ECC computed by means of the far-field patterns. This phenomenon is due to the change in radiation pattern shape due to the mutual coupling between the antenna elements. Such mutual coupling introduces a variety, diversification or difference in the shape of the patterns which is the necessary premise to obtain a diversity system. This is known in the literature as *pattern diversity* [31]. This fact adds a further degree of diversity to the spatial diversity system, reducing the ECC to acceptable levels even for spatial configurations where the antennas are separated by distances of approximately $d \approx 0.3\lambda$, as shown in Fig. 5.24.

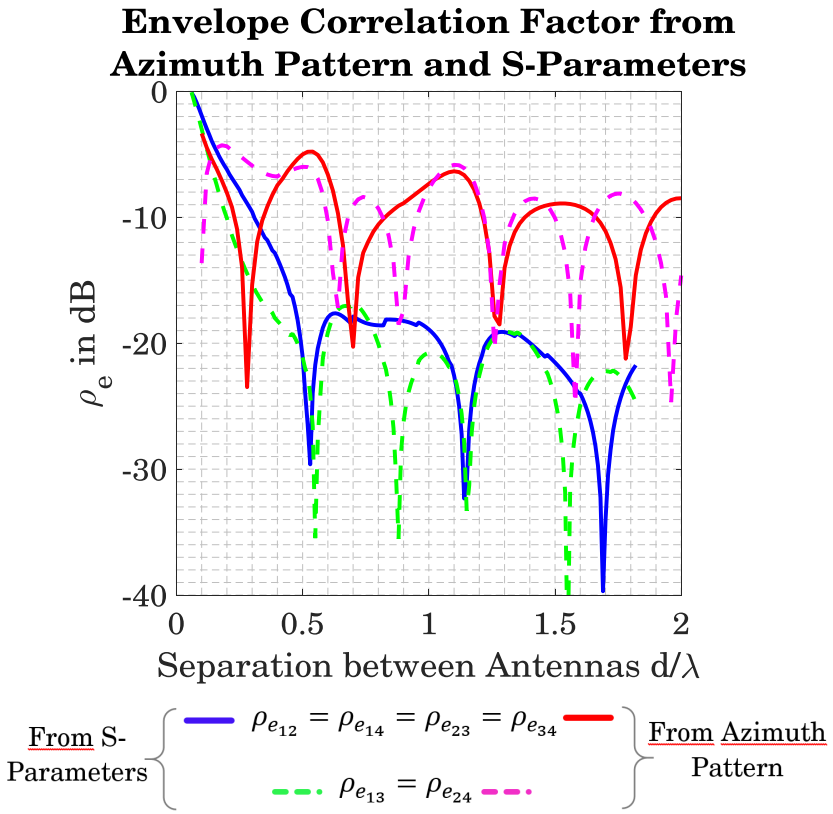

Figure 5.24: Envelope Correlation Coefficient (ECC) as a function of antenna's electrical separation d/λ. Red and pink curves are computed from far-field antenna patterns by means of equation (5.71) and blue and green curves from S-parameters using equation (5.77).

Since communication in V2X systems occurs mostly in a small elevation range around the horizontal plane, and taking into account that measurements in the Open Area Test Site (OATS) are made only in that plane, the statistical envelope correlation coefficient given by the Pearson's formula [94] is used as an objective measure throughout this dissertation. The

Pearson's correlation coefficient is defined as

$$\rho_{e_{i,j}} = \frac{\left|\sum_{i=1}^{N}\left(\underline{x}_i - \overline{x}\right)\left(\underline{y}_i - \overline{y}\right)\right|^2}{\sum_{i=1}^{N}\left|\underline{x}_i - \overline{x}\right|^2 \cdot \sum_{i=1}^{N}\left|\underline{y}_i - \overline{y}\right|^2}, \tag{5.79}$$

where $\underline{x}_i$ and $\underline{y}_i$ are the complex samples measured in the OATS for each pair of antennas when the others are terminated with 50 Ω, and $\overline{(\bullet)}$ denotes the demeaning operation over the measured samples. Comparing equation (5.72), which is the most general one, with equation (5.79), it is easy to see that both formulas are defining the same. By extension, the same can be inferred for the other formulas depending on the scenario under consideration. Equation (5.79) has the advantage that the scenario is implicit in the measured samples, so that worst case statements can be inferred from such statistical analysis.

Figure 5.25 shows the ECC over frequency for an antenna diversity set composed of 4 antennas separated by a distance of $d \approx 0.6\lambda$ and placed centered underneath the roof of the car. The values are computed by means of equation (5.79), since only samples in the horizontal plane are measured in the OATS of the university. All ECC values are below 0.4 in the whole V2X frequency range of operation. These are below the threshold factor of 0.5 for which proper diversity operation is ensured [72].

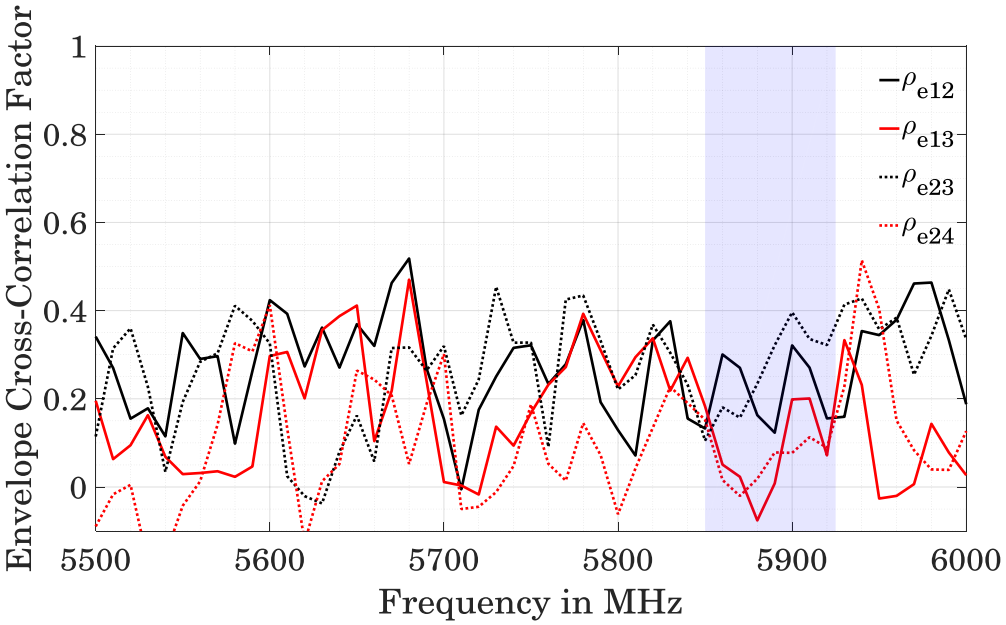

Figure 5.25: ECC from measured far-field patterns in the horizontal plane for an antenna diversity set centered underneath the roof and composed of 4 antennas separated by a distance of $d \approx 0.6\lambda$. The values are computed by means of equation (5.79).

To emphasize the importance of the demeaning operation in the envelope correlation coefficients previously defined, let us consider the actual received signal in a real scenario, which

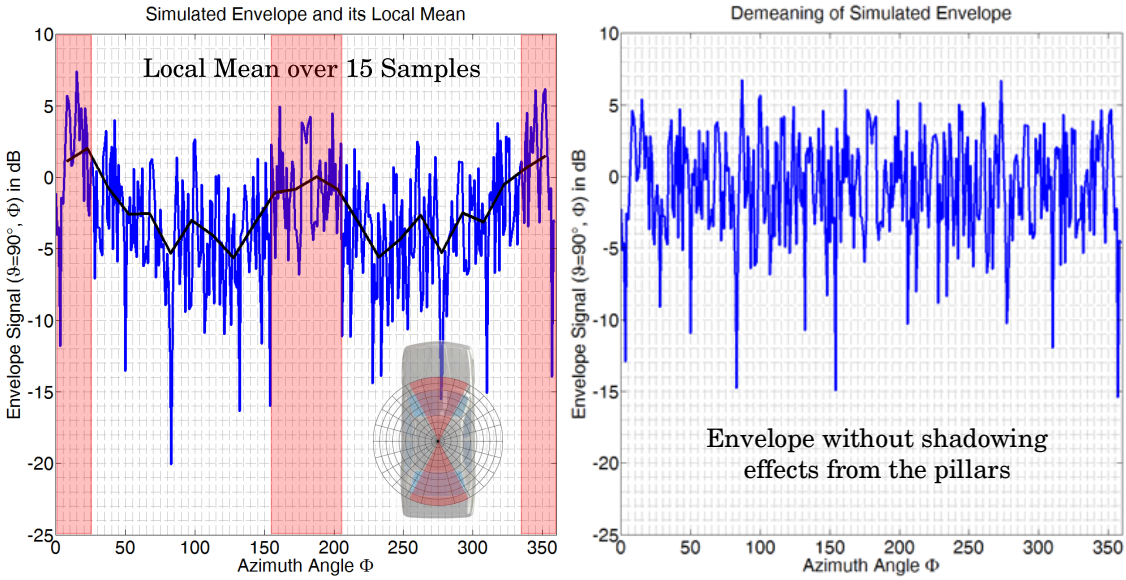

Figure 5.26: Demeaning operation: Measured radiation pattern in the horizontal plane for an antenna underneath the roof of the car before applying a moving average technique to remove the long-term fading (left), and after removing the local mean to keep only the short-term fading (right).

comprises two parts. These two parts of the received signal strength depend on the signal fading experienced due to the environment where the antennas are installed. One part is the long-term fading $m(t)$ and the other one is the short-term fading $r_0(t)$. Micro-spatial diversity systems can only alleviate the short-term fading effects, as discussed in Chapter 4, but not the long-term ones, for which macro-diversity or decentralized diversity systems will be needed. This fact implies that in order to evaluate in an objective way the improvement in efficiency and performance of the diversity system, it will be necessary to separate in an artificial way the local mean or long-term fading of the received signal strength. This is done by means of a moving average technique[5], as explained in [71].

Figure 5.26 shows a measured radiation pattern in the horizontal plane in cartesian form for an antenna underneath the roof of the car before applying a moving average technique to remove the long-term fading caused by the pillars of the car (left) and after removing the local mean to keep only the short-term fading for which the diversity system should improve the performance (right). In this example a window size for the moving average technique of 15 samples has been considered. The resulting local mean is displayed as a solid black line in the figure. The inset of Fig. 5.26 (left side) shows also a drawing of the car's prototype used in the measurement. The angles where the windows of the car are situated are highlighted in pink. It can be noticed the

[5]In this dissertation, the Matlab® function *movmean* is used to compute the local mean or long-term fading of a received signal.

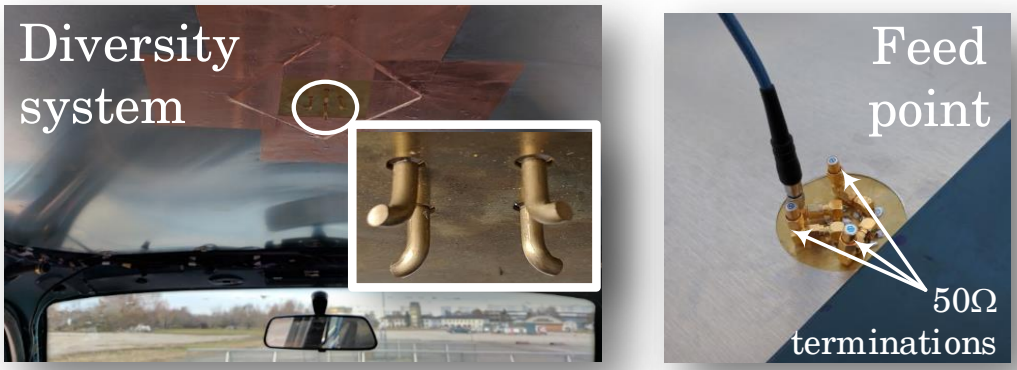

Figure 5.27: Spatial micro-diversity system composed of 4 antennas installed centered underneath the roof, inside the car's cabin (left), and detail of the rear side of the antenna set with the feeding system used in the measurements (right).

correspondence between the positions of the pillars of the car and the angular regions where the local mean of the received signal strength is considerably reduced. This is corrected by means of the demeaning operation.

5.2.3 Radiation Patterns After Applying Linear Combining Diversity Techniques for Various Benchmark Scenarios

After analyzing the antenna array from the perspective of antenna theory in the previous sections, its diversity performance installed inside the car's cabin, underneath the roof, as a real scenario will be evaluated to investigate the improvement with regard single antennas. The set up for measurement purposes is shown in Fig. 5.27 for the case where the antenna set is placed centered underneath the middle of the roof. As seen in the figure, the ground plane is attached to the metal roof through copper tape to ensure proper electrical contact with the chassis of the car. A detail of the feeding region is also shown, in which the antenna that is intended to be measured is fed through a RF coaxial cable and the rest are terminated with 50 Ω loads. The cable is passed out through a hole in the top of the roof of the car so that it can be connected to the network analyzer without interfering with the fields radiated by the antenna.

The diversity linear combining techniques introduced in section 4.2.1 of Chapter 4 are applied to the measured and simulated antenna sets installed in the car. Figure 5.28 shows the horizontal radiation patterns over azimuth (conical cuts at $\theta \approx 90°$) of the spatial micro-diversity system composed of 4 antennas separated by a distance $d \approx 0.6\lambda$ placed centered underneath the roof [21].

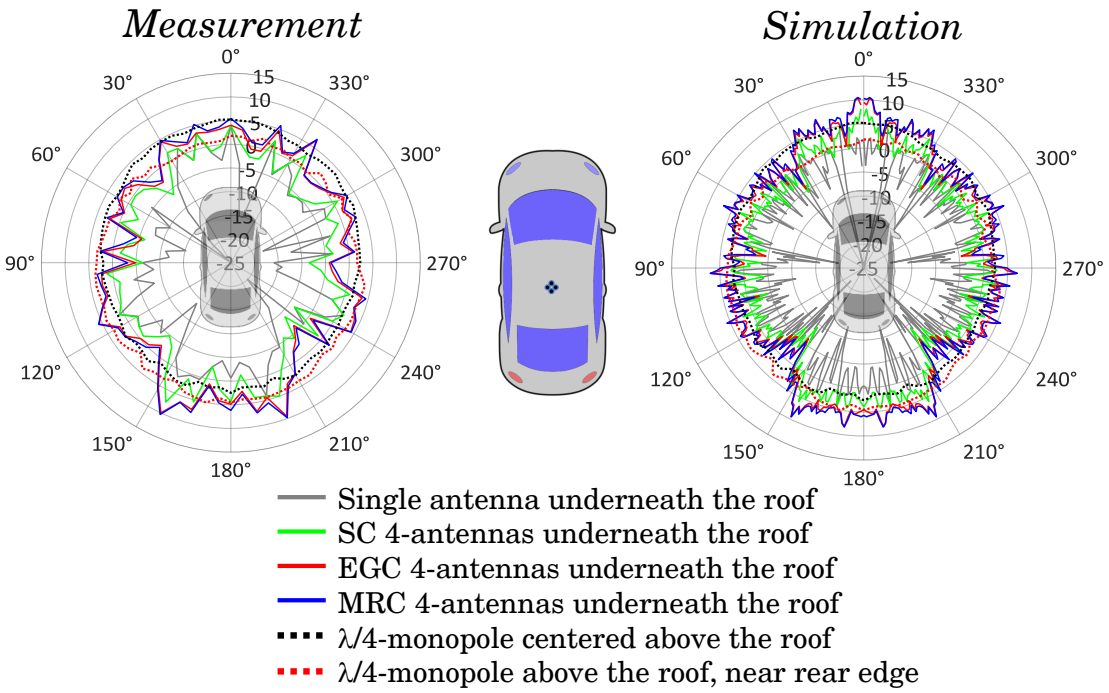

Figure 5.28: Horizontal radiation patterns (conical cuts at $\theta \approx 90°$) of the spatial micro-diversity system composed of 4 antennas separated by a distance $d \approx 0.6\lambda$ placed centered underneath the roof. Comparison of measurement results (left) and simulations (right) for various diversity linear combining techniques. Single reference quarter-wave monopole antennas are also displayed for comparison purposes. Measurement angle resolution of 5° and simulation resolution of 1°.

Measurement results are shown on the left side with an angle resolution of 5°, and simulations on the right with an angle resolution of 1°. In the middle of the figure, a top view of a sketch of the car with the antenna system position is given. Both polar plots compare the radiation patterns in decibel for the switch combining (SC), equal gain combining (EGC), and maximum-ratio combining (MRC) techniques considering 4 antennas. These patterns are compared with the far-field patterns obtained with a single antenna placed underneath the roof in the same position as the diversity set and with reference quarter-wave monopole antennas centered above the roof and on the roof near the rear edge.

As can be observed, an almost omnidirectional pattern is obtained by means of diversity, improving the deep nulls present in the pattern of a single antenna underneath the roof. This results in smoother diagrams. Moreover, a gain improvement is also achieved by means of diversity, since each of the 4 antennas is contributing to the total gain. It should also be pointed out the shadowing caused by the pillars of the car, specially that of the C-pillars at azimuth angles of about 140° and 220°. The C-pillars affect the diversity patterns more severly because they are usually wider than the A- and B-pillars. As already mentioned, micro-diversity systems,

where antennas are placed close to each other, cannot completely counteract the adverse effects of shadowing, since all antennas in the diversity set experience the same signal fading.

An important detail that can be observed in Fig. 5.28 is the range improvement in driving and opposite directions with regard to the single antennas and even when compared to the reference quarter-wave monopole antennas above the roof. Here, the windshield and rear window of the car act as an optical lens, adding constructively the electromagnetic waves impinging on the glass in an azimuthal angular sector of about 60°. This fact turns out to be very advantageous for V2X systems, especially in urban scenarios where the so-called canyon effect occurs. In such scenarios, directing a portion of the energy with the beamwidth of the antenna in those directions increases the probability of interception of safety-related messages, crucial for the proper operation of V2X communication between vehicles. Figure 5.28 also shows that, as expected, almost the same performance is obtained with EGC and MRC. Therefore, similar radiation patterns and statistical values are expected from algorithms based on *scan-phase diversity* systems discussed in [81, 116, 119, 122] for satellite antennas.

It is also worth noting the similarity of the patterns between simulations and measurements despite the difference in angle resolution. The measured radiation patterns have not been interpolated to highlight the points actually measured. The aim of showing the simulation results with an angular resolution different from that of the measurements was to highlight the diagrams that would be obtained in a real scenario and thus be able to perceive in a more objective way the actual performance of the system.

Due to the chaotic nature of the system and the bahavior experienced by the antennas when placed inside the car, the radiation patterns of the antennas represented in polar form, as usually done in antenna engineering, offer inaccurate information to characterize and evaluate the system. For this reason statistical tools are used.

Figure 5.29 shows the cumulative distribution functions (CDFs) of the samples over azimuth previously shown in Fig. 5.28 in polar form [21]. On the left side of Fig. 5.29, the agreement between measurements and simulations for a single antenna underneath the roof and for the MRC diversity system with 4 antennas is evaluated by means of confidence bands derived from the two-sided Kolmogorov-Smirnov test. As it can be seen, not only do the curves overlap in the interquartile range region, but they also lie in close proximity even at extreme cumulative or reliability probability values. The interquartile range is of the utmost importance since it corresponds to the region where the most probable values of the radiation pattern are concentrated. Moreover, both simulated and measured curves lie between the upper and lower confidence bands, corroborating the good agreement between both worlds.

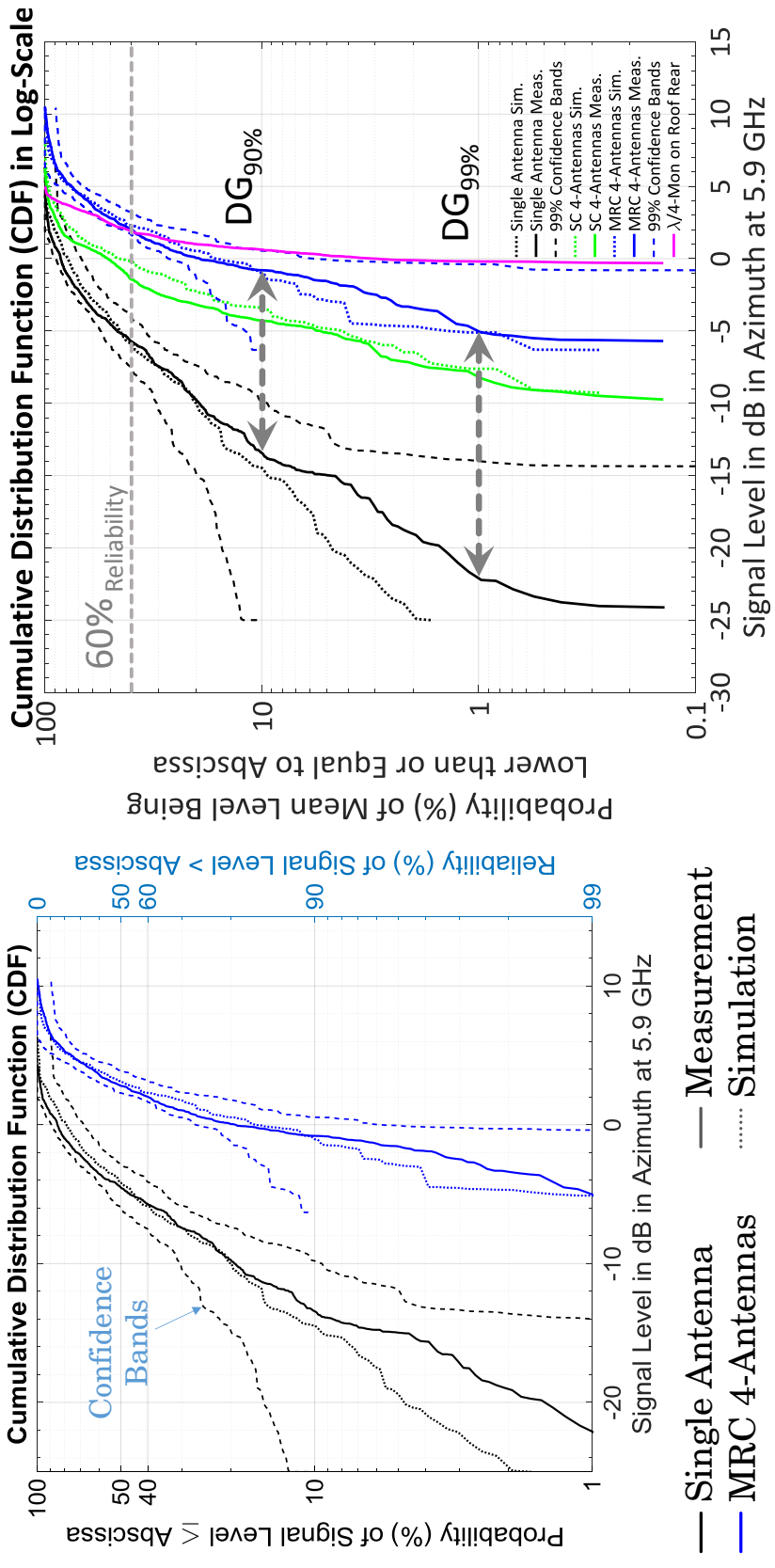

Figure 5.29: CDFs derived from the horizontal radiation patterns of Fig. 5.28 to evaluate the diversity performance. Both graphics compare simulations and measurements and various diversity linear combining techniques. CDFs of the values achieved with single reference quarter-wave monopole antennas are also displayed for comparison purposes. Confidence bands derived by means of the Kolmogorov-Smirnov test have also been plotted to corroborate the good agreement between measurements and simulations.

On the right side of Fig. 5.29 the graph is extended to show the cumulative distribution function of the SC diversity combination with 4 antennas and the reference quarter-wave monopole antenna placed above the roof near the rear edge for comparison purposes. The y-axis of the figure in logarithmic scale has been enlarged to show also cumulative probability values below 1 %. Even there, the good agreement between measurements and simulations for the SC and MRC diversity combinations is maintained. The statistical plot highlights the diversity gain at 90 % and 99 % cumulative probability, which are typical values used in the literature [132] to characterize diversity systems. They show how much improvement in decibels is achieved by means of diversity when comparing with the single antenna of the diversity set that yield the best performance.

In such statistical plots, two effects are revealed. The first one is the probability reduction of system's failure. In the case that concerns us, the CDF shows the reduction of the probability that the values of the radiation pattern are less than a certain threshold. This fact is perceived in the slope of the CDF curve of the diversity combination with regard to the slope of the CDF of the single antenna. The straighter the curve, the rounder and smoother are the patterns over azimuth. The second effect revealed is the gain enhancement obtained by adding the contribution of each of the antennas according to the diversity linear combination techniques discussed in Chapter 4. This gain enhancement achieved with diversity compared to a single antenna, results in a shift of the CDF curves to the right of the diagram when comparing with the case of a single antenna. This means that even at low cumulative probability levels, the signal strength after diversity combination will be higher than that obtained with a single antenna.

Looking closer at the right side of Fig. 5.29, the 60 % reliability level is highlighted. This point has been emphasized since it is the probability point where the MRC diversity system with 4 antennas overcome the performance obtained with reference quarter-wave monopole antennas above the roof. This means that, with a probability of 60 %, the values of the radiation pattern using the MRC diversity combination with 4 antennas are higher than that of a single antenna in the typical roof-top mounted position. Hence, it can be inferred that with the hidden diversity system investigated, even better performance than that obtained with visible and obtrusive antennas above the roof is expected in the vast majority of cases.

To give a couple of objective numbers, at the 60 % reliability, about 8 dB more signal level than the best single antenna is achieved by means of diversity. This means about 2.5 times more coverage range and more than 6 times more coverage area than with a single antenna. More than 17 dB of diversity gain is achieved with the MRC diversity system with 4 antennas at the 99 % reliability level (1 % cumulative probability level), and about 12.6 dB at the 90 % reliability level (10 % cumulative probability level).

Figure 5.30 shows the improvement that can be achieved by means of a micro-diversity antenna array composed of 2 antennas, and compares its performance with that obtained by means of an array composed of 4 antennas. It is well known that with M completely uncorrelated

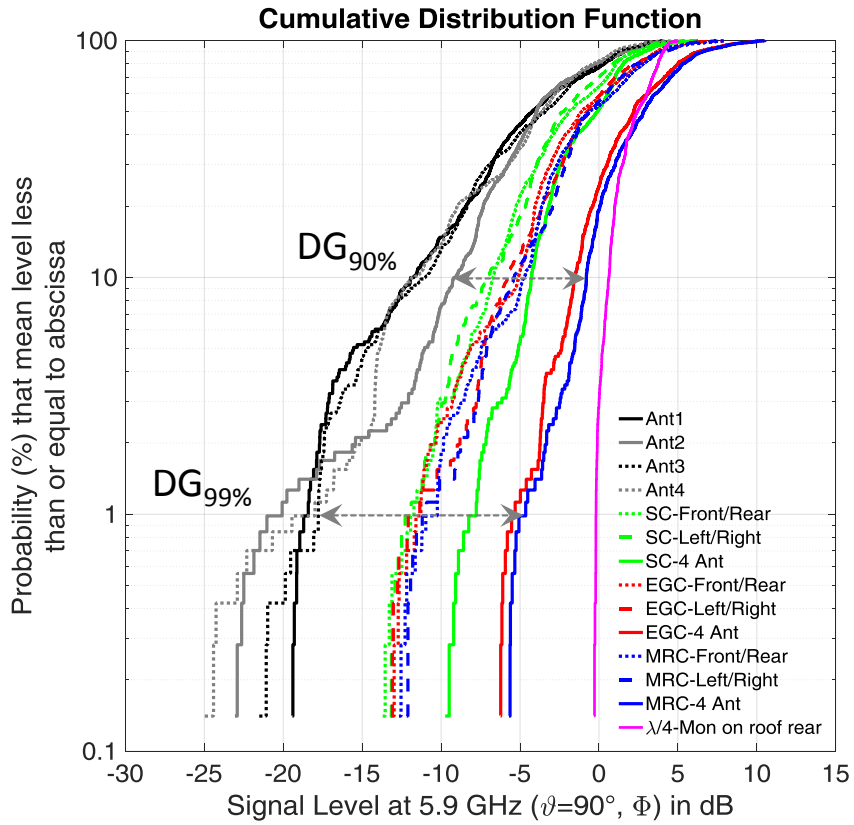

Figure 5.30: Four vs. two antenna diversity systems: CDFs of the measured horizontal radiation patterns comparing the diversity performance of arrays with four and 2 antennas. The graphic compares various diversity linear combining techniques with different antenna arrangements. The CDF of the single reference quarter-wave monopole antenna is also displayed for comparison purposes.

antennas with equal mean power level, a maximum instantaneous SNR difference in dB between EGC or MRC and the single antennas or switch or selection combining is $10 \cdot \log_{10}(M)$. With 2 antennas, a maximum instantaneous SNR difference of ≈3 dB is achieved under ideal conditions, while with 4 antennas, ≈6 dB can be achieved. However, the final user is not interested in instantaneous values, but the important thing is to ensure that the system works with a certain efficiency that exceeds a given threshold in a percentage of cases as high as possible. This information is provided by the cumulative distribution function (CDF), as the one shown in Fig. 5.30. Looking closer at the CDF, it can be inferred that with 4 antennas, roughly 2 dB more gain is achieved in median value comparing with the case of 2 antennas combined with the SC technique, while up to ≈4 dB are achieved with the MRC technique. The improvement with EGC is almost as good as that obtained with MRC, lying the EGC median value only less than 1 dB

below the MRC median value. The improvement of using 4 antennas is greatly increased at low cumulative probability values, which turn out to be the most important ones to offer a reliable system in a high percentage of cases. The improvement for MRC can be greater than 6 dB for cumulative probability values lower than 7 % or reliability levels greater than 93 %. It is also worth noting the worsening performance of EGC compared to SC at low cumulative probability values, where the signal level of the single antennas vary in a great extent. EGC performs worse after combining than SC selecting the branch with the largest SNR for a 2-antenna diversity system when the amplitude ratio between both single antennas is larger than 0.414, which means a difference in power greater than 7.66 dB. The CDF of Fig. 5.30 also shows that with two antennas the improvement with regard to a single antenna in the ideal roof-top mounting position occurs only at high cumulative probability values, and therefore, the use of at least four antennas is highly recommended to obtain a reliable V2X antenna system.

Unlike SDARS or AM/FM diversity systems, as the ones discussed in [116, 122] and [17, 104], where audio signals are evaluated, in V2X communication systems only data streams are exchanged between cars or cars and infrastructure. Since such data cannot be heard like digital radio, it is difficult to get an objective idea of how well the system works. This has been the main claim to derive graphically a value that gives an equivalent number of ideal antennas, completely uncorrelated and with equal mean power, to which the diversity antenna system under test corresponds. Similar procedures have been derived in [76] for AM/FM diversity systems, in which this value has been called *effective diversity order* or *diversity effectiveness*.

Figure 5.31 shows the graphical computation of the effective diversity order M_{eff} for the 4-antenna diversity system placed centered underneath the middle of the roof. The figure compares measurements on the left side and simulations on the right side. At a first glance, both simulations and measurements show en excellent agreement. Looking at the effective diversity order M_{eff} in the table at the bottom of Fig. 5.31, the difference between measurements and simulations is smaller than 3 %. Even a smaller difference is found when computing the power imbalance between the antennas. The difference in the envelope correlation factor is smaller than 6 %.

In Fig. 5.31, CDF curves are plotted in a linear scale. The abscissa shows the power SNR normalized with regard to the mean power SNR ($\langle SNR_{best} \rangle^2$) of the best antenna (that with the highest mean power SNR). It is well known that the quotient between the power SNR and the mean power SNR of the best antenna ($(SNR/\langle SNR_{best} \rangle)^2$) denotes, for EGC and MRC combinations, the theoretical ideal number of antennas M, which are completely uncorrelated, with equal mean power, and whose probability density functions are Rayleigh distributed. The CDF curves of such ideal antennas combined by means of MRC are shown as solid black lines as a reference for the cases of a single antenna and the MRC combinations up to four antennas, therefore there are four solid black lines. The solid red line shows the measured (on the left side) and simulated (on the right side) CDF curve of the MRC combination considering the four-antenna diversity system under test placed centered underneath the middle of the roof.

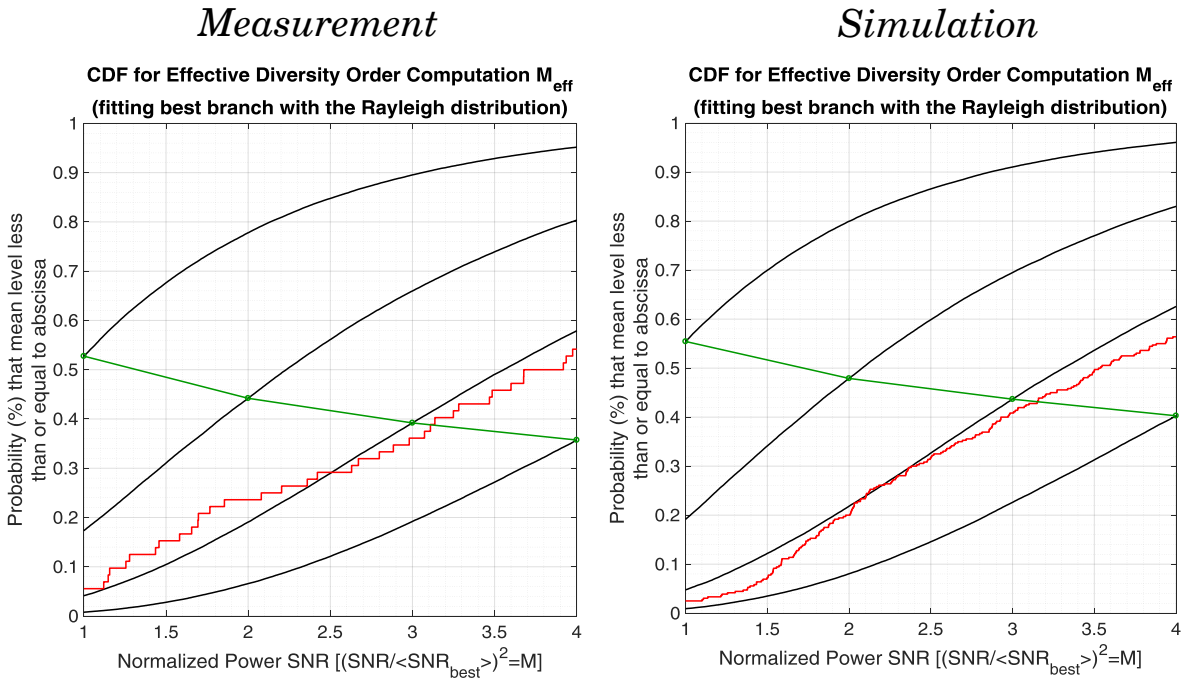

	Power Imbalance (dB)	ρ_{max}	M_{eff}
Measurement	0.7414	0.4738	3.12
Simulation	0.7466	0.5326	3.15

Figure 5.31: Effective diversity order: Graphical computation of the effective diversity order M_{eff} comparing measurements (left) with simulations (right). In the bottom of the figure, a table with a summary of the power imbalance, envelope correlation coefficient and effective diversity order values obtained with measurements and simulations.

The effective diversity order M_{eff} can be read from the abscissa at the point where the solid red line intersects the solid green line. This solid green line crosses the reference solid black lines at the corresponding number of ideal antennas. Thus, the value of the abscissa at such intersection point shows the equivalent number of ideal antennas to which the real diversity system corresponds. Considering the real environment inside the car, the four-antenna diversity system under evaluation yields an effective diversity order of $M_{eff} = 3.12$ in the measurements and $M_{eff} = 3.15$ in the simulations. According to [74], these values show that highly effective diversity systems with very low technical effort can be implemented in very compact and reduced spaces completely hidden underneath the roof. It is worth noting that Rayleigh distributed signals have been considered for the reference ideal antennas to be able to compare the performance of the investigated diversity system with the worst-case scenario. It is also important to point out that in practice the effective diversity order M_{eff} is always less than the number M of physical antennas. This is due to the fact that a correlation factor which exactly equals zero it is impossible to obtain in a real scenario. The antennas will also not show all the same mean power SNR.

Figure 5.32 shows the probability density functions (PDF's) from simulation results of each of the single antennas of the diversity set, and the SC and EGC linear combination techniques with four antennas located centered underneath the roof of the car. As already discussed and shown in Chapter 4, the statistical distribution that best fits and describes the performance of the single antennas and diversity combinations is the Nakagami distribution, due to its versatility to describe different types of communication scenarios. It is also worth noting the almost zero skewness of the PDF's obtained by means of diversity, compared to the positive skewness of each single antenna when placed underneath the roof. This effect corresponds to the diversity gain in CDF representations. A shift to larger envelope values is also obtained by means of diversity, which corresponds to an array gain due to the constructive addition of multiple antennas.

Figure 5.33 shows the probability density functions (PDF's) from measurement results of each of the four antennas that form the antenna diversity system under evaluation. The purpose of the figure is to illustrate the effect of removing the local mean or slow fading caused by the pillars of the car to characterize only the fast fading for which micro-diversity systems are intended to improve the performance. When all fading components are present, both the Rayleigh and Nakagami distributions fit very well the statistical distributions obtained, although the Nakagami distribution yields much better fit, as previously discussed and shown in Fig. 5.32 with the simulated results. When only the fast fading is considered, after a demeaning and offset operation, the Nakagami distribution clearly fits much better to the statistical distributions. The height of each bar in the histogram has been computed as (number of observations in the bin)/([total number of observations] · [bin's width]). The area of each bar is the relative number of observations. The sum of the bar areas is equal to one. A scaled plot of the fitted pdf has been overlayed to visually compare the fitted distribution with the actual measured values.

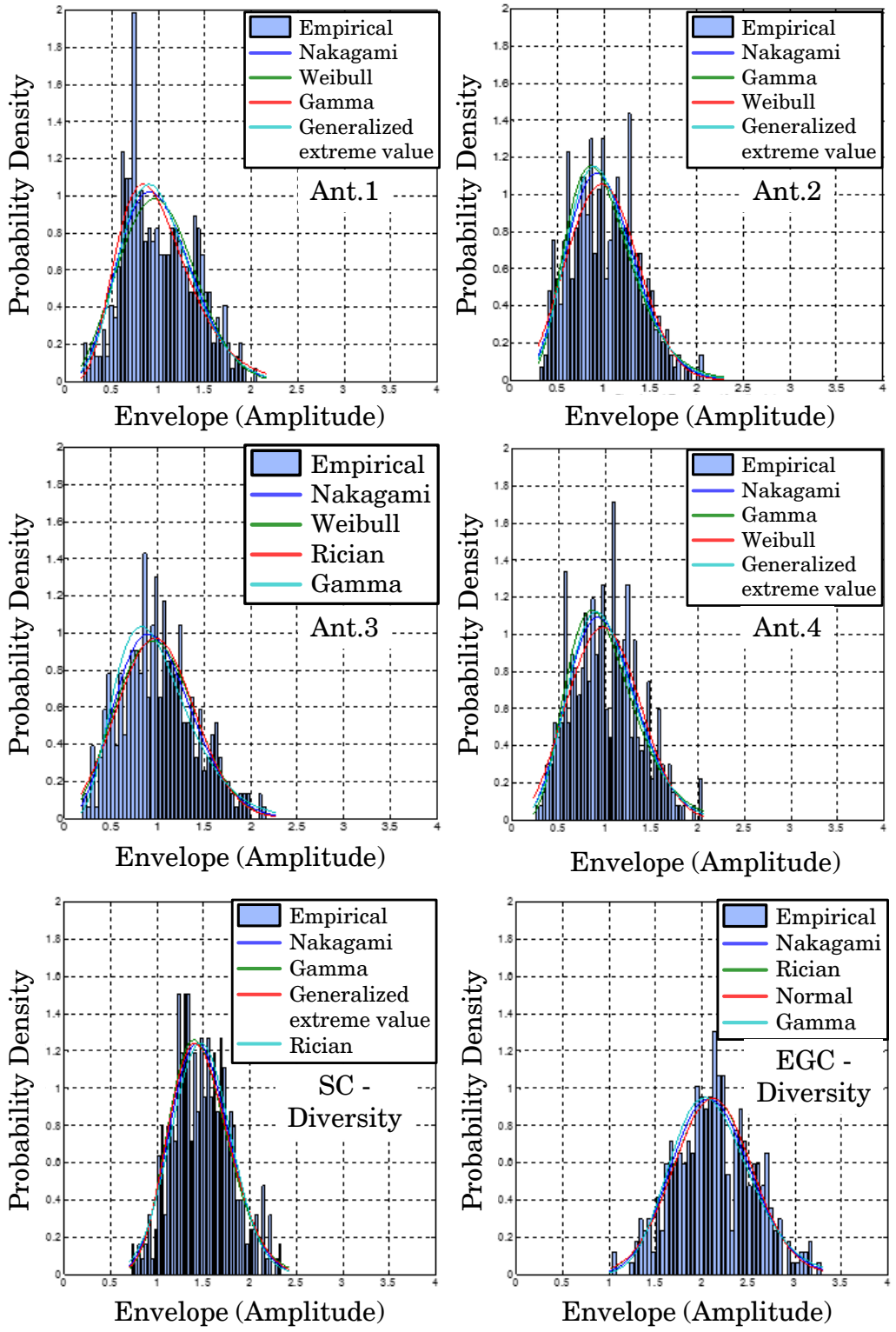

Figure 5.32: Statistical distributions of antennas underneath the roof (simulation): Probability density functions of single antennas and linear combinations in a diversity system underneath the roof.

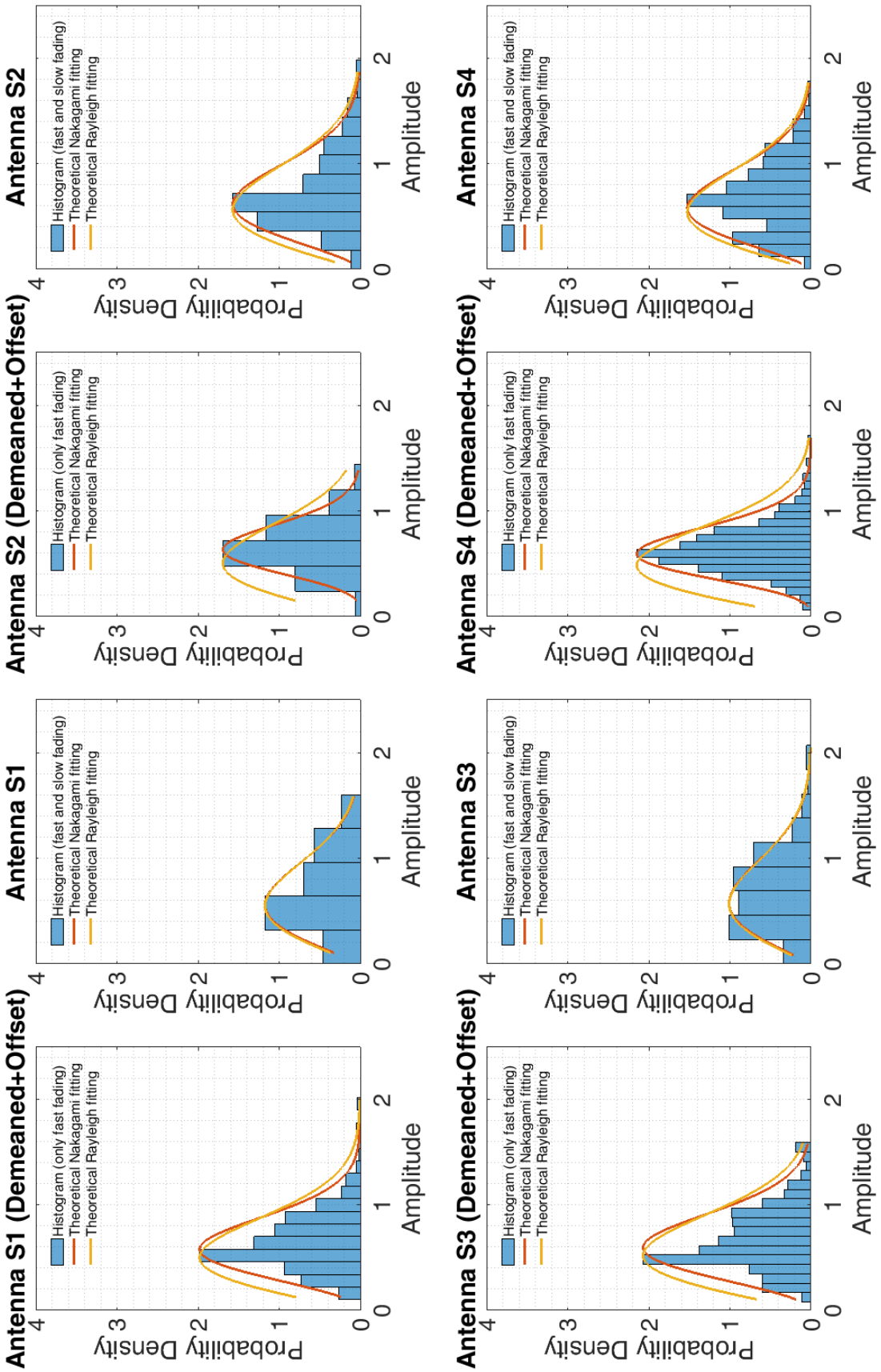

Figure 5.33: Effect of demeaning operation in statistical distributions of antennas underneath the roof (measurements): Probability density functions of single antennas in a diversity system underneath the roof before and after a demeaning and offset operation.

Figure 5.34: Spatial micro-diversity system composed of 4 antennas installed centered underneath the roof near the rear edge, inside the car's cabin (left), and detail of the rear side of the antenna set with the feeding system used in the measurements (right).

The performance of the diversity antenna system placed underneath the roof, near the rear edge, has also been investigated. This position has the advantage that the control units and front ends are usually installed near the rear edge. This fact allow the use of even shorter HF-cables, thus greatly reducing propagation losses through the cables, and the overall weight due to the cables installed. In a modern automobile, the wiring in the car can exceed 50 kg, so that a reduction in cable's length can have a great impact in fuel consumption.

Figure 5.34 shows a prototype of the diversity set under investigation installed underneath the roof, at the common distance from the rear edge of the roof where shark-fin antennas are usually placed. On the right side of the figure, the measurement setup in the OATS with a detail of the feeding system is shown. Care has been taken to ensure that the phase centre of the antenna set is located in the coordinate centre of the turntable in order to avoid phase corrections over azimuth. As can be inferred from the picture on the left side of Fig. 5.34, a ground plane provided with holes in the X- and Y-axis (referring to Fig. 5.21) and covered with copper tape has been built. The purpose of these holes is to investigate the effect on the diversity performance of different separation between the antennas. Once the antennas have been screwed into the correct position, the holes are covered again with copper tape to make a good ground plane in the vicinity of the antennas. The measured S-parameters used to compute the curves of Figures 5.22 and 5.24 are also obtained in this way. Electronic and mechanical components that may be close to the rear rim of the car's roof have been left intact to recreate more objectively the real interior of a car and their respective effects on the radiation patterns of the antennas.

Figure 5.35 shows the horizontal radiation patterns (conical cuts at $\theta \approx 90°$) of the spatial micro-diversity system composed of four inverted L-monopole antennas separated by a distance of $d \approx 0.6\lambda$ placed centered underneath the roof near the rear edge [22]. At a first glance, the

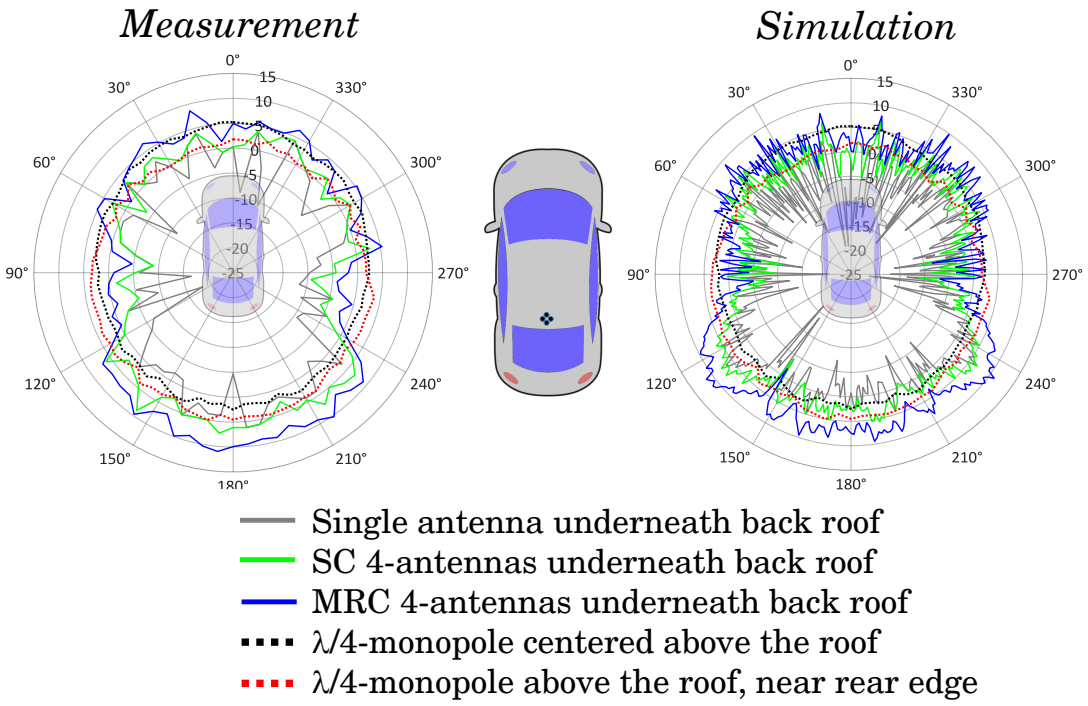

Figure 5.35: Diversity under roof in rear position: Horizontal radiation patterns (conical cuts at $\theta \approx 90°$) of the spatial micro-diversity system composed of 4 antennas separated by a distance $d \approx 0.6\lambda$ placed centered underneath the roof near the rear edge. Comparison of measurement results (left) and simulations (right) for various diversity linear combining techniques. Single reference quarter-wave monopole antennas are also displayed for comparison purposes. Measurement angle resolution of 5° and simulation resolution of 1°.

coincidence between measurements and simulations in the shape of the radiation patterns stands out. In both cases, it can be pointed out the difference in the ripple of the diagrams between driving direction and the opposite one. Due to the position of the antenna set near the rear rim of the roof, the electromagnetic waves launched by the antennas that propagate forward in driving direction have to cross a much greater distance to reach the windshield of the car, where they escape to the outside and radiate into the free space. During the way, they cross all kinds of obstacles and discontinuities that generate reflections and diffractions shedding energy in all directions. In the opposite direction of driving, the close presence of the rear window amplifies the optical effect that occurs when the wave passes through the glass with a certain angle of incidence. As a final result, nearly elliptical radiation patterns in azimuth are obtained, which can be advantageous in urban scenarios, as already discussed.

The performance trend of the various linear diversity combining techniques is the same as with the antennas placed centered underneath the middle of the roof. Significant improvement with regard to reference quarter-wave monopole antennas above the roof, in the ideal roof-top

mounted position, is achieved in an angular sector of roughly 140° around the opposite driving direction. In driving direction, almost the same range coverage than with ideal antennas above the roof is obtained with the diversity system underneath the roof.

It should be noted that for the rear position, the worst shadowing effects occur at azimuth angles around 90° and 270°, as inferred from Fig. 5.35. These angles correspond to the angular sectors where the C-pillars of the car are positioned relative to the rear antenna position. As discussed before, these long-term fading effects cannot be completely avoided with micro-diversity systems. In any case, these angular sectors are the least important ones in a V2X scenario, given that it is mostly intended to communicate with the cars ahead and behind.

Figure 5.36 shows the performance of the four-antenna diversity system underneath the roof, near the rear edge, when the side windows are down [22]. This is a common situation that has an electromagnetic relevance, since the windows of the car are made of dielectric materials that attenuate the incident wave and behave differently depending on the angle of incidence and polarization of the impinging electromagnetic wave. By way of illustration, Fig. 5.36 shows the horizontal patterns for the case where the side windows are opened. Comparing with Fig. 5.35, more directivity is achieved for angular sectors in azimuth between ≈35° and 75°, and between ≈285° and 315°. Again, these angles correspond to the angular sector where the side windows are situated with respect to the relative position of the antenna diversity system. No other changes can be seen at other azimuth angles of the radiation patterns comparing with those of Fig. 5.35.

To conclude a series of typical benchmark scenarios, the effect of human bodies inside the car has been investigated. This case is important for such antenna systems placed inside the car's cabin, due to the close proximity of the human bodies to the antenna system and their direct interaction with the fields radiated by the antennas. Figure 5.37 shows the simulation setup with the presence of the driver and passengers [22]. For the human bodies three layers of tissue have been considered. The electromagnetic properties of the human tissues used in the simulations, like the relative permittivity, loss tangent, conductivity and penetration depth, are summarized in a table inside Fig. 5.37. The dielectric properties of the human tissues have been taken from [54]. The figure also shows the Huygens' source used by the asymptotic solver. Due to the complexity of the electromagnetic problem, hybrid simulations have been performed. First the diversity antenna set has been simulated as stand-alone antenna by means of full-wave methods. The equivalent huygens' source has been computed and it is used as a main source for the asymptotic simulations considering the whole vehicle including the windows and the human bodies. Hybrid techniques allow to accelerate the simulation time with little loss of accuracy.

Figure 5.38 shows the radiation patterns of the four-antenna diversity system underneath the roof with the presence of the driver [22]. Almost no changes are observed with regard to the patterns without driver of Fig. 5.35. Only at azimuth angles around $\varphi \approx 30°$ a small magnitude variation can be seen. At elevation angles $\theta \approx 90°$, only the heads of tall human beings would be in the way of the electromagnetic wave. Moreover, looking closer at the sketch of the car with

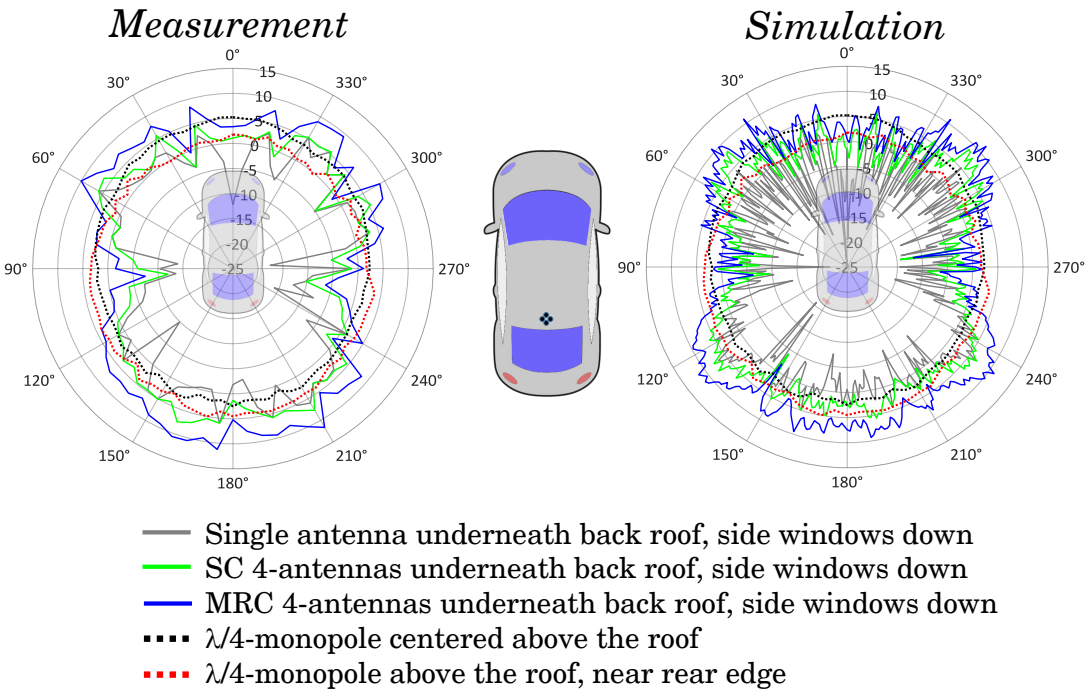

Figure 5.36: Effect of side windows down: Horizontal radiation patterns (conical cuts at $\theta \approx 90°$) of the spatial micro-diversity system composed of 4 antennas separated by a distance $d \approx 0.6\lambda$ placed centered underneath the roof near the rear edge, with the side windows opened. Comparison of measurement results (left) and simulations (right) for various diversity linear combining techniques. Single reference quarter-wave monopole antennas are also displayed for comparison purposes. Measurement angle resolution of 5° and simulation resolution of 1°.

the driver on the middle of Fig. 5.38, it can be observed that the angle relative to the antenna set position where the human head is located coincides with the relative angular position of the A-pillar of the car. This means that due to the shadowing effect of the A-pillar, the effect of the partial shadowing of the human body is masked by the former. Of course, as the elevation angle moves away from $\theta \approx 90°$, the radiation patterns become much more distorted and the omnidirectional character begins to be lost. But this fact also happens without the presence of human beings inside the car, since it is an inherent effect of the geometric structure of the car. No major changes have been observed in the case where the car is occupied by all passengers. Ony with passengers in the rear seats, a greater ripple of less than 2 dB can be observed at azimuth angles between 120° and 240°.

As before, statistical tools have been used to evaluate the diversity performance of the system considering the different benchmark scenarios discussed before and shown in Figures 5.35, 5.36, and 5.38. Figure 5.39 shows the CDF's derived from the horizontal radiation patterns of such figures [22]. On the left side of Fig. 5.39, some significant measured results for all positions and

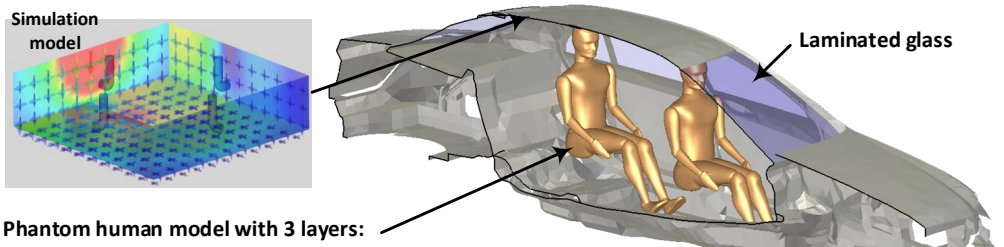

f =5.9 GHz	Dry Skin	Fat	Muscle
Relative Permittivity $[\varepsilon]$	35.03	4.95	48.35
Loss Tangent $[\tan\delta]$	0.33	0.18	0.32
Conductivity $[\sigma\,(S/m)]$	3.80	0.30	5.08
Penetration Depth $[d(mm)]$	8.37	39.56	7.36

Figure 5.37: Diversity system setup under the presence of human bodies: Spatial micro-diversity system composed of 4 antennas installed centered underneath the roof near the rear edge, inside the car's cabin, under the presence of human bodies. Full-wave simulation setup for the diversity antenna set showing the huygens' sources (left), and the complete asymptotic simulation setup with the whole car and the human bodies (right). Table with the electromagnetic properties and thicknesses of the human tissues considered (bottom) taken from [54].

cases investigated are shown together for comparison purposes. It is worth noting the power difference between a single antenna placed centered underneath the middle of the roof and in the rear position. For the MRC linear combinations, the differences between benchmark scenarios are not so high as with single antennas, especially for low cumulative probability values. However, it can be stated in general that the position under the roof near the rear edge yields better results up to reliability levels of about 80 %. It can be seen that the diversity system underneath the roof, near the rear edge, overcomes the performance of an antenna in the ideal roof-top position at a cumulative probability level lower than with the diversity system centered underneath the roof. The side windows of the car have an influence on the performance of the system for cumulative probability values between 20 % and 80 %, where the improvement is of roughly 1 dB.

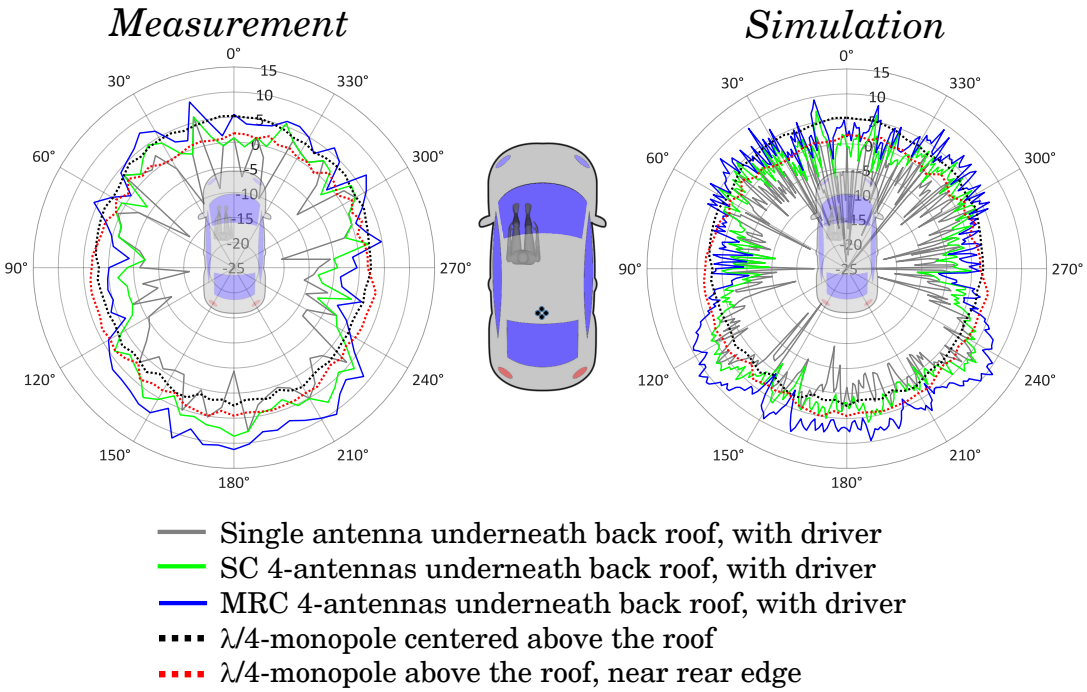

Figure 5.38: Effect of human bodies (driver): Horizontal radiation patterns (conical cuts at $\theta \approx 90°$) of the spatial micro-diversity system composed of 4 antennas separated by a distance $d \approx 0.6\lambda$ placed centered underneath the roof near the rear edge, with the presence of the driver. Comparison of measurement results (left) and simulations (right) for various diversity linear combining techniques. Single reference quarter-wave monopole antennas are also displayed for comparison purposes. Measurement angle resolution of 5° and simulation resolution of 1°.

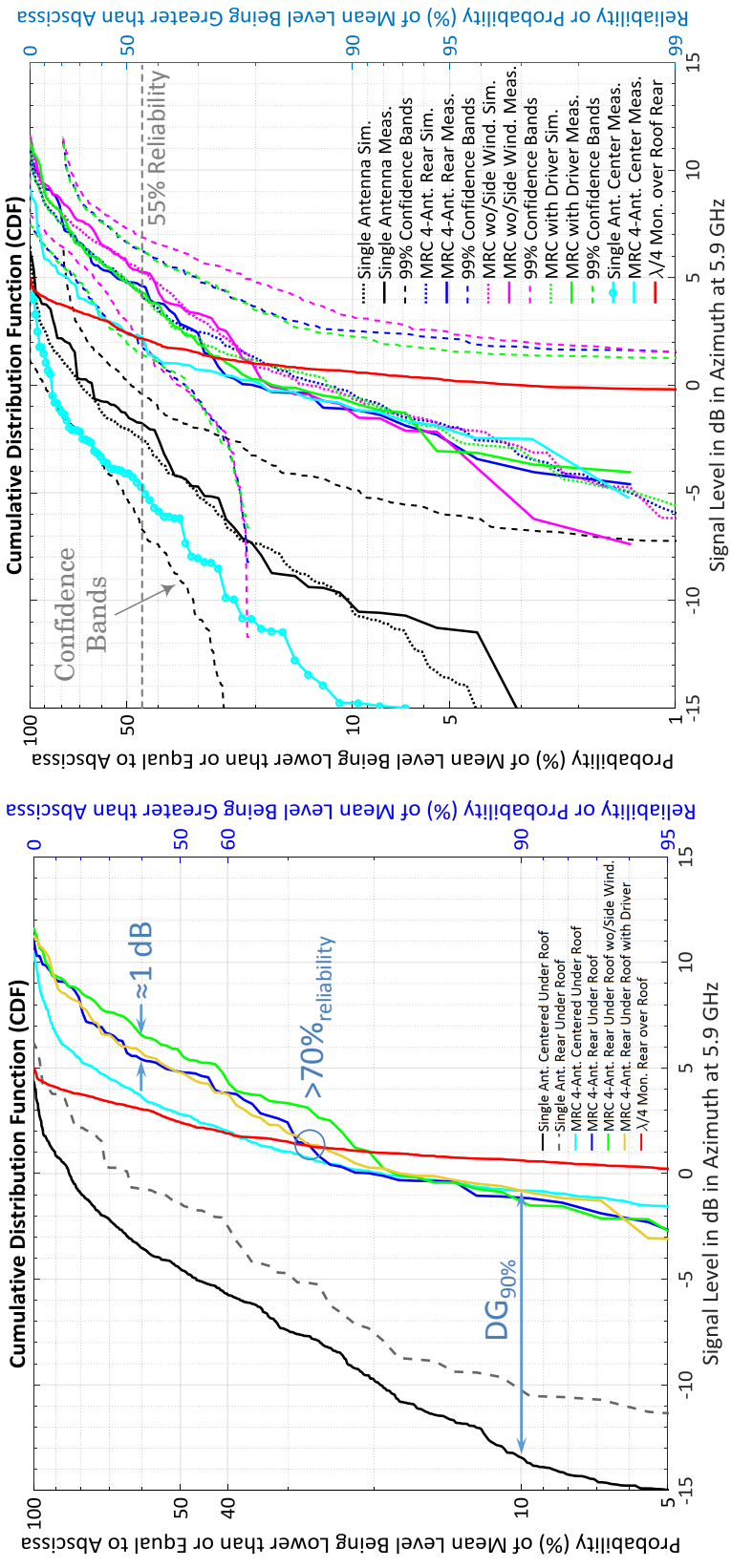

Figure 5.39: Statistical evaluation of different benchmark scenarios: CDFs derived from the horizontal radiation patterns of Figures 5.35, 5.36, and 5.38, to evaluate the diversity performance of different benchmark scenarios. On the left side, a comparison between the measured results of the different scenarios is shown, highlighting the diversity gain and some important points. On the right side, a comparison between simulations and measurements with their corresponding confidence bands is shown. CDFs of the values achieved with single reference quarter-wave monopole antennas are also displayed for completeness.

As a concluding remark, it should be noted that higher diversity gains at the 90 % cumulative probability level are obtained for the diversity system placed centered underneath the roof. However, almost the same array gain is obtained for all systems, as it could not be otherwise, since the antenna set is the same in all cases.

On the right side of Fig. 5.39, simulations and measurements are compared together to show the good agreement obtained. By means of the confidence bands derived from the Kolmogorov-Smirnov test, it can be concluded that good results can be obtained by means of simulations, saving the economic and time cost of long and tedious measurements. All curves lie within the derived confidence bands.

5.3 Frequency Selective Surface (FSS) Structures in Front and Rear Screen

Hidden antennas are increasingly in demand in the automotive sector, as already discussed. With the technology improvement in the last decades in terms of miniaturization and the increasingly demanding aesthetic requirements, hidden antennas somewhere in the car are seen as a promising solution. Among the various possibilities to hide the antennas, as the one discussed in [9, 47] in a cavity in the car's roof, one possibility and logical step to remove the antenna from the outer side of the chassis without the need to redesign the roof of the car, is to hide it somewhere inside the car's cabin. But due to the metallic enclosure of the chassis the only way that have the electromagnetic wave to radiate outwards is through the windows of the car.

Nowadays, more and more automobiles are equipped with solar control or energy saving glasses, which add a transparent electrically conducting layer to the commonly used laminated glass to selectively reflect the heat-causing infrared (IR) radiation (wavelengths between 780 and 2500 nm), and block the ultraviolet (UV) rays present in sunlight (wavelengths between 100 and 380 nm), while making possible viewing through the window [98]. Such metal-coated glasses keep a constant temperature in the inside of the car both in summer and in winter, reducing the fuel consumption to maintain a desired temperature, but they have the main drawback that they not allow microwave radiation to pass through. In order to improve the transmission properties of such electrical insulation at microwave frequencies without overly compromising the thermal and visual characteristics, a frequency selective surface (FSS) in the metal coating in the form of thin slots is proposed. The radiation coming from or going to the antenna hidden inside the car is absorbed by the metal coating and retransmitted by the slots which act as antennas.

Figure 5.40 shows the concept of the frequency selective surface (FSS) in the windshield of a car. At the top of the figure, a sketch of a V2X scenario is depicted. The sketch illustrates a car equipped with saving energy glass and a FSS structure on the metal coating of the glass, allowing the electromagnetic waves coming from the V2X antenna to pass through the glass and reflecting the heat waves coming from the sun. Of course, all this must be done in a way that is

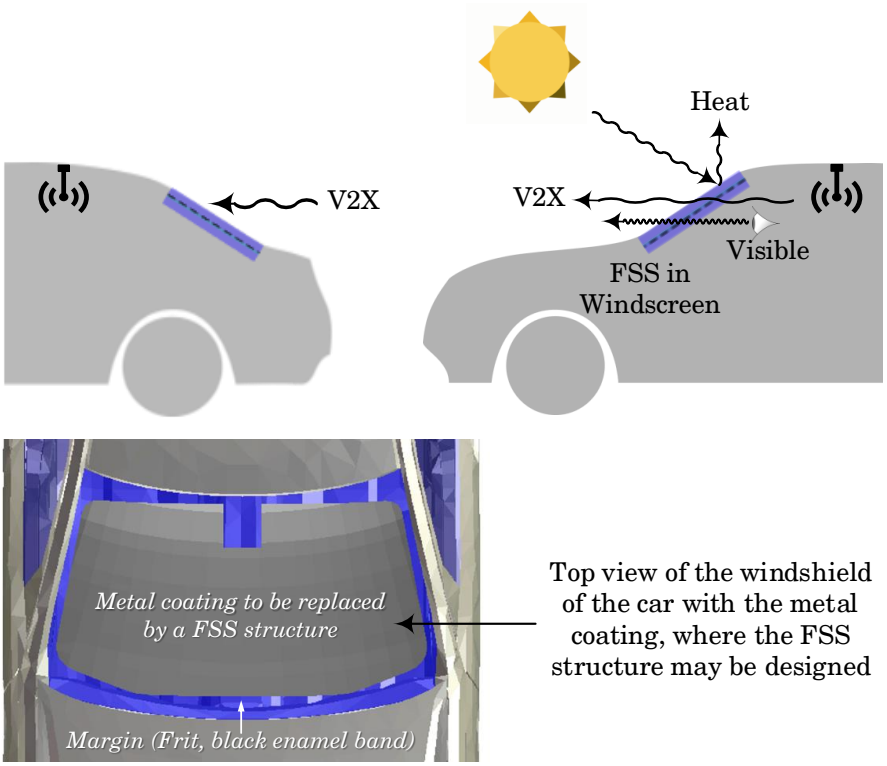

Figure 5.40: Frequency Selective Structure (FSS) concept in the windshield of a car: V2X scenario with a car equipped with energy saving windshield with a FSS structure in the metal coating (top), and CAD simulation model of a car with laminated glass and metal coating with the frit or black enamel band (bottom).

transparent to the eye, so that it can be seen without any kind of obstacle to the sight. At the bottom of Fig. 5.40, the CAD simulation model of a car with laminated glass and metal coating, where the FSS structure may be designed, is shown with a detail of the frit or black enamel band, which is the margin free of metal in such solar control windshields to commonly locate sensors or AM/FM antennas.

5.3.1 Transmittance and Reflectance of FSS Structures in Energy Saving Glass

The FSS structure is intended to be designed in the transparent metal coating between the layers of the laminated glass. This metal-coated sheet has a relatively small electrical resistance of typically 4 Ω/sq, and it makes possible to reflect the IR radiation while keeping a clear visibility. The FSS structure can be seen as a space three-dimensional filter. Unlike two-dimensional filters made of transmission lines or lumped elements, the space filters add two degrees of difficulty to their design: the angle of incidence at which the electromagnetic wave impinges the filter and the

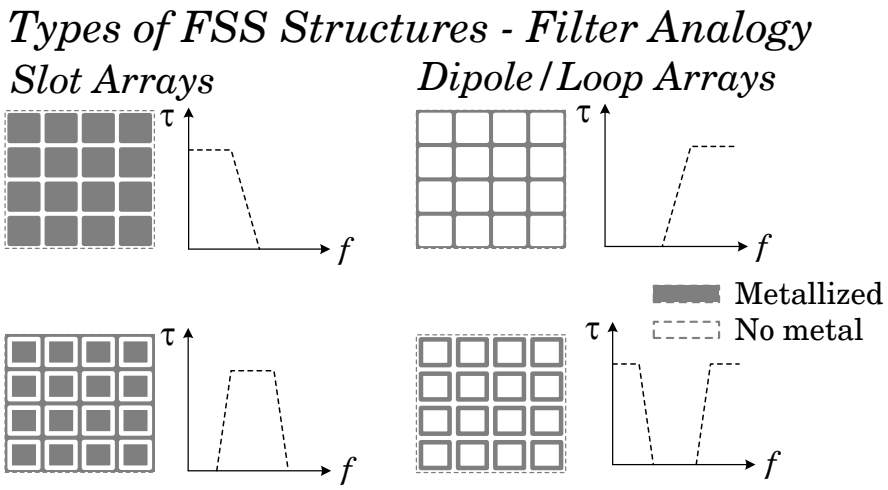

Figure 5.41: Types of FSS structures and their filter analogy: Slot arrays that minimize the non-metallized area (left), and dipole or loop arrays that minimize the metallized area (right).

polarization of the wave. FSS structures change their performance depending on the variation of these two aspects.

Figure 5.41 shows as a summary, the different types of FSS structures and their filter analogy depending on the pattern and percentage of the metallized and non-metallized region. It can be seen how slot arrays act as low-pass or band-pass filters, while dipole or loop arrays act as high-pass or band-rejection filters. It may be pointed out that for energy saving windows, the slot array case is the most interesting one, since it is intended to minimize the region without metal and hence, maximize the efficiency of such solar control glasses. Moreover, although the horizontal or vertical slot arrays (top, left in Fig. 5.41) are the ones that yield the highest frequency bandwidth, for V2X communication the slot arrays shown at the bottom of Fig. 5.41 on the left side are the most suitable ones to obtain the best frequency response. This is due to the inherently narrow bandwidth of the V2X systems.

Continuing with the analogy of filters, let us explain in more detail the operation principle of such FSS structures in the energy saving windows of the car. By means of transmission line theory, the effect of the laminated glass can be completely reproduced by varying the characteristic impedance and electrical length of the transmission line. The FSS structure can be modeled by means of lumped elements and resistances to account for ohmic losses. Both transmission lines and the lumped elements characterizing the whole energy saving glass are dependent on frequency, angle of incidence, and polarization of the impinging electromagnetic wave. Thus, the individual values of the characteristic impedances, electrical lengths and capacitors, inductors or resistances will be dependent on frequency, angle of incidence and polarization.

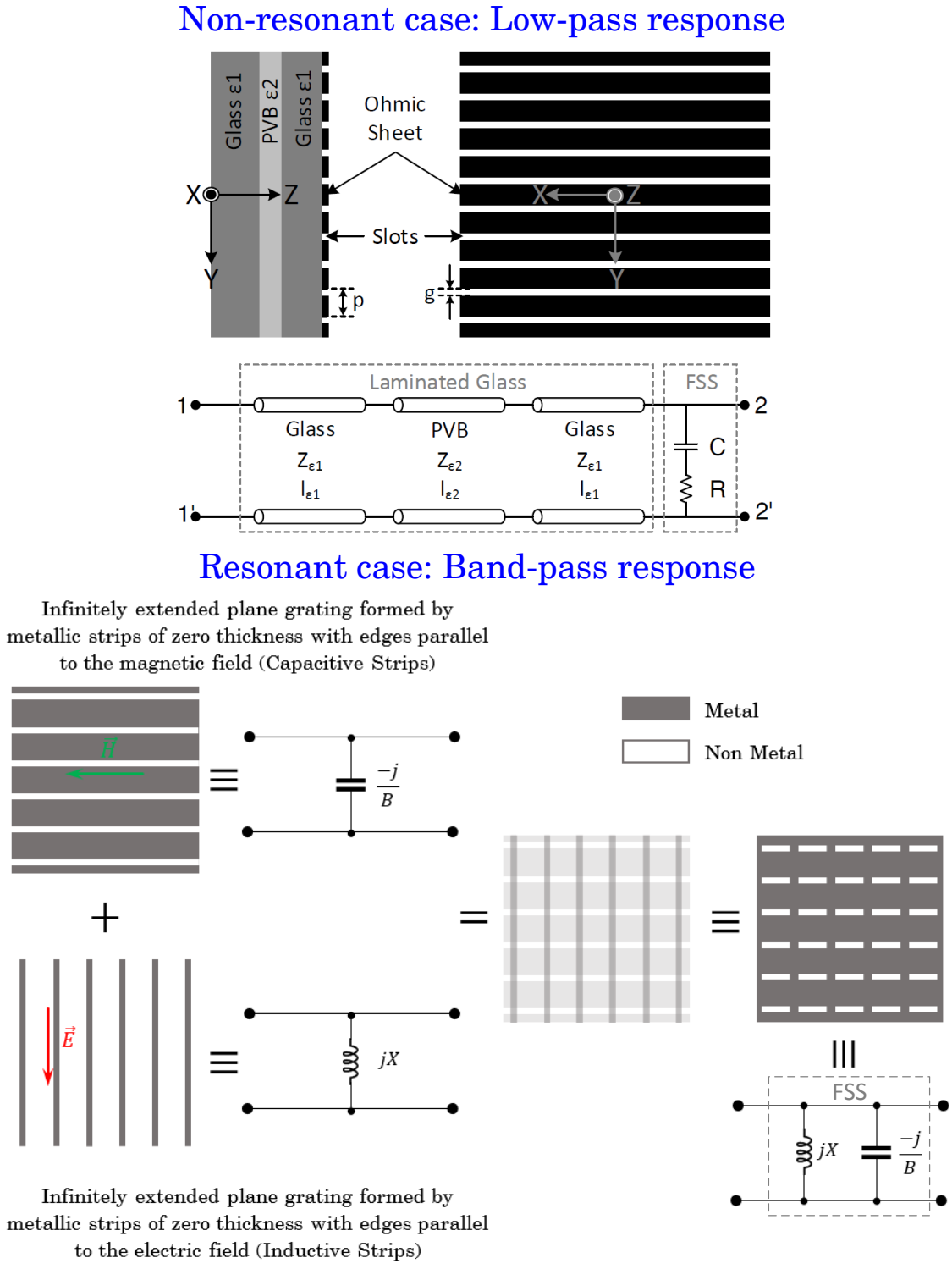

Figure 5.42: Equivalent transmission line circuit model of an energy saving glass with a FSS structure on the metal coating: Non-resonant case of infinitely extended slots yielding low-pass response (top), and resonant case with slots of finite length yielding band-pass response as a combination of infinitely extended slots and metal strips (bottom).

Figure 5.42 shows the circuit equivalent model of the laminated glass with FSS structure in the metal coating of the solar control glass. At the top of the figure, the non-resonant case is shown. It is formed by infinitely extended slots yielding a low-pass response. A high-pass response can be obtained with infinitely extended metal strips. For an electric field oriented perpendicular to the slots, these act as a capacitor. For an electric field oriented in parallel to the slots, these act as an inductor [85]. At the bottom of Fig. 5.42, the resonant case is shown. It yields a band-pass response when an array of slots is used. A band-rejection response can be obtained with dipole or loop arrays, with much better performance if they are loaded in some way, as it will be shown later[89].

These resonant structures can be thought to be composed of a combination of infinitely extended slots and infinitely extended metal strips, as shown at the bottom of Fig. 5.42 on the left side. In this way, a simple parallel LC-tank is formed, as shown at the bottom of Fig. 5.42 on the right side, causing a resonance at the resonance frequency given by $1/\left(2\pi\sqrt{LC}\right)$.

Excellent transmission properties can be obtained by tuning the resonance frequency of the FSS structure at the center frequency of the V2X communication standard. However, it is worth noting to emphasize the fact that the FSS structure in the metal coating of the energy saving glass must be optimized as a whole, considering the laminated glass effects discussed in section 5.1.2.2. Adding dielectric slabs to a FSS structure change dramatically the performance of the FSS stand-alone design [89]. Hence, the laminated glass should always be considered in the design of such electromagnetic transmission windows, as shown in the transmission line circuit at the top of Fig. 5.42. Very good transmission properties are seen for incidence angles from $\approx$ 60° to roughly 75° for vertically polarized waves in a laminated glass of the type commonly used for automotive purposes, as already shown in Fig. 5.12 of section 5.1.2.2. Luckily, these angles correspond to the most probable ones considering the inclination of the windshield or rear glass with respect to the relative position of the antenna and taking into account that the separation between the antenna and the windows is large with regard to the wavelength at V2X frequencies.

The next logical step when designing FSS structures is the choice of the basic element type to fulfill the requirements of the application under consideration. Due to the inherently narrow bandwidth of V2X communication, it may be enough to use a complementary element to that of a dipole, hence a slot with finite dimensions, more precisely, a slot of roughly half wavelength at about 5.9 GHz. With slots of 0.5λ length oriented perpendicular to the vertically polarized wave launched from a V2X antenna, thus horizontally oriented slots, a band-pass response is obtained as shown in the cartesian plot of Fig. 5.43 corresponding to the unloaded element. However, and as can be inferred from Fig. 5.43, this simple element offers a poor performance when varying the angle of incidence of the impinging wave, since the frequency response of the FSS structure is not stable with varying the angle of incidence. This unwanted effect is very important to be avoided in general, and especially for antenna systems placed underneath the roof. The reason of

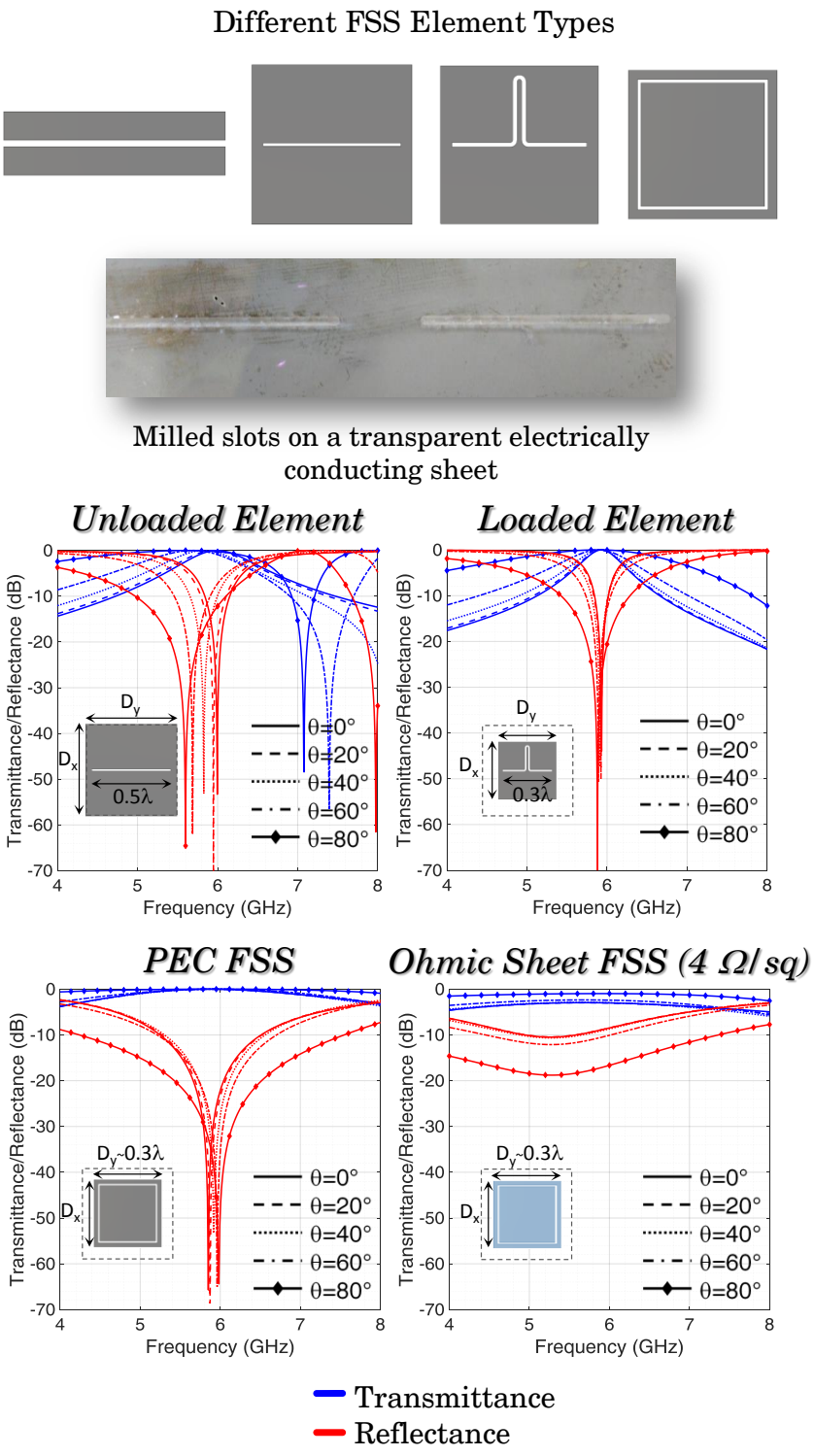

Figure 5.43: Electromagnetic behaviour of different FSS element types: Sketch of the CAD model of different FSS element types used in simulations (top), milled slots on a transparent electrically conducting sheet (middle, top), electromagnetic comparison comparison in terms of transmission and reflection coefficients between unloaded and loaded slot elements (middle, bottom), and comparison between PEC and resistive sheet with a resistance of 4 Ω/sq for a square loop (bottom).

this is the randomness of the angle at which the electromagnetic waves strike the windows of the car in such chaotic scenarios as those corresponding to antennas hidden inside the chassis of the car. Even if plane wave conditions are considered, the inclination of the windshield or the rear window of the car yields to incidence angles close to 60° with regard to the normal vector of the windows. To obtain acceptable and stable performance at such incidence angles far away from the normal incidence case and in a wide angular spectrum is a great challenge. The simple half-wavelength slot or dipole cases hide another remarkable problem, and that is the onset of grating lobes, which can be seen as multiple resonances in the transmission and reflection curves above the fundamental resonance of the slot or dipole under consideration. This effect can also be observed in the transmission curves of Fig. 5.43 corresponding to the unloaded element. The cause relates to the excessive overall length of the slot or dipole, which in a periodic structure favors the onset of grating lobes destroying the performance of the lattice structure.

In order to obtain stable performance with varying the angle of incidence, loaded elements should be used as explained in [89]. Loaded elements reduce the overall length of the basic unit cell, so that when it is periodically extended the onset of grating lobes appear at a much higher frequency away from the resonance. At the top of Fig. 5.43, different FSS element types considered in this dissertation are shown. From left to right, the infinitely extended slot, the half-wavelength slot, the loaded slot ($\approx 0.3\lambda$ long), and the square slot are shown. As already discussed, the infinitely extended slot offers low-pass response, and the other examples band-pass response. At the middle of Fig. 5.43, a comparison between unloaded and loaded elements is illustrated. The superior performance offered by the loaded element, the loaded slot, is directly recognized. The loaded element not only offers stability with varying the angle of incidence, but it also avoids the onset of grating lobes at neighboring frequencies. At the bottom of Fig. 5.43, it can be seen the worsening effects of using real materials when building a FSS prototype in a resistive sheet with a resistance of typically $4\,\Omega$/sq. Comparing with the PEC case at the bottom of Fig. 5.43 on the left side, a bandwidth reduction, displacement of the resonance frequency to the lower-end, and reduction of the transmission coefficient due to ohmic losses are the main drawbacks of such resistive sheets.

Figure 5.43 also shows another remarkable point, and this is the superior performance of the square slot comparing with all other types discussed before. The square slot is almost as stable as the loaded slot when varying the angle of incidence but the bandwidth is clearly larger. Moreover, the stability with various angles of incidence is also maintained for different polarizations as it consists of a combination of vertical and horizontal slots. The whole square is significantly smaller than 0.5λ, preventing the onset of grating lobes. It is worth noting that although the V2X frequency range is inherently narrowband, the use of real ohmic sheets and the position of the FSS structure between the dielectric layers of the laminated glass degrade the electromagnetic performance of the transmission window, reducing the bandwidth, shifting the resonance frequency and adding ohmic losses.

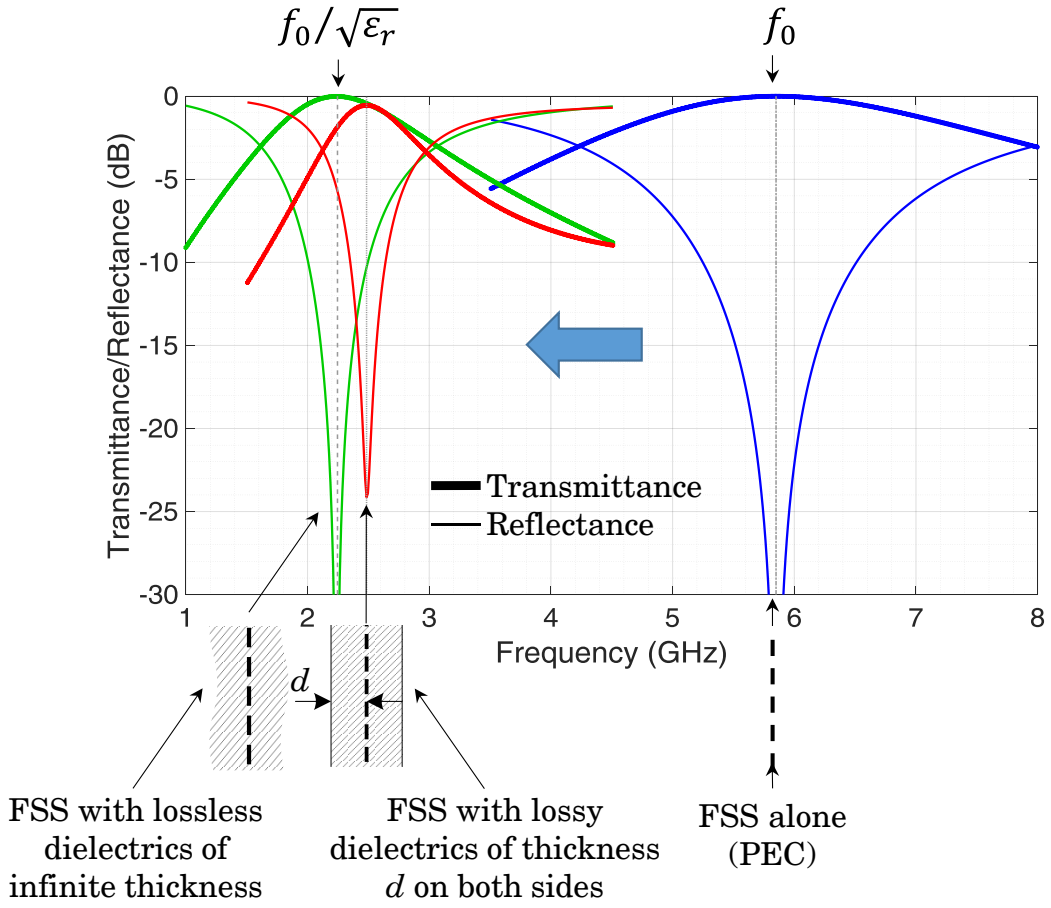

Figure 5.44: Effect of adding dielectric slabs to a FSS structure: The graphic shows the transmittance and reflectance in dB over frequency for a stand-alone FSS structure made of PEC (blue), the same structure with lossless dielectrics of infinite thickness (green), and with lossy dielectrics of finite thickness on both sides of the FSS structure (red).

There are different techniques to fabricate the FSS structure. The slots can be milled or even better lasered in the transparent resistive sheet. An example of milled slots on a transparent electrically conducting sheet performed at the university is shown in Fig. 5.43. Due to the thinness of the slots, better results can be obtained by lasering the slots in the surface.

As already mentioned and according to [89], it is a big mistake to design the FSS structure without taking into account the dielectric effects of the laminated glass where the FSS structure is intended to be sandwiched. Figure 5.44 shows schematically the effects of adding dielectric slabs on both sides of the FSS structure. The main recognizable effect is the shift of the resonance frequency towards lower frequencies. In the case of lossless dielectrics of infinite thickness on both sides of the FSS structure, the resonance frequency moves to a lower frequency by a factor of

$1/\sqrt{\varepsilon_r}$. When the dielectrics are lossy, as in real cases, the transmission and reflection coefficients degrade, further reducing the bandwidth of the structure. Figure 5.44 also shows that using dielectrics of finite thickness on both sides of the FSS structure, the resonance frequency is reduced to a frequency within the range $f_c \in \left(f_0/\sqrt{\varepsilon_r};\quad f_0\right)$. Since the laminated glass of the car has a dielectric constant close to 6.9, the electromagnetic performance of the FSS structure inside the laminated glass is drastically changed.

As in the case of the procedure of a radome design [123], the methodology used to design such FSS structures is basically the same. First, the transmittance and reflectance of the structure is investigated and then, the mounting position effects and end effects of using finite periodic structures are quantified. The first step is thus the electromagnetic characterization of the transmission and reflection properties of the energy saving glass with FSS structure in the transparent metal coating. For this purpose, only a single unit cell with the element type under investigation is considered. Periodic boundary conditions, Floquet mode ports, and plane wave incidence is considered to investigate the transmittance and reflectance of the whole structure. This procedure is shown schematically on the right side of Fig. 5.45. In order to be able to proof the simulated results by means of measurements, a Rogers 4003C substrate material [106] is used instead of the laminated glass of automotive windscreens. The reason of substituting the energy saving glass by a high-frequency substrate material is the ease with which the FSS structure can be manufactured compared to the difficulty of handling a windshield of a real car. Care has been taken to choose a material with effective dielectric properties as similar as possible to those of laminated car glass.

On the left side of Fig. 5.45, the measurement prototype with the square slots lasered on a Rogers 4003C substrate and a detail of the single unit cell from the manufactured prototype are shown at the top of the figure. At the bottom, the measurement setup at the University of the Bundeswehr with two broadband log-periodic antennas from Rohde & Schwarz [107] at each side of the periodic structure is shown for comparison purposes with the simulation setup on the right side of Fig. 5.45. The measurement setup has been equipped with a rotating disc with printed angles built at the Institute of High Frequency Technology and Mobile Communication of the University of the Bundeswehr in Munich, to be able to measure the structure under different angles of incidence. As already mentioned, the expected electromagnetic behaviour is that of a band-pass filter, as shown in the inset of Fig. 5.45.

Figure 5.46 shows the measured (left) and simulated (right) results of the transmission coefficients obtained by means of the measurement setup of Fig. 5.45. The coefficients are measured for different incidence angles and polarizations of the incoming wave, as shown in the sketch at the bottom of the figure. All curves have been normalized to the average value of the reference curve without FSS structure. The results are compared with the cases without FSS structure (free space transmission, red curve) and with a full metal sheet between both antennas (black curve).

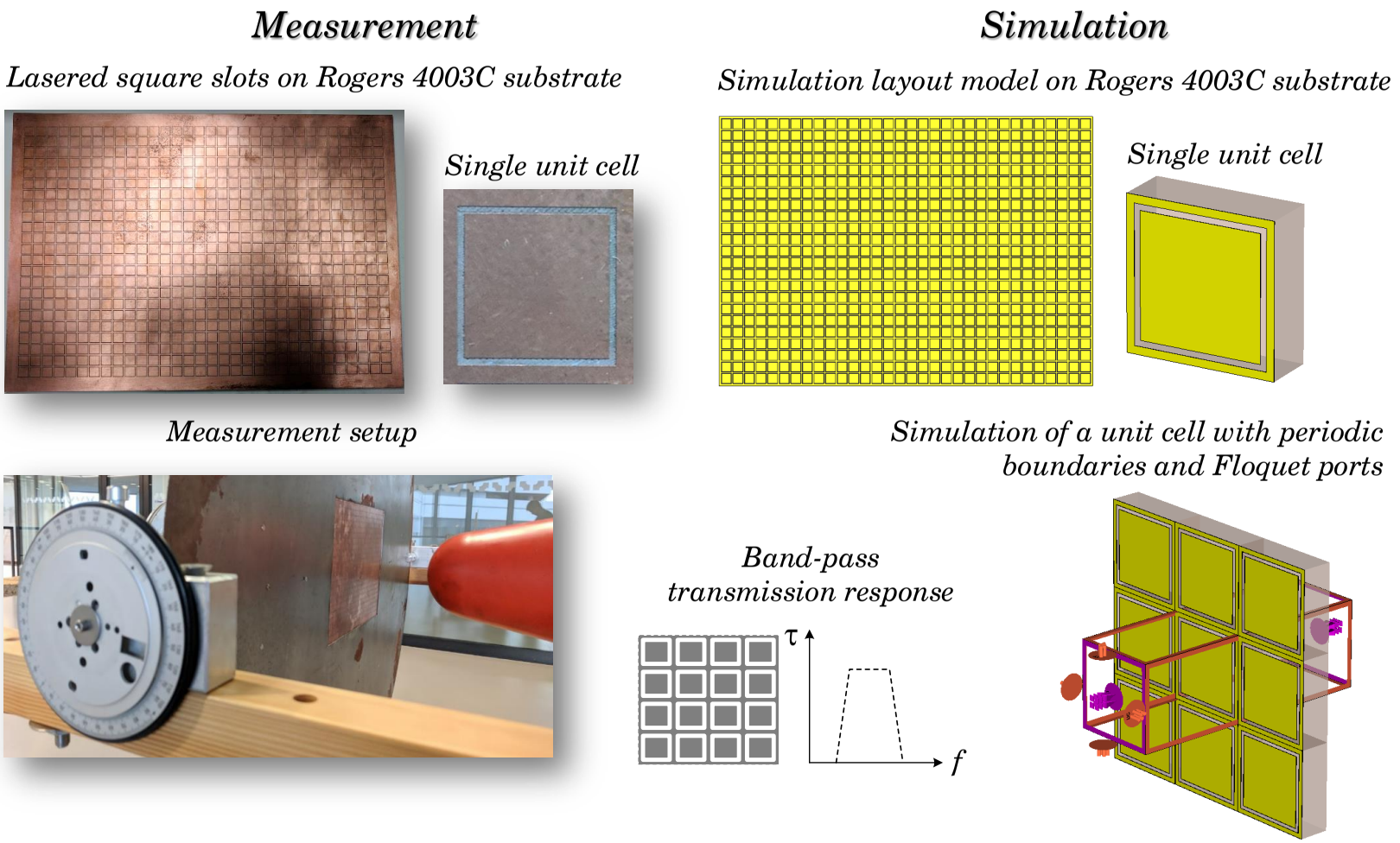

Figure 5.45: Measurement and simulation setups to characterize the transmittance and reflectance of the energy saving glass with FSS structure on the metal coating: Measurement prototype on a Rogers 4003C substrate substituting the laminated glass (left), and simulation prototype with periodic boundary conditions, floquet mode ports, and plane wave excitation (right).

Figure 5.46: Transmission coefficients of energy saving glass with FSS structure on metal coating: Measured (left) and simulated (right) results for different incidence angles and polarizations using the measurement setup of Fig. 5.45.

The first thing that stands out is the similarity between measurements and simulations. Measured curves show a small ripple due to the end effects of using a finite periodic structure, which causes reflections at the margins of the prototype. However, almost the same magnitude values are obtained in all cases.

The second important thing that can be observed in Fig. 5.46, is the fact that almost the same transmission coefficients are obtained with FSS structure and in free space transmission, although the metallized area in the FSS structure is greater than 97 %. This means that, comparing with the case of a full metal sheet between the antennas, only less than 3 % of the metal coating has been removed to laser the slots, thus maintaining the efficiency of the energy saving glass to a great extent. The transmission loss in the case of a full metal sheet between the antennas is roughly 35 dB, showing also good agreement between measurements and simulations and the importance of such FSS structures to improve the transmission properties through the windows of the car.

5.3.2 Electromagnetic Characterization of FSS Structures Considering the Vehicle

The next step in the procedure to design FSS structures, and according to [123] for the similar case of radome design, is to evaluate the effects of mounting the structure in its real position, with the real curvature of modern automotive glass windows to make the structure conformal with the mounting position and taking into account the environment surrounding the structure electromagnetically relevant at the frequency of interest.

Figure 5.47 shows the effects on radiation pattern of considering different windscreen configurations using energy saving glass with a FSS structure in the transparent metallized layer. The results are always compared to the case where only a laminated glass is considered, so that no metal-coated layer is present as a reference value.

Due to the complexity of manufacturing a prototype with such a great number of small slots in the micro meter region[6], only simulation results have been computed. However, and as shown during the dissertation, very good agreement has been always obtained between measurements and simulations and, due to the fact that the materials, dimensions, frequency of operation, geometry of the problem, and simulation methods have not been changed with regard to previous simulations, it can be inferred that the simulation results obtained in this subsection can also be trusted.

To simplify the simulations, only “infinitely” extended (to the extent of the windscreen) horizontal slots have been considered. For reasons of minimizing the simulation time and saving

[6]The width of the slots perforated in the conductive layer should be small enough to be transparent to the eye and minimize the uncoated area to ensure thermal insulation of the energy saving glass. The visual acuity in human beings reaches to see objects of dimensions in width greater than 20 µm. This means that objects narrower than 20 µm are undistinguishable. Thus, the slots in the FSS structure should be narrower than 20 µm to be transparent to the driver.

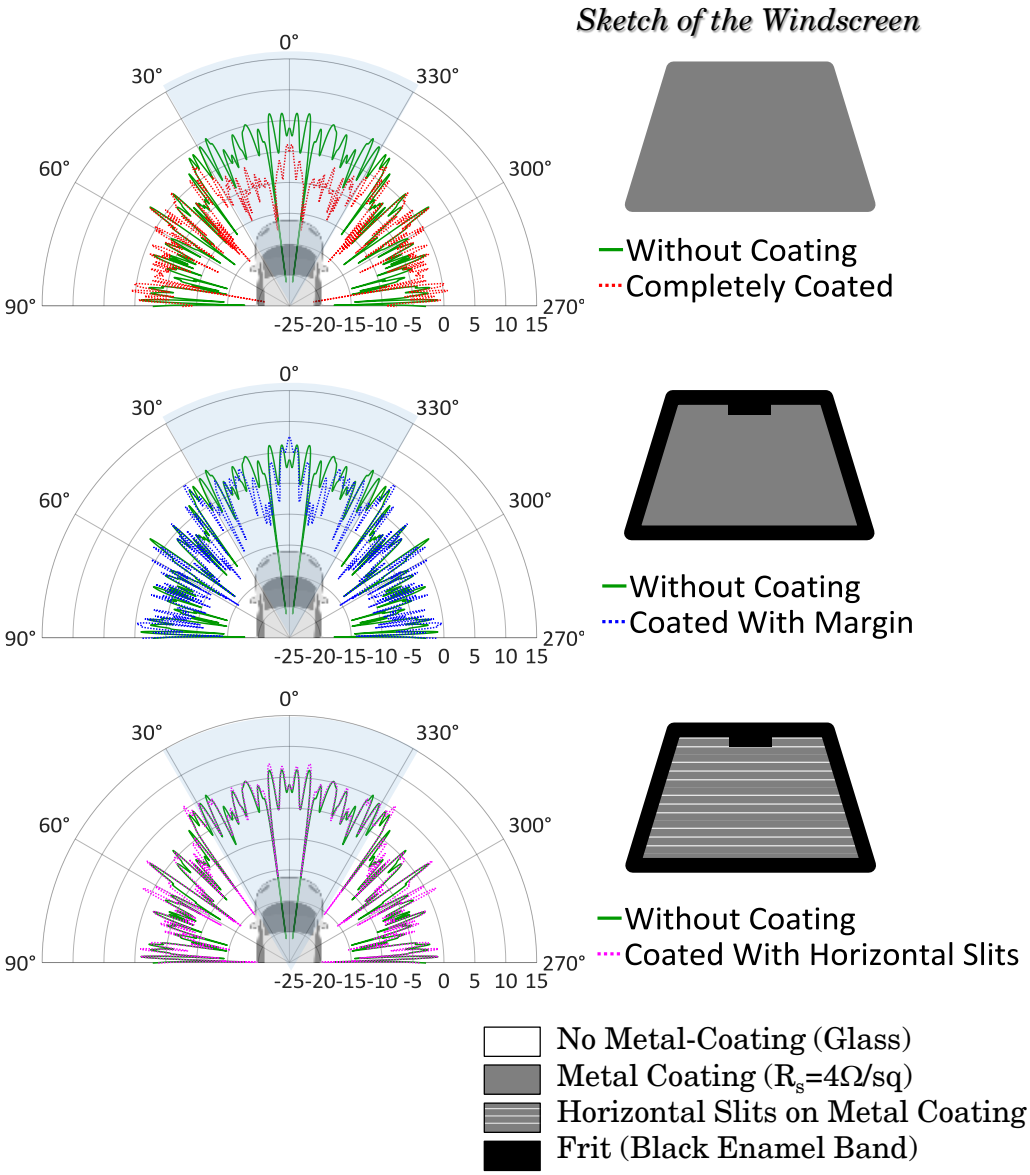

Figure 5.47: Electromagnetic characterization of FSS structures considering the vehicle: Effect on radiation pattern of different windscreen configurations, completely metal-coated window (top), metal-coated window with frit of black enamel band at the margins of the windscreen (middle), and FSS structure ("infinitely" extended horizontal slots) on metal coating with frit (bottom). The radiation patterns are compared with those obtained without metal coating, i.e. only with the laminated glass.

computational resources without affecting the validity of the results, only the front half of the car has been considered. The effects on the radiation pattern are only concentrated in an angular sector of roughly 60° around driving direction, so that the premise of considering only the front half of the car is valid. This angular sector is highlighted in light blue in the polar plots of Fig. 5.47 to emphasize the area of the diagram in which the changes are concentrated.

The first striking fact is the similarity of the radiation patterns in the case of a metal coated window with the frit or black enamel band round the margins of the windscreen (middle of Fig. 5.47) comparing with the case without metal coating. Acceptable patterns are obtained in the angular sector of about 60° around driving direction. The reason of this lies in the dimensions of the frit, which are comparable to the wavelength at the frequency of 5.9 GHz. Since we are only interested in a small angular sector in elevation around $\theta \approx 90°$, the uncoated area corresponding to the frit is enough to obtain acceptable transmission properties for antennas installed underneath the roof. Even in the case of a completely metal coated windscreen (top of Fig. 5.47), "only" ≈ 7 dB transmission loss in median is obtained. This number is not coincident with the ≈ 35 dB transmission loss seen in the measurements and simulations of Fig. 5.46 (black line). This is due to the fact that in simulations with the vehicle, a small gap has been left uncoated between the chassis of the car and the windscreen, which corresponds to the joint between both parts in which the glue is normally found. This gap is enough for a small percentage of the electromagnetic wave to pass through and to radiate outwards. Even so, the good transmission properties and the corresponding radiation pattern obtained with the lattice structure at the bottom of Fig. 5.47 should be highlighted.

Almost completely coincident radiation patterns (with those obtained with only laminated glass) are obtained using correctly dimensioned lattice structures. Hence, it can be concluded that electromagnetically transparent energy saving glass windows can be designed to maintain intact the performance of the diversity system underneath the roof previously shown in section 5.2. Moreover, the impact on the efficiency of the energy saving glass is minimal due to the small portion of metal coating removed to design the FSS structure.

As done before in previous sections and due to the randomness of the radiation patterns, a statistical evaluation by means of the CDF of the gain values of the horizontal patterns shown in Fig. 5.47 has been performed. The CDF curves are presented in Fig. 5.48 in a linear scale to emphasize values obtained in the interquartile range. Only the values of the patterns in an angular sector of ≈ 60° around driving direction has been considered as relevant. The figure shows the four cases discussed above, namely the case of the windscreen without metal coating (only with the laminated glass), the case of completely metallized windshield, the case of metal-coated window with the frit, and the one with the FSS structure. The 99 % confidence bands have been also derived from the two-sided Kolmogorov-Smirnov test for the cases without metal coating and the case with FSS structure. The purpose is to show that the same statistical distributions are obtained, and therefore, the electromagnetic field distribution is not modified by adding a

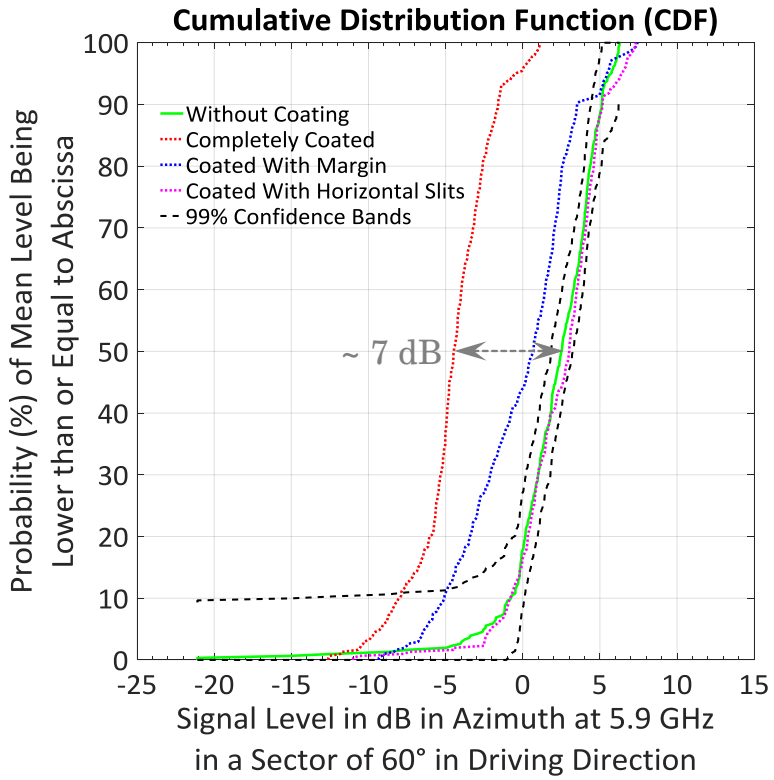

Figure 5.48: Statistical evaluation of different windscreen configurations considering the vehicle: CDF in linear scale of the horizontal patterns of Fig. 5.47 in a sector of ≈ 60° around driving direction.

metal coating with a perforated lattice structure, even if the perforations represent only an area of less than 3 % of the entire metal surface.

From Fig. 5.48, it can also be inferred that, although the radiation patterns for the case of metal coating with the frit and without coating in Fig. 5.47 were quite similar, looking at the CDF distribution of both patterns, they follow different statistical distributions. This can be recognized by the fact that the curves lie outside the confidence bands, showing that they are not completely the same as occurs with the FSS structure. The figure also highlights the ≈ 7 dB of improvement in gain as a median value (50 % cumulative probability) with regard to the case of completely metallized windows.

Once the lattice structure is well designed, a simulation has been performed with the whole vehicle and with the FSS structure placed in the front and rear windows of the car. Horizontal and vertical radiation patterns (conical and great circle cuts) are shown in Fig. 5.49. The patterns are compared with a simulation without the FSS structure, only with the laminated glass to show that both are very similar, corroborating the electromagnetic transparency of the slotted metal surface.

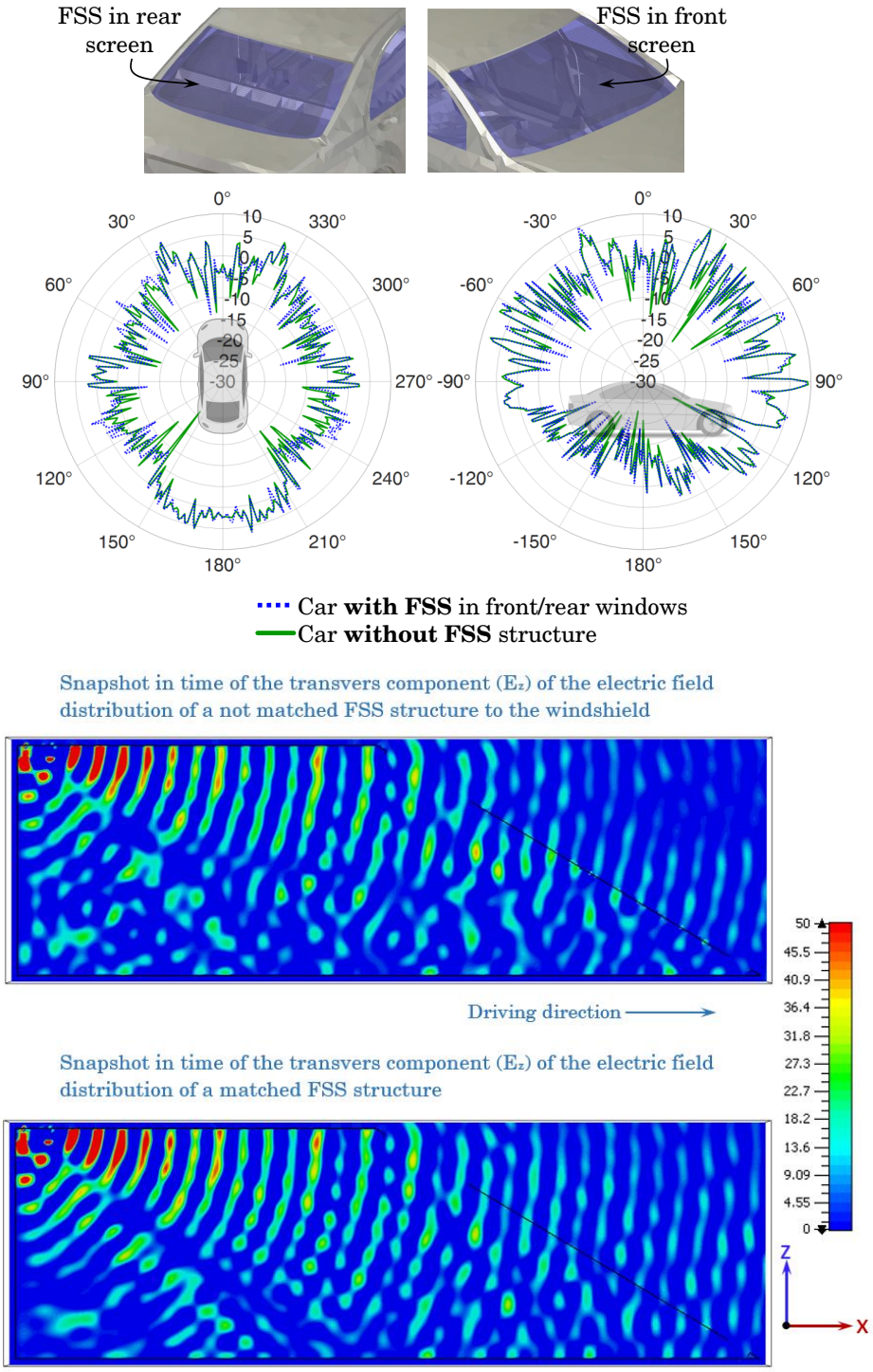

Figure 5.49: Radiation patterns and electric field distribution of antennas underneath the roof considering the whole vehicle equipped with energy saving glass with FSS structures in front and rear windows: Simulation CAD model (top), horizontal and vertical radiation patterns (middle, top), electric field distribution of an antenna underneath the roof of the car with a not matched FSS structure (middle, bottom), and with a matched FSS structure (bottom).

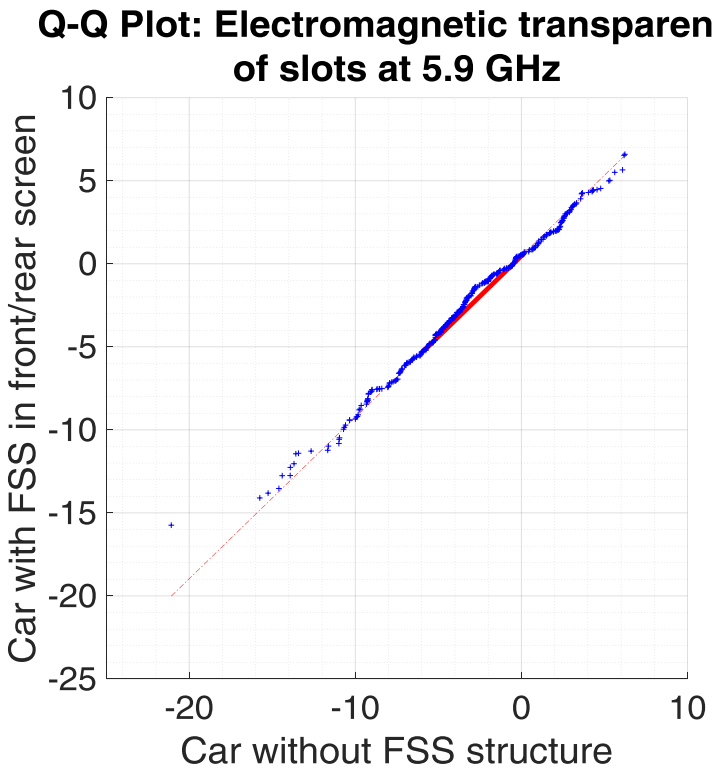

Figure 5.50: Electromagnetic transparency of the slotted structure in the metal surface of the energy saving glass at 5.9 GHz: Quantile-quantile plot (Q-Q plot) computed from the horizontal patterns of Fig. 5.49.

As discussed before in section 5.3.1, designing a FSS structure without considering the effect of the dielectric slabs where the slotted metal surface is inserted, yields to wrong results and very poor performance. As a matter of proof, a snapshot in time of the transverse component E_z of the electric field distribution of a not matched FSS structure to the windshield and that of a matched structure are shown at the bottom of Fig. 5.49 in a vertical cut showing the fields along driving direction (to the right side of the figure). It is worth noting the lack of electric fields in the region around $\theta \approx 90°$ for the not matched FSS structure.

An even better way and more powerful approach to evaluate how good is the agreement between two statistical distributions than the computation of a CDF or the use of histograms, is the use of a quantile-quantile plot (Q-Q plot). The Q-Q plot is a scatter plot created by plotting two sets of quantiles against one another. If both sets of quantiles came from the same statistical distribution, the points are aligned forming a roughly straight line with a slope of exactly 45°, so that they lie on the line $y = x$. It thus provides a graphical assessment of goodness of fit. Due to the fact that the scattered points follow a straight line, it is much easier for the human eye to visualize the agreement than with a CDF curve. All quantiles are uniquely defined and can

be obtained by inverting the CDF. The Q-Q plot of the horizontal patterns of Fig. 5.49 is shown in Fig. 5.50. It can be directly recognized the similarity of the patterns, since all points lie on a straight line following the line $y = x$. The interquartile range is highlighted in the figure with the thick solid red line.

5.3.3 Effects on Radiation Pattern of Defogger Grids on Rear Screen

The defogger, demister, or defroster of the rear windshield of an automobile consists of a grid of thin metallic strips to clear condensation and remove frost from the backglass[7]. As it is formed by thin metal strips extended along the horizontal direction of the rear window of the car or even taking other forms with metal strips vertically aligned, the influence on the radiation pattern at 5.9 GHz should be investigated since it may not be negligible.

Since the antennas for V2X communication are vertically polarized, stronger coupling is expected for the vertically-oriented metal strips of the defogger grid, since the electric field vector radiated by the antenna is parallel to the metal strips corresponding to the case of inductive behaviour, as described in [85].

As expected, and shown on the right side of Fig. 5.51, a small degradation of the patterns is seen for vertically-oriented defogger grids. For horizontally-oriented metal grids the effect can be completely neglected, as shown on the left side of Fig. 5.51. Figure 5.51 also shows a real prototype and the CAD model used for simulations. Again, to accelerate the simulations, only the rear half part of the vehicle is considered, since the relevant area lies at azimuth angles about 150° and 210°. Hence, it can be concluded that the effects of the defogger grid of the backglass on the radiation pattern at 5.9 GHz can be neglected.

[7]The defogger system was invented by the German automobile engineer Dr. Heinz Kunert in the early sixties.

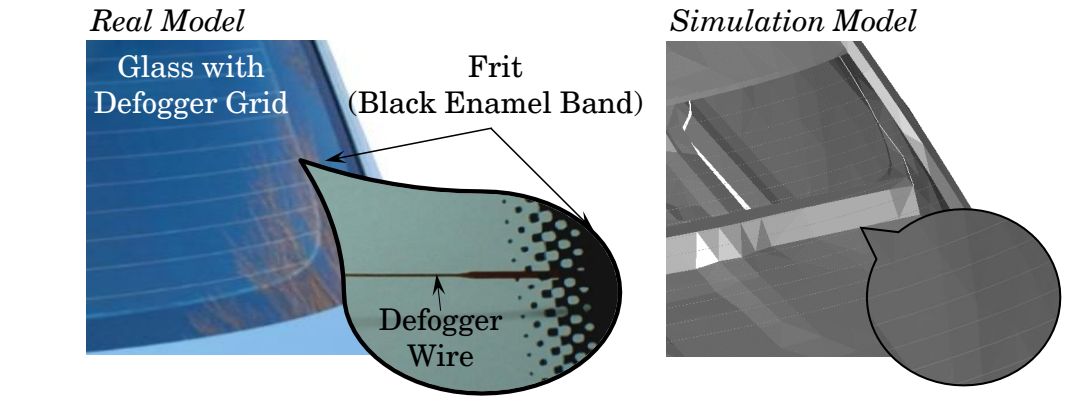

Rear window defogger assembly with a horizontal heater grid orientation

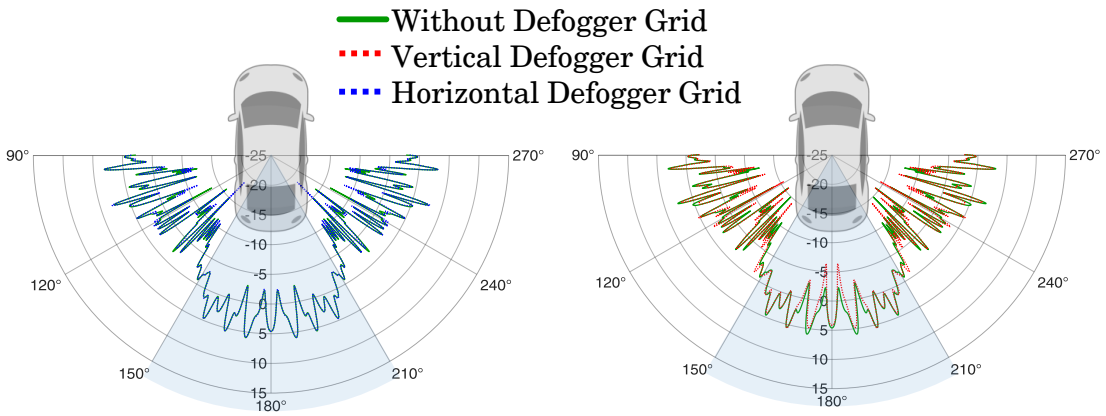

Sector of radiation pattern ($\theta \approx 90°$, $\varphi \in [150°,210°]$) at 5.9 GHz

Figure 5.51: Effects on radiation pattern at 5.9 GHz of defogger grids on the backglass of the car: Real prototype and simulation CAD model (top), and horizontal radiation patterns without defogger grid, and with horizontally- (bottom left) and vertically-oriented (bottom right) defogger grids on the rear screen of the car.

5.4 Compliance with Electromagnetic Exposure

The next question that arises for antenna systems that are intended to be installed inside the car's cabin is if the radiated fields by the antennas comply with the electromagnetic exposure guidelines in the presence of human beings.

This section shows the simulations performed to study the compliance with electromagnetic exposure guidelines. According to [54], the reference level for general public exposure to time-varying electric and magnetic fields (unperturbed root mean square value) between 2 GHz and 300 GHz is given by an electric field strength of 61 V/m.

The pictures of Fig. 5.52 show the simulated electric field distributions inside the vehicle given as a root mean square value. The electric field distributions are clamped to the reference level to guarantee the compliance for in-vehicle field exposure. The figure shows the electric field distributions for the front and rear compartment of the car (top), for the driver and rear left passenger compartment (middle), and for the middle arm plane (bottom).

Only the empty metal body shell and metal structures of the doors are included in the simulations, ensuring worst case results. Dielectric parts and composite materials have relatively small impact on the electric field strength distribution for antennas placed inside the vehicle or tend to mitigate the electromagnetic field strength as shown in [82].

All levels are below the reference value for general public exposure of 61 V/m. Only at the nearby of the antenna, which is far away enough from the human bodies, the reference values are reached. Moreover, the vast majority of the values are below the mean value of the allowed range of values, as depicted with light green in the figure.

However, as already mentioned, when including the dielectric parts of the vehicle, this value will be attenuated. In the simulations, the antenna has been modeled without any dielectric cover or radome, but for practical applications it will be somehow covered with dielectrics to hide and protect the antenna.

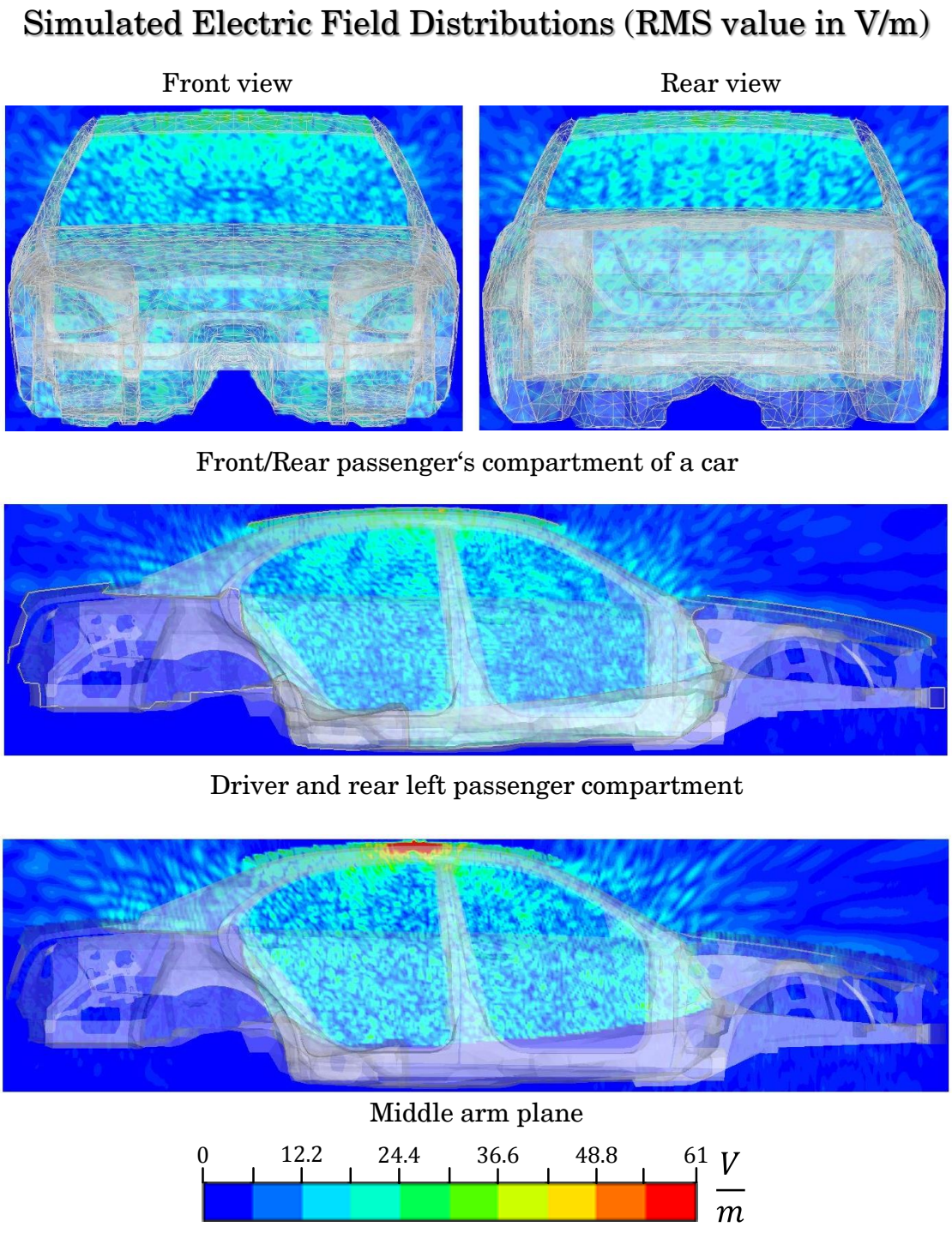

Figure 5.52: Compliance with electromagnetic exposure guidelines in the presence of human beings: Simulated electric field distributions given as root mean square value in V/m and showing the front and rear passenger's compartment of the car (top), the driver and rear left passenger compartment (middle), and the middle arm plane (bottom).

CHAPTER 6

CONCLUSIONS

In the present work, antenna systems for Vehicle-to-Everything (V2X) communication in the 5.9 GHz Intelligent Transportation Systems (ITS) spectrum under the influence of the vehicle body have been investigated. Due to the safety-related nature of the service, robust and stable propagation characteristics are mandatory to achieve the goal for which the V2X worldwide initiative was born: reduce fatal accidents, keep the ever increasing road traffic flowing in time-varying environments, and bring non-safety internet-based applications to enhance the driving experience. The various aspects of the different standards around the world on which V2X communication is based, have been discussed in Chapter 1. The standards for the physical layer in the USA and Europe, governed by IEEE 802.11p and ETSI EN 302 663 respectively, share most of the features, such as frequency range (roughly 75 MHz between 5850 MHz and 5925 MHz), number of channels (seven 10 MHz channels), waveform (OFDM), data rate per channel (3 - 27 Mbit/s) or output power (23 - 33 dBm (EIRP)). The reasonably high frequency of operation (around 5.9 GHz) with regard to most other automotive applications, offers several advantages such as short range communications (up to 1 km) with a high data rate, low weather-dependence, and global compatibility and interoperability, key features when it comes to safety applications.

V2X communication, as a safety-related service, demands certain stringent requirements on the radiation pattern of the antennas for the proper operation of the system. Omnidirectional radiation patterns are required to be able to receive and send any kind of alert in any direction of space in the horizontal plane in which car traffic flows. The circularity of the far-field patterns in the horizontal plane is notably affected by the proximity of the V2X antenna to other neighboring antennas and by the actual location of the antenna in the automobile chassis.

In this dissertation, emphasis has been placed on the electromagnetic effects arising from the interaction between the antennas and the parts of the vehicle body surrounding them, as

discussed in Chapter 2. The inclusion of the environment surrounding the antennas at an early stage of their development has been shown in numerous instances throughout this dissertation to be crucial for obtaining optimized solutions by means of simulations with minimal deviation from the measurement results. The growing trend in the automotive industry to use materials other than metal to reduce the weight of cars and improve the aesthetics of them lead to different dielectric materials in close proximity to the antennas, like the panorama glass windows investigated in Chapter 2. These dielectric materials modify to a great extent the radiation characteristics of the antennas, distorting the circularity of the patterns and modifying the main beam direction. Shadowing effects in the horizontal plane of the radiation pattern of up to roughly 15 dB in a sector of about 60° in driving direction have been reported for the panorama glass roof investigated in Chapter 2.

Modern automotive designs include curved shapes that affect the radiation pattern sometimes negatively from the antenna performance perspective, as shown in Chapters 2 and 3 for antennas placed on the roof of sedan-type cars near the rear edge of the roof. Diffraction effects in driving direction due to the curvature of the roof cause range reductions over azimuth in the horizontal plane of about 5 dB in driving direction and an inclination towards higher elevation angles of the main beam direction of the far-field pattern. The electrical performance of the investigated antenna solutions are thus analyzed and optimized considering the vehicle body as part of the antenna that modifies the near-field distribution of the antenna radiated fields.

The effects of the different ground properties, on which automobiles drive, have also been considered and investigated in Chapter 2. Unlike anechoic chambers, in non-controlled environments like Open Area Test Sites (OATS) and radomes, reflections from the ground and the environment surrounding the measurement scenario influence the recorded pattern. These electromagnetic effects may be taken into account when comparing with simulated results, where the ground is sometimes omitted due to acceleration purposes.

A highly efficient LTE-V2X multiband antenna with improved radiation characteristics in the V2X frequency band when placed on the roof of the car near the rear edge has been investigated in Chapter 3. The coexistence of many antennas for different services under a single shark-fin cover demands multiband antennas capable of covering several services through a single structure with a unique feeding point. The multiband antenna concept investigated, not only helps to reduce the space required if two different antennas were used, but it also reduces the coupling effects that occur when two different antennas working at similar frequencies are placed within the radiative near-fields of them. Broadband impedance matching is obtained with an antenna with a height of less than 55 mm and capable of effectively radiating even at the lowest frequencies in the lower LTE frequency band around 700 MHz. The required omnidirectional far-field characteristics of the antenna in the V2X spectrum considering the vehicle body has led to an antenna design that differs from that which would have resulted if it had been designed on a flat infinite ground plane. With such a common automotive antenna position, Chapter 3 evidences and illustrates the

importance of considering the electromagnetic effects of the environment in which the antenna is immersed.

For practical applications where the roof-top mounting position is not available, as in the case of convertibles, or when it is required to hide the antennas for aesthetic reasons, other antenna placements should be investigated. This has been done in Chapters 4 and 5 for V2X antenna systems in the form of decentralized macro-diversity systems distributed in the side mirrors or front and rear bumpers, and in the form of compact micro-diversity antenna arrangements underneath the roof of the car, respectively. Linear diversity combining techniques are applied with two- and four-antenna combinations. The feasibility of decentralized antenna distributions behind the bumpers and within the side mirrors has been investigated in Chapter 4. Although very good circularity values of less than 3 dB in the horizontal plane are obtained with macro-diversity combinations by means of switch or selection combining (SC) and maximum ratio combining (MRC) with four antennas, the excessive length of the radio frequency cables to connect the antennas with the RF front-end and the attenuation losses that this fact implies, can be prohibitive depending on the system, especially considering the relative high frequency at which V2X systems operate. Due to shadowing effects caused by the vehicle body, significant power differences at certain azimuth angles exist between decentralized antennas, yielding high power imbalance values. In such cases, equal gain combining techniques do not provide optimum results and the use of switch or selection combining techniques provide a good compromise solution.

The research conducted in Chapter 4 and the restrictions derived from it form the basis for the hidden antenna micro-diversity system underneath the roof of the car presented in Chapter 5. As discussed in Chapters 2 and 5, antennas hidden underneath the roof suffer from deep fadings on their radiation patterns, due to diffractions along the curved roof and at the edges, shadowing effects from the pillars of the car, and reflections and diffuse scattering from the inside of the cabin of the car. To improve the radiation patterns a spatial micro-diversity system has been implemented, which with a compact four-antenna set with a size of less than $10 \times 48 \times 48\text{mm}^3$, a smoothing of the radiation patterns and mitigation of the Rayleigh-fading have been accomplished. The good diversity performance is ensured by means of low power imbalance values of less then 0.74 dB and low envelope correlation coefficient (ECC) values from far-field patterns lower than 0.5. Due to the random behavior of the far-field patterns underneath the roof, the results are presented under an statistical approach by means of cumulative distribution functions of the radiation pattern gain levels in azimuth at 5.9 GHz, and the similitude of the statistical distributions is evaluated by means of 2-sample Kolmogorov-Smirnov test statistics and the corresponding confidence bands derived from the cumulative distribution functions. As proved by means of statistics, the investigated micro-diversity concept outperforms the results achieved with a $\lambda/4$-monopole antenna on the ideal roof top mounting position in driving direction and in the opposite one. These are critical directions for V2X communication.

BIBLIOGRAPHY

[1] *IEEE standard for definitions of terms for antennas*, IEEE Std 145-2013 (Revision of IEEE Std 145-1993), (2014), pp. 1–50.

[2] *IEEE standard for information technology–telecommunications and information exchange between systems local and metropolitan area networks–specific requirements - part 11: Wireless LAN medium access control (MAC) and physical layer (PHY) specifications*, IEEE Std 802.11-2016 (Revision of IEEE Std 802.11-2012), (2016), pp. 1–3534.

[3] T. ABBAS, J. KAREDAL, AND F. TUFVESSON, *Measurement-based analysis: The effect of complementary antennas and diversity on vehicle-to-vehicle communication*, IEEE Antennas and Wireless Propagation Letters, 12 (2013), pp. 309–312.

[4] D. N. ALOI, M. POSSA, A. BARGHOUTI, J. TLUSTY, AND M. S. SHARAWI, *Printed DSRC antennas for enhanced gain coverage towards front and rear of vehicle for automotive applications*, in 2014 IEEE-APS Topical Conference on Antennas and Propagation in Wireless Communications (APWC), IEEE, 2014, pp. 349–352.

[5] M. G. N. ALSATH AND M. KANAGASABAI, *A shared-aperture multiservice antenna for automotive communications*, IEEE Antennas and Wireless Propagation Letters, 13 (2014), pp. 1417–1420.

[6] A. ANDUJAR, J. ANGUERA, C. PUENTE, AND A. PÉREZ, *On the radiation pattern of the L-shaped wire antenna*, Progress In Electromagnetics Research M, 6 (2009), pp. 91–105.

[7] J. R. ARGAND, *Essai sur une manière de représenter les quantités imaginaires dans les constructions géométriques*, Gauthier-Villars, 1874.

[8] L. R. ARNAUT, *Compound exponential distributions for undermoded reverberation chambers*, IEEE Transactions on Electromagnetic Compatibility, 44 (2002), pp. 442–457.

[9] G. ARTNER, J. KOWALEWSKI, C. F. MECKLENBRÄUKER, AND T. ZWICK, *Pattern reconfigurable antenna with four directions hidden in the vehicle roof*, in 2017 International Workshop on Antenna Technology: Small Antennas, Innovative Structures, and Applications (iWAT), March 2017, pp. 82–85.

[10] ASSOCIATION OF RADIO INDUSTRIES AND BUSINESSES (ARIB), *Std-t109*. https://www.arib.or.jp/english/std_tr/telecommunications/std-t109.html. Accessed: 2018-07-03.

[11] AUTOMOTIVE ASSOCIATION (5GAA). http://5gaa.org. Accessed: 2018-07-03.

[12] C. BALANIS, *Modern Antenna Handbook*, Wiley, 2011.

[13] ——, *Antenna Theory: Analysis and Design*, Wiley, 2012.

[14] D. BARIÉ, S. SENEGA, L. REITER, AND S. LINDENMEIER, *Concept studies of scanning and combined scan/phase antenna diversity systems for SDARS*, in German Microwave Conference, VDE, 2008, pp. 1–3.

[15] S. R. BEST AND D. L. HANNA, *A performance comparison of fundamental small-antenna designs*, IEEE Antennas and Propagation Magazine, 52 (2010), pp. 47–70.

[16] S. BLANCH, J. ROMEU, AND I. CORBELLA, *Exact representation of antenna system diversity performance from input parameter description*, Electronics Letters, 39 (2003), pp. 705–707.

[17] A. BÖGE, *Unobtrusive Active Multiband Car Antennas for Reception of Terrestrial Broadcasting Services*, PhD thesis, Universität der Bundeswehr München, 2018.

[18] J. T. BOLLJAHN, *Antennas near conducting sheets of finite size*, PhD thesis, 1950.

[19] D. G. BRENNAN, *Linear diversity combining techniques*, Proceedings of the IEEE, 91 (2003), pp. 331–356.

[20] M. BUENO DIEZ AND S. LINDENMEIER, *A highly efficient Car2Car-multiband rooftop automotive antenna*, in 2015 IEEE International Symposium on Antennas and Propagation & USNC/URSI National Radio Science Meeting, IEEE, 2015, pp. 1606–1607.

[21] ——, *Antenna micro-diversity systems hidden underneath the car roof for vehicle-to-X applications*, in 12th European Conference on Antennas and Propagation (EuCAP 2018), April 2018, pp. 1–5.

[22] ——, *Diversity performance of benchmark scenarios for hidden vehicle-to-X antennas underneath the roof*, in 2018 48th European Microwave Conference (EuMC), Sep. 2018, pp. 308–311.

[23] M. BUENO DIEZ, W. PASCHER, AND S. LINDENMEIER, *C2C-WLAN antenna systems with optimized characteristics under vehicle body influence*, in 2015 ITG im VDE 3. Workshop Automotive Antennen (WSAA), 2015.

[24] ——, *Electromagnetic characterization of automotive sunroofs for car-to-X applications*, in 2016 46th European Microwave Conference (EuMC), 2016, pp. 1323–1326.

[25] M. BUENO DIEZ, P. PLITT, W. PASCHER, AND S. LINDENMEIER, *Antenna placement and wave propagation for car-to-car communication*, in 2015 European Microwave Conference (EuMC), 2015, pp. 207–210.

[26] J. BURKE, *Lateral shifts of light beams on total reflection*, Opt. Sci. Newsletter, 5 (Univ. Arizona, 1971), p. 31.

[27] F. CARRERA, D. NAVARRO, M. CABEDO, D. SÁNCHEZ, M. FERRANDO, M. GALLO, S. BRUNI, M. PANNOZZO, AND D. ZAMBERLAN, *Wideband monopole for mobile, WLAN and C2C services in vehicular applications*, in 2013 IEEE Antennas and Propagation Society International Symposium (APSURSI), IEEE, 2013, pp. 2071–2072.

[28] R. H. CLARKE, *A statistical theory of mobile-radio reception*, The Bell System Technical Journal, 47 (1968), pp. 957–1000.

[29] R. COLLIN AND F. ZUCKER, *Antenna Theory*, Part II, McGraw-Hill, 1969.

[30] CST, *Computer simulation technology*.
`https://www.cst.com`.
Accessed: 2017-09-04.

[31] C. B. DIETRICH, K. DIETZE, J. R. NEALY, AND W. L. STUTZMAN, *Spatial, polarization, and pattern diversity for wireless handheld terminals*, IEEE Transactions on Antennas and Propagation, 49 (2001), pp. 1271–1281.

[32] K. DIETZE, *Analysis of a two-branch maximal ratio and selection diversity system with unequal branch powers and correlated inputs for a rayleigh fading channel*, PhD thesis, Virginia Tech, 2001.

[33] A. DUZDAR AND C. THIAM, *Integrating V2V functionality at 5.9 GHz into an existing quad-band antenna for automotive applications*, by Laird Technologies, (2011).

[34] L. EKIZ, T. PATELCZYK, O. KLEMP, AND C. F. MECKLENBRÄUKER, *Compensation of vehicle-specific antenna radome effects at 5.9 GHz*, in IECON 2013-39th Annual Conference of the IEEE Industrial Electronics Society, IEEE, 2013, pp. 6880–6884.

[35] FEDERAL COMMUNICATIONS COMISSION (US) (FCC), *Title 47: Telecommunication*. https://www.ecfr.gov.
Accessed: 2018-07-03.

[36] S. FIKAR, W. WALZIK, AND A. L. SCHOLTZ, *Vehicular multi/broadband mimo antenna for terrestrial communication*, in 2010 IEEE Antennas and Propagation Society International Symposium, IEEE, 2010, pp. 1–4.

[37] M. GALLO, S. BRUNI, M. PANNOZZO, AND D. ZAMBERLAN, *Performance evaluation of C2C antennas on car body*, in 2013 7th European Conference on Antennas and Propagation (EuCAP), 2013, pp. 3136–3139.

[38] M. GALLO, S. BRUNI, M. PANNOZZO, D. ZAMBERLAN, R. CASO, AND P. NEPA, *Design and experimental validation of a windscreen patch array for C2C communications*, in 2013 IEEE Antennas and Propagation Society International Symposium (APSURSI), IEEE, 2013, pp. 2063–2064.

[39] M. GALLO, S. BRUNI, AND D. ZAMBERLAN, *A novel fully integrated fin antenna for automotive application*, in The 8th European Conference on Antennas and Propagation (EuCAP 2014), 2014, pp. 2986–2989.

[40] J. K. GAMAGE, M. ENGJOM, AND I. A. JENSEN, *Design of a low profile multi-band antenna for vehicular communication system*, in 2013 7th European Conference on Antennas and Propagation (EuCAP), 2013, pp. 1273–1277.

[41] N. GENG AND W. WIESBECK, *Planungsmethoden für die Mobilkommunikation. Funknetzplanung unter realen physikalischen Ausbreitungsbedingungen.*, Springer-Verlag Berlin Heidelberg, 1998.

[42] E. GHAFARI, A. FUCHS, D. EBLENKAMP, AND D. N. ALOI, *A vehicular rooftop, shark-fin, multiband antenna for the GPS/LTE/cellular/DSRC systems*, in 2014 IEEE-APS Topical Conference on Antennas and Propagation in Wireless Communications (APWC), IEEE, 2014, pp. 237–240.

[43] I. GONCHAROVA AND S. LINDENMEIER, *A high-efficient 3-D Nefer-antenna for LTE communication on a car*, in The 8th European Conference on Antennas and Propagation (EuCAP 2014), April 2014, pp. 3273–3277.

[44] F. GOOS AND H. HÄNCHEN, *Ein neuer und fundamentaler versuch zur totalreflexion*, Annalen der Physik, 436 (1947), pp. 333–346.

[45] M. GUSTAFSSON, M. CISMASU, AND B. L. G. JONSSON, *Physical bounds and optimal currents on antennas*, IEEE Transactions on Antennas and Propagation, 60 (2012), pp. 2672–2681.

[46] J. HÄRRI, H. TCHOUANKEM, O. KLEMP, AND O. DEMCHENKO, *Impact of vehicular integration effects on the performance of DSRC communications*, in 2013 IEEE Wireless Communications and Networking Conference (WCNC), IEEE, 2013, pp. 1645–1650.

[47] S. HASTÜRKOĜLU AND S. LINDENMEIER, *A wideband automotive antenna for actual and future mobile communication 5G/LTE/WLAN with low profile*, in 2017 11th European Conference on Antennas and Propagation (EUCAP), March 2017, pp. 602–605.

[48] D. A. HILL, *Electromagnetic theory of reverberation chambers*, Tech. Rep. 1506, National Institute of Standards and Technology, NIST, Technology Administration, U.S. Department of Commerce, December 1998.

[49] ——, *Aperture Excitation of Electrically Large, Lossy Cavities*, Wiley-IEEE Press, 2009, pp. 151–164.

[50] D. A. HILL, *Electromagnetic Fields in Cavities: Deterministic and Statistical Theories*, IEEE Press Series on Electromagnetic Wave Theory, John Wiley & Sons, Inc., Hoboken, New Jersey, 2009.

[51] P. HOEKSTRA AND A. DELANEY, *Dielectric properties of soils at UHF and microwave frequencies*, Journal of Geophysical Research, 79 (1974), pp. 1699–1708.

[52] M. IDEMEN AND L. FELSEN, *Diffraction of a whispering gallery mode by the edge of a thin concave cylindrically curved surface*, IEEE Transactions on Antennas and Propagation, 29 (1981), pp. 571–579.

[53] S. IMAI, K. TAGUCHI, AND T. KASHIWA, *Effect of car antenna position on radio propagation characteristics at intersection for 760MHz inter-vehicle communications*, in 2014 International Symposium on Antennas and Propagation Conference Proceedings, IEEE, 2014, pp. 349–350.

[54] INTERNATIONAL COMMISSION ON NON-IONIZING RADIATION PROTECTION (ICNIRP), *Guidelines for limiting exposure to time-varying electric, magnetic, and electromagnetic fields (up to 300 GHz)*, Health Physics, 74 (1998), pp. 494–522.

[55] W. JAKES, *Microwave mobile communications*, IEEE Press classic reissue, IEEE Press, 1974.

[56] E. J. JASELSKIS, J. GRIGAS, AND A. BRILINGAS, *Dielectric properties of asphalt pavement*, Journal of Materials in Civil Engineering, 15:5 (2003).

[57] E. C. JORDAN AND K. G. BALMAIN, *Electromagnetic Waves and Radiating Systems*, Prentice-Hall, 1968.

[58] R.-T. JUANG, *Performance analysis of V2V DSRC communications with reconfigurable antenna*, in of the 19th ITS World Congress, 2012.

[59] K. WEVERS AND M. LU, *V2X communication for ITS - from IEEE 802.11p towards 5G*, IEEE 5G Tech Focus, 1 (2017).

[60] N. KANARI, J. L. PINEAU, AND S. SHALLARI, *End-of-life vehicle recycling in the european union*, JOM, 55 (2003), pp. 15–19.

[61] S. KAUL, K. RAMACHANDRAN, P. SHANKAR, S. OH, M. GRUTESER, I. SESKAR, AND T. NADEEM, *Effect of antenna placement and diversity on vehicular network communications*, in 2007 4th Annual IEEE Communications Society Conference on Sensor, Mesh and Ad Hoc Communications and Networks, IEEE, 2007, pp. 112–121.

[62] J. B. KELLER, *Geometrical theory of diffraction*, J. Opt. Soc. Am., 52 (1962), pp. 116–130.

[63] G. I. KIANI, A. KARLSSON, L. OLSSON, AND K. P. ESSELLE, *Glass characterization for designing frequency selective surfaces to improve transmission through energy saving glass windows*, in 2007 Asia-Pacific Microwave Conference, Dec 2007, pp. 1–4.

[64] O. KLEMP, *Performance considerations for automotive antenna equipment in vehicle-to-vehicle communications*, in 2010 URSI International Symposium on Electromagnetic Theory, IEEE, 2010, pp. 934–937.

[65] G. KOCH AND K. KOLBIG, *The transmission coefficient of elliptical and rectangular apertures for electromagnetic waves*, IEEE Transactions on Antennas and Propagation, 16 (1968), pp. 78–83.

[66] H. KOGELNIK, *Theory of Optical Waveguides*, Springer Berlin Heidelberg, Berlin, Heidelberg, 1988, pp. 7–88.

[67] H. KOGELNIK AND V. RAMASWAMY, *Scaling rules for thin-film optical waveguides*, Appl. Opt., 13 (1974), pp. 1857–1862.

[68] D. KORNEK, M. SCHACK, E. SLOTTKE, O. KLEMP, I. ROLFES, AND T. KURNER, *Effects of antenna characteristics and placements on a vehicle-to-vehicle channel scenario*, in 2010 IEEE International Conference on Communications Workshops, IEEE, 2010, pp. 1–5.

[69] J. D. KRAUS AND R. J. MARHEFKA, *Antennas for all applications*, John Wiley & Sons, Inc., 2002.

[70] A. KWOCZEK, Z. RAIDA, J. LÁČÍK, M. POKORNY, J. PUSKELÝ, AND P. VÁGNER, *Influence of car panorama glass roofs on Car2Car communication (poster)*, in 2011 IEEE Vehicular Networking Conference (VNC), Nov 2011, pp. 246–251.

[71] W. LEE, *Mobile Communications Design Fundamentals*, Wiley Series in Telecommunications and Signal Processing, Wiley, 1993.

[72] ——, *Mobile Communications Engineering: Theory and Applications*, McGraw-Hill telecommunications, McGraw-Hill Education, 1997.

[73] O. LEONARDI, M. PAVONE, T. CADILI, G. SORBELLO, AND T. ISERNIA, *Monolithic patch antenna for dedicated short-range communications*, Electronics Letters, 49 (2013), pp. 85–86.

[74] H. LINDENMEIER, J. HOPF, L. REITER, AND R. KRONBERGER, *Optimization of the antenna-diversity-effectiveness of complex FM-car-antenna systems*, in IEEE Antennas and Propagation Society International Symposium. 1999 Digest. Held in conjunction with: USNC/URSI National Radio Science Meeting (Cat. No.99CH37010), vol. 3, July 1999, pp. 2058–2061 vol.3.

[75] H. K. LINDENMEIER, L. REITE, J. F. HOPF, S. M. LINDENMEIER, H.-G. SCHÜRING, AND G.-H. HASSMANN, *Vehicle-conformal SDARS diversity antenna system by a fast operating diversity algorithm*, in 2005 IEEE Antennas and Propagation Society International Symposium, vol. 1, IEEE, 2005, pp. 76–79.

[76] H. K. LINDENMEIER, L. M. REITER, AND J. F. HOPF, *Multiantenna scanning diversity system for mobile TV reception with independently optimized picture and sound quality*, Radio Science, 28 (1993), pp. 1267–1276.

[77] H. K. LINDENMEIER, L. M. REITER, J. F. HOPF, S. M. LINDENMEIER, H.-G. SCHUERING, AND G.-H. HASSMANN, *SDARS-antenna-diversity-schemes for a better radio-link in vehicles*, in SAE 2005 World Congress & Exhibition, SAE International, apr 2005.

[78] K. LINDENMEIER AND L. REITER, *Multipath reception in FM car radio receivers and antenna diversity by means of a distortion detector*, in 1983 Antennas and Propagation Society International Symposium, vol. 21, May 1983, pp. 187–190.

[79] S. LINDENMEIER, M. BUENO DIEZ, I. GONCHAROVA, A. BÖGE, AND W. PASCHER, *Automotive antennas under vehicle influence and aspects of their numerical modeling*, in 2015 CST European Automotive Workshop, BMW Welt München, 2015.

[80] S. LINDENMEIER, I. GONCHAROVA, S. HASTÜRKOĜLU, AND M. BUENO DIEZ, *Antennas for terrestrial communication in vehicles and their interaction with antennas for satellite services*, in 2017 IEEE-APS Topical Conference on Antennas and Propagation in Wireless Communications (APWC), IEEE, 2017, pp. 334–337.

[81] S. LINDENMEIER AND S. SENEGA, *Satellite Antennas on Vehicles*, Springer Singapore, Singapore, 2016, pp. 2501–2540.

[82] L. LOW, H. ZHANG, J. M. RIGELSFORD, R. J. LANGLEY, AND A. R. RUDDLE, *An automated system for measuring electric field distributions within a vehicle*, IEEE Transactions on Electromagnetic Compatibility, 55 (2013), pp. 3–12.

[83] A. MALARKY, G. Z. RAFI, S. SAFAVI-NAEINI, AND L. DELGROSSI, *A planar dual band GPS and DSRC antenna for road vehicles*, in 2007 IEEE 66th Vehicular Technology Conference, IEEE, 2007, pp. 2096–2100.

[84] D. MARCUSE, *Theory of dielectric optical waveguides*, Quantum electronics–principles and applications, Academic Press, 1974.

[85] N. MARCUVITZ, *Waveguide Handbook*, Electromagnetics and Radar Series, McGraw-Hill, 1951.

[86] MATLAB R2017; THE MATHWORKS, INC.
`https://de.mathworks.com/products/matlab.html`.
Accessed: 2018-05-07.

[87] D. MCNAMARA, C. PISTORIUS, AND J. MALHERBE, *Introduction to the Uniform Geometrical Theory of Diffraction*, Antennas and Propagation Library, Artech House, 1990.

[88] H. MEINKE AND F. GUNDLACH, *Taschenbuch der Hochfrequenztechnik*, Springer Berlin Heidelberg, 1968.

[89] B. MUNK, *Frequency Selective Surfaces: Theory and Design*, Wiley, 2005.

[90] A. NASSAR, S. SENEGA, AND S. LINDENMEIER, *A multi-channel algorithm for antenna diversity of SiriusXM high band satellite reception in vehicles*, in 2018 48th European Microwave Conference (EuMC), 2018, pp. 312–315.

[91] I. NEWTON, *Opticks: Or, A Treatise Of The Reflections, Refractions, Inflections and Colours Of Light*, Printed for Sam. Smith, and Benj. Walford, London, 1704.

[92] K. A. NORTON, *The propagation of radio waves over the surface of the earth and in the upper atmosphere*, Proceedings of the Institute of Radio Engineers, 24 (1936), pp. 1367–1387.

[93] ——, *The propagation of radio waves over the surface of the earth and in the upper atmosphere*, Proceedings of the Institute of Radio Engineers, 25 (1937), pp. 1203–1236.

[94] A. PAPOULIS AND S. PILLAI, *Probability, random variables, and stochastic processes*, McGraw-Hill electrical and electronic engineering series, McGraw-Hill, 2002.

[95] P. PATHAK, W. BURNSIDE, AND R. MARHEFKA, *A uniform gtd analysis of the diffraction of electromagnetic waves by a smooth convex surface*, IEEE Transactions on Antennas and Propagation, 28 (1980), pp. 631–642.

[96] P. H. PATHAK, *Techniques for High-Frequency Problems*, Springer US, Boston, MA, 1988, pp. 195–311.

[97] Y. PHANG AND P. HALL, *Vehicle window patch and slot antennas for 5.8 ghz communication systems*, in Tenth International Conference on Antennas and Propagation (Conf. Publ. No. 436), vol. 1, IET, 1997, pp. 1370–1373.

[98] PILKINGTON, *Glass for automotive*.
`http://www.pilkington.com/en-gb/uk/automotive/original-equipment/automotive-overview/glass-growth-in-vehicles`.
Accessed: 2018-04-03.

[99] R. H. PRICE, H. T. DAVIS, AND E. P. WENAAS, *Determination of the statistical distribution of electromagnetic-field amplitudes in complex cavities*, Phys. Rev. E, 48 (1993), pp. 4716–4729.

[100] QUALCOMM TECHNOLOGIES, INC., *Accelerating c-v2x commercialization*.
`https://www.qualcomm.com/invention/5g/cellular-v2x`, 2017.
Accessed: 2018-07-03.

[101] G. Z. RAFI, M. MOHAJER, A. MALARKY, P. MOUSAVI, AND S. SAFAVI-NAEINI, *Low-profile integrated microstrip antenna for GPS-DSRC application*, IEEE Antennas and Wireless Propagation Letters, 8 (2009), pp. 44–48.

[102] L. REICHARDT, *Methodik für den Entwurf von kapazitätsoptimierten Mehrantennensystemen am Fahrzeug*, PhD thesis, Karlsruher Institut für Technologie (KIT), 2013.

[103] L. REICHARDT, T. FUGEN, AND T. ZWICK, *Influence of antennas placement on car to car communications channel*, in 2009 3rd European Conference on Antennas and Propagation, 2009, pp. 630–634.

[104] L. REITER, A. BÖGE, A. NEGUT, AND S. LINDENMEIER, *A new low-cost active rod antenna for automotive reception of all terrestrial audio broadcast services*, in The 8th European Conference on Antennas and Propagation (EuCAP 2014), 2014, pp. 2981–2984.

[105] M. P. ROBINSON, J. CLEGG, AND A. C. MARVIN, *Radio frequency electromagnetic fields in large conducting enclosures: effects of apertures and human bodies on propagation and field-statistics*, IEEE Transactions on Electromagnetic Compatibility, 48 (2006), pp. 304–310.

[106] ROGERS CORPORATION, *RO4003C laminates*.
`https://www.rogerscorp.com/acs/products/54/RO4003C-Laminates.aspx`.
Accessed: 2019-04-07.

[107] ROHDE & SCHWARZ GMBH UND CO. KG, *Measurement antennas*.
https://www.rohde-schwarz.com/hu/products/aerospace-defense-security/antennas/pg_measurement-antennas_229504.html.
Accessed: 2019-04-07.

[108] ROSENBERGER.
http://www.rosenberger.de/en/products/automotive/fakra.php.
Accessed: 2017-12-01.

[109] A. R. RUDDLE, H. ZHANG, L. LOW, J. RIGELSFORD, AND R. J. LANGLEY, *Numerical investigation of the impact of dielectric components on electromagnetic field distributions in the passenger compartment of a vehicle*, in 2009 20th International Zurich Symposium on Electromagnetic Compatibility, Jan 2009, pp. 213–216.

[110] M. SCHACK, D. KORNEK, E. SLOTTKE, AND T. KURNER, *Analysis of channel parameters for different antenna configurations in vehicular environments*, in 2010 IEEE 72nd Vehicular Technology Conference-Fall, IEEE, 2010, pp. 1–5.

[111] H. SCHANTZ, *The Art and Science of Ultrawideband Antennas, Second Edition:*, Artech House antennas and propagation library, Artech House Publishers, 2015.

[112] S. SCHELKUNOFF, *Anatomy of "surface waves"*, IRE Transactions on Antennas and Propagation, 7 (1959), pp. 133–139.

[113] S. SCHELKUNOFF AND H. FRIIS, *Antennas: theory and practice*, Applied mathematics series, John Wiley & Sons, 1952.

[114] S. A. SCHELKUNOFF, *Advanced antenna theory*, John Wiley & Sons, 1952.

[115] M. SCHICK, R. FIEDLER, E. LEZAR, AND U. JAKOBUS, *Car-to-car communication using efficient far-field rcs simulations to account for reflecting objects in the communication path*, in 2012 6th European Conference on Antennas and Propagation (EuCAP), 2012, pp. 2039–2042.

[116] S. SENEGA, *Mehrdienstfähiges Antennendiversity für den mobilen Satellitenrundfunkempfang*, PhD thesis, Universitätsbibliothek der Universität der Bundeswehr, 2013.

[117] S. SENEGA, J. KAMMERER, AND S. LINDENMEIER, *Scan-phase antenna diversity for digital satellite radio (SDARS) in a single automotive side mirror*, in The 8th European Conference on Antennas and Propagation (EuCAP 2014), 2014, pp. 3255–3259.

[118] S. SENEGA AND S. LINDENMEIER, *Antenna module with integrated scan-phase antenna diversity system for SDARS*, in 2012 6th European Conference on Antennas and Propagation (EUCAP), 2012, pp. 2807–2810.

[119] S. SENEGA AND S. M. LINDENMEIER, *A fast switching antenna diversity system for improved mobile reception of digital radio signals of a geostationary satellite*, in Proceedings of the 5th European Conference on Antennas and Propagation (EUCAP), 2011, pp. 262–264.

[120] S. SENEGA, D. J. MÜLLER, L. M. REITER, AND S. M. LINDENMEIER, *A fast-switching diversity-and beam-forming-circuit for s-band satellite reception in fading scenarios*, in The 40th European Microwave Conference, 2010, pp. 648–651.

[121] S. SENEGA, A. NASSAR, AND S. LINDENMEIER, *Compact scan-phase antenna diversity system for high driving speeds*, in 2015 European Microwave Conference (EuMC), 2015, pp. 1459–1462.

[122] S. SENEGA, A. NASSAR, AND S. LINDENMEIER, *Automotive antenna diversity system for satellite radio with high phase accuracy in low SNR-scenarios*, International Journal of Microwave and Wireless Technologies, 10 (2018), pp. 578–586.

[123] S. SILVER, *Microwave Antenna Theory and Design*, Electromagnetics and Radar Series, IET, 1984.

[124] T. SMITS, S. SUCKROW, J. CHRIST, AND M. GEISSLER, *Active intelligent antenna system for car2car*, in 2013 International Workshop on Antenna Technology (iWAT), IEEE, 2013, pp. 67–70.

[125] A. SOMMERFELD, *Über die ausbreitung der wellen in der drahtlosen telegraphie*, Annalen der Physik, 333 (1909), pp. 665–736.

[126] J. E. STORER, *The impedance of an antenna over a large circular screen*, Journal of Applied Physics, 22 (1951), pp. 1058–1066.

[127] T. TAGA, *Analysis for mean effective gain of mobile antennas in land mobile radio environments*, IEEE Transactions on Vehicular Technology, 39 (1990), pp. 117–131.

[128] H. TAZI, C. ULLRICH, AND T. F. EIBERT, *Application of the finite volume time domain method for evaluation and development of wideband automotive antenna systems*, in Proceedings of the 5th European Conference on Antennas and Propagation (EUCAP), 2011, pp. 3048–3052.

[129] A. THIEL AND O. KLEMP, *Initial results of multielement antenna performance in 5.85 ghz vehicle-to-vehicle scenarios*, in 2008 38th European Microwave Conference, 2008, pp. 1743–1746.

[130] A. THIEL, O. KLEMP, A. PAIERA, L. BERNADÓ, J. KAREDAL, AND A. KWOCZEK, *In-situ vehicular antenna integration and design aspects for vehicle-to-vehicle communications*,

in Proceedings of the Fourth European Conference on Antennas and Propagation, 2010, pp. 1–5.

[131] T. VARUM, J. N. MATOS, P. PINHO, AND A. OLIVEIRA, *Printed antenna for DSRC systems with omnidirectional circular polarization*, in 2012 15th International IEEE Conference on Intelligent Transportation Systems, IEEE, 2012, pp. 475–478.

[132] R. VAUGHAN AND J. BACH ANDERSEN, *Channels, propagation and antennas for mobile communications*, Institution of Electrical Engineers, London, 2003.

[133] R. G. VAUGHAN AND J. B. ANDERSEN, *Antenna diversity in mobile communications*, IEEE Transactions on Vehicular Technology, 36 (1987), pp. 149–172.

[134] J. WAIT, *Preface to the surface wave papers*, IRE Transactions on Antennas and Propagation, 7 (1959), p. 132.

[135] Y. WANG, M. REIT, AND W. MATHIS, *Entwurfskonzept einer Car2Car-Multiband-Dachantenne*, Advances in Radio Science, 10 (2012), pp. 63–68.

[136] L. WARD AND M. SIMON, *Intelligent transportation systems using IEEE 802.11p. Rohde & Schwarz Application Note*, 2019.

[137] M. WESTRICK, M. ALMALKAWI, V. DEVABHAKTUNI, AND C. BUNTING, *A low-profile, low-cost antenna system with improved gain for dsrc vehicle-to-vehicle communications*, International Journal of RF and Microwave Computer-Aided Engineering, 23 (2013), pp. 111–117.

[138] Y. XIA AND J. LUO, *RHCP patch antenna for automotive DSRC system*, in 2010 6th International Conference on Wireless Communications Networking and Mobile Computing (WiCOM), IEEE, 2010, pp. 1–3.